Transition metal complexes with 1,2-dicarbonylhydrazine:

A study on mixed-valency and non-innocent ligand behaviour

Von der Fakultät Chemie der Universität Stuttgart

Zur Erlangung der Würde eines

Doktors der Naturwissenschaften

(Dr. rer. nat.)

genehmigte Abhandlung

Vorgelegt von

Sudipta Mondal

aus West Bengal, Indien

Hauptberichter: Prof. Dr. W. Kaim

Mitberichter: Prof. Dr. D. Gudat

Tag der mündlichen Prüfung: 30.04.2018

Institut für Anorganische Chemie der Universität Stuttgart

2018

To my parents……

Acknowledgements

Contents

Chapter 1

Introduction.

The "noninnocent" behaviour[1-7] of redox-active ligands in co-ordination compounds has drawn attention from the scientific community because its understanding established a vibrant area of research in connection with chemical transformations. In fact, "redox-noninnocent" ligands have emerged in diverse research platforms including catalysis[5], chemical biology[3e] and material science[6].

Among the library of "redox-noninnocent" ligands, azo (-N=N-) containing compounds[7] have played an important role in co-ordination chemistry, with azodicarbonyl ligands (adc-R) as one special example. The low-lying π* MOs centred on C=O and N=N form result from an unusual electron acceptor combination. This gives rise to a two-step redox system $(adc-R)^{0/\cdot-/2-}$ which contains a highly conjugated, stable radical intermediate and a fully reduced, resonance stabilised $(dihydrazido)^{2-}$ form (Scheme 1.1). Moreover, all these redox states can be monitored by structural identification, focusing especially on the N-N bond distance (Scheme 1.1) in respective complexes.[8]
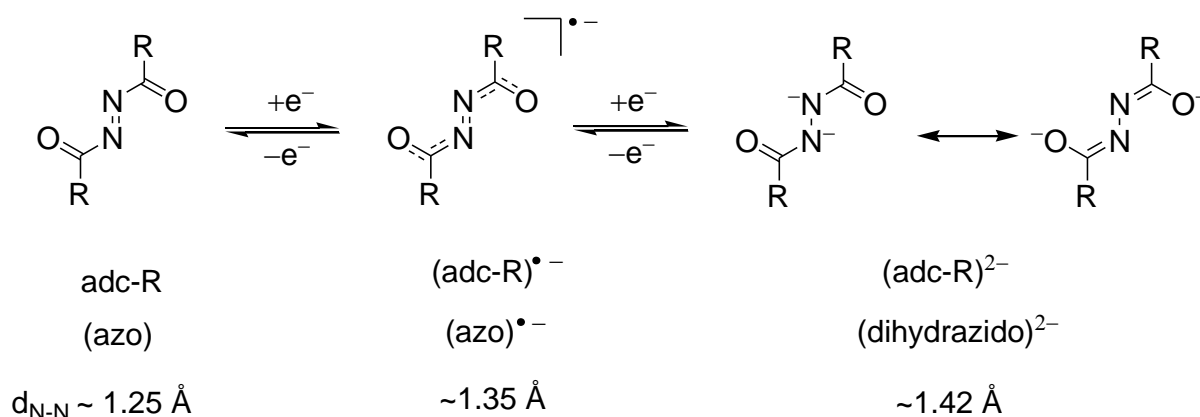
Scheme 1.1: Two-step redox system based on adc-R ligands.

All three members of the above mentioned redox scheme (Scheme 1.1) can bind one or two metal centres by forming mono- or bis(five-membered) chelate rings,

respectively. Scheme 1.2 shows the binding modes of the hydrazido(2−) form, L_n refers to the ancillary ligands. The fully reduced hydrazido state can be protonated to the 1,2-dicarbonylhydrazine (H_2adc-R) form.

.
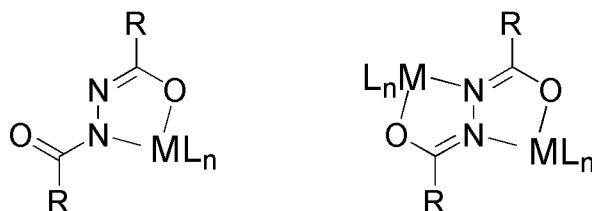
Scheme 1.2: Mononuclear and dinuclear metal complexes of (adc-R)$^{2-}$ ligands.

The first part of my thesis focuses on mononuclear complexes incorporating adc-R ligands. A remarkable metal-ligand interface involving the four-centre, two-step redox system with an N,O donor combination (O=C-X=N, X = C, N) results. This particular combination has been widely studied in o-quinonemonoimines (X=C) but there are very few reports with X=N.[9,10] Therefore, an effort in search for unusual redox properties of such systems in metal complexes has been made.

Chapter 2 deals with mononuclear complexes of ruthenium and osmium with 1,2-bis(pivaloyl)hydrazine (H_2adc-^{t}Bu). The hydrazido form, adc-^{t}Bu(2−), designated as L^{2-}, was combined with [Ru(bpy)$_2$]$^{n+}$ in different states. Singly protonated HL^-, methylated CH_3L^- and the radical anion $L^{\cdot-}$ give rise to three monocationic ruthenium complexes [Ru(bpy)$_2$(HL)]$^+$, [Ru(bpy)$_2$(CH$_3$L)]$^+$ and [Ru(bpy)$_2$(L)]$^+$, respectively. Chapter 2 mainly focuses on the electronic properties of the open-shell Ru complex and on comparing it with its Os analogue, [Os(bpy)$_2$(L)]$^+$, in combination with experimental and calculated results (Dr. V. Filippou). The studies of complexes with the protonated and methylated ligand provide further opportunities for comparison. All four complexes (Scheme 1.3) have been characterised by standard analytical techniques, cyclic voltammetry and UV-Vis-NIR-IR-spectroelectrochemical studies. X-band EPR spectroscopy has been used for the paramagnetic states.

[Ru(bpy)₂(HL)]⁺, X = H

[Ru(bpy)₂(CH₃L)]⁺, X = CH₃

[Ru(bpy)₂(L)]⁺

[Os(bpy)₂(L)]⁺
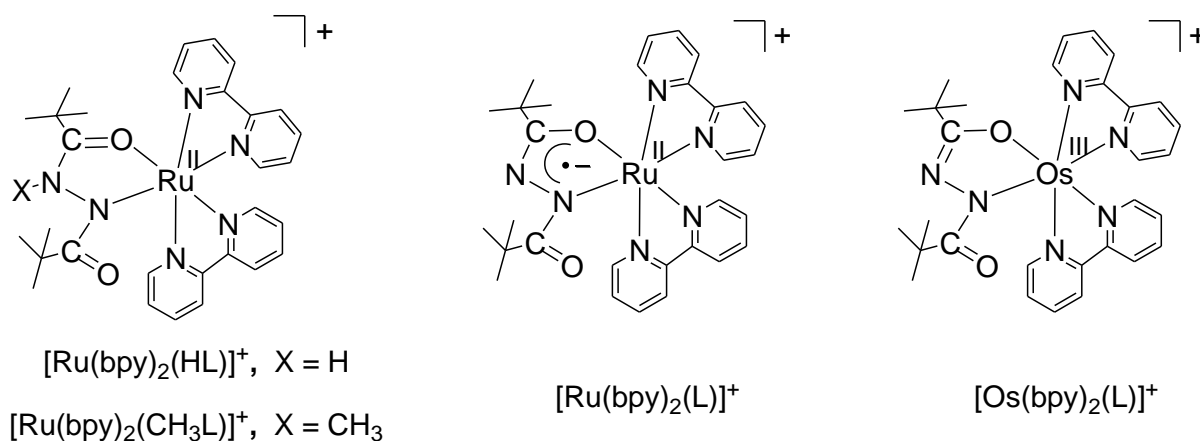
Scheme 1.3: Chemical structures of singly charged mononuclear complexes.

Dinuclear complexes of adc-R allow for metal-ligand-metal (M-L-M) arrangements, which are ideal in studying intra-molecular electron-transfer (ET) in mixed-valence (MV) complexes, exemplified by the Creutz-Taube ion (I) for which H.Taube received the Nobel Prize in chemistry in 1984.[11,12]

$(H_3N)_5Ru^{II}-N\bigcirc N-Ru^{III}(NH_3)_5$ $\rceil$ 5+   (I)
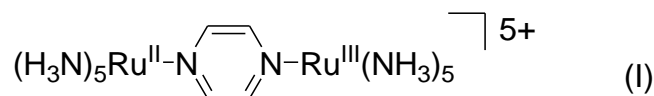
Mixed-valence is a fascinating concept that is applicable to a wide range of chemical compounds. For example, it comprises the smallest molecular ion H_2^+, minerals like magnetite ($Fe^{II}Fe^{III}_2O_4$), and the solid state pigment Prussian Blue, $Fe^{III}_4[Fe^{II}(CN)_6]_3.xH_2O$. Generally, MV systems are viewed as molecules or materials in which two or more redox centres are present in different formal oxidation states, potentially bridged by an organic component. A discrimination may arise between inorganic and organic MV systems when formal oxidation states differ by more than one electron. In this situation, organic MV systems remain closed-shell in their ground state and are then classified as donor-acceptor compounds.[13] However, the present thesis will be restricted to inorganic MV systems where the formal oxidation states vary by one unit, leading to an open shell system (especially low spin d^5/d^6) like the Creutz-Taube ion. In such systems, the ET process occurs between two metal centres, and the bridging unit plays an important role in mediating the charge or electron transfer. For example, in case of the ion (I), an electron-transfer mechanism is believed to involve a low-lying π^* orbital centred on the pyrazine, an

acceptor bridge. On the other hand, such processes can also follow a hole-transfer route in the case of an electron-rich bridging ligand, if a corresponding ligand π orbital is available for electron transfer. As a result, enormous efforts[14-18] have been made in search for acceptor and donor bridging units. Non-innocence aspects of the bridging or terminal ligands extend the research to another level, giving rise to rich electrochemical properties.[19-21] Besides, the ET event is a key step in biological processes and several systems (e.g., photosystem II, cytochrome c oxidase, ferredoxins, etc.) involve an MV intermediate state for that.[22-25] Consequently, the research area on MV systems has become more and more active as new branches started opening. An important such field is Molecular Electronics. The extent of electron transfer between two or more redox centres has been used to create various molecular electronic devices.[26,27] Moreover, the importance of MV systems is clearly reflected by the huge number of review articles from different scientific communities.[28-34]

Many low spin d^5/d^6 MV complexes exhibit characteristical absorptions in the near-infrared (NIR) region as was observed for the Creutz-Taube ion at around 1570 nm. Such low energy absorptions result from the electronic coupling between two metal centres and are defined as inter-valence-charge-transfer (IVCT) transitions. Based on Marcus and Hush theory,[35,36] (R. A. Marcus was awarded the Nobel Prize in 1992)[35b] the NIR absorption parameters such as width, shape, intensity and energy of the bands have been considered as most powerful to understand the factors which govern the activation barrier of intra-molecular inter-metallic electron transfer. An important issue gradually arising concerns dinuclear MV complexes with a "redox-noninnocent" bridging ligand. Both possible electronic alternatives, mixed-valent $M^nBL^mM^{n+1}$(localised or delocalised) and radical bridged, $M^nBL^{m+1}M^n$, can produce the NIR absorption. Under these circumstances, EPR spectroscopy serves as an important tool to distinguish between metal- or ligand-centred spin.[32b] In this regard, ^1H NMR spectroscopy is an another useful but not frequently used method. Although the substances under investigation may be paramagnetic, it is possible to detect highly shifted (downfield or upfield) NMR signals if the rate of electron spin relaxation becomes fast enough for nuclear relaxation in solution. In dinuclear systems, such as the biferrocenium salt, this method has been applied successfully to elucidate the nature of metal-ligand bonding and electron distribution in the mixed-valence state.[37] Other spectroscopic methods include infrared (IR)[38,39], Mössbauer[40] and

electroabsorption (Stark effect) spectroscopy[41] according to their applicability in respective cases. The energies and the time scales of the various spectroscopic techniques are quite different. Such differences need to be considered when discussing the ET process because there are MV examples which exhibit different behaviour on different time scales of the experimental techniques.[33] Such examples have been described as a borderline situation between charge localisation and delocalisation, and they usually have very low ET activation barriers. Instead of spectroscopic data, the comproportionation constants (K_c) of the MV states are also being used in assessing the degree of electronic coupling. Nevertheless, these electrochemical parameters show discrepancies in several cases, which were discussed recently in a review article.[42] Furthermore, a review of a series of diruthenium complexes clearly states that the coordination situation must be taken care of, along with electrochemical and spectroscopic results, to describe the localisation vs. delocalisation situation in MV systems.[14]

In contrast to several mixed-valence units bridged by atomic ions, by bis-monodentate ($\mu,\eta^1{:}\eta^1$) or by bis-bidentate ($\mu,\eta^2{:}\eta^2$) chelate ligands, investigations on bis-tridentate ($\mu,\eta^3{:}\eta^3$) linkers are still rare.[14,50,94] Increase in denticity facilitates multiple metal-ligand donor interactions and consequently affects metal-metal communication. Also, efforts in constructing an asymmetric dinuclear unit are not as common as symmetric examples. There are relevant examples on heterobimetallic[43,44] systems but incorporation of ligand asymmetry can also give rise to interesting properties such as mixed-valence isomerism.[45] The adc-R($2-$) ligands can be useful in this regard, and diruthenium mixed-valent complexes with such π-donor bridges have exhibited strong NIR absorptions similarly to the Creutz-Taube ion.[46] The adc-R ligand family is of significance in coordination chemistry because of its possible *cis/trans/cis* (S-Frame[47]: Scheme 1.2) arrangement, which allow two metals to be connected at a very short distance (< 5 Å)[48]. Electronic properties of these ligands can be greatly tuned by varying the substituent R (e.g. R = NR_2, OR, alkyl, aryl). In addition, it is also possible to introduce additional co-ordinating arms like 2-pyridyl or 2-phenoxide moieties as R. In this way, extending the number of chelate denticity can effect interesting electronic and geometrical features. 1,2-Dicarbonylhydrazine molecules as in Scheme 1.4 were used in synthesising different diruthenium complexes in this doctoral work. Several of these hydrazine molecules,

especially aryl substituted ones, were studied earlier in the development of new HIV-1 integrase inhibitors or as antitumor agents.[49] The newly synthesised dinuclear complexes involving electron transfer active $[Ru(trpy^*)]^{n+}$ (trpy* = 4,4′,4″-tri-*tert*-butyl-2,2′:6′,2″-terpyridine) or $[Ru(bpy)_2]^{n+}$ fragments were studied by various spectroscopic and electrochemical techniques.

1,2-bis(trifluoroacetyl)hydrazine
H_2adc-CF_3

1,2-bis(benzoyl)hydrazine
H_2adc-Ph

1,2-bis(salicyloyl)hydrazine
H_4adc-Sal

1-benzoyl-2-salicyloylhydrazine
H_3adc-Salph

1,2-bis(picolinoyl)hydrazine
H_2adc-Py
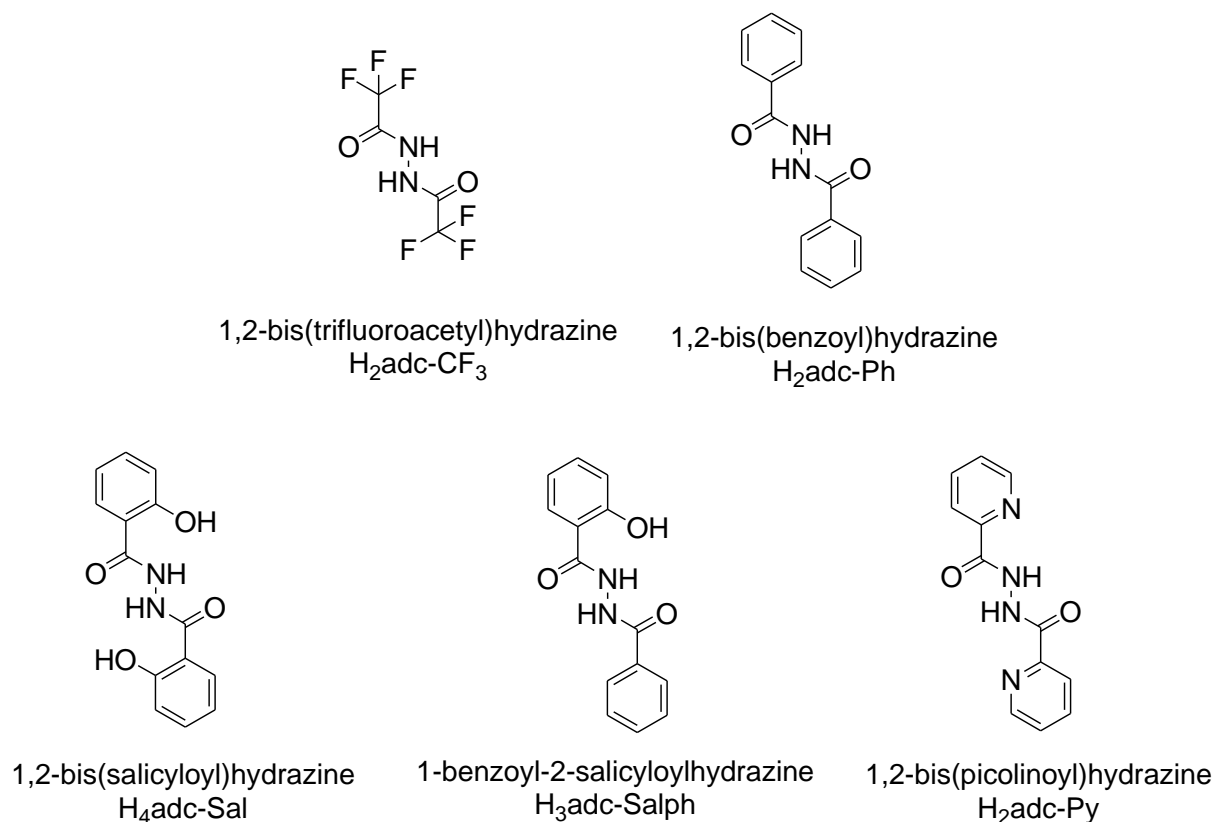
Scheme 1.4: Hydrazine forms of the ligands used for synthesising dinuclear complexes.

Chapter 3 describes diruthenium complexes of adc-R(2−) (R= Ph, CF_3), from which the complex $[\{(trpy^*)ClRu\}_2(\mu,\eta^2:\eta^2$-adc-$CF_3)]$ was reported earlier in the bachelor thesis of Lorenz Fahrner. The aim of this chapter was to bridge two $[Ru(trpy^*)Cl]^{n+}$ centres by bis-bidentate N,O coordinating adc-R(2−) ligands, and to study the changes in structural and spectroelectrochemical properties due to different R groups. All experimental methods (except IR spectroscopy) as utilised in Chapter 2 were being re-implemented in this chapter.

Chapter 4 highlights the diruthenium complex of the bis-tridentate bridging ligand adc-Sal(4−). The potential of the bridging ligand in mediating metal-metal interaction will be discussed for the mixed valence monocation, $[\{(trpy^*)Ru\}_2(\mu,\eta^3:\eta^3\text{-adc-Sal})]^+$. Theoretical calculations (TD-DFT, Dr. S. Záliš / Prague) and useful experimental methods have been applied to study the monocation structurally, spectroscopically and electrochemically.

In Chapter 5, aspects of non-symmetrical bridging ligands in mixed-valent complexes have been emphasised. One such ligand adc-Salph(3−) with $\mu,\eta^2:\eta^3$ coordination was employed to synthesise and structurally characterise a mixed-valent species, $[(trpy^*)Ru(\mu,\eta^2:\eta^3\text{-adc-Salph})Ru(trpy^*)Cl]PF_6$. With the help of spectroscopic (UV-Vis-NIR, EPR) analysis of the complex an insight will be given on mixed-valency in asymmetrical dinuclear units.

Chapter 6 comprises the idea of different coordination modes of the ligand adc-Py(2−): twisted bis(N,N') and planar bis(N,N',O) coordination (A and B, respectively in Scheme 1.5). Two complexes were prepared from precursor complexes *cis*-Ru(bpy)$_2$Cl$_2$ and Ru(trpy*)Cl$_3$, representing A and B, respectively. Both of them have been studied by UV-Vis-NIR and IR spectroelectrochemistry to examine the intra-molecular metal-metal coupling in the mixed-valence states, especially where the bridging ligand can freely rotate at the N-N bond. A difference in electronic situations will be sought in the mixed-valence states with bis(N,N'O) and bis(N,N') bridging ligand coordination.
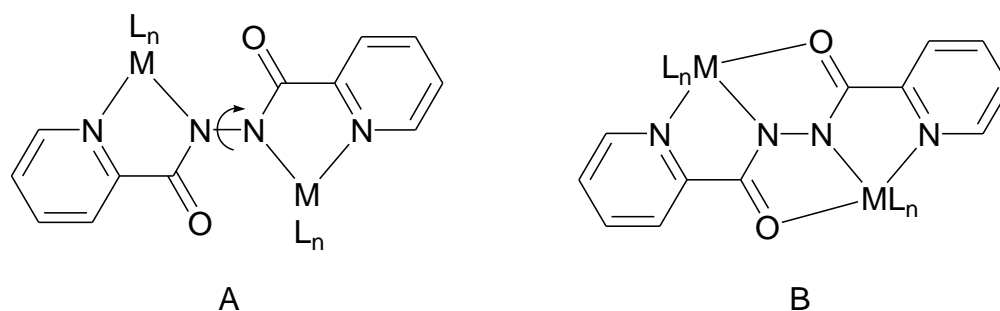
Scheme 1.5: Representation of different binding modes of adc-Py(2−).

The research goal was aimed at developing new MV systems with variable ligand (adc-R) coordination and at exploring the effect of electron transfer on metal/ligand oxidation states in different dinuclear as well as in mononuclear complexes.

Chapter 2

Mononuclear complexes with the non-innocent N,O-chelating ligand 1,2-bispivaloylhydrazido($2-$) = L^{2-} in its protonated (HL^-), oxidised radical ($L^{\cdot-}$) and methylated (CH_3L^-) state.

2.1 Introduction.

Transition metal complexes with non-innocent azodicarbonyl (adc-R) ligands have been studied for several years.[48,50b,51,53] These ligands are very much prone to ligate two metal centres in an S-frame fashion by bis-N,O chelation which makes them popular in mixed-valence chemistry. In contrast, very few reports[54,10] on corresponding mononuclear complexes can be found in the literature until now, even though it is possible to isolate such complexes by introducing steric hindrance to the metal surroundings and thus disturbing the S-frame coordination. The 1,2-bispivaloylhydrazido ligand (L^{2-}) might be an interesting choice because the bulky *tert*-butyl group (^tBu) as substituent R can create the required hindrance (Scheme 2.1.1).
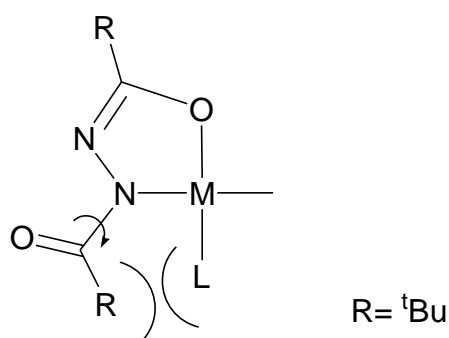
$R= {}^tBu$

Scheme 2.1.1

The L^{2-} ligand belongs to a redox series of rather uncommon composition, RNNC(R´)O (R= C(O)^tBu and R´= ^tBu), among N,O-coordinating non-innocent ligands. Scheme 2.1.2 represents a series where an M^{II} centre is interacting with different ligand redox states L^{2-}, $L^{\cdot-}$ and L^0, forming neutral, monocationic and dicationic complexes, respectively. The principal interest of this report lies in the

synthesis and characterisation of the intermediate monocationic species with the radical $L^{\cdot-}$. Especially the charge distribution at the metal-ligand interface has been investigated by EPR and UV-Vis-NIR spectroscopy. It has become a challenge in coordination chemistry to provide a proper electronic description for such open shell systems where frontier metal and ligand orbitals are of similar energy.[55]

M = Ru, Os   R' = ^tBu
                  R = C(O)^tBu
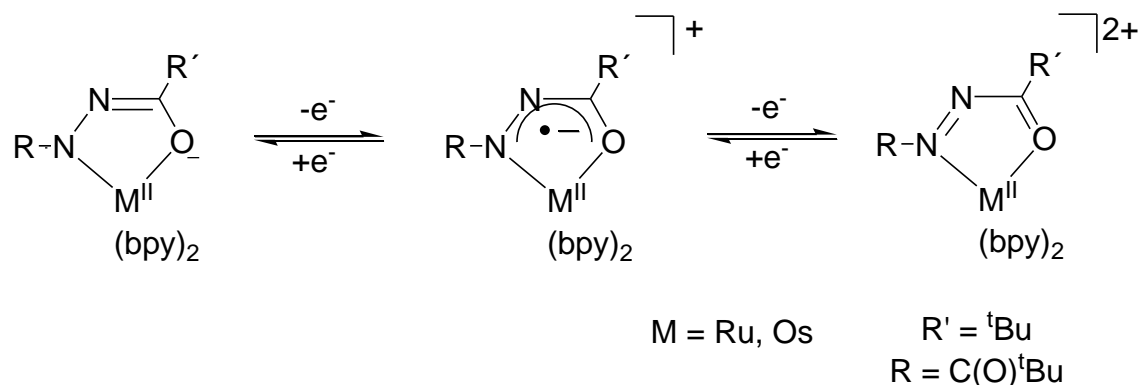
Scheme 2.1.2: Representation of different charged species $[M(bpy)_2(L)]^{0/+/2+}$ incorporating different ligand redox state ($L^{2-/\cdot-/0}$).

Metal-ligand redox behaviour can be manipulated by several means. For example, the donor or acceptor properties of a co-ligand, like 2,2'-bipyridine (bpy) in the present case, can significantly influence the charge on the metal.[56] Similarly, periodic trends of metal d-orbital energy also may have a significant effect on the charge distribution. There are reports on transition metal complexes containing quinonoid ($Q^{2-}/Q^{\cdot-}/Q^0$) ligands where the semiquinone state ($Q^{\cdot-}$) is being stabilised gradually in $M^n(Q^{\cdot-})_m$ / $M^{n+m}(Q^{2-})_m$ as the d-orbital energy decreases.[57] This feature has motivated us to do a comparative study of ruthenium and osmium complexes in this report.

The ligand L^{2-} exists in its doubly protonated form as 1,2-bispivaloylhydrazine (H_2L / H_2adc-^tBu). Singly protonated HL^- can coordinate a metal centre as depicted in Scheme 2.1.3. There are two equivalent N-H groups in the hydrazine molecule H_2L, coordination through one N atom makes them uneven. As a result, the attached proton becomes more acidic and easy to deprotonate in comparison with the non-coordinated N-H. The protonated ruthenium complex (Scheme 2.1.3), another monocation thus obtained, consists an amide moiety (-NHC(O)-) which coordinates

through O atom. Such type of amide coordination has been found in several biological systems.[58]
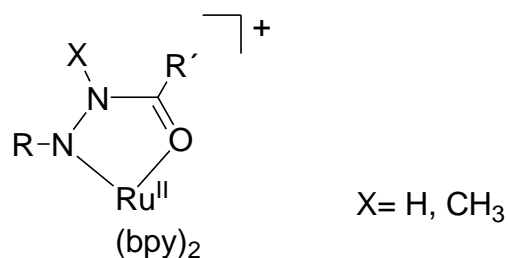
Scheme 2.1.3: Binding mode of the protonated (HL⁻) and the methylated (CH₃L⁻) ligands in [Ru(bpy)₂(XL)]⁺.

The study has been extended to include one N-methylated ligand CH₃L⁻ (Scheme 2.1.3). The comparison of the two mononuclear complexes with HL⁻ and CH₃L⁻ with regard to their respective spectroelectrochemical behaviour will give further insight in understanding the redox properties of the complexes with L·⁻.

2.2 Syntheses and characterisation.

The protonated complex [Ru(bpy)₂(HL)]PF₆ ([1.H]PF₆) was obtained with a reasonable yield (60 %) by reacting *cis*-Ru(bpy)₂Cl₂ and H₂adc-ᵗBu (H₂L) in presence of one equivalent of sodium hydroxide as described in Scheme 2.2.1. Similarly, [1.H]ClO₄ was synthesised by using the perchlorate salt (NaClO₄) instead of KPF₆ to precipitate the desired singly charged complex from a concentrated ethanol solution. Use of excess base (>1eq) always resulted a green coloured, oxidised species, [Ru(bpy)₂(L)]PF₆ ([1]PF₆) and a blue coloured, dinuclear complex [{Ru(bpy)₂}₂(L)](PF₆)₂ as side products. [Ru(bpy)₂(CH₃L)]PF₆ ([1.CH₃]PF₆) was formed after treating [1.H]PF₆ with excess methyl iodide in CH₃CN in presence of sodium hydroxide as a base. This method resulted the methylated complex with a good yield (around 80%) under an inert atmosphere, which reduces the probability of the formation of [1]PF₆. The product was purified by column chromatography (neutral alumina) to obtain a rose red coloured solid substance. Protonated and methylated

complexes have been characterised by mass spectroscopy and elemental analysis (Chapter 7.3.1). These complexes were not characterised structurally as single crystals suitable for the X-ray crystal structure analysis were not found. [1.H]PF$_6$ and [1.CH$_3$]PF$_6$ have been identified by NMR (^{1}H and ^{13}C) spectroscopy. The ^{1}H NMR spectrum of [1.H]PF$_6$ shows a signal at 11.79 ppm corresponding to N-H while the N-CH$_3$ protons from the methylated species are resonating at 2.73 ppm in CD$_2$Cl$_2$ (Figure 2.2.1). Protons from the *tert*-butyl (C(CH$_3$)$_3$) and pyridyl groups give resonances at characteristic chemical shifts in the alkyl and aromatic regions, respectively, for both complexes. A calculated number of sixteen overlapping resonances have been found in the aromatic region. They are supposedly composed of doublet (eight protons) and triplet (eight protons) signals for the marked protons (3,6 and 4,5, respectively) in Scheme 2.2.1. A few of these signals can be assigned (Figure 2.2.1; without specifying pyridyl groups) by following the chemical shift behaviour of the protons from Ru(bpy)$_2$ fragment in reported complexes.[67] However, the absence of an N-H signal for [1.CH$_3$]PF$_6$ indicates that the proton at the N atom has been methylated.
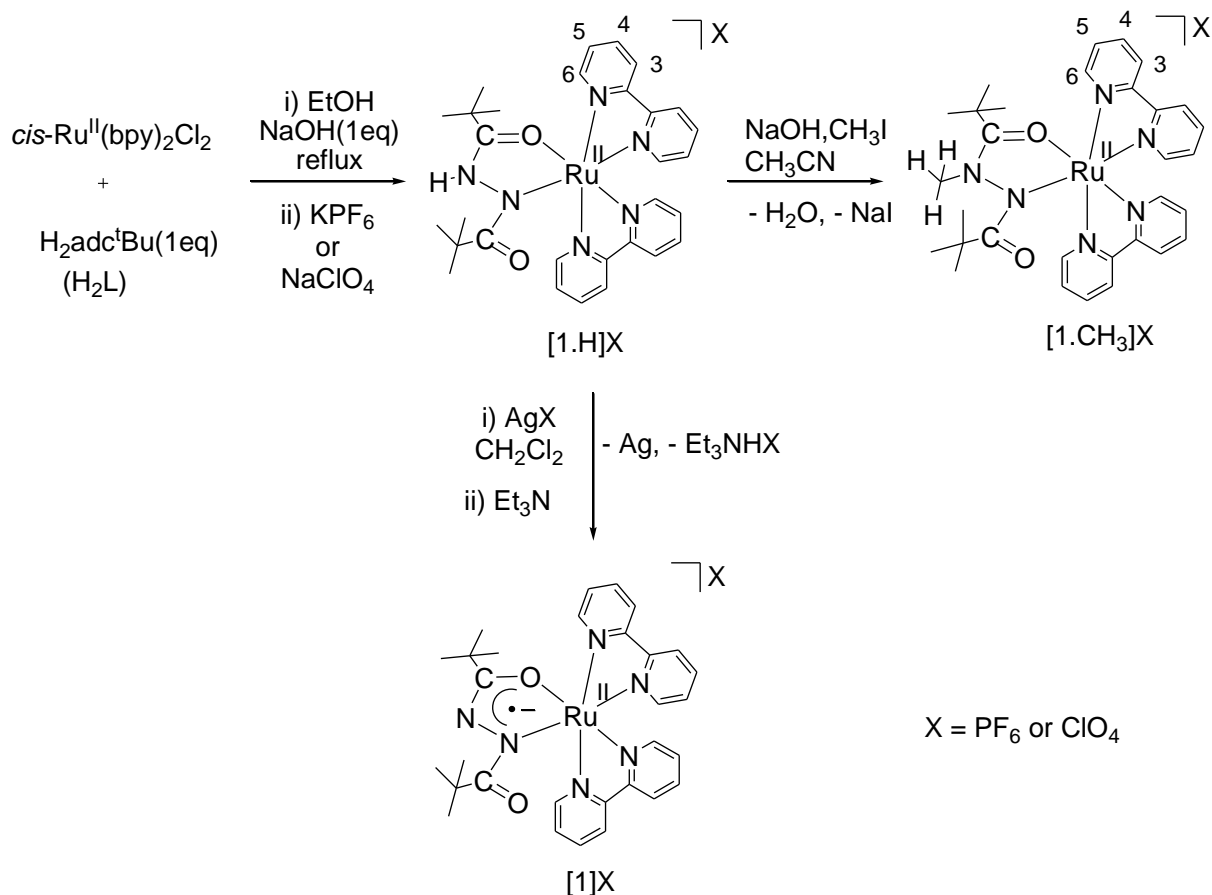
Scheme 2.2.1: Reaction scheme for mononuclear ruthenium complexes.
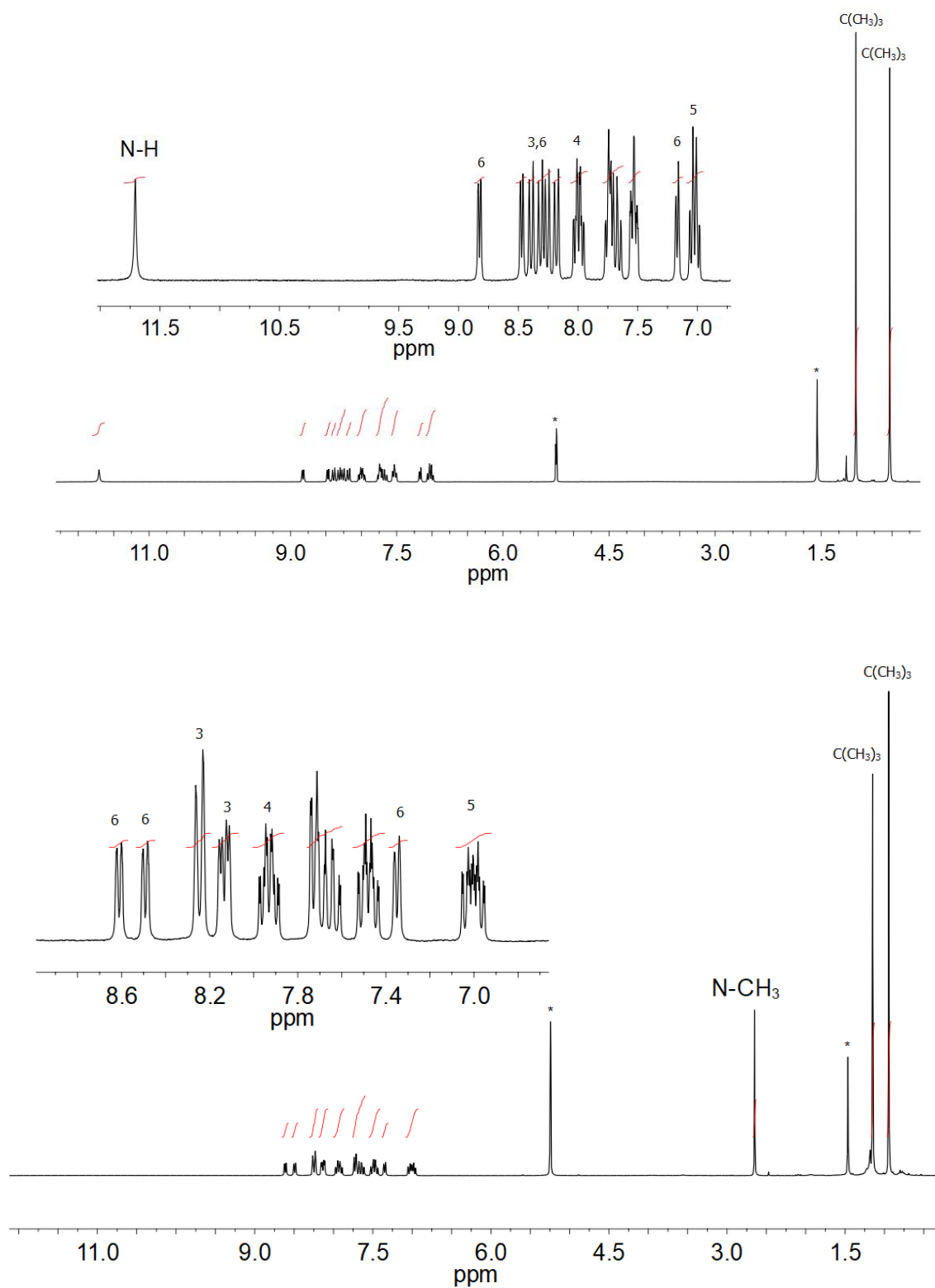
Figure 2.2.1: ^{1}H NMR spectra of [1.H]PF$_6$ (top) and [1.CH$_3$]PF$_6$ (bottom) in CD$_2$Cl$_2$ at 250 MHz. *Signals from solvent residual.

Also in ^{13}C NMR, a signal assigned to N-CH$_3$ has appeared for [1.CH$_3$]PF$_6$. Otherwise, signals related to *tert*-butyl, bpy and O=C-N-N-C=O backbone exhibit similar trend for both protonated and methylated complexes. A general assignment of these signals has been made in Figure 2.2.2. The sharp resonances in both ^{13}C and ^1H NMR spectra confirm the diamagnetic nature of [1.H]PF$_6$ and [1.CH$_3$]PF$_6$.
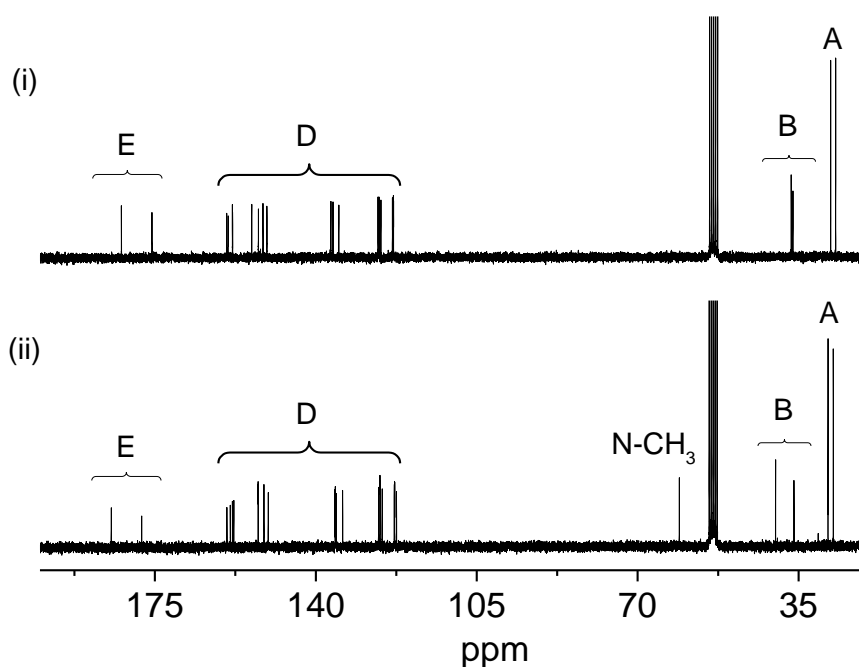
Figure 2.2.2: ^{13}C NMR spectra of [1.H]PF$_6$ (i), [1.CH$_3$]PF$_6$ (ii) in CD$_2$Cl$_2$.

A = CH$_3$ of ^{t}Bu, B = C of ^{t}Bu, D = C of bpy, E = C=O

The paramagnetic Ru complexes, [1]PF$_6$ and [1]ClO$_4$, and their Os analogue, [2]PF$_6$, have been synthesised as described in Scheme 2.2.1 and 2.2.2, respectively. The protonated complex, [1.H]PF$_6$ and [1.H]ClO$_4$ were oxidised with a silver salt followed by addition of Et$_3$N as a base to generate the Ru complexes, [1]X (X= (PF$_6$)$^-$ or (ClO$_4$)$^-$). On the other hand, the corresponding Os complex was prepared directly from *cis*-Os(bpy)$_2$Cl$_2$ in a refluxing EtOH/H$_2$O mixture in the presence of the base (≥ 2eq) and elemental analysis confirmed a mono-cationic oxidised species [2]PF$_6$. The reaction has been done under atmospheric condition, allowing the oxidised product to be formed by areal oxidation. It was possible to isolate and purify the complex, [2]PF$_6$ by column chromatographic separation (Chapter 7.3.2). Due to their paramagnetic nature, it was not possible to obtain high-resolution ^1H NMR

resonances, but they have been characterised by single crystal analysis and EPR spectroscopy.
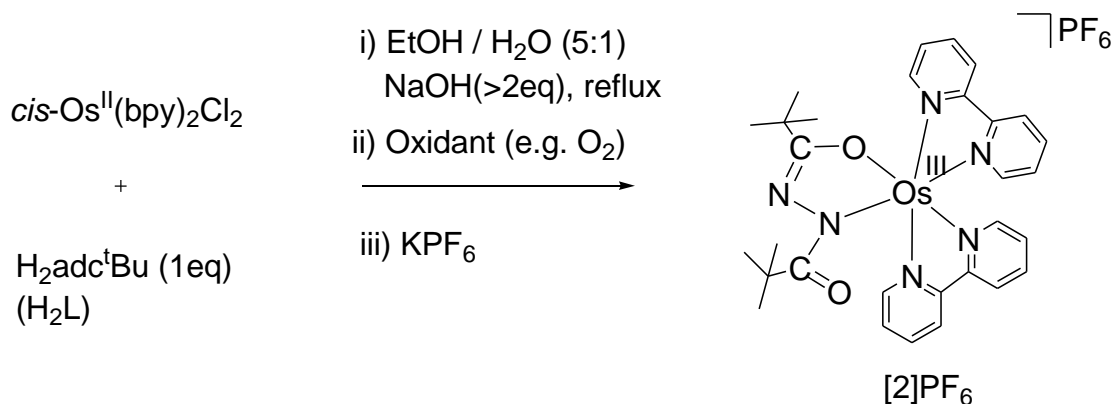
Scheme 2.2.2: Reaction scheme for mononuclear osmium complex.

2.3 Crystal structures.

Single crystals for [1]ClO$_4$ suitable for x-ray diffraction were grown by slow diffusion of Et$_2$O into a CH$_2$Cl$_2$ solution of [1]ClO$_4$. Crystals of [2]PF$_6$ were grown in DCE by slow evaporation at around -8°C. Molecular structures are shown in Figure 2.3.1. In case of the Os complex, two independent molecules (A and B) with very similar geometry have been found in the asymmetric unit. Crystallographic data are given in Chapter 7 (Table 7.4.1).

As mentioned earlier in Chapter 1, the ligand redox states of adc-R might be identifiable by their characteristic N-N bond distances. Additionally, M-O$_{adc-R}$ and M-N$_{adc-R}$ distances can also help to determine the electronic structure of a complex. But often, the high extent of metal-ligand orbital mixing makes the situation hard to interpret and thus structural data become less informative, similar to the situation in complexes with quinone ligands.[57b] In particular, complications arise for the odd electron species, in this case the monocation (Scheme 2.1.2), where three electronic descriptions are possible, localised $M^{II}L^{\cdot-}$ and $M^{III}L^{2-}$ or a completely delocalised ($M^{II}L^{\cdot-}$ <–> $M^{III}L^{2-}$) situation. Selected bond lengths and dihedral angles with DFT calculated values for comparison are summarised in Table 2.3.1 for [1]ClO$_4$ and [2]PF$_6$. N-N distances fall near the borderline between reported radical (1.35 Å) and

fully reduced dihydrazido^{2-} (1.45 Å) states.[9,48,71] Bond lengths from the chelating N,O ligand and M-O$_{coordinated}$, M-O$_{free}$ or M-N distances are almost identical in both Ru and Os complexes. The C-N bond lengths in- and outside of the chelate ring exhibit considerable differences of around 0.07 Å. This signifies that the exocyclic C=O group is not properly conjugated with the chelate ring. The dihedral angles listed in Table 2.3.1 suggest the same. The distortion from the coplanar configuration creates interruption of ligand conjugation. Nevertheless, the structural analyses depict an intermediate values between the fully oxidised dication and the reduced neutral species but it fails to reach conclusive evidence for the electron distribution.
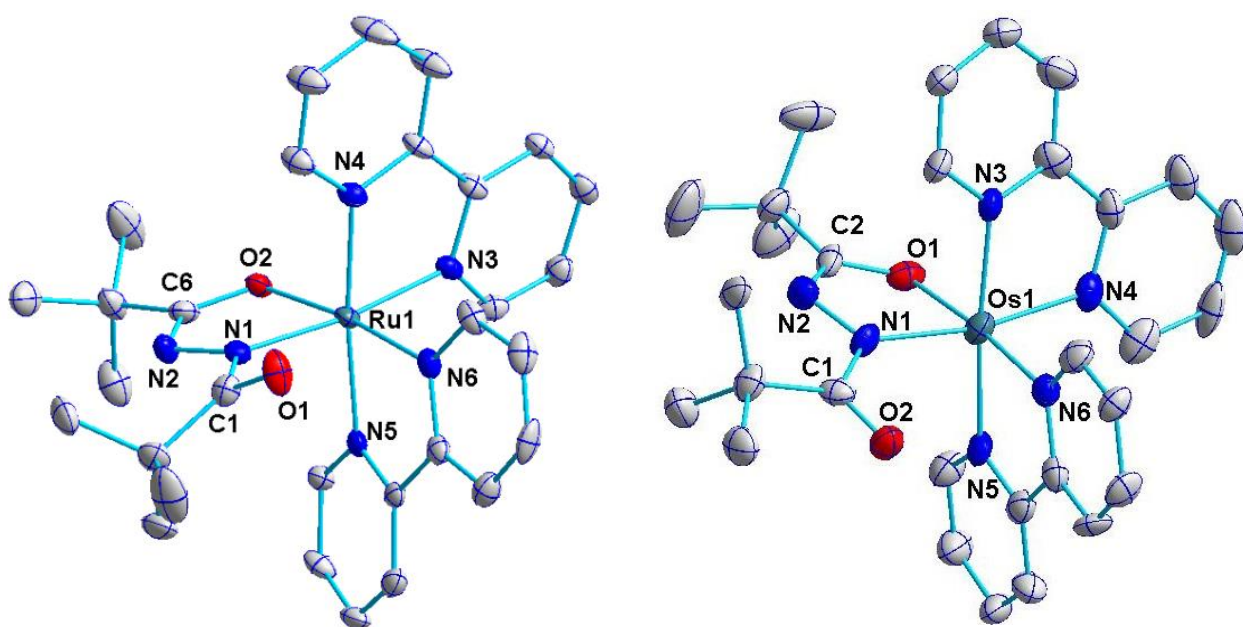
Figure 2.3.1: Molecular structures of the cation in the crystal of [1]ClO$_4$ (left) and the cation B in the crystal of [2]PF$_6$ (right). Thermal ellipsoids are shown at the 50% probability level; hydrogen atoms are omitted for clarity.

Table 2.3.1: Selected experimental and *in vacuo* DFT calculated bond lengths (Å) and torsion angles (º) of [1]ClO₄ and [2]PF₆.
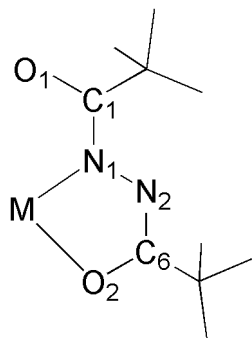
	M = Ru		M = Os		
Bond	Exp.	Calc.	Exp.(A)	Exp.(B)	Calc.
$M-O_2$	2.055(2)	2.051	2.048(7)	2.053(6)	2.054
$M-N_1$	1.999(3)	2.015	1.999(7)	1.991(8)	2.011
C_6-O_2	1.295(4)	1.301	1.325(11)	1.328(11)	1.311
C_1-O_1	1.215(4)	1.229	1.237(11)	1.223(11)	1.229
N_1-N_2	1.385(3)	1.351	1.386(10)	1.393(10)	1.369
C_1-N_1	1.397(4)	1.418	1.386(12)	1.384(12)	1.418
C_6-N_2	1.325(4)	1.335	1.325(12)	1.311(12)	1.325
$M-O_1$	3.286	3.262	3.237	3.268	3.230
Torsion angle					
$O_2-C_6-N_2-N_1$	1.8(4)	0.6	-1.5(13)	1.8(12)	2.53
$N_2-N_1-C_1-O_1$	-158.6(3)	-159.8	162.8(8)	171.9(8)	164.1
$M-N_1-C_1-O_1$	30.5(4)	15.5	-11.3(13)	-5.4(12)	-11.98

2.4 EPR spectroscopy.

2.4.1 Theory.

EPR is a necessary and powerful tool to characterise paramagnetic molecules. It gives information about the location of the electron spin, e.g., whether it is metal or

ligand centred in a complex. In the present study of [1]PF$_6$ and [2]PF$_6$ there are several possibilities of electron spin distribution between a d^5 metal centre and an anion radical ligand L$^{\cdot-}$ as mentioned in the previous section. Before going to any detailed analysis, a short discussion on the three sources of information from EPR spectroscopy will be given from a theoretical point of view.

a) The isotropic g value: When a free electron is placed inside a molecule, it causes a deviation of the value for the free electron, g$_e$, to the value of the whole molecule, g. This change, which is comparable to the chemical shift in NMR is due to the spin orbit coupling contribution from excited states to the radical ground state. The magnitude of such contribution is directional because of different orbital orientations and depends upon the size of involved nucleus. Thus, a larger shift of g from g$_e$ will be expected for transition metals than for organic free radicals. Stone's approximation[59] explains the phenomenon that is described in the following equation.

$$g = g_e - \frac{2}{3}\sum_i\sum_n\sum_{kj}\frac{\langle\Psi_0|\xi_k L_{ik}\delta_k|\Psi_n\rangle\langle\Psi_n|L_{ij}\delta_j|\Psi_0\rangle}{E_n - E_0} = g_e + \Delta g_s$$

g$_e$ = 2.0023

Ψ_0 : MO of the unpaired electron in the ground state

Ψ_n : all other MOs

ξ_k : spin-orbit coupling constant

$L_{ik/ij}$: angular momentum operator for AO at nucleus *k,j*

$L_{ik}\delta_k$ = 0 except at atom k

E$_0$: energy of a singly occupied molecular orbital (SOMO)

E$_n$: energies of empty or doubly occupied molecular orbitals (LUMO or HOMO)

Apart from the involvement of a spin orbit coupling function, the equation also defines the sign of the shift considering the denominator part. As significant contributions only arise from neighbouring levels, two possible conditions are

i)   SOMO is closer to HOMO (E$_0$ > E$_n$): Δg_s is positive,

ii) SOMO is closer to LUMO (E$_n$ > E$_0$): Δg_s is negative.

On the other hand, the g factor is anisotropic. However, in a low viscosity solution, due to fast molecular rotation, the anisotropy is averaged out and an isotropic g value is observed.

b) The g anisotropy: In a powder or in a frozen solution molecular rotation is inhibited resulting in three principal g values in a EPR signal (first derivative Spectrum). Depending upon molecular symmetry, it can be axial ($g_x = g_y \neq g_z$) or rhombic ($g_x \neq g_y \neq g_z$). By convention, g values are expressed as $g_\perp$ and $g_{\parallel}$ or as g_1, g_2 and g_3. The g anisotropy, Δg (g_1-g_3), is an important parameter for a transition metal centred spin. Due to rapid spin relaxation, which originates from high spin orbit interaction, compounds with the heavier transition metals are often EPR silent in solution.

c) The hyperfine coupling: The interaction between the unpaired electron and a nucleus with nonzero spin is called hyperfine coupling. The magnitude of this coupling is defined by a coupling constant (A), generally expressed in G or mT. An idea of spin distribution in a molecule could be understood by the nature of hyperfine splitting and the magnitude of the coupling constant. The nature of the splitting depends upon the number of coupling nucleus and corresponding nuclear spin, while the magnitude is related with the amount of spin density at the coupling nucleus. But a substantial amount of metal hyperfine coupling can result insufficient data. Due to a large line width, well resolved hyperfine splitting is often being concealed in case of transition metal complexes.

2.4.2 Results and discussion.

The paramagnetic monocationic ruthenium complex [1]PF$_6$ shows an isotropic EPR signal at g = 2.027 in CH$_2$Cl$_2$ solution at 298 K (Figure 2.4.1). The positive deviation from the free electron g value ($\Delta g_s \approx 0.024$) indicates a ligand-based SOMO with some metal contribution. A metal hyperfine coupling (^{99}Ru, I = 5/2, 12.7 % nat. abundance; ^{101}Ru, I = 5/2, 17.0 % nat. abundance)) of 13 G has been observed as compared to similar ruthenium bipyridyl complexes with ligand centred spin.[60] This observation is also supported by the DFT calculated spin density plot (Figure 2.4.3) with 29 % of total spin density on Ru. The complex also exhibits a rhombic EPR signal at 110 K with $\Delta g = 0.145$ in frozen CH$_2$Cl$_2$ solution. This g anisotropy value is

quite large (Δg > 0.1). In fact, it exhibits an identical situation as reported for Ru(acac)$_2$ complexes of α-azocarbonyl (L$_O$) or α-azothiocarbonyl (L$_S$) ligands.[9] The data are summarised in Table 2.4.1 to give a comparison with the present system which can be better explained as a valence delocalised formulation Ru^{II}(bpy)$_2$L$^{·-}$ <–> Ru^{III}(bpy)$_2$L^{2-}. It is clear from the comparison that the π donor co-ligand (acac) was mainly responsible for stabilising the higher metal oxidation state in previous report. The high π acceptance of the ligand L$^{·-}$ is considered to be a dominant factor in the present case.

In contrast to the ruthenium complex, the Os complex [2]PF$_6$ is EPR silent at 110 K. Instead, It displays a rhombic EPR signal at 5 K (Figure 2.4.2) with a high g anisotropy value of 1.104 (Table 2.4.1). Such a high value exhibits an effect of large spin-orbit coupling and suggest dominant metal participation in the SOMO.[68] Accordingly, the DFT-calculated 46 % of spin density on the Os atom allows a formulation Os^{III}(bpy)$_2$L^{2-} for the monocation in comparison to the Ru counterpart. It is not unprecedented that 5d elements stabilise higher metal oxidation states more than their 4d analogues in a situation like (bpy)$_2$M^{II}(L$^{·-}$) / (bpy)$_2$M^{III}(L^{2-}).[57b]
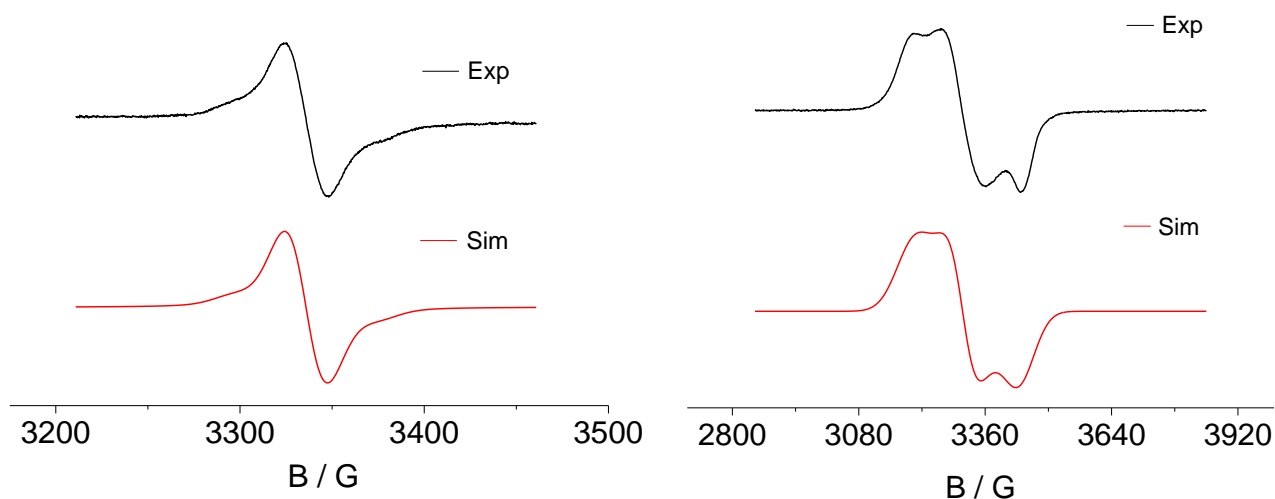
Figure 2.4.1: EPR spectra of [1]PF$_6$ in CH$_2$Cl$_2$ at 298K (left) at 110K (right) with computer simulation.
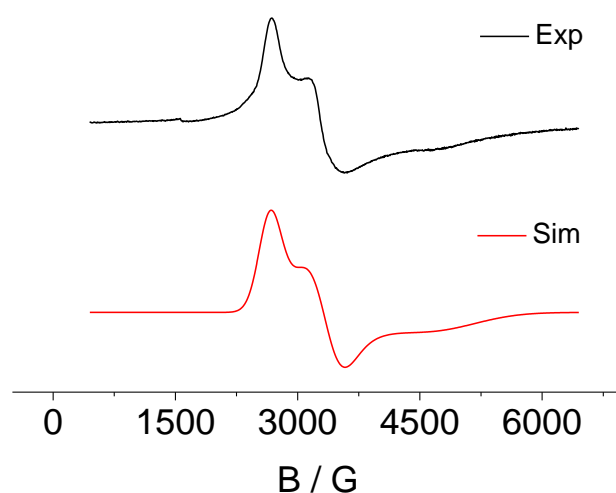
Figure 2.4.2: EPR spectrum of [2]PF$_6$ in CH$_2$Cl$_2$ at 5 K with computer simulation.

Table 2.4.1: EPR data of paramagnetic states for complexes.

	g^a	$g_1{}^b$	$g_2{}^b$	$g_3{}^b$	$< g >^d$	g_1-g_3	$A(^{99,101}Ru)^e$
[(bpy)$_2$Ru(L)]$^+$	2.027	2.110	2.044	1.965	2.041	0.145	13
[(bpy)$_2$Ru(L$_O$)]$^+$	2.007					<0.05	10
[(bpy)$_2$Ru(L$_S$)]$^+$	2.011					<0.05	13.8
[(acac)$_2$Ru(L$_O$)]	2.035	2.085	2.045	1.966	2.032	0.119	
[(acac)$_2$Ru(L$_S$)]	2.025	2.092	2.034	1.930	2.020	0.162	
[(bpy)$_2$Os(L)]$^+$	n.o.	2.497^c	1.987^c	1.393^c	2.010	1.104	

^{a} 298 K. ^{b}110 K. ^{c} 5 K. ^{d} Calculated from <g> = $((g_1{}^2 + g_2{}^2 + g_3{}^2)/3)^{1/2}$. ^{e} Coupling constants A in Gauss from 298 K spectra.

L$_O$ = N-benzoyl-N'-phenyldiazene[9], L$_S$ = N-thiobenzoyl-N'- phenyldiazene[9].
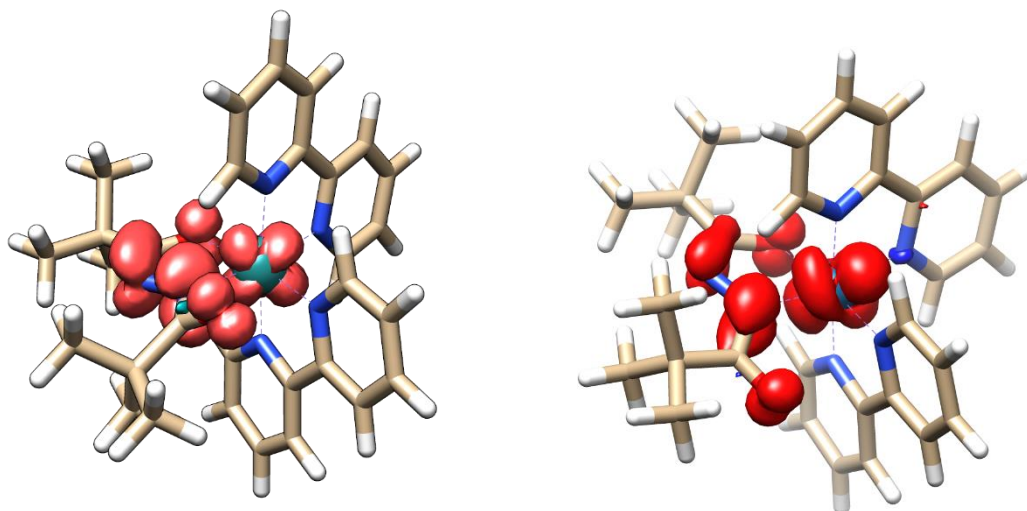
Figure 2.4.3: DFT calculated spin density plots of [1]$^+$ (left) and [2]$^+$ (right).

2.5 Cyclic voltammetry.

Electrochemical data were obtained by cyclic voltammetry or differential pulse voltammetry (dpv) as mentioned in Table 2.5.1. [Bu$_4$N]PF$_6$ was used as an electrolyte maintaining 0.1 M concentration, and the ferrocene/ferrocenium (Fc$^{+/0}$) couple was taken as an internal reference to avoid junction potential effects.[61]

Both paramagnetic monocations [1]$^+$ and [2]$^+$ exhibit each one reversible one-electron oxidation as well as one one-electron reduction process, as shown by Figure 2.5.1. In case of [1]$^+$, notably for the reduction process, a negative shift of about 0.30 V has been found in the less polar solvent CH$_2$Cl$_2$ in comparison to CH$_3$CN. Additionally, the peak-to-peak separation (ΔE_P) for each redox process is also larger in CH$_2$Cl$_2$ vs CH$_3$CN (Table 2.5.1). This indicates considerable solute-solvent interaction in case of CH$_2$Cl$_2$, resulting in quasi-reversible oxidation and reduction processes in cyclic voltammetry. The differences between oxidation and reduction potentials are 1.16 V (K$_c$ = 10$^{19.6}$) and 0.86 V (K$_c$ = 10$^{14.6}$) for measurements of [1]$^+$ in CH$_2$Cl$_2$ and CH$_3$CN, respectively. This gap between two redox processes is smaller for the Os analogue (0.76 V in CH$_2$Cl$_2$) which corresponds to less metal-ligand orbital mixing, as reported for similar type of systems.[57b,60]
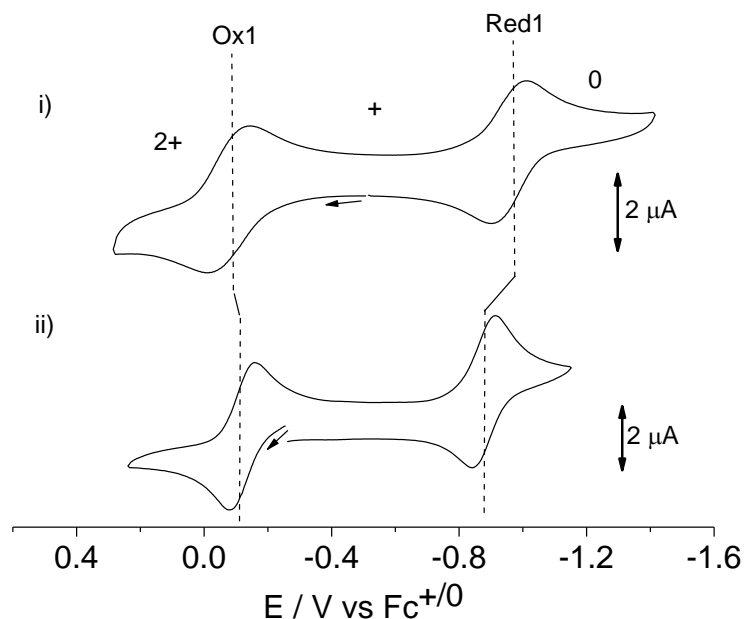
Figure 2.5.1: Cyclic voltammograms of i) [1]$^+$ in CH$_3$CN / 0.1 M Bu$_4$NPF$_6$ ii)) [2]$^+$ in CH$_2$Cl$_2$ / 0.1 M Bu$_4$NPF$_6$ at a scan rate of 100 mv / s.

Consequently, the K$_c$ value ($10^{12.9}$) is also lower; a similar trend which has been found for dinuclear ruthenium and osmium complexes with adc-R(2−) ligands.[69] This behaviour can be understood by the *hole transfer* mechanism (*see* Chapter 3.6) which involves high-lying ligand π or σ orbitals for ligand mediated metal-to-metal electron transfer. As the energy of the metal d orbital increases (from Ru to Os), the extent of electron transfer between metal/ligand sites goes down.

The protonated complex [1.H]$^+$ shows an irreversible behaviour in cyclic voltammetry (Figure 2.5.2), it exhibits two oxidation steps in dpv at -0.20 V and -0.07 V. These sequential oxidation processes may be accompanied by the loss of a proton. Such a behaviour can be reasonably explained by an ECE process which involves a dication [Ru(bpy)$_2$(HL)]$^{2+}$ ([1.H]$^{2+}$), and leads to a similar species [Ru(bpy)$_2$(L)]$^{2+}$ ([1]$^{2+}$) as obtained after one-electron oxidation of [1]$^+$ (Scheme 2.5.1). A similar situation was observed in case of Ru complexes with quinone-related ligands.[62] A significant hint towards this chemical transformation will be discussed in IR and UV-Vis-NIR spectroelectrochemistry part. A detailed pH-dependence study in combination with kinetic analyses would be needed to properly understand the process. On the other hand, the methylated complex [1.CH$_3$]$^+$ only shows one reversible oxidation (Figure

2.5.3) at a potential of 0.17 V which can be attributed to a Ru^{III}/Ru^{II} couple. An EPR signal corresponding to the oxidised $[1.CH_3]^{2+}$ was not identified after electrolysing the monocation. The metal-centred process has been confirmed by IR spectroelectrochemistry (*see* later), supported by DFT calculated 51% of the total spin density on the metal centre for $[1.CH_3]^{2+}$. The absence of an EPR signal (even at 4K) is unusual for a Ru-centred spin but fast relaxation of the electron spin may cause severe line-broadening, resulting the signal undetectable.[70] According to the redox behaviour of the methylated species, it can be assumed that a Ru^{III} centre is present in $[1.H]^{2+}$. This Lewis acidic metal centre may enhance the acidity of the N-H proton from the coordinated amide resulting a spontaneous release of the proton from $[1.H]^{2+}$ during electrochemical oxiditation of $[1.H]^+$ in CH_3CN / 0.1 M Bu_4NPF_6. It was not possible to characterise $[1.H]^{2+}$ by EPR spectroscopy. DFT calculation predicts that 62 % of the spin density resides on the metal centre, which supports the presence of a Ru^{III} centre in the dication $[1.H]^{2+}$.

i) $[Ru(bpy)_2(HL)]^+$ $\underset{+e^-}{\overset{-e^-}{\rightleftharpoons}}$ $[Ru(bpy)_2(HL)]^{2+}$ **E**

ii) $[Ru(bpy)_2(HL)]^{2+}$ $\xrightarrow{-H^+}$ $[Ru(bpy)_2(L)]^+$ **C**

iii) $[Ru(bpy)_2(L)]^+$ $\underset{+e^-}{\overset{-e^-}{\rightleftharpoons}}$ $[Ru(bpy)_2(L)]^{2+}$ **E**
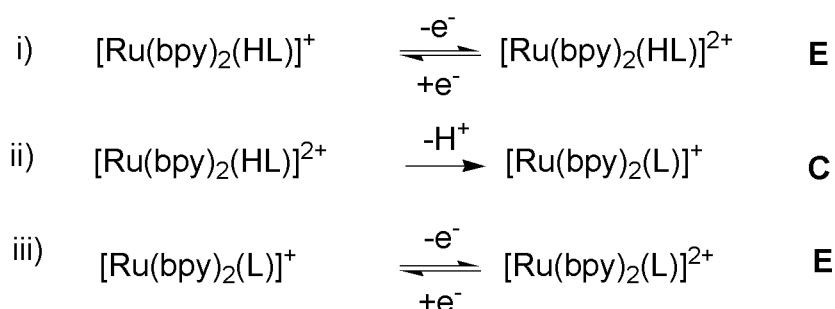
Scheme 2.5.1
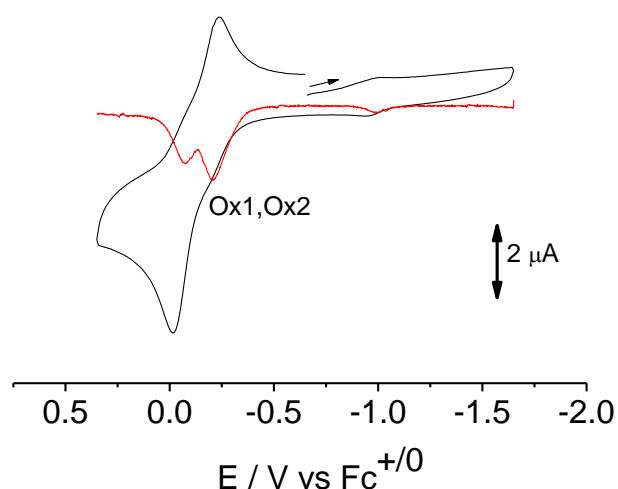
Figure 2.5.2: Cyclic voltammogram (black) and differential pulse voltammogram. (Red) of $[1.H]^+$ in CH_3CN / 0.1 M Bu_4NPF_6 at a scan rate of 100 mv / s.
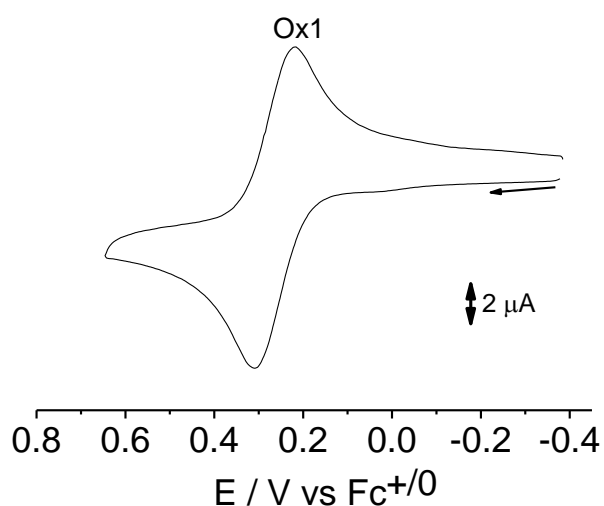
Figure 2.5.3: Cyclic voltammogram of [1.CH_3]^+ in CH_2Cl_2 / 0.1 M Bu_4NPF_6 at a scan rate of 100 mv /s.

Table 2.5.1: Redox potentials from cyclic voltammetry[a]

compound	$E°_{298}$/V (ΔE_p/mv)		
	Ox1	Ox2	Red1
[1]^{+b}	-0.08 (200)	n.o.	-1.24 (186)
[1]^{+c}	-0.08 (107)	n.o.	-0.94 (100)
[2]^{+b}	-0.11 (76)	n.o.	-0.87 (69)
[1.H]^{+c}	-0.20[d]	-0.07[d]	n.o.
[1.CH_3]^{+b}	0.17 (92)	n.o.	n.o.

[a]Potentials in V vs Fc^{+/0}, [b]measurements in CH_2Cl_2 / 0.1 M Bu_4NPF_6, [c]measurements in CH_3CN / 0.1 M Bu_4NPF_6, [d]data taken from differential pulse voltammetry.

2.6 IR spectroelectrochemistry.

IR spectroelectrochemical measurements for $[1]^+$, $[2]^+$, $[1.H]^+$ and $[1.CH_3]^+$ were carried out in an OTTLE[72] cell using respective electrolyte solutions (Table 2.6.1). Two types of carbonyl functions (C=O), one coordinated to the respective metal and one non-coordinated are present in such complexes. Generally, the C=O stretching frequencies for coordinated C=O fall in the fingerprint region ($\nu < 1500$ cm^{-1}) for complexes of the heavier transition metals like Ru or Os, as evident from relatively long bonds of about 1.30 Å in isolated paramagnetic complexes (Table 2.3.1). A recognisable correlation has been found in the case of non-coordinated or free C=O stretching during redox processes. On oxidation this C=O stretch is shifted from 1635 to 1755 cm^{-1} in case of $[1]^+$ while it is shifted to lower energy, 1525 cm^{-1}, on reduction (Figure 2.6.1).
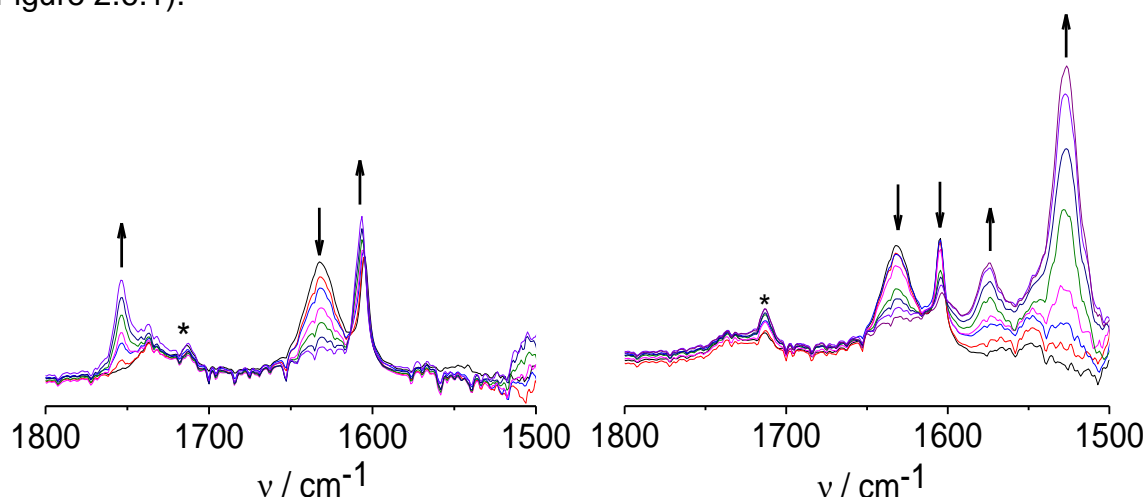
Figure 2.6.1: IR spectroelectrochemical response on oxidation (left) and reduction (right) of $[1]^+$ in CH_3CN/0.1 M Bu_4NPF_6. *Small peaks can be associated with a littile amount of decomposition of the compound during electrolysis.

Such a lower value represents the ligand as a conjugated system including the exocyclic C=O function in the reduced neutral species. On going towards monocationic and dicationic species, the electron is released from metal-ligand mixed orbitals. It causes a decrease in the extent of conjugation with subsequent distortion of the coplanarity between the chelated ring and the non-coordinated C=O fragment.

Therefore, the stretching frequency of the band under discussion is gradually increasing to higher wavenumbers. The Os monocation, [2]⁺, exhibits similar spectral shifts for the C=O stretch according to the data given in Table 2.6.1. An explanation similar to that of the Ru complex is applicable here, revealing that the charge distribution between metal and the ligand fragment in a particular redox species does not affect the stretching frequency of the exocyclic C=O band .

Following the same trend, IR spectra of [1.H]⁺ showed a band at 1545 cm^{-1} (Table 2.6.1). On oxidation, a new band was generated at 1755 cm^{-1} which is similar to that seen on oxidation of [1]⁺. This is the hint which led to the assignment of the ECE process mentioned in Scheme 2.5.1. It indicates the formation of elctrogenerated [1]$^{2+}$ during oxidation of the protonated complex [1.H]⁺. During the IR spectroelectrochemical measurement, it was not possible to identify those two successive one-electron oxidation processes separately. The methylated complex [1.CH$_3$]PF$_6$ exhibits a different behaviour where no such band is formed on oxidation. Instead, it is shifted slightly from 1533 to 1562 cm^{-1} (Figure 2.6.2) which indicates a metal-centred oxidation. At the same time, it also points to the rigidity of the ligand fragment which does not allow the uncoordinated part to rotate freely.

Additionally, for all complexes, a band at around 1600 cm^{-1} has been found. The intensity of that band increases on oxidation while it is shifted to lower wavenumber on reduction in respective complexes (Table 2.6.1). This band is tentatively assigned to a vibration mode of bpy ligand.[63]
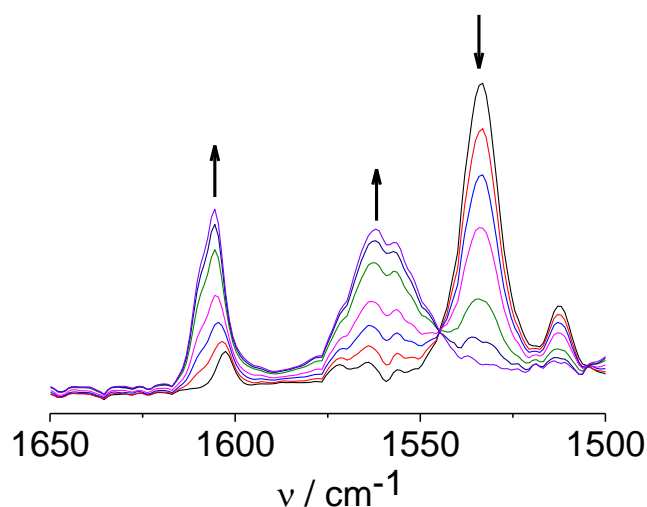
Figure 2.6.2: IR spectroelectrochemical response on oxidation of [1.CH$_3$]⁺ in CH$_2$Cl$_2$/0.1 M Bu$_4$NPF$_6$.

Table 2.6.1: Selected IR vibrational data from spectroelectrochemistry[a]

n+	$[1.H]^{n+b}$	$[1.CH_3]^{n+c}$	$[1]^{n+b}$	$[2]^{n+c}$
0			$1575(\nu_{bpy})$	$1590(\nu_{bpy})$
			1525	1530
1+	$1605(\nu_{bpy})$	$1602(\nu_{bpy})$	$1605(\nu_{bpy})$	$1605(\nu_{bpy})$
	1545	1533	1635	1625
		1512		
2+		$1605(\nu_{bpy})$	$1605(\nu_{bpy})$	$1610(\nu_{bpy})$
		1562	1755	1740

[a] Wavenumbers ν in cm^{-1}, related to the vibration mode of free C=O,

[b] measurements in 0.1 M Bu_4NPF_6/CH_2Cl_2, [c] measurements in 0.1 M Bu_4NPF_6/CH_3CN.

2.7 UV-Vis-NIR spectroelectrochemistry.

Measurements were carried out in an OTTLE[72] cell with respective electrolyte solutions of the complexes. All data are listed in Table 2.7.3 and the spectral changes during redox processes are shown in Figures 2.7.3, 2.7.4 and 2.7.5 for $[1]^+$, $[2]^+$ and $[1.CH_3]^+$, respectively.

At first, absorptions related to the open shell complexes, $[1]PF_6$ and $[2]PF_6$, will be discussed in combination with EPR and TD-DFT results. Experimental and calculated electronic transitions are tabulated in Table 2.7.1 and 2.7.2. $[1]PF_6$ gives a low energy absorption with a maximum at 735 nm. This band is assigned to a metal-to-ligand (MLCT) charge transfer transition from a donor Ru^{II} to an acceptor L$^{·-}$ with a

little admixture of intra-ligand character. The corresponding band is calculated at 635 nm and arises from a βHOMO-2 $\rightarrow$ βLUMO excitation. Also, surprisingly, a weak transition has been found at about 1230 nm (ε = 200 $M^{-1}cm^{-1}$). Such transitions are generally observed for Ru^{III} centres, arising from a forbidden d-d excitation.[64] However, a similar transition was also encountered for the intermediate ruthenium complex in a catechol-quinone redox series.[65] The probability of an intra-ligand n$\rightarrow\pi^*$ transition has been discussed in that report. Still, the origin for the weak NIR absorption is unclear yet. In the present case, the probability of a Ru^{III} centre can not be ruled out, as EPR data give a g anisotropy (Δg=0.145) value between a true metal-centred spin, $Ru^{III}L^{2-}$, and a radical, $Ru^{II}L^{\cdot-}$. In connection with the weak NIR absorption the calculation predicts two weak transitions at 1122 nm (βHOMO $\rightarrow$ βLUMO, f_{osc} = 0.0006) and 977 nm (βHOMO-1 $\rightarrow$ βLUMO, f_{osc} = 0.002) which have a predominant MLCT character with admixture of MC transition.

[2]PF$_6$ shows two NIR transitions around 1950 and 1180 nm, typical for an Os^{III} centre. With respect to the observed band around 650 nm, TD-DFT calculation predicts transitions at 728, 641 and 611 nm. Those are mainly due to the excitations from the SOMO into bpy-based orbitals αLUMO or αLUMO+1.The band might be assigned as a charge transfer transition with a donor, $Os^{III}L^{2-}$, and an acceptor, bpy. Such transition can be formulated as metal-ligand-to-ligand (MLLCT)[66] transition. Another absorption with similar character has been found at a lower wavelength around 460 nm. In contrast to Ru, all these observations are clearly indicating a $Os^{III}L^{2-}$ formulation in this case, which is also in accordance with the EPR result (Δg=1.104).

Table 2.7.1: TD-DFT (ORCA/ PBE0/ ZORA/ COSMO-CH$_3$CN) calculated electronic transitions[a] for [1]+.

λ /nm (exp.) (10^{-4}ε / M^{-1}cm^{-1})	states	λ /nm (DFT) (f$_{osc}$)	transitions	assignment
1230 (0.02)	1	1122 (0.0006)	βHOMO → βLUMO (76%)	ML$_{adc-R}$CT/MC
			βHOMO-1 → βLUMO (11%)	
	2	977 (0.002)	βHOMO-1 → βLUMO (78%)	ML$_{adc-R}$CT/MC
			βHOMO → βLUMO (13%)	
725 (0.52)	3	635 (0.090)	βHOMO-2 → βLUMO (76%)	ML$_{adc-R}$CT/IL$_{adc-R}$CT
			SOMO → αLUMO (8%)	
460 (0.68)	11	479 (0.025)	αHOMO-1 →αLUMO (41%)	ML$_{bpy}$CT
			αHOMO-2 → αLUMO (28%)	
	15	436 (0.084)	βHOMO-2 → βLUMO+2 (29%)	ML$_{adc-R}$L$_{bpy}$CT
			αHOMO-2 → αLUMO (24%)	
			βHOMO-2 → βLUMO+1 (23%)	

[a] Shapes of frontier MOs involved in the excitations are presented in Figures 10.A1, 10.A2.

Table 2.7.2: TD-DFT (ORCA/ PBE0/ ZORA/ COSMO-CH_2Cl_2) calculated electronic transitions[a] for [2]+.

λ /nm (exp.) (10^{-4}ε / M^{-1}cm^{-1})	states	λ /nm (DFT) (f_{osc})	transitions	assignment
1950 (0.04)	1	1412 (0.002)	βHOMO → βLUMO (72%) βHOMO-1 → βLUMO (11%)	$ML_{adc-R}CT/MC$
1180 (0.02)	2	1111.4 (0.006)	βHOMO-1 → βLUMO (75%) βHOMO → βLUMO (12%)	$ML_{adc-R}CT/MC$
650 (0.59)	3	728.9 (0.021)	SOMO → αLUMO (88%)	$ML_{adc-R}L_{bpy}CT$
	4	641.8 (0.034)	SOMO → αLUMO+1 (58%) βHOMO-2 → βLUMO (30%)	$ML_{adc-R}L_{bpy}CT$
	5	611.4 (0.061)	βHOMO-2 → βLUMO (44%) SOMO → αLUMO+1 (29%)	$ML_{adc-R}L_{bpy}CT$
485 (0.63)	13	500.9 (0.069)	αHOMO-2 → αLUMO (51%) βHOMO-1 → βLUMO+1 19%)	$ML_{bpy}CT$

[a] Shapes of frontier MOs involved in the excitations are presented in Figures 10.A3, 10.A4

During the oxidation of both monocations [1]+ and [2]+, intense absorptions have been found around 455 (ε = 9800 M^{-1}cm^{-1}) and 410 (ε = 13400 M^{-1}cm^{-1}) nm, respectively, and the weak NIR absorptions have disappeared (Figures 2.7.3, 2.7.4). On going to the reduced species [(bpy)$_2$M^{II}L^{2-}$], the visible region is dominated by

MLCT(bpy) transitions. Absorption shoulders at lower energy ($\lambda > 700$ nm) can be assigned as ligand-to-ligand (LL'CT) charge transfer transition, an observation well known for similar systems.[9]
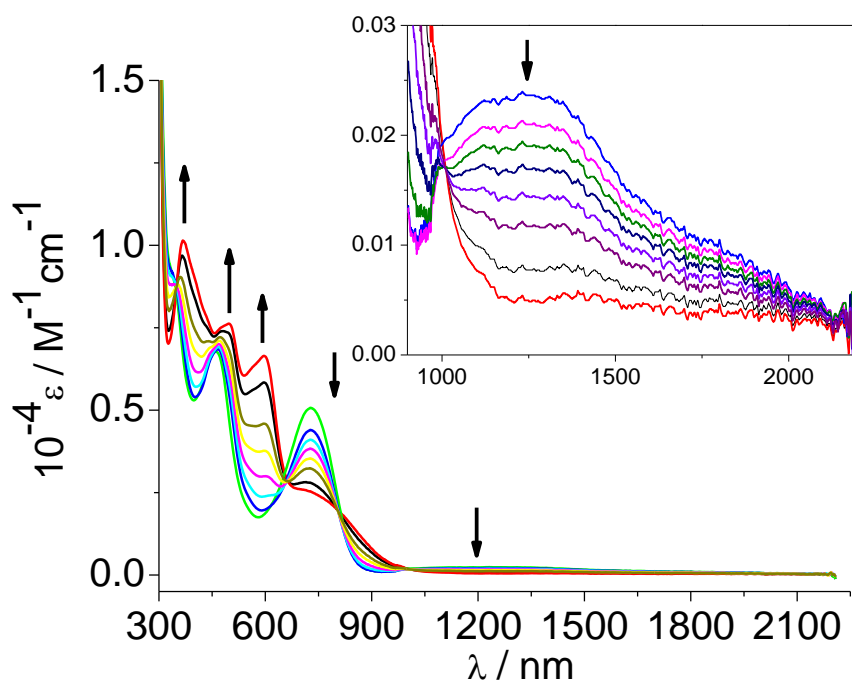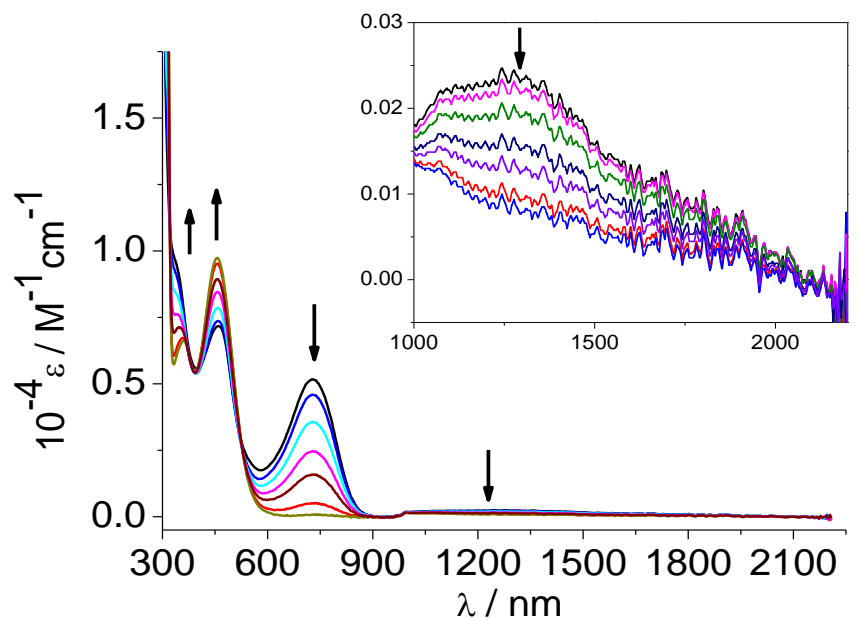
Figure 2.7.3: UV-Vis-NIR spectroelectrochemical response on oxidation (top) and reduction (bottom) of [1]$^+$ in CH$_3$CN/0.1 M Bu$_4$NPF$_6$.
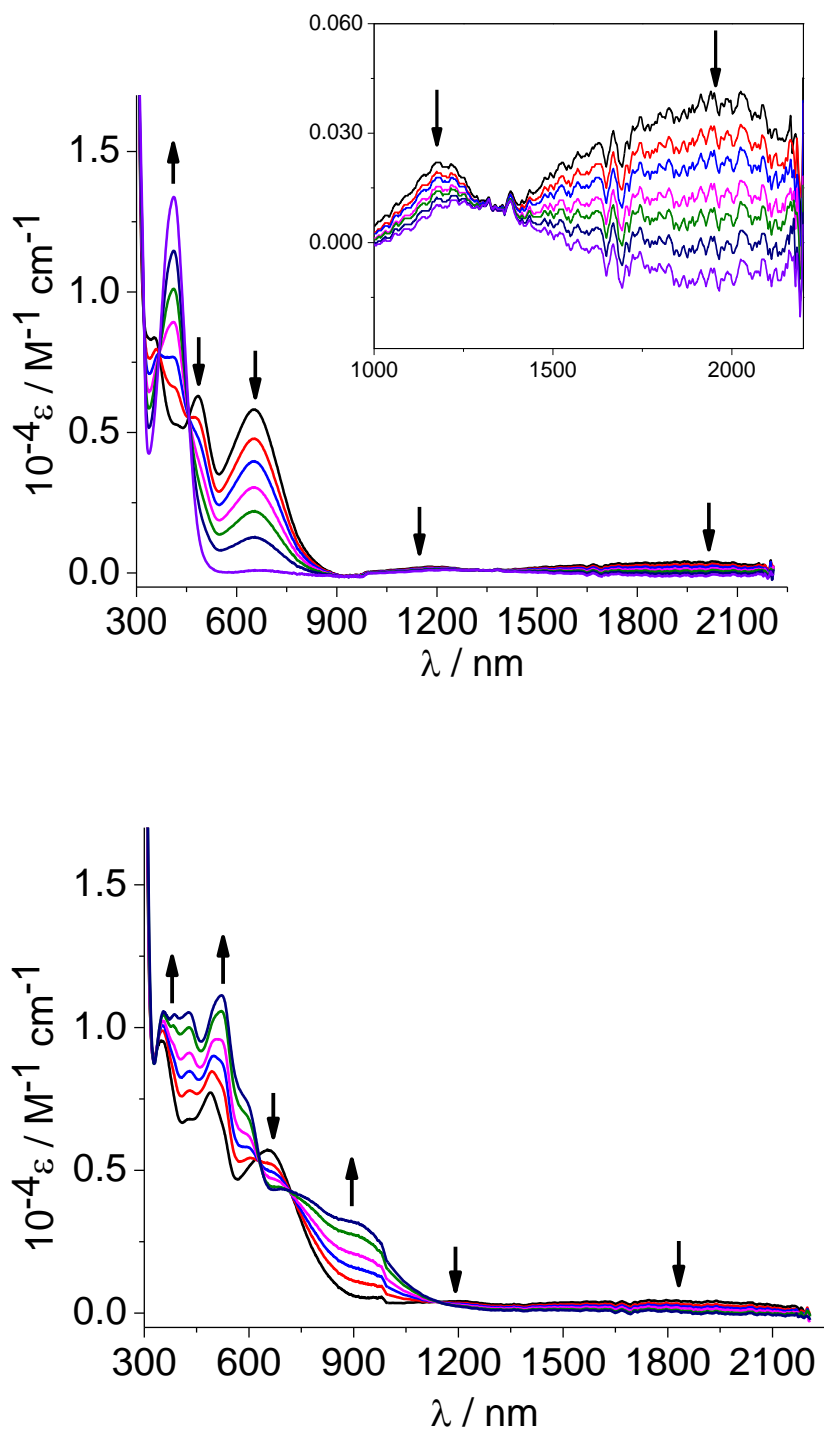
Figure 2.7.4: UV-Vis-NIR spectroelectrochemical response on oxidation (top) and reduction (bottom) of [2]+ in CH_2Cl_2/0.1 M Bu_4NPF_6.

The protonated and methylated Ru complexes [1.H]PF$_6$ and [1.CH$_3$]PF$_6$, respectively exhibit almost identical spectra in the visible region (Table 2.7.3). Those absorptions have mainly MLCT(bpy) character. Similar to the experiment from IR spectroscopy, the 2nd oxidation of the protonated complex showed a band with a maximum around 430 nm which can be related to the redox species [1]$^{2+}$. During the course of two successive one-electron oxidations, a band around 730 nm, which was initially arising, decreased again on continuing the electrolysis. The two processes were not properly separated due to the closeness of the potential values. Anyway, the result supports the proposed ECE mechanism as described in the cyclic voltammetry part. The methylated complex shows reversible behaviour in spectroelectrochemistry. On going to the oxidised [1.CH$_3$]$^{2+}$, MLCT absorptions are diminishing where a weak transition at 715 nm appears (ε = 800 M^{-1} cm^{-1}) which can be assigned as an intra-ligand or d-d transition within [(bpy)$_2$M^{III}CH$_3$L$^-$]$^{2+}$. The EPR silent dication made the ligand-centred radical formulation impossible.
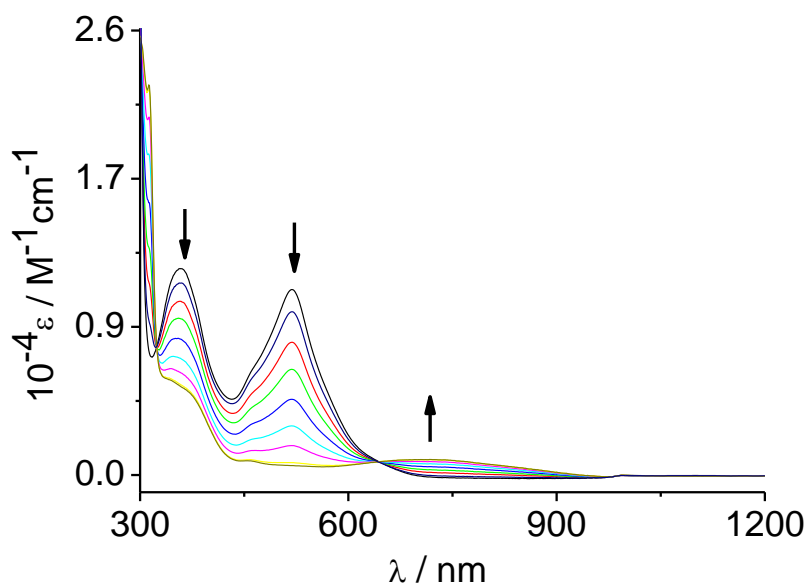
Figure 2.7.5: UV-Vis-NIR spectroelectrochemical response on oxidation of [1.CH$_3$]$^+$ in CH$_2$Cl$_2$/0.1 M Bu$_4$NPF$_6$.

Table 2.7.3: UV-Vis-NIR data from spectroelectrochemistry[a]

n+	[1.H]$^{n+b}$	[1.CH$_3$]$^{n+c}$	[1]$^{n+b}$	[2]$^{n+c}$
0			370 (1.01)	355 (1.06)
			500 (0.76)	380 (1.05)
			595 (0.67)	425 (1.05)
			750 (sh)	520 (1.11)
				600 (sh)
				730 (0.42)
				925 (sh)
1+	355 (0.94)	358 (1.20)	345 (sh)	350 (0.83)
	507 (1.10)	520 (1.08)	460 (0.68)	485 (0.63)
	570 (sh)		725 (0.50)	650 (0.59)
			1230 (0.02)	1180 (0.02)
				1950 (0.04)
2+		370 (sh)	360 (0.67)	410 (1.34)
		715 (0.08)	455 (0.98)	

[a] Wavelengths λ_{max} in nm, 10^{-4} ε in M^{-1} cm^{-1} in parentheses,

[b] measurements in 0.1 M Bu$_4$NPF$_6$/CH$_3$CN, [c] measurements in 0.1 M Bu$_4$NPF$_6$/CH$_2$Cl$_2$.

2.8 Conclusion.

This chapter has portrayed the redox series [(bpy)$_2$M(adc-^{t}Bu)]$^{n+}$ (M = Ru, Os ; n = 0,1,2; Scheme 2.8.1). Spectroscopic and electrochemical properties have shown a periodic trend as expected for second and third row transition metals. Remarkably, the intermediate Ru species in the series (n = 1) exhibits ambiguity in depicting correct electronic description between ligand-based radical and a metal-centred spin situation. It has been described as a borderline situation Ru^{II}(bpy)$_2$(adc-^{t}Bu)$^{·-}$ <–> Ru^{III}(bpy)$_2$(adc-^{t}Bu)$^{2-}$, based on EPR spectroscopy and confirmed by DFT calculation.

Such behaviour has been rarely observed with a π-accepting ancillary ligand bpy and it points to the non-innocent feature of the N,O coordinating ligand, i.e metal and ligand redox states are not evidently distinguishable. Since the complexes contain a free C=O group, its effect on the redox series has now been established properly. The EPR analysis of the present (A) and the previous[9] (B) system clearly point to the high electron accepting ability of the uncoordinated C=O containing azo ligand.

(A)   (B)
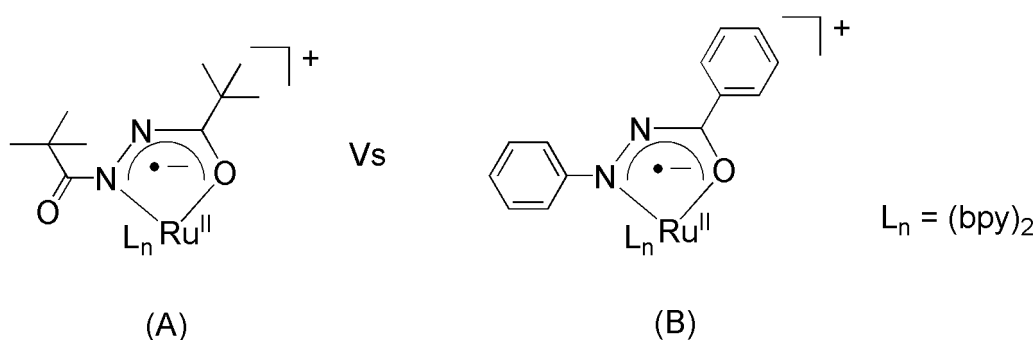
Additionally, the protonated ([1.H]$^+$) and methylated ([1.CH$_3$]$^+$) complexes exhibit different electrochemical behaviour but they effectuate a parallel redox path (Scheme 2.8.1) relating to the typical Ru/Os redox series.
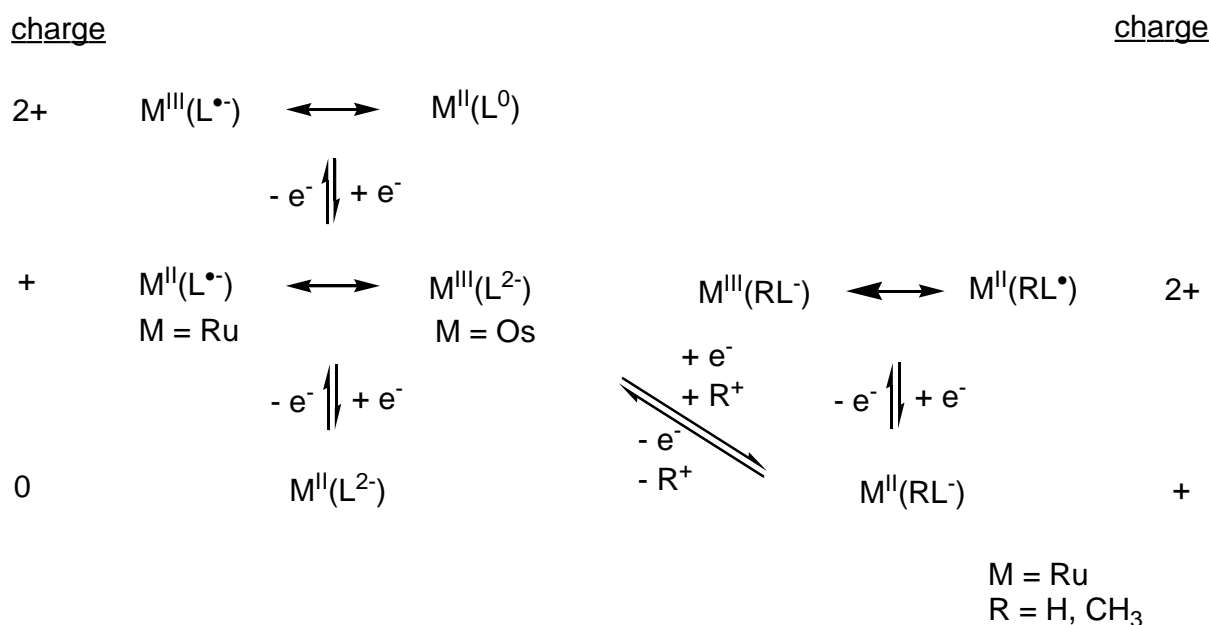
Scheme 2.8.1 Redox scheme for various monocationic complexes ([M(bpy)$_2$(Radc-tBu)]$^+$, L = adc-^{t}Bu) showing assumed metal/ligand electron distributions.

The protonated species exhibit irreversible redox behaviour leading to the dication of the Ru-Os series while the methylated species undergoes one reversible oxidation to generate $[1.CH_3]^{2+}$. DFT calculation predicts the electronic situations of the one-electron oxidised species ($[1.H]^{2+}$ and $[1.CH_3]^{2+}$) to have a dominant metal-centred spin. In conclusion, this chapter encompasses probable electron distributions on the metal/ligand interfaces involving different ligand states ($L^{0/\cdot-/2-}$, $HL^{\cdot/-}$, $CH_3L^{\cdot/-}$) as well as different transition elements (Ru,Os).

Chapter 3

Diruthenium complexes with bis-bidentate bridging ligands OC(R)NN(R)CO: A comparative structural and spectroelectrochemical study.

3.1 Introduction.

There is an increasing number of reports[53b,73-79] covering the chemical reactivity of electronically active azodicarbonyl ligands (adc-R$^{0/\cdot-/2-}$), especially using the high electron accepting ability of the azo(0) form. Carreira and co-workers have shown such applications of adc-OR derivatives in catalytic transformation reaction like hydrohydrazination.[73,74] The adc-R (such as R = NH$_2$ and OCH$_3$) ligands have also been employed to cleave metal-metal bonds in compounds like R$_2$Ga-GaR$_2$ (R = CH(SiCH$_3$)$_2$) and Os$_3$(CO)$_{11}$(CH$_3$CN), respectively.[77,78] In both cases, the chemical conversion is initiated by metal to ligand electron transfer, which eventually causes incorporation of the hydrazido(2−) form between two metal centres.

The dinuclear galium[77] and a few others diruthenium[79,48,70], dicopper[71] and diiridium[53c,80] complexes with bis-bidentate bridging adc-R ligands show "S-frame" **(I)** coordination, and they have exhibited a good correlation between structural (e.g. N-N distances) and electronic (e.g. ligand redox states) properties.

(I)
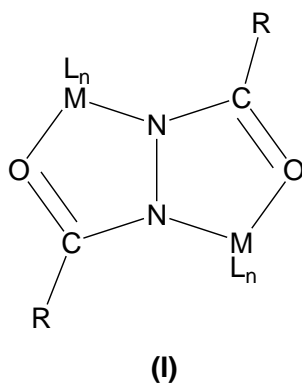
The diruthenium complexes, particularly with terminal ligands like 2,2′ bipyridine (bpy) or acetylacetonate (acac), are researched with regard to their charge or electron transfer property in the mixed-valent (MV) states.[48,70] A survey[51] on diruthenium MV

complexes ([(bpy)$_2$Ru(μ-adc-R)]$^{3+}$) has shown a clear influence of different R substituents (such as alkyl, aryl, -OR, -NR$_2$) in the electronic description as well as in the electronic absorption behaviour of the complexes. Following the same strategy, adc-R(2$-$) ligands with aromatic (R = C$_6$H$_5$/Ph) and aliphatic (R=CF$_3$) substituents have been combined with two [Ru(trpy*)Cl]$^{n+}$ (trpy* = 4,4′,4″-tri-tert-butyl-2,2′:6′,2″-terpyridine) fragments, as described in this chapter. A switch of bpy to trpy* in the ancillary part is not only interesting for the structural difference (e.g. meridional coordination of terpyridine based ligands) but also for chemical applications. Ruthenium fragments like [Ru(trpy*)(L)Cl]$^{n+}$ (L = bidentate ligand) give access to different[81-84] catalytic reactions if the chloride atom can be replaced with relatively labile solvent molecules like acetonitrile or water. Moreover, such ruthenium fragments have established an important platform to study the redox and binding properties of various nitrogen oxides (NO, NO$_2^-$).[85,86]

Thus the complexes [{(trpy*)ClRu}$_2$(μ-adc-Ph)]PF$_6$ and [{(trpy*)ClRu}$_2$(μ-adc-CF$_3$)] will be discussed here to understand the substitutional effects of the ligands (Scheme 3.1) on their structural, electrochemical and spectroscopic properties.

R = C$_6$H$_5$, H$_2$adc-Ph
R = CF$_3$, H$_2$adc-CF$_3$
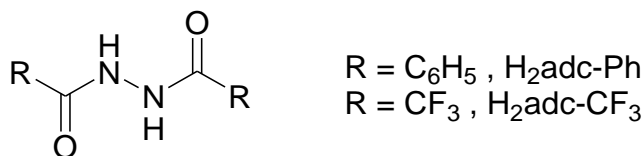
Scheme 3.1

3.2 Syntheses and characterisation.

The complex [{(trpy*)ClRu}$_2$(μ-adc-Ph)]PF$_6$ ([1]PF$_6$) was synthesised from the precursor complex *mer*-Ru(trpy*)Cl$_3$ under refluxing conditions in ethanol as described in Scheme 3.2.1. The counter anion PF$_6^-$ was incorporated by precipitating the desired product with aqueous KPF$_6$ solution from the reaction mixture. The product was further purified using column chromatography (neutral alumina,

dichloromethane/methanol) and obtained as a purple solid. The single charge i.e. the presence of one PF_6^- anion in the complex was confirmed by elemental analysis and ESI-MS spectroscopy (M-PF$_6$ peak) (*see* Chapter 7.3.3).

In a similar manner [{(trpy*)ClRu}$_2$(μ-adc-CF$_3$)] ([2]) was synthesised as shown in Scheme 3.2.1 and purified. It was characterised by elemental analysis as a neutral species, which indicates both ruthenium atoms are in their +2 oxidation state (Ru^{II}). Nevertheless, in the precursor complex ruthenium is present in its +3 oxidation state (Ru^{III}) which signifies that the ruthenium centres are reduced during the reaction. It can be postulated that the reducing equivalents are coming from the reaction solvent (methanol in the presence of a base).[52] A Similar reasoning is also applicable for [1]PF$_6$ for which the reaction was performed in ethanol instead of methanol. But the relatively strong π donating ligand adc-Ph(2−) might stabilise a mixed-valent species with Ru^{II} and Ru^{III} centres, forming a singly charged species in that case.
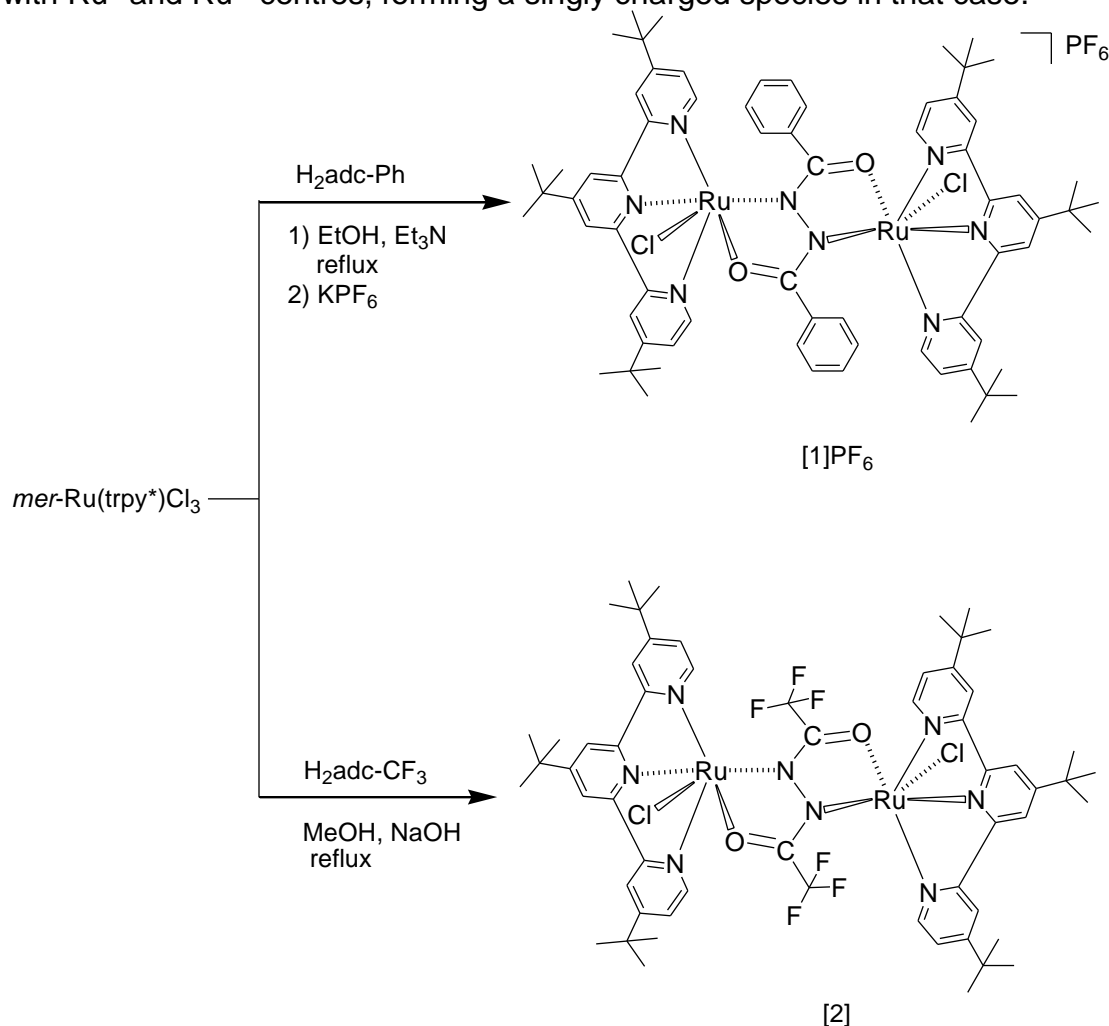
Scheme 3.2.1: Synthetic scheme for [1]PF$_6$ and [2].

*[2] was synthesised by Lorenz Julian Fahrne*r.

[1]PF$_6$ and [2] were also examined by ^{1}H NMR spectroscopy. The monocationic species can be distinguished from the neutral one by highly shifted signals for the aromatic ring protons as depicted in Figure 3.2.1. Such chemical shifts are also indicative for the presence of a Ru^{III} centre or the paramagnetic nature of [1]PF$_6$. For both complexes, resonances are integrated with respect to the signals from *tert*-butyl groups that come in the alkyl region of the NMR spectra. Spectral data are listed in the experimental section (Chapter 7.3.3).
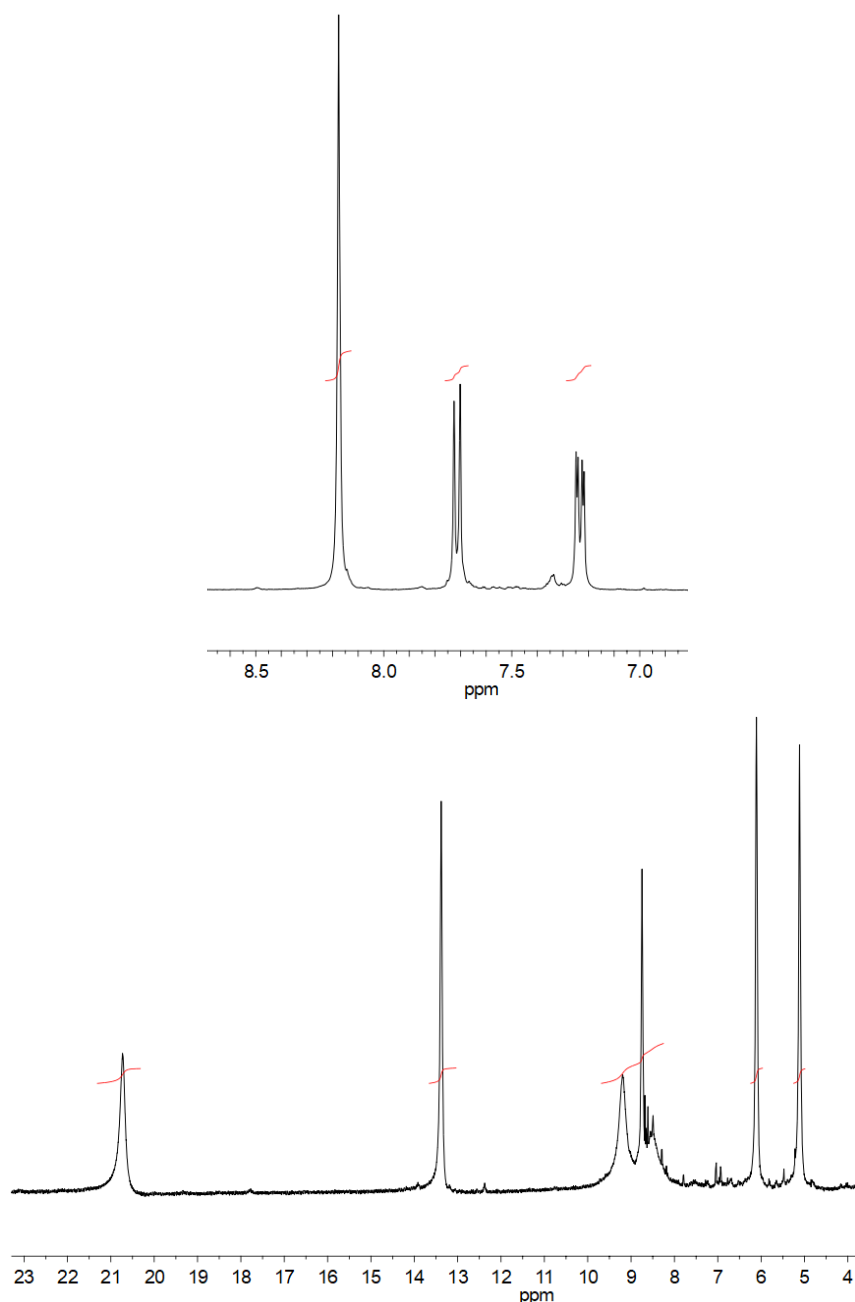
Figure 3.2.1: ^{1}H NMR signals (except *tert*-butyl protons) of [2] in CD$_2$Cl$_2$ (top) and of [1]PF$_6$ in (CD$_3$)$_2$CO (bottom).

3.3 Molecular structures.

Single crystals were obtained by slow diffusion of *n*-hexane into a dichloromethane solution of the complex [1]PF$_6$ at room temperature. The complex crystallises in the space group P2$_1$/C with several highly disordered solvent molecules. The PLATON programme[140] was used to squeeze all such solvent molecules to improve the accuracy of structural parameters of the target molecule. The molecular structure is presented in Figure 3.3.1, crystallographic data are summarised in Chapter 7.4.2 and selected bond parameters are given in Table 3.3.1.

The trpy* ligand is coordinated to each ruthenium ion in a meridional fashion thus forming a pseudo-octahedral geometry in the complex. Short Ru2-N7 (1.954(3) Å) and Ru1-N3 (1.959(3) Å) bond distances (nitrogen atoms from central pyridyl ring in trpy*) in comparison with terminal Ru-N (nitrogen atoms from the terminal pyridyl ring in trpy*) distances (in between 2.060 to 2.077 Å; Table 3.3.1) have been observed similar to those in previously reported metal-terpyridine complexes.[52a] As a result, the bite angles N6-Ru2-N8 (158.55°) and N5-Ru1-N4 (158.38°) have shifted from 180° which is ideal for a perfect octahedral geometry. It also indicates relatively strong interactions of the central pyridyl ring as an electron acceptor with the donor ruthenium fragment.

The bridging adc-R(2−) ligand (R = Ph) forms two five-membered chelate rings by sharing a common edge though the N1-N2 bond (Figure 3.3.1). Interestingly, the planes consisting of two individual chelate rings form an angle of about 25°. This distortion from a planar metal-ligand-metal arrangement forces two ruthenium fragments to tilt towards each other. The distortion is further assisted by a strong π-π interaction between the phenyl ring and the central pyridyl ring from the trpy* (Figure 3.3.1). The distances between two π-π interacting ring centroids are around 3.50 Å for N3 and N7 bearing pyridyl ring. In addition, the molecular structure confirms the isomer (A) exclusively, where chloride is ligated *trans* to the N atom from the bridging ligand (Scheme 3.3.1).
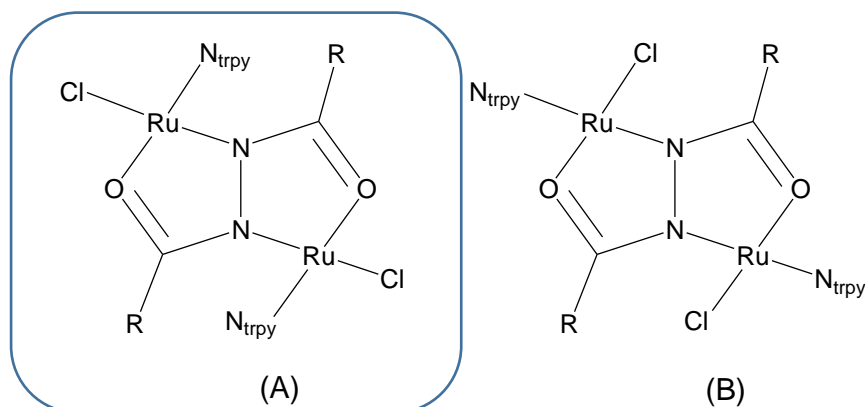
Scheme 3.3.1: Representation of possible *cis* and *trans* symmetric isomers of [1]PF$_6$.

The stoichiometric 1:1 cation / anion ratio of the complex points to a mixed-valent Ru^{II}/Ru^{III} unit where a charged and potentially redox active azodicarbonylhydrazido function adc-Ph(2−) (2− form in the adc-R$^{0/\cdot-/2-}$ series) bridges two metal centres. The N-N bond distance (1.437(4) Å) also indicates the presence of the 2− form of the bridging ligand.[48] An interesting observation in the present system is the almost equivalent coordination environment across the metal-ligand-metal bridge. Similar Ru2-N2 (2.057(3) Å) and Ru1-N1 (2.051(3) Å) distances manifest this observation. The structural parameters are hence consistent with a valence-delocalised description Ru$^{2.5}$(adc-Ph)$^{2-}$Ru$^{2.5}$ for the complex in the crystal.
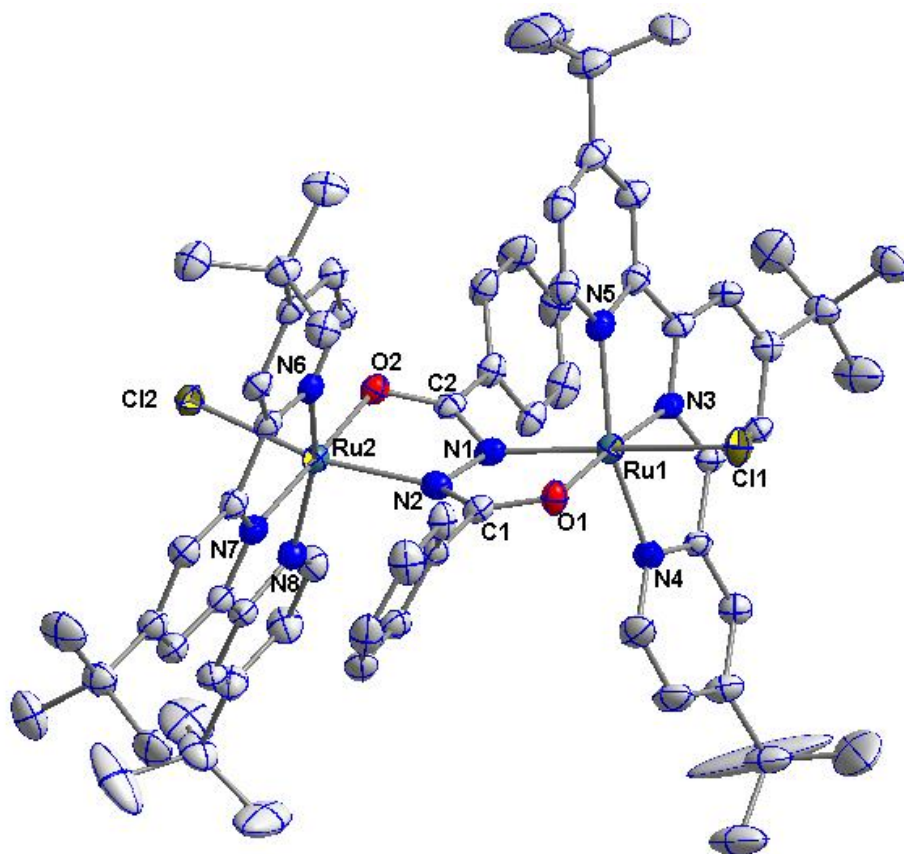
Figure 3.3.1: Molecular structure of the cation in the crystal of [1]PF₆. Thermal ellipsoids are given at the 50% probability level; H atoms are removed for clarity.

Table 3.3.1: Selected experimental bond distances (Å) and angles (°) of the complex [1]PF$_6$.

Bond distances			
Ru1-Cl1	2.3623(10)	Ru2-N6	2.077(3)
Ru1-O1	2.037(3)	Ru2-N7	1.954(3)
Ru1-N1	2.051(3)	Ru2-N8	2.066(3)
Ru1-N3	1.959(3)	C1-O1	1.270(5)
Ru1-N4	2.061(3)	N1-N2	1.437(4)
Ru1-N5	2.060(3)	C2-N1	1.328(5)
Ru2-Cl2	2.3770(10)	C2-O2	1.276(5)
Ru2-O2	2.053(3)	C1-N2	1.342(5)
Ru2-N2	2.057(3)	Ru1-Ru2	4.851
Bond angles and torsion angles			
O1-Ru1-N1	76.74(11)	N6-Ru2-N7	79.09(13)
Cl1-Ru1-N1	168.50(9)	N7-Ru2-N8	79.59(13)
N5-Ru1-N3	79.31(13)	C1-N2-N1-C2	-160.1(3)
N3-Ru1-N4	79.28(12)	Ru1-N1-N2-Ru2	163.15(14)
O2-Ru2-N2	76.39(11)		
Cl2-Ru2-N2	165.79(9)		

Single crystals of [{(trpy*)ClRu}$_2$(µ-adc-CF$_3$)] ([2]) were grown in dichloromethane/n-hexane solution by the diffusion method in a similar manner as in the case of the [1]PF$_6$. The crystal system is again monoclinic with the space group P2$_1$/C. Crystallographic data are summarised in Chapter 7.4.2. Selected bond lengths and torsion angles of [1]PF$_6$ and 2 are listed in Table 3.3.2.

The coordination fashion of the ligands in the neutral complex with R = CF$_3$ is identical to that of the cationic fragment with R = Ph. The difference obviously lies in

the bond parameters as both of them crystallise in different redox states. For example, the Ru-N_{adc-R} distances are approximately 0.03 Å longer and the Ru-N_{trpy*} distances are slightly shorter (in the order of 0.02 Å) in the case of the neutral complex where two $Ru^{II}(trpy*)Cl$ fragments are connected via the adc-$CF_3(2-)$ bridge. The difference in bond parameters is as expected as the charge on the ruthenium centres has decreased from the phenyl substituted monocationic complex. The most important finding in comparing the two structures (R = Ph and R = CF_3) is the planar metal-ligand-metal arrangement for the latter. The wireframe representation in Figure 3.3.2 and the torsion angles (Table 3.3.2) illustrates the different geometries in both crystal structures.
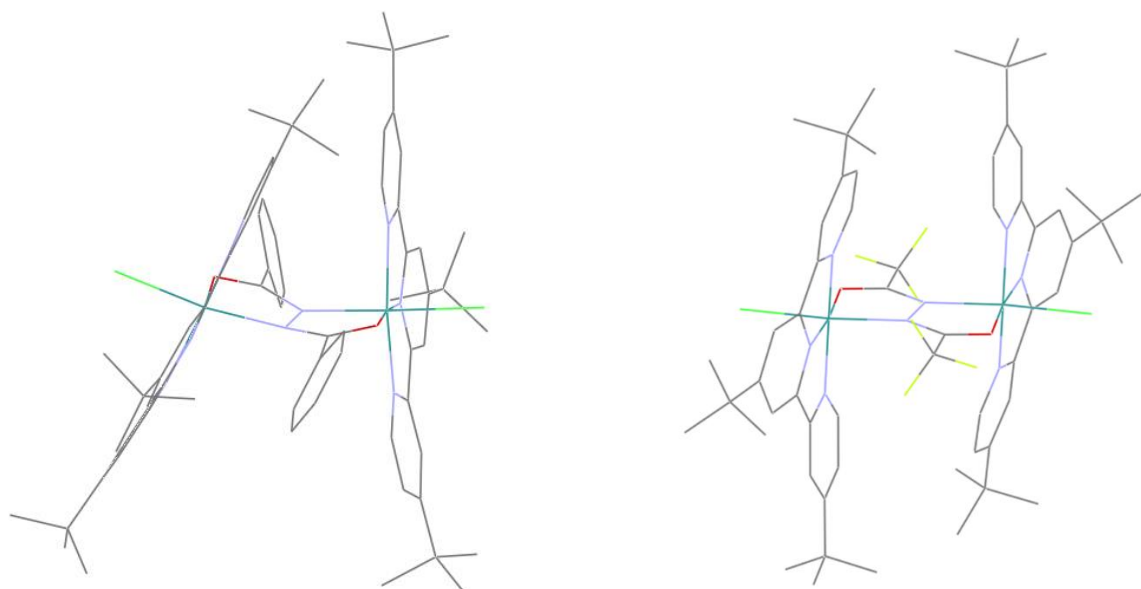
Figure 3.3.2: Wireframe representations of the different geometries in the crystal structure of [1]PF_6 with R = Ph (left) and of [2] with R = CF_3 (right). H atoms, solvent molecules and counter anion are removed for clarity.

Table 3.3.2: Selected experimental bond distances (Å) and torsion angles (°) of [1]PF_6 with R = Ph and of 2 with R = CF_3.
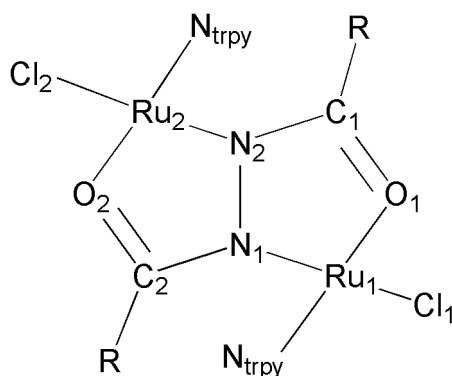
	Bond distances				
	R = Ph	R = CF_3		R = Ph	R = CF_3
Ru1-Cl1	2.3623(10)	2.3888(6)	N1-N2	1.437(4)	1.468(4)
Ru1-O1	2.037(3)	2.0841(16)	C1-N2	1.342(5)	1.310(3)
Ru1-N1	2.051(3)	2.082(2)	C2-N1	1.328(5)	1.310(3)
Ru1-N$_{trpy}$	1.959(3)	1.937(2)	C2-O2	1.276(5)	1.272(3)
Ru1-Ru1	4.851	4.920	C1-O1	1.270(5)	1.272(3)

	Torsion angles	
	R = Ph	R = CF_3
C1-N2-N1-C1	-160.1(3)	180
Ru1-N1-N2-Ru2	163.15(14)	180

3.4 Cyclic voltammetry.

In cyclic voltammetry in CH_2Cl_2 solution both complexes [1]PF_6 and [2] exhibit two one-electron reversible processes in the region between -0.42 V and +0.20 V vs. $Fc^{+/0}$ which are mainly located on the ruthenium centres (Ru^{III}/Ru^{II} couple). The trpy* reduction waves, which are expected to be observed at highly negative potentials[50], were not detected inside the feasible potential window of the measurement in CH_2Cl_2/0.1 M Bu_4NPF_6 (1.4 to 2.4 vs. $Fc^{+/0}$). The voltammograms are shown in Figure 3.4.1 and the potentials are listed in Table 3.4.1. The potentials E(+/0) and E(2+/+) undergo an anodic shift on going from the redox series [1]^n to [2]^n. This behaviour is due to the higher donor effect of the phenyl substituent as compared to trifluoromethyl, nevertheless the K_c values of the + forms, which depend on the difference of these potentials (ΔE = 0.5 V), are very similar. Such high K_c values ($10^{8.5}$) generally point to a strong metal-metal electronic coupling according to previous literature reports related to mixed-valency.[48,51] However, an observation is notable in comparing these supposedly metal-centred redox potentials with previously reported complex series [{(bpy)$_2$Ru}$_2$(μ-adc-R)]^n.[48,51] Replacement of a pyridyl function with a chloride ligand in the ancillary part of the complexes cause a cathodic shift (around 0.5 V, Table 3.4.1). The K_c values for the MV intermediates remain almost unaltered, on the other hand.
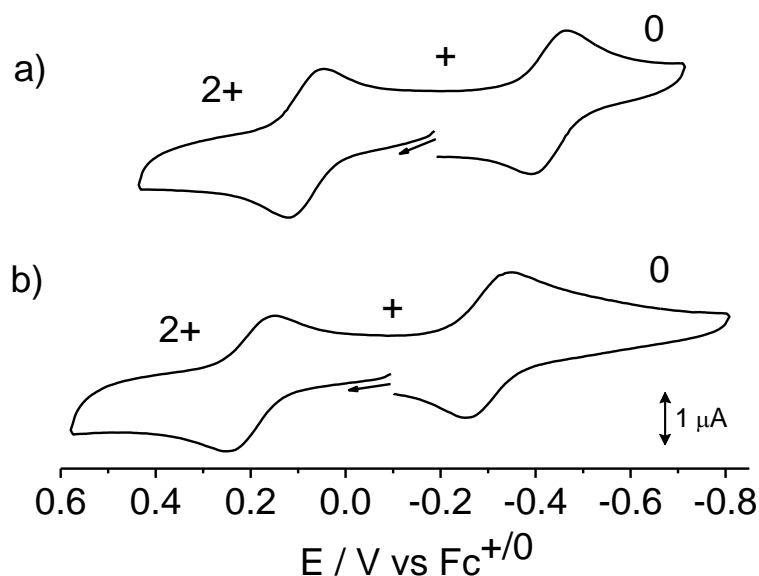
Figure 3.4.1: Cyclic voltammogram of a) [1]PF_6 and b) [2] (preoxidised to [2]$^+$) in CH_2Cl_2/0.1 M Bu_4NPF_6 at 100mV scan rate.

Table 3.4.1: Redox potentials from Cyclic Voltammetry[a]

compound	E^0/V (ΔE_p/mv)		
	Ru^{II}-Ru^{III}/Ru^{II}-Ru^{II}	Ru^{III}-Ru^{III}/Ru^{II}-Ru^{III}	$K_c(n)$
$[1]^n$	-0.42(70) [E(+/0)]	0.08(60) [E(2+/+)]	$10^{8.5}$ (+)
$[2]^n$	-0.30(80) [E(+/0)]	0.20(80) [E(2+/+)]	$10^{8.5}$ (+)
$[3]^{nb}$	0.15(60) [E(3+/2+)]	0.72(70) [E(4+/3+)]	$46{\times}10^8$ (3+)
$[4]^{nb}$	0.10 [E(3+/2+)]	0.62 [E(4+/3+)]	$10^{8.8}$ (3+)

[a] Potentials in V vs $Fc^{+/0}$ in CH_2Cl_2 0.1 M Bu_4NPF_6 at RT, [b] measurements in CH_3CN 0.1 M Bu_4NPF_6 at RT. $[\{(bpy)_2Ru\}_2(\mu\text{-adc-Ph})]^n$ $([3]^n)^{51}$, $[\{(bpy)_2Ru\}_2(\mu\text{-adc-CF}_3)]^n$ $([4]^n)^{48}$.

3.5 EPR spectroscopy.

EPR measurements were carried out for the native mixed-valent species ($[1]PF_6$) and after chemical oxidation of the neutral complex ($[2]$) with a ferrocenium salt. $[1]PF_6$ exhibits a rhombic (g_1 = 2.217, g_2 = 2.057, g_3 = 1.902) X-band EPR signal whereas the later gives a nearly axial (g_1 = 2.178, g_2 = 2.165, g_3 = 1.80) signal in dichloromethane in the glassy frozen state (Figure 3.5.1 and 3.5.2). The results indicate that the isolated neutral complex ($[2]$; R = CF_3) retains its planar arrangement even after one-electron oxidation and the distorted geometry in the case of R = Ph becomes responsible for the different EPR spectra. The g anisotropies for both paramagnetic states are close to the reported Ru(bpy)$_2$ complexes with adc-R ligands (R = Ph, CF_3; Table 3.5.1). Such values in the range between 0.30 to 0.45 signify partial ligand participation in the singly occupied MO (SOMO) as well as an adc-R(2–) bridge mixed-valent diruthenium (Ru^{II}-Ru^{III}) system.[87] This statement gets further support from the structural analysis of the present system $[1]PF_6$ where N-N bond distance (1.437 Å) has confirmed the hydrazido(2–) redox state of the ligand. However, the EPR signal for phenyl-substituted complex was recorded at 120 K at which temperature the trifluromethyl-

substituted complex is EPR silent. The reason for the observed difference is not clear yet, but this temperature dependency arises because of different relaxation behaviour of complexes. Sometimes, fast relaxation even concealed the EPR signal, especially in case of heavier transition metal complexes with high spin-orbit coupling constant.[70]
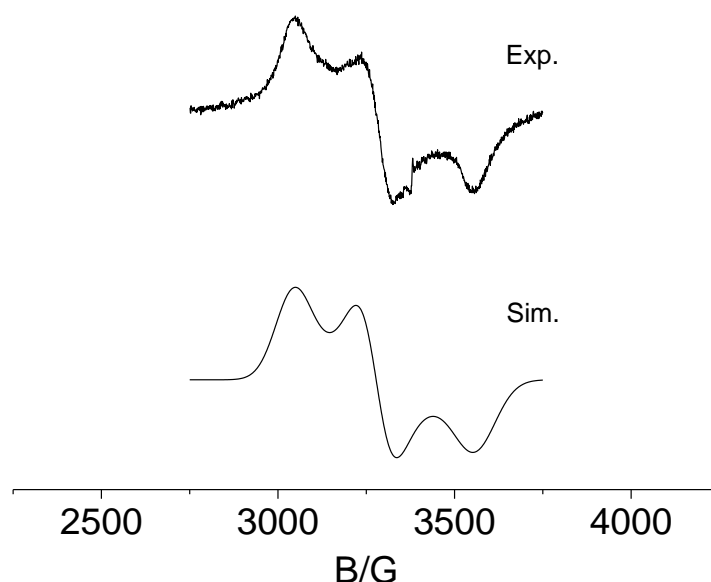
Figure 3.5.1: EPR spectrum of [1]PF$_6$ in CH$_2$Cl$_2$ at 120 K with computer simulation (g_1 = 2.217, g_2 = 2.057, g_3 = 1.902).
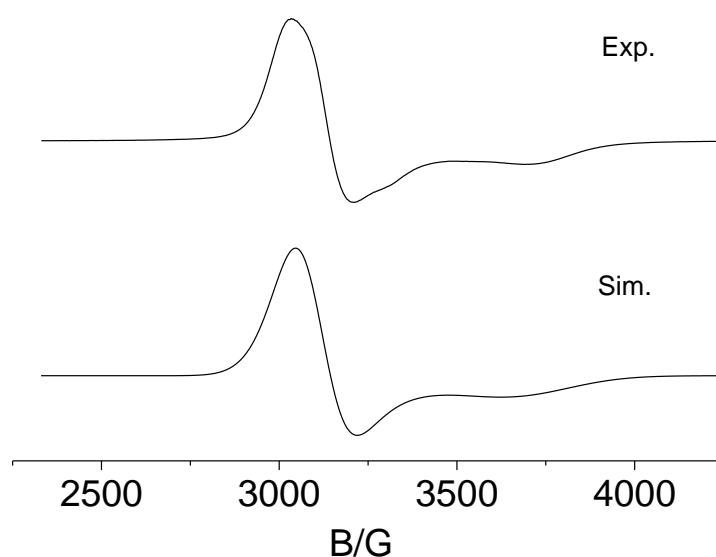
Figure 3.5.2: EPR spectrum of [2]PF$_6$ (obtained from chemical oxidation of [2] with one eq of FcPF$_6$ in CH$_2$Cl$_2$) in CH$_2$Cl$_2$ at 5 K with computer simulation (g_1 = 2.178, g_2 = 2.165, g_3 = 1.80).

Table 3.5.1: EPR data of paramagnetic states.

	[1]PF$_6$	[2]PF$_6$	[3]$^{3+}$	[4]$^{3+}$
g$_1$	2.217	2.178	2.344	2.239
g$_2$	2.057	2.165	2.003	2.065
g$_3$	1.902	1.80	1.895	1.891
g$_{av}$	2.063	2.048	2.089	2.101
g$_1$-g$_3$	0.315	0.378	0.449	0.348
Solvent(temp.)	CH$_2$Cl$_2$ (120 K)	CH$_2$Cl$_2$ (5 K)	(CH$_3$)$_2$CO (3.8 K)	CH$_3$CN (5 K)

$g_{av} = [(g_1{}^2 + g_2{}^2 + g_3{}^2)/3]^{1/2}$

[{(bpy)$_2$Ru}$_2$(μ-adc-Ph)]$^{3+}$ ([3]$^{3+}$)[51],

[{(bpy)$_2$Ru}$_2$(μ-adc-CF$_3$)]$^{3+}$ ([4]$^{3+}$)[48].

3.6 UV-Vis-NIR spectroelectrochemistry.

The absorptions in the UV-Vis-NIR region of each redox species in the series [{(trpy*)ClRu}$_2$(μ-adc-R)]$^{0/+/2+}$ ([1]$^{0/+/2+}$, R = Ph; [2]$^{0/+/2+}$, R = CF$_3$) were measured by using an OTTLE[72] cell. Spectral changes of [1]PF$_6$ and [2], which are shown in Figure 3.6.1 and 3.6.2, respectively, are very similar. Absorption values are summarised in Table 3.6.1. Terpyridine-based (in this case trpy*, 4,4′,4″-tri-*tert*-butyl-2,2′:6′,2″-terpyridine) MLCT transitions were found in the visible region for the neutral states. They arise at λ$_{max}$ = 408, 536 nm for [1] and 375, 490 nm for [2]. Such transitions have been well investigated with regard to excited-state-chemical properties in transition metal complexes.[88] Additionally, multiple weak shoulders were also found in the wavelength range between 600 to 800 nm. These can be attributed to the typical LLCT transitions (π[(adc-R)$^{2-}$] to π*[trpy*]).[50b] On going from the neutral (Ru^{II}-Ru^{II}) to the monocationic (Ru^{II}-Ru^{III}) form, MLCT transitions exhibit expected high energy shift where the long-wavelength shoulders are diminished. The main features of the Ru^{II}-Ru^{III} states are the intense NIR absorption bands, found at the maxima 1530 (ε ≈ 9000 M^{-1}cm^{-1}) and 1572 (ε ≈ 14000 M^{-1}cm^{-1}) nm for [1]$^+$ and [2]$^+$,

respectively. Though the NIR-band structures are indicating a superimposition of two or more bands, approximate band-widths can be determined which are around 1860 cm^{-1} for [1]$^+$ and 1500 cm^{-1} for [2]$^+$, much lower than the values (3878 and 3825 cm^{-1}, respectively) calculated from the Hush equation[36] (A) for a weakly coupled system.

$$\Delta v_{1/2} \text{ / cm}^{-1} = [2.301 \times 10^3 \, (E_{max} \text{ / cm}^{-1})]^{1/2} \qquad\qquad (A)$$

$\Delta v_{1/2}$ = Bandwidth at half height, E_{max} = Band energy maximum.

Such low bandwidths and the high intensities indicate strong metal-metal electronic coupling i.e. a valence averaged situation (Ru$^{2.5}$-Ru$^{2.5}$), which was already postulated from the molecular structure analysis of the mixed-valent R = Ph analogue. In this situation the character of the bands can be better described as a charge transfer transition between delocalised metal-ligand-metal orbitals.[32b,33] There is a low energy shift of the NIR absorption maxima upon decreasing the donor ability of the substituent R (Ph to CF$_3$), similar to those reported for dinuclear Ru(bpy)$_2$ complexes with these ligands.[48,51] This behaviour can be explained by the hole transfer mechanism[69] (Scheme 3.6.1) between two ruthenium sites via the bridging ligand. The trifluoromethyl substituent, which is a relatively better acceptor, stabilises the ligand π orbitals. This results in a decrease in metal-metal coupling and hence a decrease in band energy.

L: donor ligand
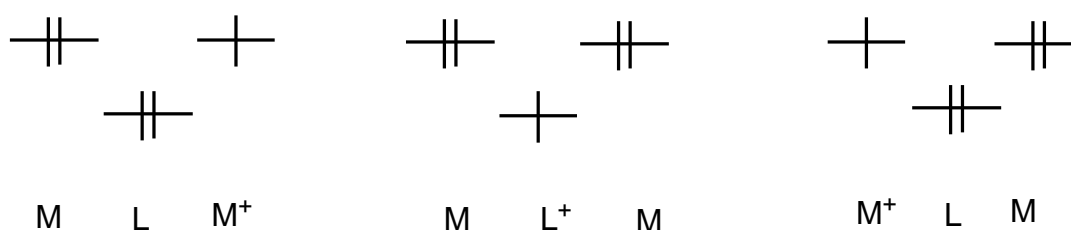
hole transfer mechanism

Scheme 3.6.1

During the redox process from + (Ru^{II}-Ru^{III}) to 2+ (Ru^{III}-Ru^{III}) form, the NIR absorptions have been completely disappeared.
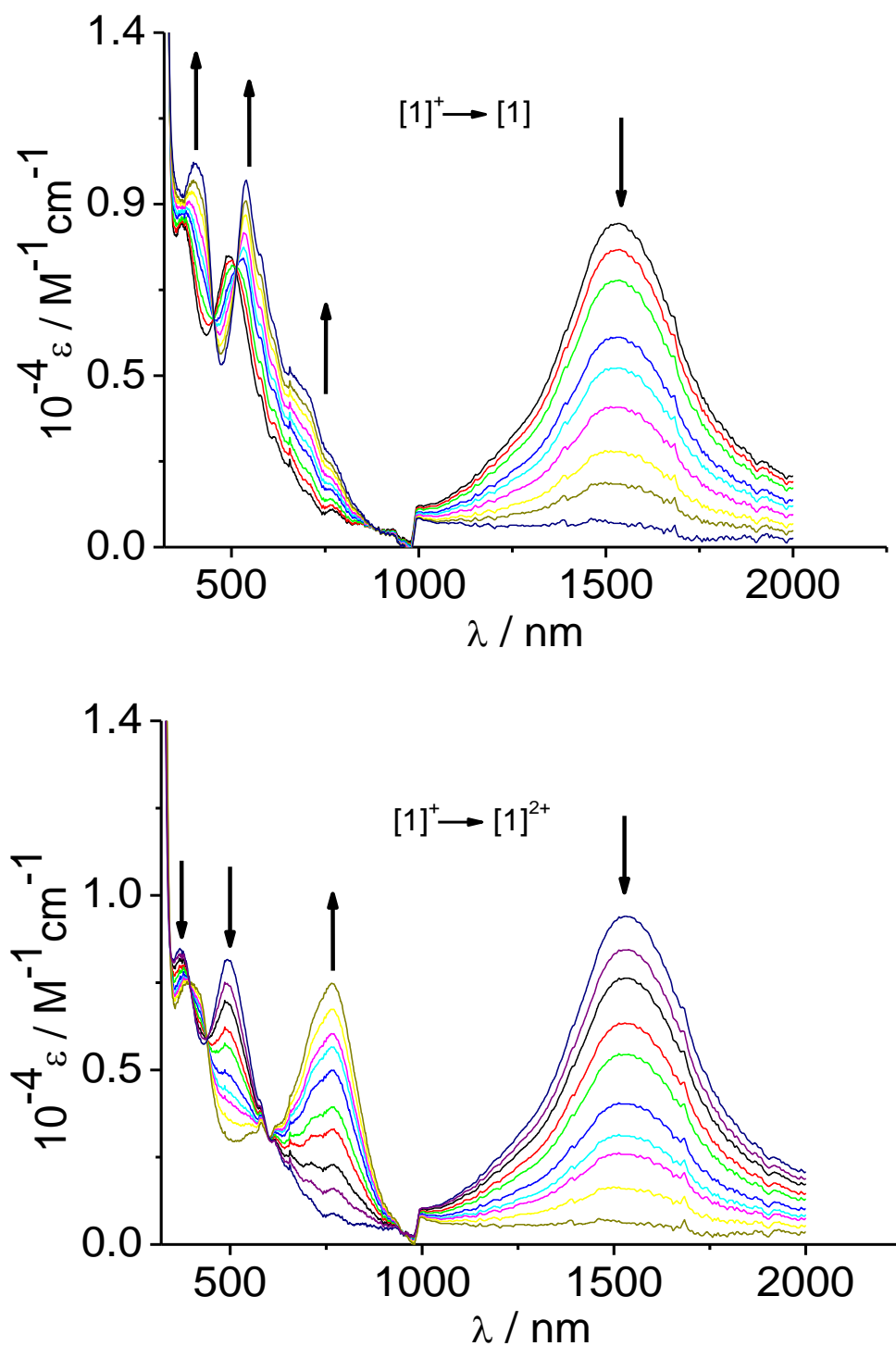
Figure 3.6.1: UV-Vis-NIR spectroelectrochemical changes of [1]^n ; n = + to 0 (top) , n = + to 2+ (bottom) in CH$_2$Cl$_2$/0.1 M Bu$_4$NPF$_6$.
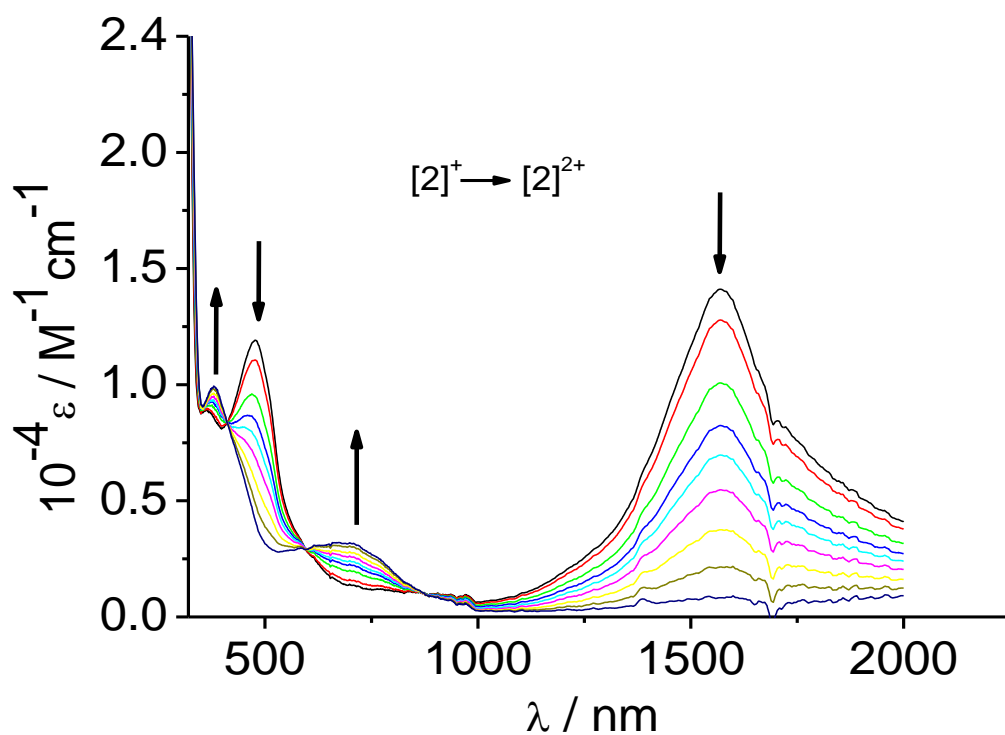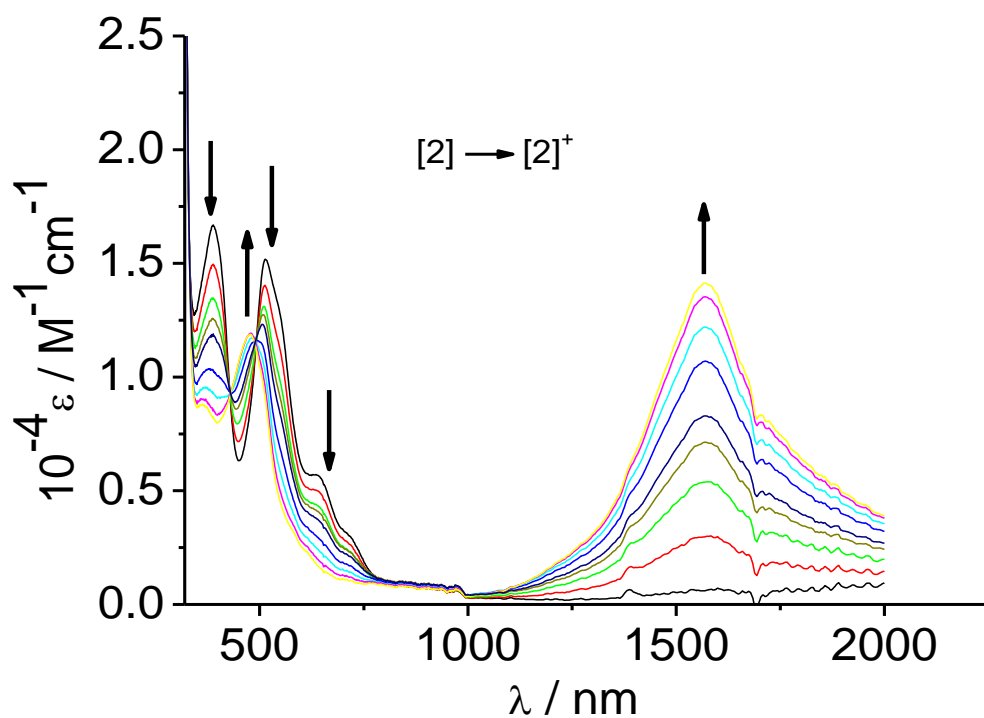
Figure 3.6.2: UV-vis-NIR spectroelectrochemical changes of $[2]^n$; n = 0 to + (top) , n = + to 2+ (bottom) in CH_2Cl_2/0.1 M Bu_4NPF_6.

Table 3.6.1: Absorption Values from UV-Vis-NIR Spectroelectrochemistry.

Compound	λ_{max}/nm (10^{-4} ε / M^{-1} cm^{-1})
[1]	408(1.1), 536(1.0), 700(sh), 780(sh)
[1]$^+$ (native)	375(0.8), 490(0.8), 1530(0.9)
[1]$^{2+}$	770(0.7), 408(0.7)
[2] (native)	390(1.6), 515(1.5), 645(sh),730(sh)
[2]$^+$	370(0.8), 480(1.2),1572(1.4)
[2]$^{2+}$	380(1.0), 705(0.3)

3.7 Conclusion.

This chapter describes diruthenium complexes in which two [Ru(trpy*)Cl]^n fragments are interacting with noninnocent bridging adc-R(2$-$) ligands (R = Ph, CF$_3$). The electrochemical and spectroscopic studies reveal similar behaviour as has been observed for Ru(bpy)$_2$ complexes[48,51] with different adc-R ligands. They exhibit two reversible redox processes with a stable mixed-valent intermediate. Apart from the structural difference between bpy and trpy*, these redox potentials have shown considerable cathodic shift (around 0.5 V) in present case. This behaviour, which increases the accessibility of higher oxidation states, can be useful in oxidation or reduction catalysis.

The structural characterisations of the trifluoromethyl ([2]) and phenyl substituted ([1]PF$_6$) complexes have shown a planar and a bent metal-ligand-metal geometry, respectively. Additionally, the bond parameters are indicating that the complexes are in different redox states, but the differences are strikingly small. However, the N-N bond distance (1.437 Å), EPR data (Δg = 0.315) and the UV-Vis-NIR results (intense NIR absorption) for [1]PF$_6$ confirm a delocalised MV description (Ru$^{2.5}$-L^{2-}-Ru$^{2.5}$) against a radical bridge situation (Ru^{II}-L$^{\cdot-}$-Ru^{II}).

Moreover, this comparative study stimulates us in extending the work for the adc-R ligands with highly donating R substituents (such as –OR, –NR$_2$). Especially, the structural characterisation of the MV states will help to correlate structural property (e.g. N-N bond lengths) with EPR spectroscopy, an important technique for characterisation of MV complexes with noninnocent bridging ligands.

Chapter 4

The diruthenium complex of a redox active bis(mer-tridentate) bridging ligand: At the borderline between metal-metal mixed-valence and a radical bridge situation.

4.1 Introduction.

Bridging organic ligands are the backbone of oligonuclear interaction between metal-organic frameworks (MOFs) in terms of a structural function to mediate multiple metal fragments. Especially, the incorporation of redox-active ligands has received great attention in studies of magnetic coupling, valence exchange or energy and electron transfer properties.[118,119] That is why the development of new redox-active bridging ligands with regard to their donor combinations and denticity is very attractive in coordination chemistry. A plethora of bis(monodentate) and bis(bidentate) organic linkers can be found in the literature.[14,120] In comparison, bis(tridentate) ligands specifically with meridional coordination have limited existence.[15,50,94,121] One such rare example is 1,2-bis(salicyloy)hydrazine (H_4adc-Sal) which has been studied in various first-row transition metal complexes. These studies are mainly focused on the magnetic coupling between metal centres.[122]

In this chapter new diruthenium monocationic complexes [{(trpy*)Ru}$_2$(μ,η^3:η^3-adc-Sal)]X (X = PF_6^-, ClO_4^-) are presented, in which azo/hydrazide(2−) and phenolate/phenoxyl constituents from the bridging ligand (adc-Sal)$^{4-}$ interact with two (trpy*)Ru^{n+} centres (trpy* = 4,4',4"-tri-*tert*-butyl-2,6,2',6"-terpyridine). This monocation is investigated as a mixed-valence (d^5/d^6) intermediate within a three-step reversible redox system [{(trpy*)Ru}$_2$(μ-adc-Sal)]$^{0/+/2+/3+}$. A comment on mixed-valence description for the monocation will be deduced based on the structural interpretation, EPR analysis in connection with DFT calculated spin density, and NIR band analysis, supported by TD-DFT calculations.

4.2 Syntheses and characterisation.

The complex cation $[\{(trpy^*)Ru\}_2(\mu,\eta^3:\eta^3\text{-adc-Sal})]^+$ with the counter anions perchlorate (ClO_4^-) or hexafluorophosphate (PF_6^-) was prepared by reacting two equivalents of *mer*-$Ru^{III}(trpy^*)Cl_3$ with 1,2-bis(salicyloyl)hydrazine, $H_4(adc\text{-Sal})$ under basic conditions as described in Scheme 4.2.1. Both isolated complexes were characterised by ^1H-NMR spectroscopy, with large paramagnetic chemical shifts, and by elemental analysis (Chapter 7.3.3). The paramagnetic nature and the charge of the complexes indicate a mixed-valence state $Ru^{II}Ru^{III}$ for the dinuclear unit. The partial reduction of a ruthenium centre during reaction has been seen quite often in such a reducing environment, a combination of alcohol and base in refluxing condition.[52] The hexafluorophosphate complex was oxidised with ferrocenium salt to obtain the $Ru^{III}Ru^{III}$ form, a dicationic complex $[\{(trpy^*)Ru\}_2(\mu,\eta^3:\eta^3\text{-adc-Sal})](PF_6)_2$, characterised by ^1H-NMR spectroscopy and elemental analysis (Chapter 7.3.3). Interestingly, this supposedly paramagnetic complex also exhibited the calculated number of ^1H-NMR resonances ranging from 28.72 to -31.74 ppm. The resonances were integrated relative to the number of protons from *the tert*-butyl group of trpy* which show characteristic peaks in the alkyl region of the NMR spectrum (Figure 4.2.1).

$[(trpy^*)Ru^{II}(\mu\text{-adc-Sal})Ru^{III}(trpy^*)]X$
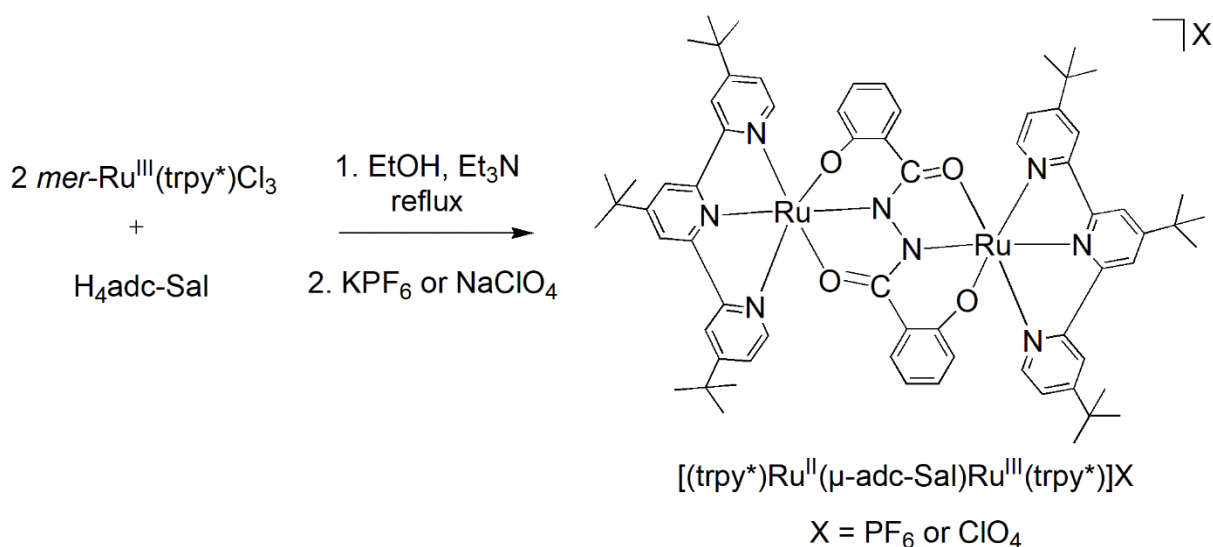
$X = PF_6$ or ClO_4

Scheme 4.2.1: Reaction scheme for obtaining $[\{(trpy^*)Ru\}_2(\mu,\eta^3:\eta^3\text{-adc-Sal})]X$ (X = PF_6 or ClO_4).
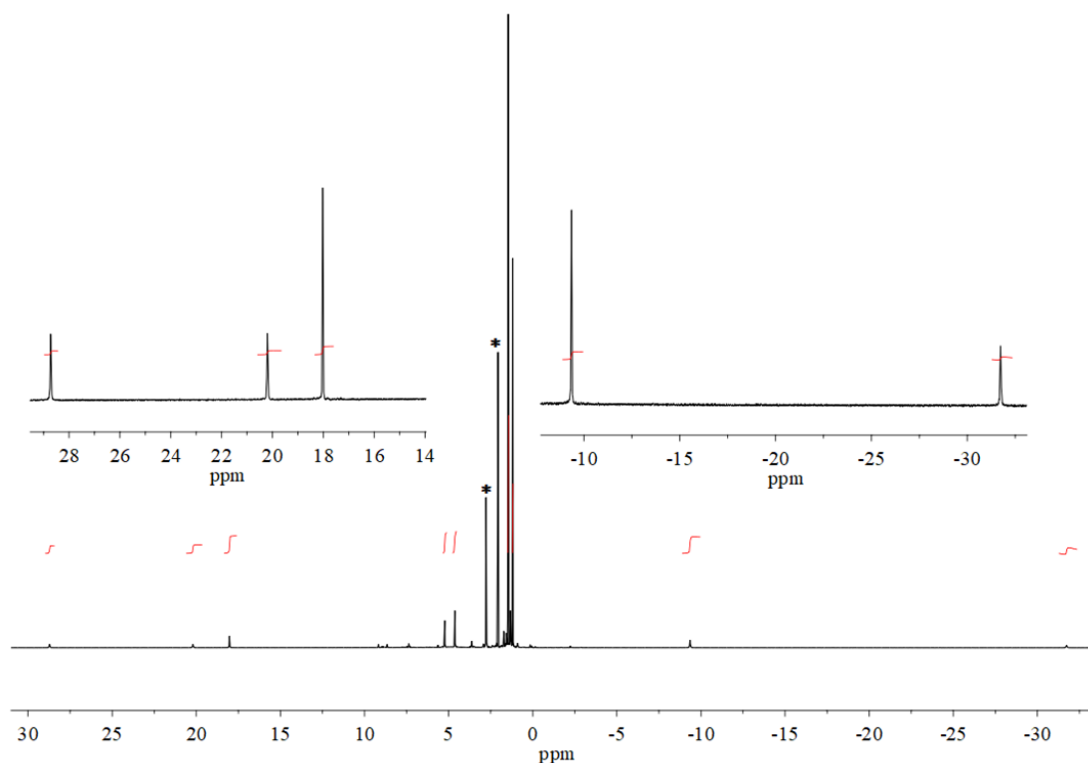
Figure 4.2.1: ^{1}H NMR spectrum of [{(trpy*)Ru}$_2$(μ,η^3:η^3-adc-Sal)](PF$_6$)$_2$ in (CD$_3$)$_2$CO. Insets represent highly shifted signals. *Signals from solvent residual.

4.3 Molecular structures.

Single crystals suitable for X-ray diffraction were prepared by slow crystallisation from a dichloromethane solution at 8°C in case of the hexafluorophosphate as counter anion and from a 1,2-dichloroethane solution at 8 °C in case of the perchlorate.

The perchlorate formed crystals only of limited quality, whereas bis(dichloromethane) solvate of the hexaflurophpsphate produced informative structural parameters, which were well reproduced by DFT calculations. Selected bond lengths and angles of the crystal structure are given in Table 4.3.1 and compared to the calculated values. Structural parameters of the perchlorate are listed in Table 4.3.2 and crystallographic parameters of both crystals are included in Chapter 7 (Table 7.4.3).

The molecular structure, shown in Figure 4.3.1 establishes a bis-meridional coordination and a planar geometry of the Ru(μ-adc-Sal)Ru fragment (C8-N1-N2-C1 and Ru1-N1-N2-Ru2 torsion angles are 170° and 174°, respectively) consisting fused 5 and 6 membered chelate rings. N-Ru-O angles reveal that the bite angles for the 5

and 6 membered ring lie around 78° and 90°, respectively. The N-N bond length, an important marker in depicting the ligand redox states, falls into an intermediate region between a single (hydrazido) and a double (azo) bond, in the present case. In addition to metal/ligand orbital mixing as was discussed in Chapter 2, the presence of a multicyclic chelate system restricts the unambiguous assignment of the intermediate ligand redox states for noninnocent ligands.[123] Also, the bond lengths exhibit only small differences from those of the free H_4adc-Sal molecule.[122a] However, important findings relevant to the mixed-valence description (localisation or delocalisation) are the equivalent coordination environment across the bridging ligand as evidenced by the Ru-N bond lengths (Ru1-N1 1.990(4), Ru2-N2 1.990(4), Ru1-N4 1.965(4), Ru2-N7 1.967(4) Å) and the remarkably short metal-metal distance of 4.727 Å. Identical Ru-N and relatively short N-N distances (1.392(6) Å) are compatible with both valence delocalised ($Ru^{2.5}(\mu\text{-adc-Sal})^{4-}Ru^{2.5}$) and radical bridged ($Ru^{II}(\mu\text{-adc-Sal})^{3\bullet-}Ru^{II}$) descriptions.
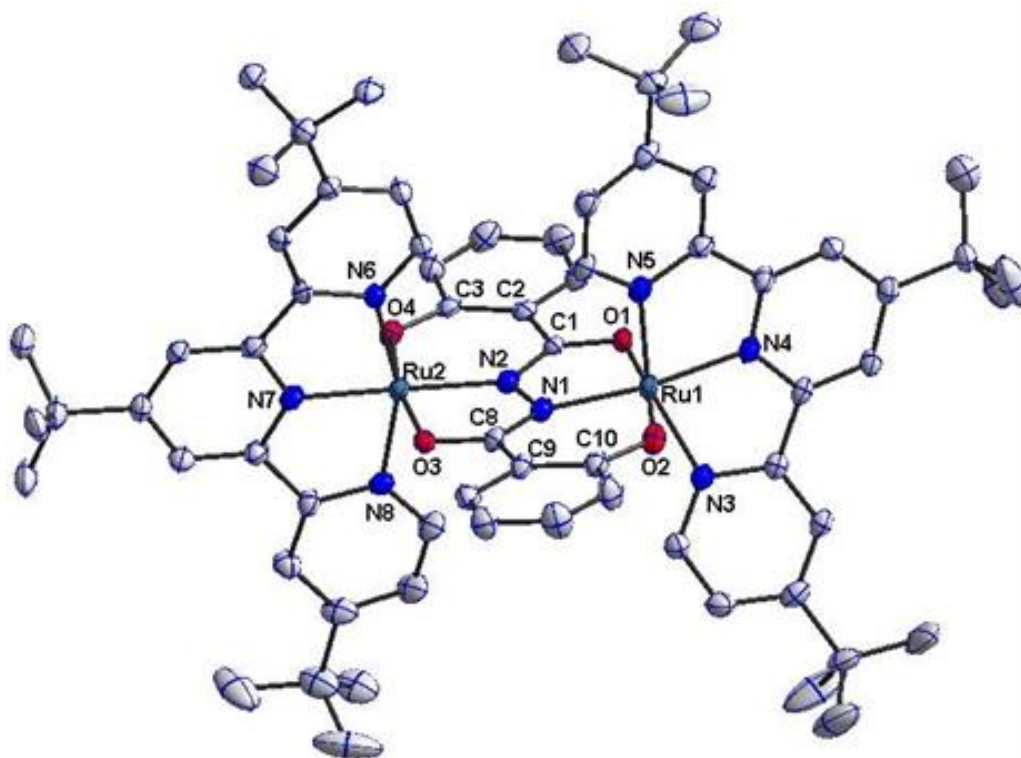
Figure 4.3.1: Molecular structure of the cation in the crystal of [{(trpy*)Ru}$_2$(μ-adc-Sal)]PF$_6$.2(CH$_2$Cl$_2$).Thermal ellipsoids are given at the 50% probability level; H atoms and the solvent molecules have been removed for clarity.

Table 4.3.1: Selected experimental and *in vacuo* DFT-calculated[a] bond lengths (Å) and angles (°) of the complex [{(trpy*)Ru}$_2$(μ-adc-Sal)]PF$_6$ and of [{(trpy')Ru}$_2$(μ-adc-Sal)]$^+$.[a]

bond	exp.	calc. [a]	bond	exp.	calc. [a]
Ru2-O4	2.013(4)	2.034	Ru1-N4	1.965(4)	1.974
Ru2-O3	2.054(4)	2.089	Ru1-N3	2.075(4)	2.069
Ru2-N6	2.065(4)	2.069	N1-N2	1.392(6)	1.391
Ru2-N2	1.990(4)	1.995	N1-C8	1.335(7)	1.355
Ru2-N7	1.967(4)	1.974	N2-C1	1.337(7)	1.355
Ru2-N8	2.056(4)	2.069	C1-O1	1.304(6)	1.284
Ru1-O1	2.038(4)	2.034	C3-O4	1.324(6)	1.309
Ru1-O2	2.039(4)	2.089	C8-O3	1.305(6)	1.284
Ru1-N1	1.990(4)	1.995	C10-O2	1.323(7)	1.309
Ru1-N5	2.055(4)	2.069			

angle	exp.	calc.[a]	angle	exp.	calc.[a]
O2-Ru1-O1	169.47(14)	168.4	N4 Ru1 N5	78.74(17)	78.9
N1-Ru1-O1	78.69(16)	91.4	N3 Ru1 O1	96.09(16)	93.5
N1-Ru1-O2	90.78(16)	77.0	N3 Ru1 O2	86.35(16)	88.7
N5-Ru1-O1	94.27(16)	93.5	N3 Ru1 N1	105.58(17)	101.2
N5-Ru1-O2	87.52(16)	88.7	N3 Ru1 N5	155.36(17)	157.4
N4 Ru1 N1	169.47(14)	174.5	N3 Ru1 N4	78.72(17)	78.9

[a] trpy'= 4,4',4″-trimethyl-2,2':6',2″-terpyridine. Dr. S. Záliš performed calculations.

Table 4.3.2: Selected experimental bond lengths (Å) and angles (º) of the complex [{(trpy*)Ru}$_2$(μ-adc-Sal)]ClO$_4$.

bond	exp.	bond	exp.
Ru2-O4	2.030(10)	Ru1-N4	1.995(9)
Ru2-O3	2.034(10)	Ru1-N3	2.052(12)
Ru2-N6	2.107(11)	N1-N2	1.374(14)
Ru2-N2	2.004(10)	N1-C8	1.335(15)
Ru2-N7	1.972(11)	N2-C1	1.319(15)
Ru2-N8	2.000(10)	C1-O1	1.339(17)
Ru1-O1	1.960(11)	C3-O4	1.336(18)
Ru1-O2	2.035(9)	C8-O3	1.312(15)
Ru1-N1	2.006(10)	C10-O2	1.336(14)
Ru1-N5	2.071(12)		

angle	exp.	angle	exp.
O2-Ru1-O1	169.9(3)	N4 Ru1 N5	78.2(4)
N1-Ru1-O1	79.1(4)	N3 Ru1 O1	87.9(4)
N1-Ru1-O2	91.2(4)	N3 Ru1 O2	91.0(4)
N5-Ru1-O1	94.6(4)	N3 Ru1 N1	99.7(4)
N5-Ru1-O2	90.1(4)	N3 Ru1 N5	158.2(4)
N4 Ru1 N1	174.5(4)	N3 Ru1 N4	79.9(4)

4.4 Cyclic voltammetry.

The complex [{(trpy*)Ru}$_2$(μ-adc-Sal)]PF$_6$ was examined by cyclic voltammetry and it exhibits three reversible redox processes (Figure 4.4.1). Generally polypyridyl

diruthenium systems ($[(bpy)_2Ru^{II}(BL)Ru^{II}(bpy)_2]^{n+}$, BL = bridging ligand) with highly charged bridging ligands (2− form in $BL^{0/\cdot-/2-}$) belong to a two-step redox system with a mixed-valent or radical intermediate.[51] The occurrence of the third reversible process is thought to be driven by the additional coordination of the π-donor phenolate substituent in the adc-R(2−) unit. A general redox scheme has been proposed here (Scheme 4.4.1) which depicts the sequential occurrence of d^5/d^6 and d^4/d^5 mixed-valent states in a single M-BL-M motif. Alternative electronic descriptions applicable to the individual redox species will be discussed in following sections as seen by UV-Vis-NIR and EPR spectroscopy. The comproportionation constants K_c = $10^{\Delta E/59 \text{ mV}}$ for both the mono- and di-cation are $10^{8.2}$ and $10^{13.3}$, respectively. These high values allowed isolating these species, while the higher value for the dication might be related to the antiferromagnetic interaction present in that redox state.[70]
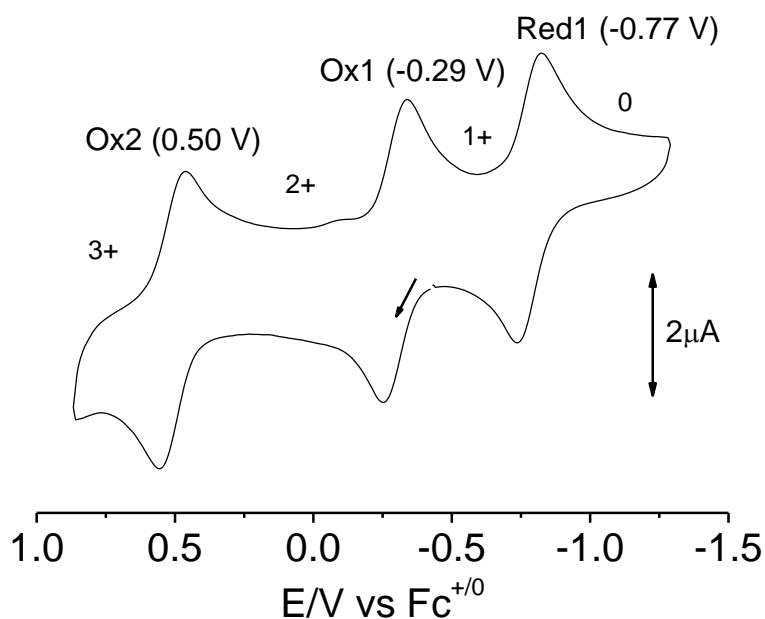
Figure 4.4.1: Cyclic voltammogram of [{(trpy*)Ru}$_2$(μ-adc-Sal)]PF$_6$ in CH$_2$Cl$_2$ / 0.1 M Bu$_4$NPF$_6$ at 100 mV / s scan rate. Potentials (in parenthesis) in V vs. Fc$^{+/0}$.

$$[L_xRu^{II}(BL)Ru^{II}L_x] \quad \underset{+e^-}{\overset{-e^-}{\rightleftharpoons}} \quad [L_xRu^{II}(BL)Ru^{III}L_x]^+ \quad \underset{+e^-}{\overset{-e^-}{\rightleftharpoons}} \quad [L_xRu^{III}(BL)Ru^{III}L_x]^{2+}$$

Red1   Ox1

$+e^- \Big\Vert -e^-$ Ox2

L_x = trpy*
BL = adc-Sal^{4-}

$$[L_xRu^{III}(BL)Ru^{IV}L_x]^{3+}$$
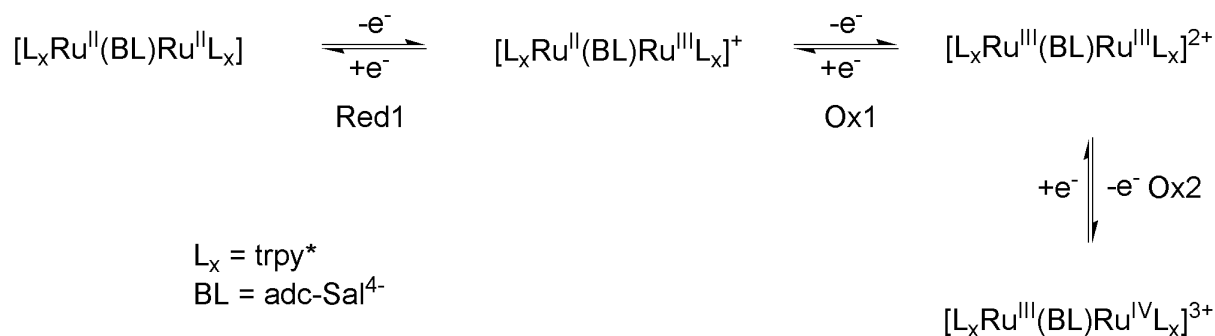
Scheme 4.4.1: A general redox scheme for [{(trpy*)Ru}$_2$(μ-adc-Sal)]$^+$.

4.5 EPR spectroscopy.

The monocationic species (1+) in the three-step reversible redox system [{(trpy*)Ru}$_2$(μ-adc-Sal)]$^{0/1+/2+/3+}$ has a paramagnetic nature. The presence of an unpaired electron allowed us to carry out an EPR spectroscopic study to differentiate between a possible mixed-valence (Ru^{II}/Ru^{III}) and a radical-bridged situation. The X-band EPR spectrum at 4.5 K (Figure 4.5.1) exhibits a rhombic signal with a relatively large g anisotropy (Δg = 0.45). It indicates that the unpaired spin is metal centred and the SOMO has partial contribution from the bridging ligand. The value of Δg is smaller than that of the bench mark Creutz-Taube ion (Δg = 1.141) and other mixed-valence units with a true Ru(III) centre.[120a,127] Calculated spin densities are listed in Table 4.5.2. The values remarkably indicate that the spin is almost equally distributed over three centres. Each Ru contains a spin density of 0.31 while the bridging ligand has 0.36. These calculated numbers resemble findings for another diruthenium complex with the bis-tridentate non-innocent bridging ligand 1,2,4,5-tetra(2-pyridyl)benzene[50a] which has been proposed as a fully delocalised Robin and Day Class III system. However, structural parameters point towards equivalent Ru centres, and the short N-N distance (1.392 Å) is also compatible with DFT-calculated spin densities and EPR data. These observations lead to a resonance hybrid formulation Ru$^{2.5}$(adc-Sal)$^{4-}$Ru$^{2.5}$ <–> Ru^{II}(adc-Sal)$^{3\bullet-}$Ru^{II} for the intermediate monocation.
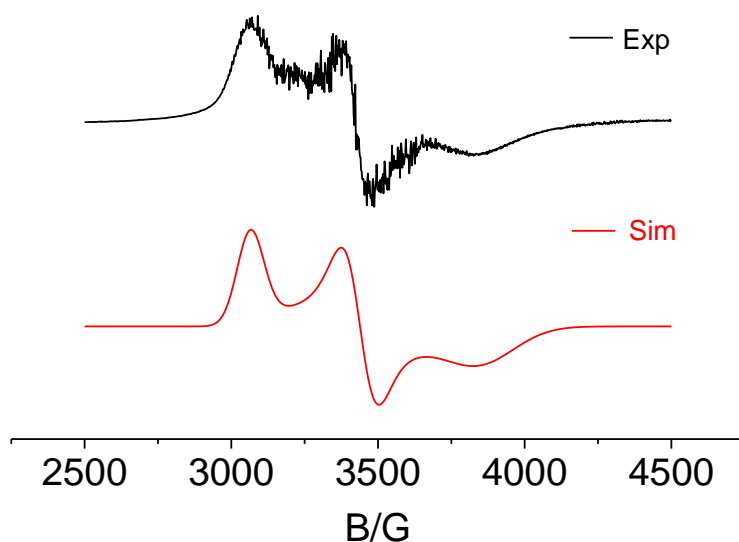
Figure 4.5.1: EPR spectrum of [{(trpy*)Ru}$_2$(μ-adc-Sal)]PF$_6$ in CH$_2$Cl$_2$ at 4.5 K with computer simulation.

The dication [{(trpy*)Ru}$_2$(μ-adc-Sal)]$^{2+}$ is also paramagnetic in nature as revealed from the ^{1}H NMR shifts at room temperature (Figure 4.2.1). EPR measurements were carried out for the native state (2+), the *in situ* electrochemically generated 2+ state and after chemical oxidation of the 1+ form with FcPF$_6$ in CH$_2$Cl$_2$. In all cases, no EPR signal was observed, even at 4 K. Geometrical optimisations were performed for possible electronic states: ^{3}A, UKS ^{1}A with two anti-parallel spins and RKS ^{1}A. The state ^{3}A has been found to be the lowest energy state and it differs from the UKS ^{1}A state with only 0.025 eV in free energy. The closed shell ^{1}A state lies 0.444 eV above the ^{3}A state. Calculated spin densities for ^{3}A and UKS ^{1}A states are listed in Table 4.5.2. Individual Ru atoms bear a spin density of 0.76 and 0.74 in case of the ^{3}A state, 0.69 and -0.75 for the UKS ^{1}A state. These observations infer that the ground ^{3}A term (S = 1) with ruthenium localised spin can be responsible for the absence of a proper signal. The rapid relaxation due to several accessible energy states in such systems often causes severe EPR line broadening and can eventually render the signal unidentifiable.[124]

The EPR spectrum of the trication (3+) was obtained at 5 K, after chemical oxidation of the 1+ form with two equivalents of AgPF$_6$ in CH$_2$Cl$_2$. It exhibits a rhombic signal with g anisotropy (Δg = 0.51). Though the spectral pattern is similar to the 1+ form, a considerable shift of the isotropic g factor to a higher value (2.09 vs. 1.96 for 1+ form)

and a slightly greater g anisotropy has been observed (Figure 4.5.2, Table 4.5.1). Two plausible electronic descriptions $Ru^{III}(adc-Sal)^{4-}Ru^{IV}$ and $Ru^{III}(adc-Sal)^{3\bullet-}Ru^{III}$, can be ascribed to this state (3+). DFT calculation predicts the lowest energy state as ^2A (S = ½) with antiparallel spin on the Ru centres, the individual Ru centres bear the spin density of 0.98 and -0.65. According to the calculated result, the Ru centres are antiferromagnetically coupled which should lead to a ligand based radical EPR signal.[125] Our current spectroscopic data is compatible with either the mixed-valence (Ru^{III}/Ru^{IV}) state or a 3-spin coupled situation[126] where antiferromagnetic coupling between metal and the bridging ligand dominates leaving the spin on the Ru. However, it becomes difficult to impose a proper electronic description for highly charged complexes because of increased covalency as in the present case.
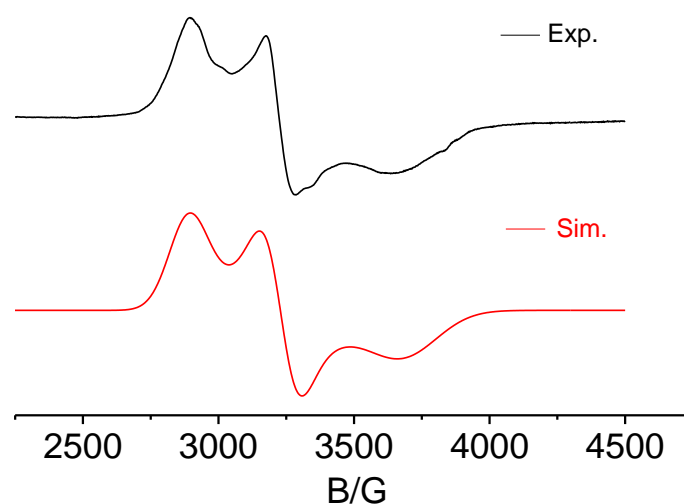
Figure 4.5.2: EPR spectrum of $[\{(trpy^*)Ru\}_2(\mu-adc-Sal)]^{3+}$ from chemical oxidation of $[\{(trpy^*)Ru\}_2(\mu-adc-Sal)]PF_6$ with 2 eq of $AgPF_6$ in CH_2Cl_2 at 5 K.

Table 4.5.1: EPR data of paramagnetic states.

	$[\{(trpy^*)Ru\}_2(\mu-adc-Sal)]^+$	$[\{(trpy^*)Ru\}_2(\mu-adc-Sal)]^{3+}$
g_1	2.19	2.33
g_2	1.95	2.09
g_3	1.74	1.82
g_{av}	1.96	2.09
g_1-g_3	0.45	0.51
solvents (temp.)	CH_2Cl_2 (4.5 K)	CH_2Cl_2 (5 K)

$g_{av} = [(g_1^2 + g_2^2 + g_3^2)/3]^{1/2}$

Table 4.5.2: DFT calculated spin densities for [{(trpy')Ru}$_2$(μ-adc-Sal)]^n.
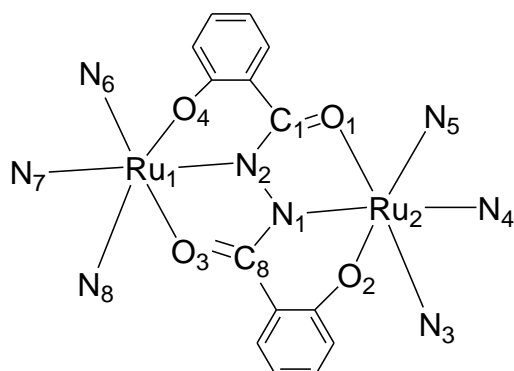
atom	spin density			
	n = +1 (^{2}A)	n = +2 (^{3}A)	n = +2 (UKS ^{1}A)	n = +3 (^{2}A)
Ru1	0.310	0.764	-0.750	0.977
Ru2	0.311	0.740	0.694	-0.652
N1	0.091	0.059	-0.033	0.220
N2	0.091	0.045	0.117	0.095
O1	0.111	0.141	0.059	0.099
O2	-0.008	0.055	-0.142	0.107
O3	0.111	0.051	0.038	0.099
O4	-0.008	0.005	0.016	-0.157
N3	0.002	-0.012	0.011	-0.011
N4	0.005	-0.008	0.008	-0.019
N5	0.002	-0.012	0.018	0.001
N6	0.002	0.002	0.015	0.009
N7	0.005	-0.010	-0.012	0.009
N8	0.002	0.006	0.014	0.020
C1	0.001	0.053	0.003	0.027
C8	0.001	-0.035	0.027	-0.025

4.6 UV-Vis-NIR spectroelectrochemistry.

Spectroelectrochemical measurements for [{(trpy*)Ru}$_2$(μ-adc-Sal)]^n (n= 0, 1+, 2+, 3+) were performed in CH_2Cl_2/0.1 M Bu_4NPF_6 using an OTTLE[72] cell to investigate the spectral changes in the UV-Vis-NIR region during all reversible redox processes. Experimental and TD-DFT calculated absorption values are given in Table 4.6.2. The monocation [{(trpy*)Ru}$_2$(μ-adc-Sal)]$^+$ exhibits NIR bands around 1600 nm, characteristic for the mixed-valence unit Ru^{II}(μ-adc-Sal)$^{4-}$Ru^{III}. These bands disappear completely on both one-electron reduction and oxidation (Figure 4.6.4).

NIR band analysis for the mixed-valent species (n = 1+): The asymmetric NIR feature, corresponding to the mixed-valent species (n = 1+), can be deconvoluted into three bands employing Lorentzian functions (Figure 4.6.1) which points to multiple absorptions as a result of multiple metal-ligand-metal orbital interactions. Five expected transitions designated as IT (Inter-valence transfer) and IC (inter-configurational) type can be observed for d^5/d^6 mixed-valent transitions according to the model by Rocha, Meyer and coworkers (Scheme 4.6.1).[17] However, there are very few examples of diruthenium species showing such splitting.[17,50a]
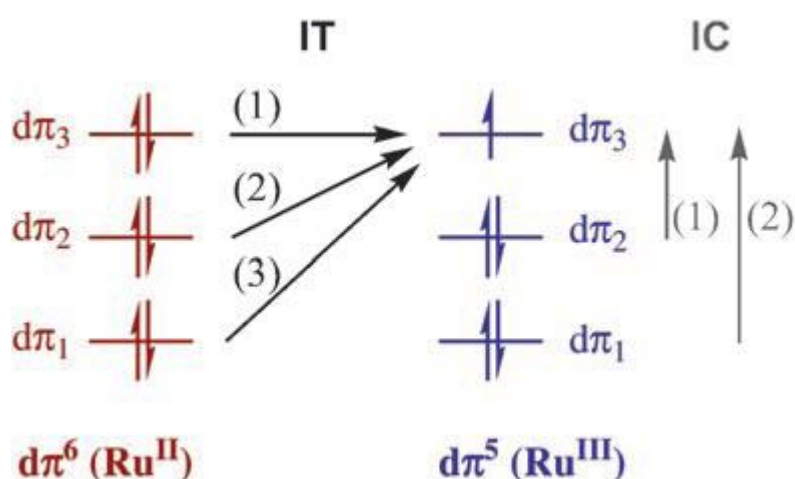
Scheme 4.6.1

(*Taken from the ref. 17*)
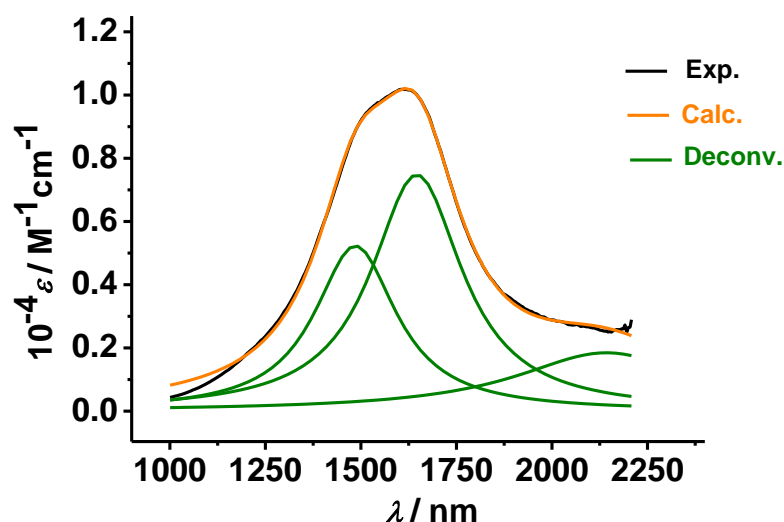
Figure 4.6.1: Deconvolution of near-IR band for [{(trpy*)Ru}$_2$(μ-adc-Sal)]$^+$ assuming Lorentzian line shape.

Table 4.6.1: Deconvoluted NIR transition data.

compound	λ$_{max}$/nm (10^{-4} ε / M^{-1} cm^{-1})	Δν$_{1/2}$^{a} /cm^{-1}	H$_{ab}$^{b} (cm^{-1})
[{(trpy*)Ru}$_2$(μ-adc-Sal)]$^+$	2140(0.1), 1645(0.7), 1485(0.5)	1290,1078, 1190	2336,3039, 3367

^{a} Experimental bandwidths at half height in cm^{-1}, ^{b} H$_{ab}$ = 1/2 ν$_{max}$ for a Robin and Day Class III system.

However, in the present system the deconvoluted bands can be assigned to three narrow and fairly intense IT transitions originating at λ$_{max}$ = 2140 nm (IT(1), ε ≈ 1000 M^{-1}cm^{-1}, Δν$_{1/2}$ ≈ 1290 cm^{-1}), 1645 nm (IT(2), ε ≈ 7000 M^{-1}cm^{-1}, Δν$_{1/2}$ = 1078 cm^{-1}) and 1485 (IT(3), ε ≈ 5000 M^{-1}cm^{-1}, Δν$_{1/2}$ = 1190 cm^{-1}). Intensities of these IT bands exhibit a similar pattern (ε$_{IT(2)}$,ε$_{IT(3)}$ >> ε$_{IT(1)}$) as reported by T.J. Meyer and co-workers.[17] Approximate IC(1) and IC(2) absorption energies which are 1407 cm^{-1} and 2062 cm^{-1}, respectively can be deduce from IT band energies (E$_{IT(2)}$ ≈ E$_{IT(1)}$+E$_{IC(1)}$, and E$_{IT(3)}$ ≈ E$_{IT(1)}$+E$_{IC(2)}$). Absorption bands corresponding to IC transitions were not detectable as ligand vibrational peaks in the respective IR region obscure them.

TD-DFT calculations predict the NIR absorption at 1580 nm and the transition is formed by combined βHOMO-1 → βLUMO, βHOMO-2 → βLUMO excitations. These MOs are presented in Figure 4.6.3. Calculation of corresponding electron density

redistribution (Figure 4.6.2) can be described as ML$_{(adc-Sal)}$CT with an admixture of IL$_{(adc-Sal)}$ and MC (metal-centred) transitions. Two low intense absorptions are also calculated with similar character at 2156 and 1373 nm.
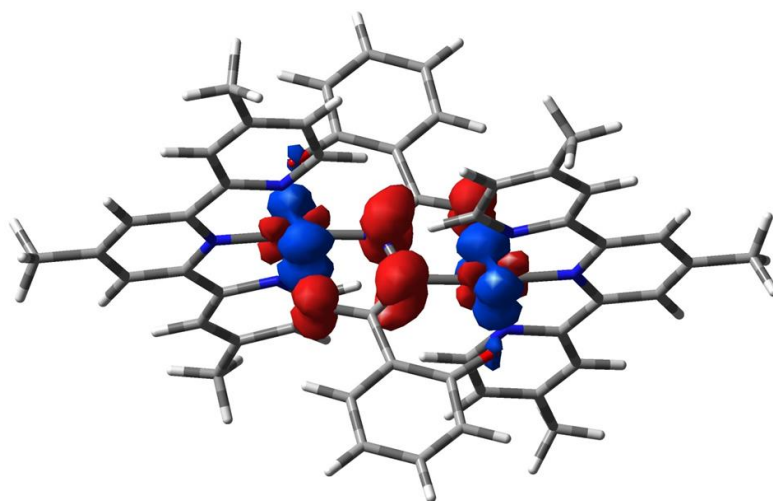
Figure 4.6.2: Electron density redistribution accompanying the NIR transition of [(trpy')Ru(μ-adc-Sal)Ru(trpy')]$^+$ calculated at 1580 nm. Red and blue colours indicate increasing and diminishing electron density, respectively.

αHOMO, βLUMO

αHOMO-1, βHOMO

βHOMO-1   βHOMO-2
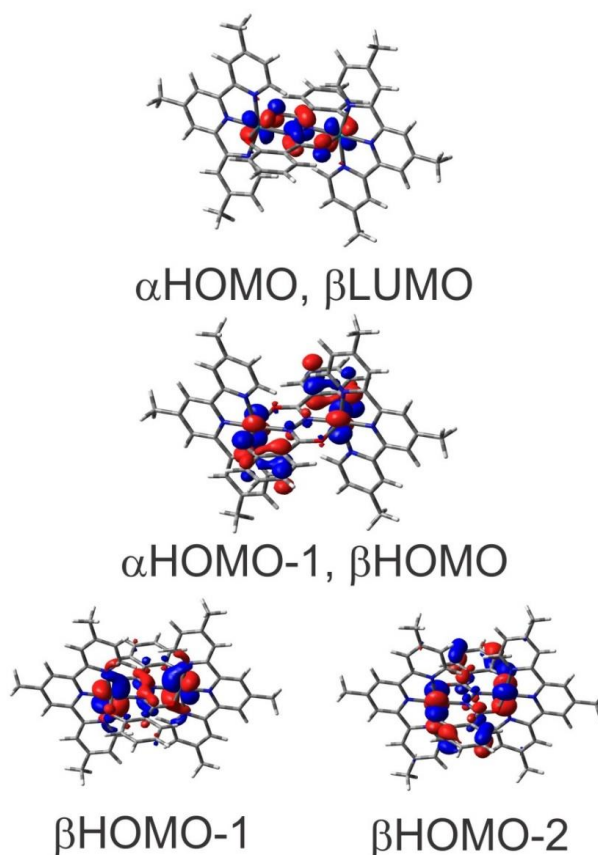
Figure 4.6.3: MOs involved in the NIR transition of [(trpy')Ru(μ-adc-Sal)Ru(trpy')]$^+$ calculated at 1580 nm. Dr. S. Záliš performed calculations.

The visible region displays mainly trpy* based MLCT transitions for all redox species (n = 0, 1+, 2+, 3+). They are hypsochromically shifted with decreased intensity on going from the reduced (n=0) (λ_{max} = 605, 439 nm) to the oxidized (n=2+) (λ_{max} = 406 nm) form, as expected.[50b] A weak long-wavelength shoulder corresponding to an LLCT transition (π-(adc-Sal)$^{4-}$ $\longrightarrow$ π^*-trpy*) has been also observed for the reduced species. It is commonly seen in Ru polypyridyl complexes with π-donor ligands.[48,50b] On the other hand, the green oxidised (n=2+) species gives multiple low energy absorptions (λ_{max} = 717 nm with a shoulder at around 926 nm) which were calculated to have a predominant MLCT/IL character and shifted to the short wavelength region with respect to the NIR transition observed for the native mixed-valence state (n=1+). Gradual increase of charge on the metal centre can be attributed to the short wavelength shift of the band. After the 2nd oxidation to the n= 3+ form, an intense ($\varepsilon \approx$ 11000 $M^{-1}cm^{-1}$) and asymmetric band at λ_{max} = 777 nm appears with a long tail, extending into the NIR region (Figure 4.6.4). According to TD-DFT calculation, this band can be assigned to sizeable mixing of MLCT and MC transitions. Notably, calculated absorption values are reasonably fitting with the experimentally found absorption values according to Table 4.6.2.

Table 4.6.2: Absorption values from UV-Vis-NIR spectroelectrochemistry[a] of [{(trpy*)Ru}$_2$(μ-adc-Sal)]^n

n	Exp. λ_{max}/nm (10^{-4} ε / M^{-1} cm^{-1}) [Calc. λ_{max} / nm] [b]
0	798 (sh), 605(2.1), 439(2.4), 309(4.9) [750, 570, 543, 414]
1+	2140(0.1), 1645(0.7), 1485(0.5), 541(1.6), 421(1.4), 309(5.0) [2156, 1580, 1373, 484]
2+	926 (sh), 717(0.6), 449 (sh), 406(1.4), 309(4.8) [961, 791, 467, 406]
3+	983(sh), 777(1.1), 437(1.3), 311(4.3) [1067, 765, 440]

[a] In CH_2Cl_2/0.1 M Bu_4NPF_6. [b] Absorption values from TD-DFT calculations of [{(trpy')Ru}$_2$(μ-adc-Sal)]^n, for simulated spectra and details *see* Table 10.A1 and Figures 10.A5-10.A7.
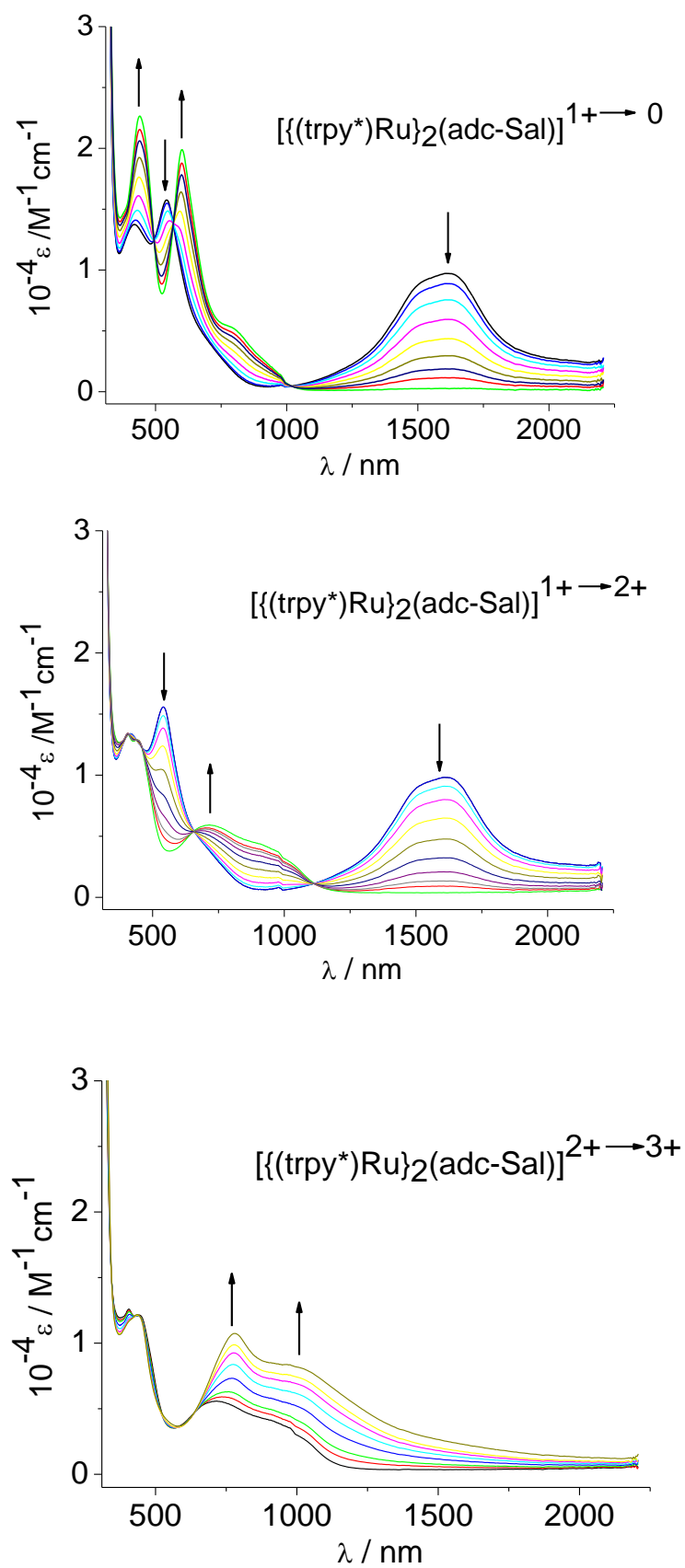
Figure 4.6.4: UV-Vis-NIR spectroelectrochemical reduction and oxidations of [{(trpy*)Ru}$_2$(adc-Sal)]PF$_6$ in CH$_2$Cl$_2$/0.1 M Bu$_4$NPF$_6$ at 298 K.

4.7 IR spectroelectrochemistry.

The species involved in the redox system [{(trpy*)Ru}$_2$(μ-adc-Sal)]^n (n = 0, 1+, 2+, 3+) were investigated by IR spectroscopy. Spectral changes of n = 1+ during reduction and two-step oxidations in CH_2Cl_2/0.1 M Bu_4NPF_6 are depicted in Figure 4.7.1. Several bands such as C=O/C=N stretching from the bridging ligand, aromatic ring stretching from trpy* can be observed in the range 1700-1500 cm^{-1}. The broad band of electronic transitions, which extend from the NIR to IR region, affect these vibrational bands, making them less comprehensible. However, during the reduction (n = 1+$\rightarrow$ 0) infrared spectrum changes significantly by appearance of strong bands at 1549 and 1512 cm^{-1}, which indicates a change in resonating form of the bridging ligand (Scheme 4.7.1). The bands around 1600 cm^{-1}, which can be assigned to the stretching from trpy*, does not change significantly during reduction. Besides, during two-step oxidations there is also no significant change in the IR spectra, which corresponds to less structural changes of the bridging ligand in compared to that occurred during the reduction.
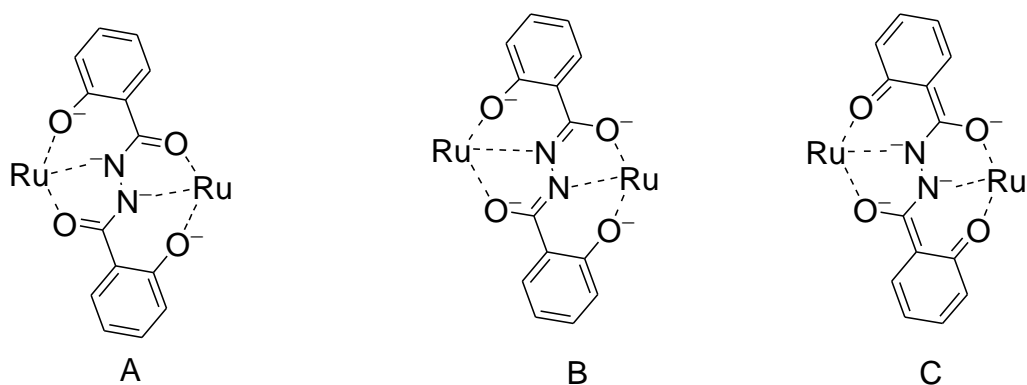
Scheme 4.7.1: Resonance forms of the bis(tridentate) bridging ligand adc-Sal(4-).
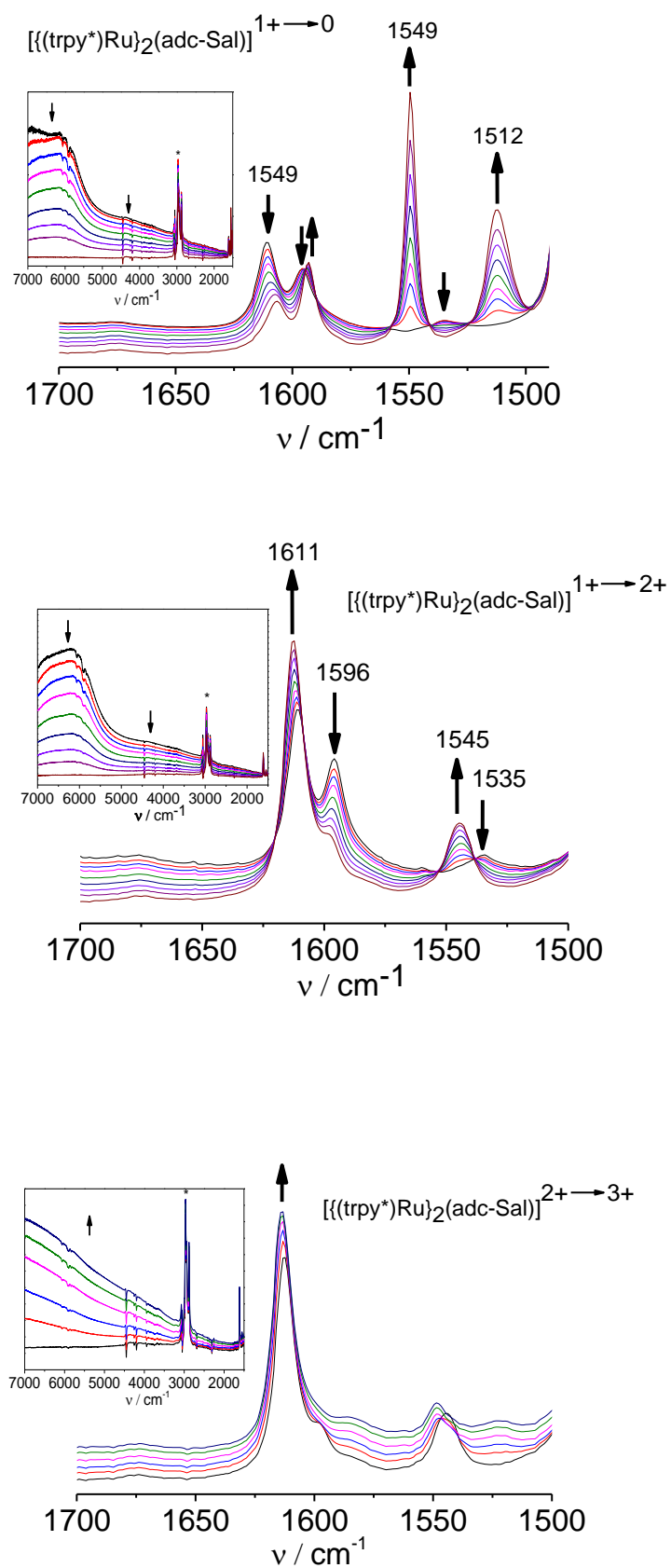
Figure 4.7.1: IR spectroelectrochemical reduction and oxidations of [{(trpy*)Ru}₂(adc-Sal)]PF₆ in CH₂Cl₂/0.1 M Bu₄NPF₆ at 298 K (* strong absorption of the solvent).

Conclusion.

This chapter presents a new, structurally characterised mixed-valence (Ru^{II}/Ru^{III}) monocation [{(trpy*)Ru}$_2$(μ-adc-Sal)]$^+$ with unusual μ,η^3:η^3 coordination. The bond properties gave an initial but ambiguous idea of valence description between delocalized mixed-valence (similar Ru-N distances) and a radical bridged (short N-N distance of 1.392(6) Å) situation. Eventually, the small g anisotropy in comparison to the benchmark Creutz-Taube ion and the DFT calculated spin densities allow proposing a borderline situation Ru$^{2.5}$(adc-Sal)$^{4-}$Ru$^{2.5}$ <—> Ru^{II}(adc-Sal)$^{3\cdot-}$Ru^{II}. This description is further supported by the intense, narrow NIR absortions and their character (a charge resonance band) predicted by the TD-DFT calculation. The monocation also belongs to those few examples of ruthenium mixed-valence complexes, which show multiple NIR transitions. This nature indicates a strong orbital interaction of bridging (adc-Sal)$^{4-}$ ligand with two metal centres, which also justify the potential of the bridging ligand to transfer charge or electrons. Such ability makes the ligand a promising candidate in designing materials like molecular wires.[26]

The present system with a bis-tridentate bridging (adc-R)$^{4-}$ can be distinguished from related bis-bidentate systems[51] by its extended redox steps involving a Ru^{III}/Ru^{IV} state as has been shown in Scheme 4.4.1. The additional phenolate/phenoxyl component as R in the hydrazide ligand (adc-R)$^{2-}$ stabiles higher oxidation states of ruthenium. Modification of this additional component with different substituents or with different donor sites may produce interesting electrochemical and spectroscopic features. Attention should be provided to develop new such ligands in future.

Chapter 5

A dinuclear ruthenium complex with an asymmetrical bridging ligand.

5.1 Introduction.

Mixed-valent (MV) dinuclear complexes (low spin d^5/d^6) have served well as models in the study of intramolecular electron transfer processes. Many of such symmetrical[14,32a] complexes have been investigated, but asymmetrical complexes are equally important because most electron-transfer-active biological systems are asymmetrical.[111] There are examples of heterobimetallic complexes[43,89-93] covering Ru-Os, Ru-Fe, Ru-Mo or Ru-Re systems and cyclometalated as well as non-cyclometalated asymmetrical diruthenium systems[94-98]. The focus of the present study is on non-cyclometalated diruthenium systems; very few such examples[98] are known which exhibit strong ($\varepsilon \approx 5000$ M^{-1} cm^{-1}) NIR absorptions, an important property for potential applications[99].

Symmetrical 1,2-dicarbonylhydrazido(2−) (adc-R(2−)) ligands have shown their ability in establishing efficient electronic communication between two metal centres in diruthenium complexes.[51,69] For these donor ligands, the metal-ligand-metal electronic interaction can be understood by a super-exchange mechanism, the *hole transfer*.[69] The similar potential of an asymmetrical ligand, designated as adc-Salph(3−) (Scheme 5.1.1), will be presented here. This ligand has the ability to coordinate two metal centres in a μ-η^2:η^3 fashion (N,O/O,N,O'), which has been used to prepare supramolecular complexes like metallacrowns.[100,101] Therefore, complexes with this kind of bridging ligand with an odd number of donor sites would be interesting from a structural point of view. A few other polynuclear complexes (not metallacrowns) with adc-Salph(3−) or coordination-wise related adc-R ligands have been reported,[102-105] but dinuclear complexes are extremely rare, at least, no such

dimers have been studied electrochemically or with respect to mixed-valency (low spin d^5/d^6).
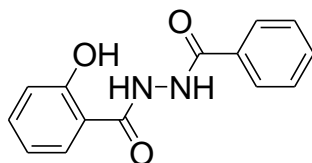
1-benzoyl-2-salicyloylhydrazine
H$_3$adc-Salph

Scheme 5.1.1: Protonated form of the ligand adc-Salph(3-).

The complex [51]PF$_6$ (Scheme 5.1.2) has been studied structurally, electrochemically and spectroscopically (EPR, NMR, UV-Vis-NIR), and the results can be compared to those from the symmetrical complexes from Chapters 3 and 4 (named as [31]PF$_6$ and [41]PF$_6$ in Scheme 5.1.2, respectively).

[51]PF$_6$ [31]PF$_6$ [41]PF$_6$

M = Ru   L$_n$ =
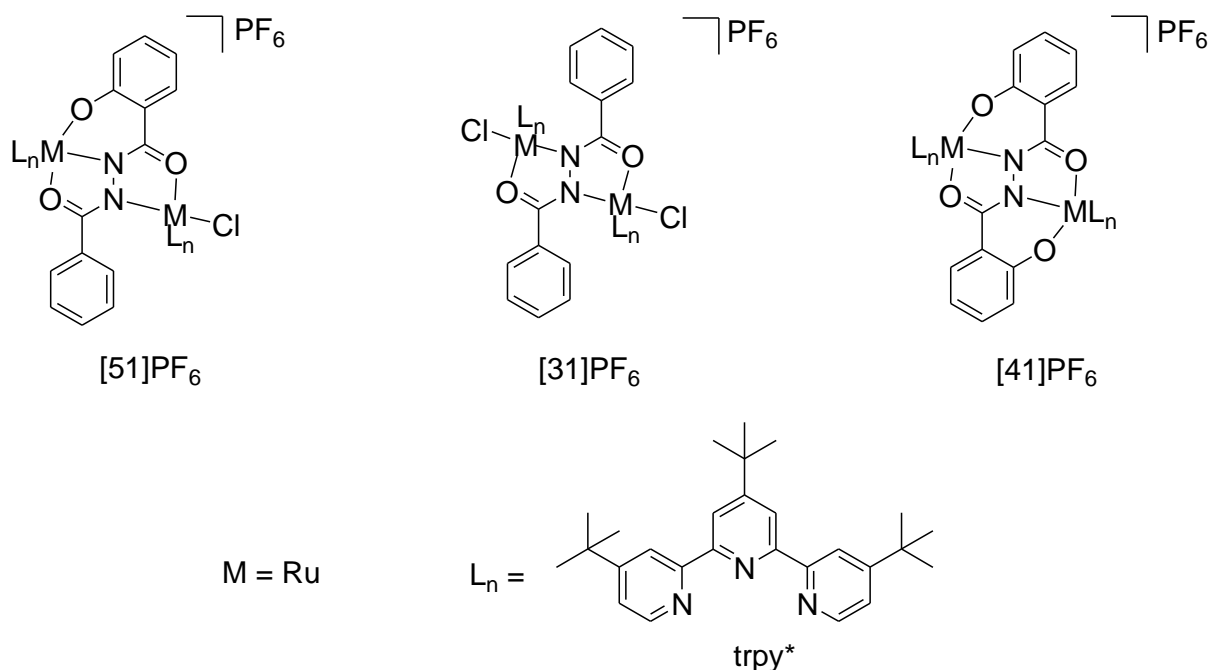
trpy*

Scheme 5.1.2: Symmetrical and asymmetrical complexes of 1,2-dicarbonylhydrazido(2−) ligands with different aryl substituents.

5.2 Synthesis and characterisation.

Reaction of H_3adc-Salph with two equivalents of *mer*-Ru(trpy*)Cl$_3$ in the presence of triethylamine as a base in refluxing ethanol resulted in the asymmetric complex, [{(trpy*)Ru}$_2$(μ-adc-Salph)Cl]PF$_6$ ([51]PF$_6$). The cation/anion ratio (1:1) has been confirmed by elemental analysis and mass spectroscopy (*see* Chapter 7.3.3).This ratio indicates the presence of Ru^{II} and Ru^{III} centres in [51]PF$_6$, resulting in a paramagnetic complex. The bidentate/tridentate ligand adc-Salph(3−) is interacting with two different ruthenium fragments, and thus results in two different halves A and B (Scheme 5.2.1) in the complex. Meridional coordination of trpy* and the N,O donor combination from the bridging ligand gives rise to two possibilities B1 and B2 which results in different constitutional isomers; these were named as AB1 and AB2 according to the different combinations of the molecular halves.

O,O' : carbonyl-O, phenolate-O

N$_{azo}$: N atom involved in NN bond

A

B1   B2
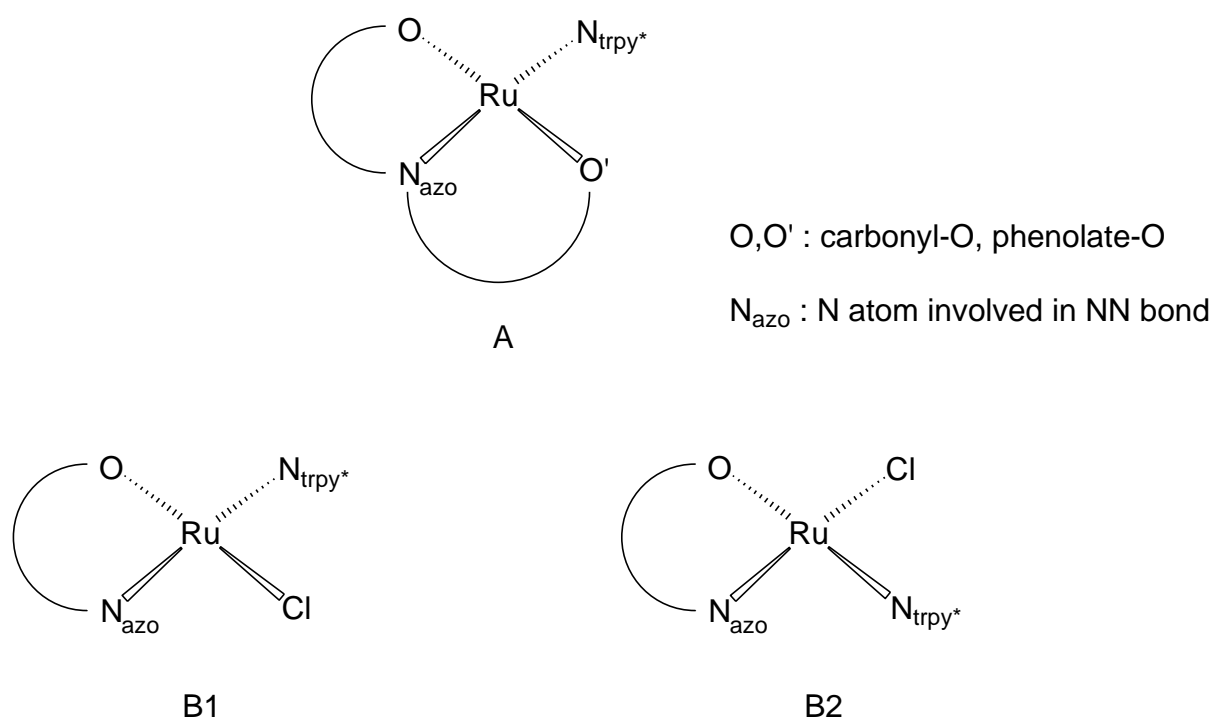
Scheme 5.2.1: Coordination environments (only equatorial positions shown in an octahedral geometry) of different molecular halves of the complex cation [51]$^+$.

Structural characterisation (*see* 5.3) has confirmed the formation of the isomer AB2 where the chloride function is ligated *trans* to an N_{azo} atom. Generally, symmetrical complexes like [{Cl(trpy*)Ru}$_2$(μ,η^2:η^2-adc-Ph)]PF$_6$ ([31]PF$_6$) and [{(trpy*)Ru}$_2$(μ,η^3:η^3-adc-Sal)]PF$_6$ (([41]PF$_6$)) exhibit two singlets for *tert*-butyl protons from trpy* in their ^{1}H NMR spectra. They appear in the characteristic alkane region between 1.3 and 1.9 ppm (*see* Chapter 7.3.3); one singlet corresponds to nine protons from the *tert*-butyl group connected to the central pyridyl ring and the other to 18 protons from those connected to the terminal pyridyl rings. In contrast, four signals between 1 and 1.8 ppm were observed for [51]PF$_6$, as depicted in Figure 5.2.1. Two points can play an important role here, i) different coordinative environment of trpy* in A and B2 and ii) non-uniform charge distribution over both ruthenium complex fragments, induced by the asymmetrical ligand coordination.
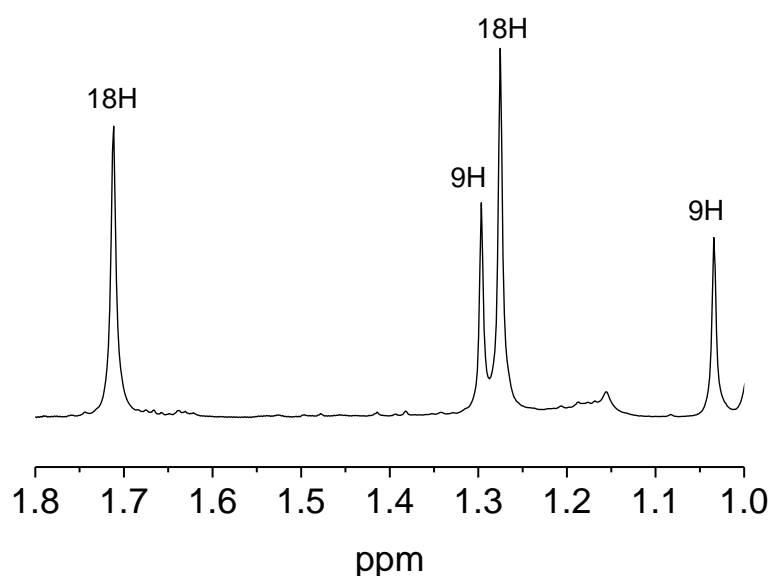
Figure 5.2.1: ^{1}H NMR resonances (only *tert*-butyl protons) of [51]PF$_6$ in (CD$_3$)$_2$CO.

The reaction procedure and the chemical structure depicting the AB2 isomer for [51]PF$_6$ are given in the following Scheme 5.2.2.
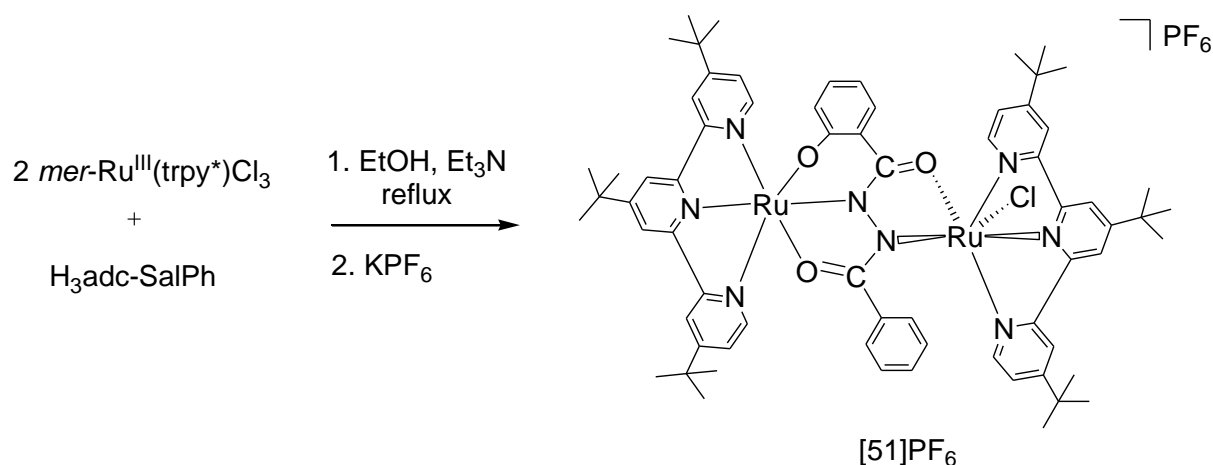
Scheme 5.2.2: Reaction scheme for [51]PF$_6$.

5.3 Molecular structure analysis.

Single crystals appropriate for X-ray diffraction were grown by slow diffusion of hexane into a 1,2-dichloroethane solution of [51]PF$_6$. The asymmetrical complex [51]PF$_6$ crystallises in the space group Pbca. The molecular structure is shown in Figure 5.3.1. All crystallographic data are given in Chapter 7.4.4 and selected bond lengths and angles are listed in Table 5.3.1.

Structural information like the N-N bond distance is important for characterising "odd-electron" mono- or dinuclear complexes with azo-containing redox-active ligands.[9,71] Structural information can also be an additional support along with widely used NIR-band-analysis in characterising a diruthenium mixed-valent species. Especially when communicating ruthenium fragments are in different environments, structural data can play a pivotal role in establishing the proper mixed-valence assignment. Meyer and co-workers have presented one symmetrical mixed-valent compound [Cl$_3$Ru(tppz)RuCl$_3$]$^-$ (tppz = 2,3,5,6-tetrakis(2-pyridyl)pyrazine) for which the structural characterisation helped to assign a Class II-III mixed-valence nature.[17]

The molecular structure clearly confirms the formation of the AB2 constitutional isomer as mentioned previously. In the molecular half A, one ruthenium ion (Ru2 in Figure 5.3.1) is coordinated with trpy* and with the O2, N2 and O3 donor atoms of

the bridging ligand in a bis-meridional fashion, forming four five-membered and one six-membered chelate rings. On the other hand, in the molecular half B2, the ruthenium ion (Ru1 in Figure 5.3.1) is surrounded by three five-membered chelate rings. The molecular structure also depicts a π- π interaction between the phenyl ring from the bridging ligand and the central pyridyl ring from trpy*. The distance between these two ring centroids is 3.527 Å.
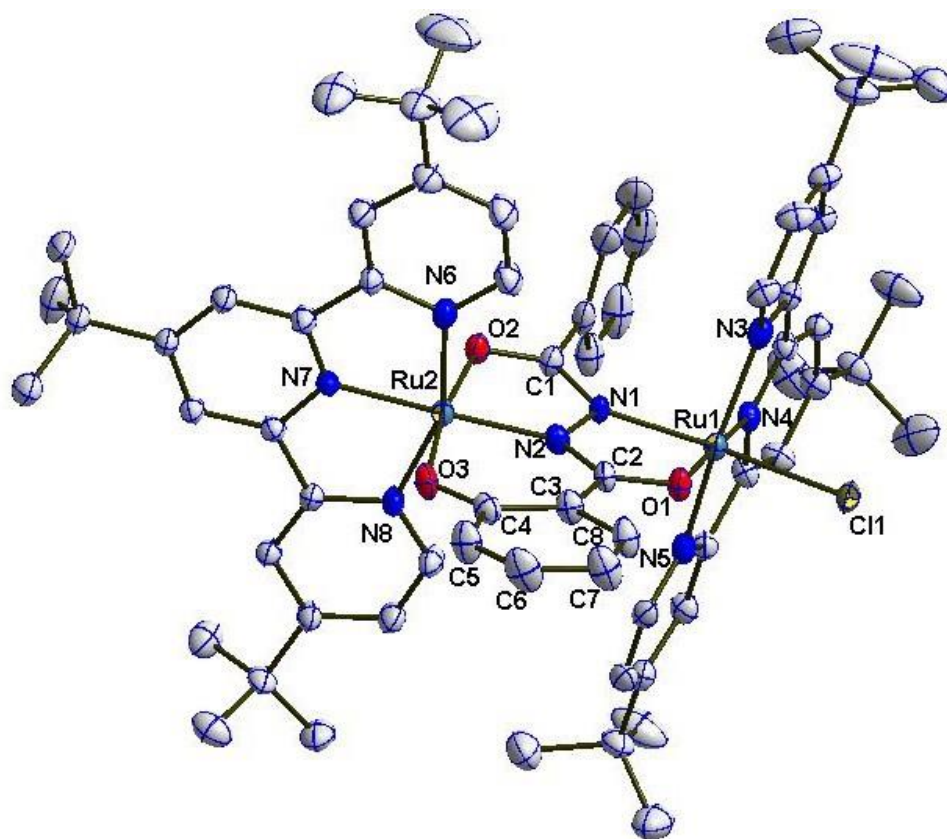
Figure 5.3.1: Molecular structure of the cation in the crystal of [51]PF$_6$ x C$_2$H$_4$Cl$_2$. Thermal ellipsoids are given at the 50% probability level; H atoms and the solvent molecule of dichloroethane are removed for clarity.

Three electronic descriptions including mixed-valence and radical-bridged situations are possible in the present case. They are as follows:

I) [(trpy*)Ru^{II}(μ-adc-Salph)$^{3-}$Ru^{III}(trpy*)Cl]$^+$

II) [(trpy*)Ru^{III}(μ-adc-Salph)$^{3-}$Ru^{II}(trpy*)Cl]$^+$

III) [(trpy*)Ru^{II}(μ-adc-Salph)$^{2•-}$Ru^{II}(trpy*)Cl]$^+$

The valence delocalised ($Ru^{2.5}$- $Ru^{2.5}$) description is questionable here because, even in the case of a strong interaction between the two metal centres, there should be a residual charge difference as the coordination environments of the two metal fragments are different. In addition, the $Ru-N_{adc\text{-}Salph}$ bonds, which could be an important structural marker in proposing a proper MV description, should differ in the molecular halves A and B2 because of the similar reason. The $Ru-N_{trpy*}$ and $Ru-N_{adc\text{-}Salph}$ bond lengths from these two molecular halves are considerably different in the complex (Table 5.3.1). In particular, the $Ru-N_{adc\text{-}Salph}$ (Ru2-N2) bond length displays a significantly shorter value (1.968(4) Å) than the $Ru-N_{adcSal}$ distance (1.990(4) Å) in the symmetrical MV complex [41]PF_6 (*see* Chapter 4). The coordination environment surrounding ruthenium in this symmetrical complex resembles the molecular half A and it should be noted that the complex has been described as a resonance hybrid, $Ru^{2.5}(adc\text{-}Sal)^{4-}Ru^{2.5}$ <–> $Ru^{II}(adc\text{-}Sal)^{3\bullet-}Ru^{II}$. An assumption can be made from this analogy that section A contains a Ru^{III} ion in [51]PF_6, resulting in an electronic situation $[(trpy*)Ru^{III}(adc\text{-}Salph)^{3-}Ru^{II}(trpy*)Cl]^+$. This assumption is also based on the strong donor ability of the phenolate function as compared to chloride. It is expected that the phenolate coordinated ruthenium fragment will prefer higher charge.

The third electronic description, which is a radical bridged situation, can be neglected because the N-N bond length (1.427(6) Å) suggests a single-bond.[48] Noticeably, the C3-C4 bond distance (1.426(8) Å) exhibits a slightly greater value when compared to other C-C distances in the salicyloyl ring. Especially the C5-C6 and C7-C8 distances exhibit lower value ($\approx$1.36 Å) than the standard aromatic C-C distance (1.39 Å). These results along with other bond parameters (C-O/C-N distances) from the bridging ligand (Table 5.3.1) point to different resonance structures A to E (Scheme 5.3.1) of adc-Salph(3–), combining a hydrazido(2–) and a phenolate function. Specifically D is expected to have a greater contribution according to different C-O distances ($d_{C1\text{-}O2}$, $d_{C2\text{-}O1}$ = 1.293(6), 1.274(6) Å) from the OCNNCO core.
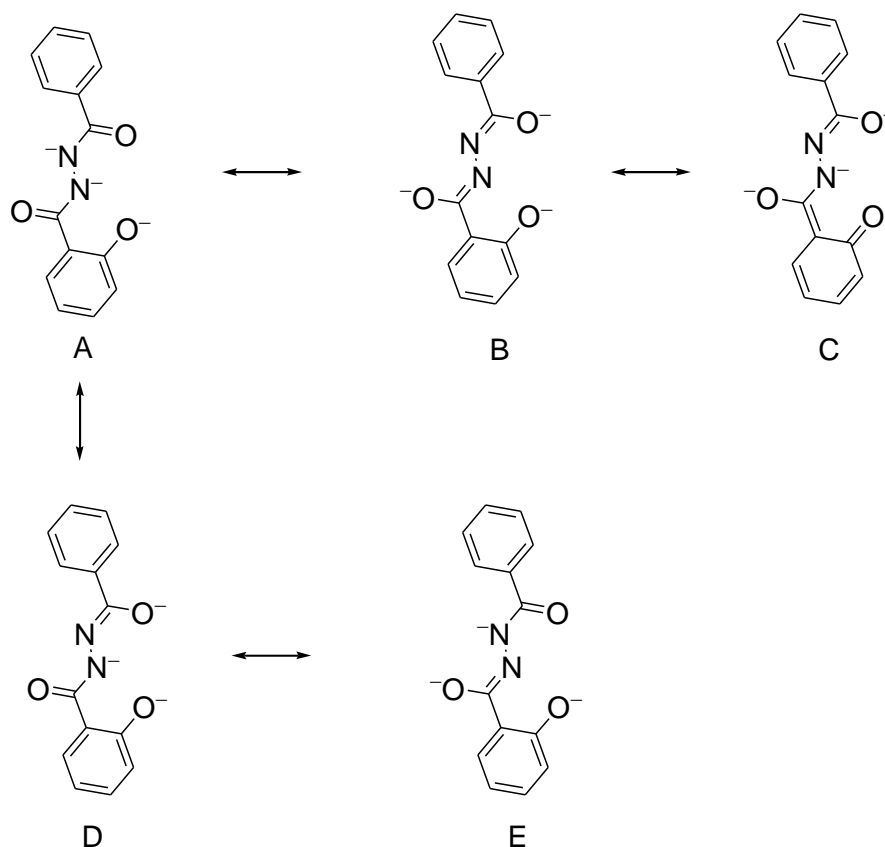
Scheme 5.3.1: Different resonance structures of adc-Salph(3−).

Table 5.3.1: Selected experimental bond distances (Å) and angles (°) of the complex [51]PF$_6$.

Bond distances							
Ru2-N2	1.968(4)	Ru1-N1	2.041(4)	N1-N2	1.427(6)	C2-C3	1.470(7)
Ru2-N6	2.063(5)	Ru1-N3	2.072(5)	C2-N2	1.347(6)	C5-C6	1.368(10)
Ru2-N7	1.983(4)	Ru1-N4	1.941(4)	C1-N1	1.337(6)	C6-C7	1.393(10)
Ru2-N8	2.062(5)	Ru1-N5	2.053(5)	C1-O2	1.293(6)	C7-C8	1.364(9)
Ru2-O3	2.017(4)	Ru1 -O1	2.074(4)	C2-O1	1.274(6)	C3-C8	1.421(8)
Ru2-O2	2.046(4)	Ru1-Cl1	2.382(13)	C4-O3	1.315(7)	C3-C4	1.426(8)
Ru1-Ru2	4.783					C4-C5	1.426(8)

Angles			
O2-Ru2-N2	78.23(16)	O1-Ru1-N4	177.16(18)
O2-Ru2-O3	171.02(16)	Ru2-N2-C2	129.8(3)
N2-Ru2-O3	92.79(17)	Ru1-N1-N2	113.3(3)
N7-Ru2-N6	78.41(18)	N1-N2-C2	113.7(4)
N7-Ru2-N8	79.07(17)	N2-N1-C1	110.3(4)
N6-Ru2-N8	157.40(17)	N4-Ru1-N5	80.10(19)
N1-Ru1-O1	76.93(16)	N3-Ru1-N5	159.67(18)
N3-Ru1-N4	79.57(18)		
Torsion angles			
Ru2-N2-N1-Ru1	-175.92	C2-N2-N1-C1	-168.82

5.4 EPR spectroscopy.

The paramagnetic nature of the isolated complex [51]PF$_6$ is reflected by its considerably shifted ^{1}H NMR signals (Figure 5.4.1). Resonances related to a calculated number of 25 aromatic protons were found in the range between 5 to 15 ppm.
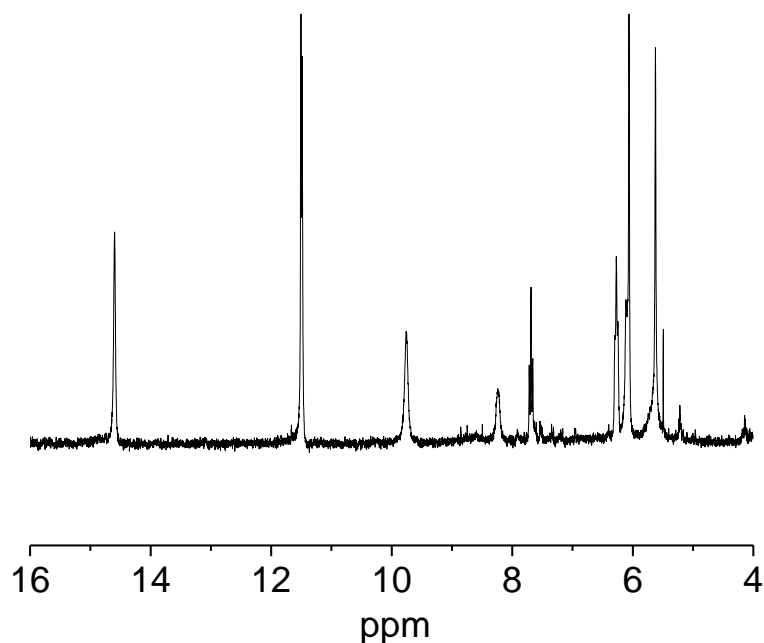
Figure 5.4.1: ^{1}H NMR spectrum of [51]PF$_6$, showing highly shifted resonances for "aromatic" protons in (CD$_3$)$_2$CO.

An EPR response corresponding to the open-shell complex [51]PF$_6$ was not found at room temperature or in the glassy frozen state (in dichloromethane) at 110 K. On measuring at 4.5 K, a rhombic signal was found in which the g components are highly affected by EPR line broadening.[70] However, the g-values can be obtained from the simulated spectrum (Figure 5.4.1) which reveals a large g-anisotropy (g$_1$-g$_3$ ≈ 0.34) in comparison to reported organic-radical-bridged diruthenium species (g$_1$-g$_3$ < 0.1).[106] Therefore, the EPR data suggest that the SOMO has a predominant metal character in the present case. The splitting of the g-factors is very similar to that observed for other symmetrical diruthenium systems with adc-R(2−), which have been described as delocalised mixed-valent states.[51] This observation indicates that the SOMO has similar contributions from metal and ligand orbitals in both the symmetrical and asymmetrical cases.

Considering the structural asymmetry (*see* 5.3) and similarities of EPR features with related symmetrical systems, it can be proposed that the spin is distributed non-uniformly on both metal centres and the bridging ligand. Accordingly, a valence

localised description $Ru^{III}(\mu\text{-adc-Salph})^{3-}Ru^{II}$ can be assumed for the asymmetrical mixed-valent complex [51]PF$_6$.
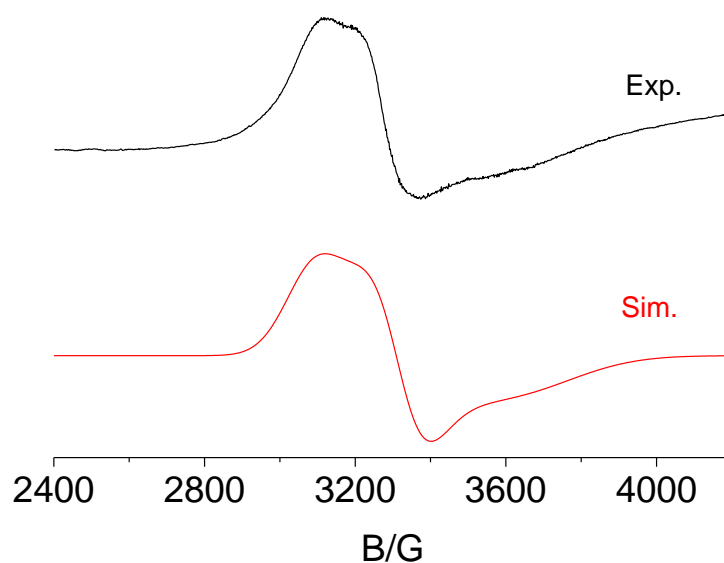
Figure 5.4.1: EPR spectrum of [51]PF$_6$ in CH$_2$Cl$_2$ at 4.5 K with computer simulation (g_1 = 2.175, g_2 = 2.025, g_3 = 1.84; linewidths (l_x, l_y and l_z) = 150, 130 and 330 G; simulated assuming Gaussian lineshapes).

5.5 Cyclic voltammetry.

In its cyclic voltammogram the compound [51]PF$_6$ exhibits one reversible oxidation at -0.11 V (vs. Fc$^{+/0}$) and one reversible reduction at -0.69 V. These redox processes are expected to be largely metal-based (Ru^{II}/Ru^{III} couples) as has been observed for previously reported dinuclear ruthenium complexes incorporating an adc-R(2−) bridge.[51] Additionally, one irreversible oxidation is observed at around 0.90 V. The voltammogram is shown in the following Figure 5.5.1 along with the redox potentials for oxidation and reduction processes.
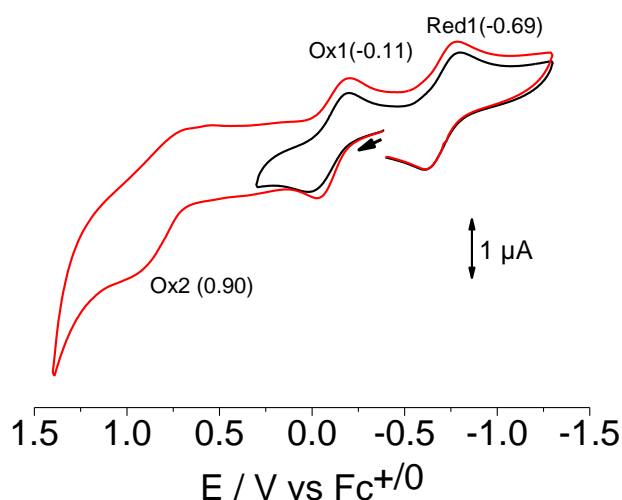
Figure 5.5.1: Cyclic voltammogram of $[51]^+$ in CH_2Cl_2 / 0.1 M Bu_4NPF_6 at 100 mV scan rate.

The importance of the comproportionation constant (K_c, Scheme 5.5.1) in assessing metal-metal electronic coupling in symmetrical MV systems has been discussed in Chapters 3 and 4. This electrochemical parameter plays a vital role for unsymmetrical MV systems also.[89-91] In symmetrical systems, the magnitude of the difference $\Delta E_{1/2}$ depends upon several factors such as the electrostatic interaction between two metal centres, the solvation energy of individual redox species and the charge delocalisation in the MV intermediate.[32b] In asymmetrical systems, an additional factor, the internal redox asymmetry, comes into play which is arising because of different coordinative situations of the redox-active metal sites. As a result, the K_c values of asymmetrical MV dimers are always found to be higher than those of the structurally related symmetrical dimers.[89-91,110] Thus it could be misleading to judge an asymmetrical mixed-valent system only by considering the K_c value.

$$[L_xRu^{II}(BL)Ru^{III}L_x]^{n+1}$$

$$[L_xRu^{II}(BL)Ru^{II}L_x]^n \quad \underset{+e^-}{\overset{-e^-}{\rightleftharpoons}} \quad \qquad \underset{+e^-}{\overset{-e^-}{\rightleftharpoons}} \quad [L_xRu^{III}(BL)Ru^{III}L_x]^{n+2}$$

$$E_{1/2}\,(1) \qquad\qquad\qquad E_{1/2}\,(2)$$

$$[L_xRu^{III}(BL)Ru^{II}L_x]^{n+1}$$

MV intermediate

L_x = ancillary ligand
BL = bridging ligand
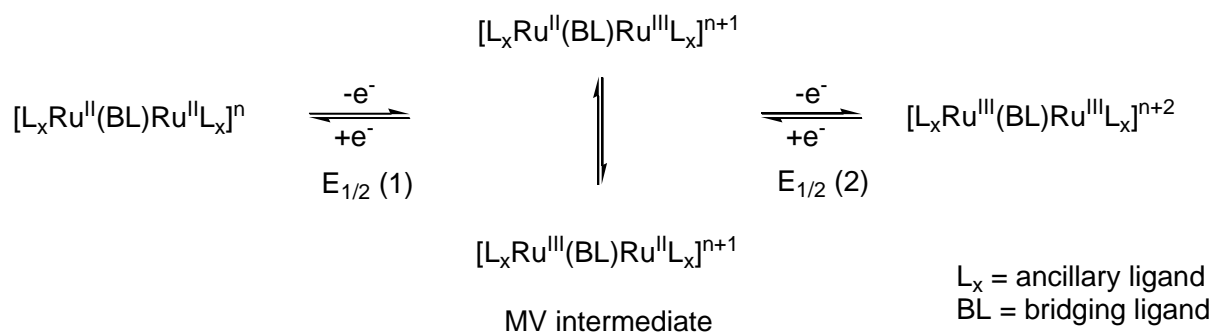
Comproportionation constant $(K_c) = 10^{(\Delta E1/2)/59\text{ mV}}$ $\Delta E_{1/2} = E_{1/2}\,(1) - E_{1/2}\,(2)$

Scheme 5.5.1: Two-step redox scheme for diruthenium complexes incorporating MV intermediate.

Redox potentials ($E_{1/2}\,(1)$ and $E_{1/2}\,(2)$ in Scheme 5.5.1) for [41]PF$_6$, [31]PF$_6$, [51]PF$_6$ and of a few other[90,107,108] symmetrical and asymmetrical diruthenium complexes with pyrazine- and anthraquinone-based bridging ligands (Scheme 5.5.2) are compared in Table 5.5.1.

BL$_1$ $R_1 = CO_2H, R_2 = CO_2H$

BL$_2$ $R_1 = CO_2H, R_2 = H$

BL$_3$ $R_1 = H, R_2 = H$

pyrazine-based

H$_2$BL$_4$ $R_1 = OH, R_2 = OH$

H$_2$BL$_5$ $R_1 = NH_2, R_2 = OH$

H$_2$BL$_6$ $R_1 = NH_2, R_2 = NH_2$
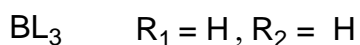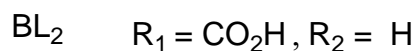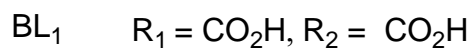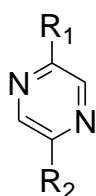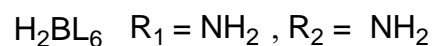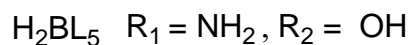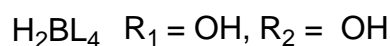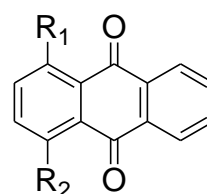
anthraquinone-based

Scheme 5.5.2: Representation of symmetrical and non-symmetrical bridging ligands.

It is clearly seen from the comparison that the asymmetrical complexes have higher K_c values with respect to their symmetrical analogues for respective adc-R-, pyrazine- and anthraquinone-based bridging ligands. Noticeably, for pyrazine-based ligands the K_c value for the asymmetrical one is much higher than the symmetrical complexes while for adc-R based ligands, they are almost similar which indicates comparatively less redox asymmetry in the case of [51]PF$_6$ in this study.

Table 5.5.1: Redox potentials from cyclic voltammetry

complex (adc-R-based bridging ligands)	E^0/V			solvent
	$E_{1/2}$ (1)	$E_{1/2}$ (2)	K_c(n)	
[41]^{na}	-0.77	-0.29	$10^{8.1}$ (+)	CH_2Cl_2
[51]^{na}	-0.69	-0.11	$10^{9.8}$ (+)	CH_2Cl_2
[31]^{na}	-0.42	0.08	$10^{8.5}$ (+)	CH_2Cl_2
(pyrazine-based bridging ligands)[90,107]				
[(bpy)$_2$Ru(BL$_1$)Ru(bpy)$_2$]^{nc}	0.98	1.16	$10^{3.1}$(3+)	MeCN
[Cl(bpy)$_2$Ru(BL$_2$)Ru(bpy)$_2$]^{nb}	0.62	1.06	$10^{7.5}$ (3+)	MeCN
[Cl(bpy)$_2$Ru(BL$_3$)Ru(bpy)$_2$Cl]^{nb}	0.89	1.02	$10^{2.2}$ (3+)	MeCN
(anthraquinone-based bridging ligands)[108]				
[(bpy)$_2$Ru(BL$_6$)Ru(bpy)$_2$]nd	0.05	0.43	$10^{6.4}$ (3+)	MeCN
[(bpy)$_2$Ru(BL$_5$)Ru(bpy)$_2$]nd	0.23	0.69	$10^{7.8}$ (3+)	MeCN
[(bpy)$_2$Ru(BL$_4$)Ru(bpy)$_2$]nd	0.55	0.81	$10^{4.4}$ (3+)	MeCN

[a] Potentials in V vs Fc$^{+/0}$ in CH_2Cl_2 0.1 M Bu$_4$NPF$_6$ at RT.

[b] Potentials in V vs SSCE in CH_3CN / 0.1 M Bu$_4$NPF$_6$ at RT.

[c] Potentials in V vs NHE in CH_3CN / 0.1 M Bu$_4$NPF$_6$ at RT.

[d] Potentials in V vs SCE in CH_3CN / 0.1 M TEAP at RT, TEAP = tetraethylammonium perchlorate.

Based on just electrochemical results, it is difficult to reach a conclusive understanding about the redox asymmetry, which causes a potential energy gap between the two possible MV intermediates (Scheme 5.5.1) and therefore is a very important parameter for studying inter-metal electron transfer in asymmetrical dinuclear systems. Nevertheless, a logical guess can be made about the electronic situation of [51]PF$_6$ from the comparison of the redox potentials of the complexes with adc-R based ligands. An anodic shift of the redox potentials (Table 5.5.1) has been observed from bis(tridentate) system [41]^n to the bis(bidentate) system [31]^n. This indicates that the oxidation of the ruthenium centres becomes easier by coordination of a phenolate moiety. Therefore, it is possible to identify the energetically more stable MV intermediate or, according to Kubiak and co-workers the major "MV isomer"[45,109] in which the molecular half A (bis-meridionally coordinated Ru; Scheme 5.2.1) contains a Ru^{III} centre.

5.6 UV-Vis-NIR spectroelectrochemistry.

Spectroelectrochemical measurements for [51]PF$_6$ were carried out in CH$_2$Cl$_2$/0.1 M Bu$_4$NPF$_6$ using an OTTLE cell[72]. Spectral changes in the UV-Vis-NIR region are shown in Figure 5.6.1 for both oxidation and reduction processes. Absorption values are listed in Table 5.6.1.

The complex [51]PF$_6$ exhibits an intense (ε = 7000 M^{-1}cm^{-1}) absorption band in the NIR region (λ_{max} = 1464 nm), which probably appears due to an inter-valence charge-transfer (IVCT) from the Ru^{II}-Cl centre (molecular half B2) to the bis-meridionally coordinated Ru^{III} centre (molecular half A). NIR absorptions with considerable intensity ($\varepsilon \approx$ 5000 M^{-1}cm^{-1}) have previously been found for a few other non-cyclometalated[98] and cyclometalated[97] diruthenium complexes. Different coordination environments of two metal centres in a mixed-valent state can sometimes create redox asymmetry to such an extent that it may cause a very weak or even zero interaction between metal centres, resulting in an absence of an IVCT band in the NIR region.[95] According to the Hush equation,[36] which is applicable for a localised system (Class II system according to Robin and Day classification), the half-

bandwidth ($\Delta\nu_{1/2}$) of the IVCT band can be estimated by applying the following equations (i and ii) for a symmetrical (i) and an asymmetrical (ii) system, respectively.

$$\Delta\nu_{1/2} / cm^{-1} = [2.31 \times 10^3 (\nu_{max} / cm^{-1})]^{1/2} \qquad \text{(i)}$$

$$\Delta\nu_{1/2} / cm^{-1} = [2.31 \times 10^3 \{(\nu_{max} - \Delta E_0) / cm^{-1}\}]^{1/2} \qquad \text{(ii)}^{[36,96]}$$

In these equations, $\Delta\nu_{1/2}$ is the bandwidth at half height, ν_{max} the band energy maximum, and the quantity ΔE_0 is the potential difference between two redox isomers of the mixed-valent state (Scheme 5.5.1) which is non-zero for the asymmetrical case. As there is no straightforward way to calculate this quantity, we are assuming here that the ΔE_0 value for [51]PF$_6$ is equal to the difference in redox potentials ($E_{1/2}(1)$, Scheme 5) of the structurally related symmetrical dimers, listed in Table 5.5.1. Using this difference of 0.35 V (2823 cm^{-1}), the theoretical bandwidth is calculated to be 3042 cm^{-1}, which is somewhat larger than the observed value, of 2228 cm^{-1}. Therefore, we predict that a strong metal/ligand/metal interaction is present in the asymmetrical mixed-valent complex [51]PF$_6$.

The NIR band shown by [51]PF$_6$ is absent in both one-electron reduced and one-electron oxidised states. A structured band forms at λ_{max} = 795 nm during oxidation which can be attributed to a ligand-to-metal charge-transfer (LMCT) inside the Ru^{III}-(adc-Salph)$^{3-}$-Ru^{III} motif. Terpyridine-based MLCT transitions (λ_{max} = 390, 510 nm) are shifted to longer wavelengths (λ_{max} = 420, 585 nm) on reduction. This behaviour indicates that the charge on the ruthenium centres has decreased on reduction. The reduced species also exhibit a shoulder at around 815 nm, which can be attributed to a ligand-to-ligand charge transfer transition (LLCT). In fact, the complex exhibits similar spectroelectrochemical behaviour as other symmetric dinuclear complexes with adc-R bridging ligands.[48,51,69]
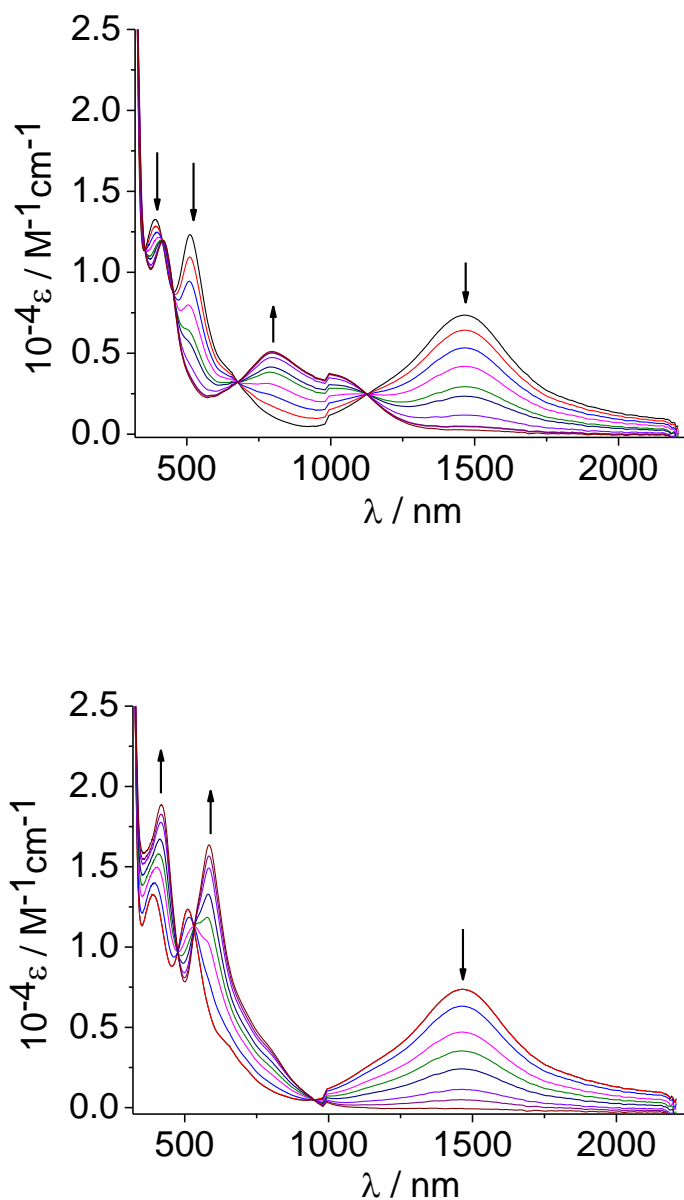
Figure 5.6.1: UV-Vis-NIR spectroelectrochemical responses on oxidation (top) and reduction (bottom) of [51]$^+$ in CH$_2$Cl$_2$/0.1 M Bu$_4$NPF$_6$.

Table 5.6.1: Absorption Values from UV-Vis-NIR Spectroelectrochemistry.

compound	λ_{max} / nm (10^{-4} ε / M^{-1}cm^{-1})
[51]$^{2+}$	415(1.2), 795(0.5)
[51]$^+$	390(1.3), 510(1.2), 680(sh), 1464(0.7)
[51]	420(1.9), 585(1.6), 815(sh)

5.7 Conclusion and outlook.

This Chapter contains a description of the following remarkable results:

i) A new asymmetrical diruthenium complex [51]PF$_6$ has been synthesised.

ii) Structural characterisation of the mixed-valent cation [51]$^+$ has revealed the asymmetrical nature of the metal/ligand interface and of the bridging ligand adc-Salph(3−).

iii) Strong NIR absorption (ε = 7000 M^{-1}cm^{-1}) has been found for the monocationic complex.

Besides, the electrochemical results, after comparing those with related symmetrical dimers (presented in Scheme 5.1.2), reflect the strong donating ability of the phenolate moiety in compared to the chloride ion because the redox potentials increases from the bis(tridentate) system ([41]^n) to the bis(bidentate) system ([31]^n) as depicted in Table 5.5.1. By combining these electrochemical results with structural investigations and EPR data (Δg = 0.34), the electronic situation of [51]$^+$ may be formulated as [(trpy*)Ru^{III}(adc-Salph)$^{3-}$Ru^{II}(trpy*)Cl]$^+$ where bis-meridionally coordinated ruthenium bears most of the spin density. In fact, the intense IVCT band in the NIR region reveals the capability of the asymmetrical ligand adc-Salph(3−) to mediate electron transfer between the Ru centres in respective molecular halves (A and B2, Scheme 5.2.1) as depicted in the following diagram.

<div align="center">

Donor (B2)   Acceptor (A)

[Cl——M^{II}(μ,η^2:η^3-adc-Salph)M^{III}]

IVCT | hν M = Ru(trpy*)

↓

[Cl——M^{III}(μ,η^2:η^3-adc-Salph)M^{II}]*

</div>
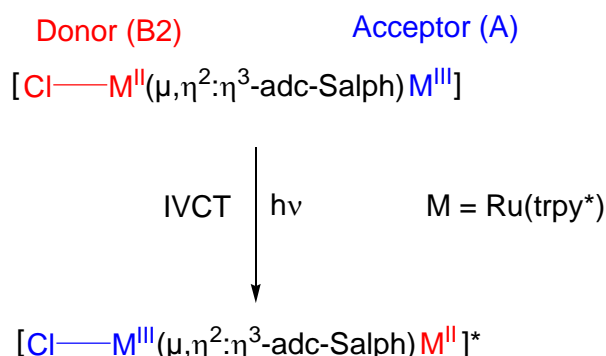
Moreover, the structural frame work of [51]PF$_6$ creates the possibility of tuning inter-metal electron transfer and redox properties of the complex by replacing the chloride with other electron transfer active anions like CH$_3$$^-$, NO$_2$$^-$ etc.

Chapter 6

Diruthenium complexes with 1,2-bis(picolinoyl)hydrazido(2-): A variety in ligand coordination.

6.1 Introduction.

Metal-ligand interactions are essential in coordination chemistry, and the binding mode of the ligand is very crucial. The 1,2-bis(picolinoyl)hydrazido(2-) ligand (adc-Py(2-)) can bind two metal centres in a bis(meridional) fashion and the ligand has the potential to strongly mediate metal-metal interactions.[50b] The ligand belongs to the adc-R ligand family which exhibit two reversible redox processes, including a stable radical intermediate (adc-R$^{0/.-/2-}$). Besides, this ligand has bridging modes as depicted in Scheme 6.1.1.

A
bis(N,N',O)

B
bis(N,N')

C
(N,N';N,N',O)
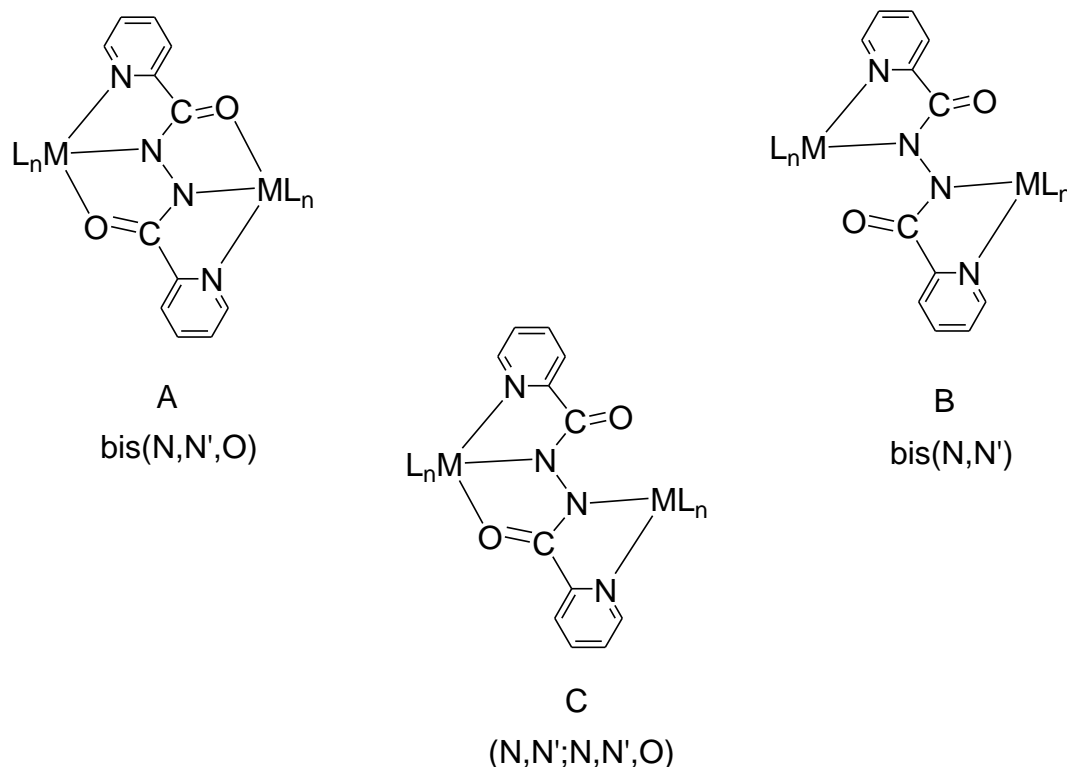
Scheme 6.1.1: Different binding modes of the bridging ligand.

Binding modes B and C have been found in dinuclear Au,[112] Fe[113] and tetranuclear Cu[53a,114] complexes, respectively. The present Chapter describes two complexes ([61](PF$_6$)$_2$ and [62](PF$_6$)$_2$) with type A and B bridging modes where the bridging ligand is interacting with electron-transfer active Ru^{II}(trpy*) (trpy* = 4,4′,4″-tri-*tert*-butyl-2,2′:6′,2″-terpyridine) and Ru^{II}(bpy)$_2$ fragments, respectively. The Chapter aims at revealing the different spectroelectrochemical behaviour (UV-Vis-NIR and IR) of the complexes as a result of different ligand coordination.

6.2 Syntheses and characterisation.

The complex [{(trpy*)Ru}$_2$(μ-adc-Py)](PF$_6$)$_2$ ([61](PF$_6$)$_2$) was prepared from *mer*-Ru(trpy*)Cl$_3$ by following the procedure described in Scheme 6.2.1. In this synthetic route, a silver salt was applied to de-halogenate the precursor complex. The *in-situ* generated solvated *mer*-Ru(trpy*)(PF$_6$)$_3$ was then directly treated with H$_2$adc-Py under basic conditions after changing the solvent medium from acetone to ethanol. In the course of the reaction, the Ru^{III} centre was reduced to Ru^{II} and [61](PF$_6$)$_2$ was formed. Reductions of such ruthenium(III) centres are typical reaction in reducing (here: alcohol in presence of base) conditions.[52] The air stable compound [61](PF$_6$)$_2$ was purified by neutral alumina column chromatography to obtain a brown solid. The charge of the complex and the product formation have been confirmed by elemental analysis and mass spectroscopy (*see* Chapter 7.3.3).
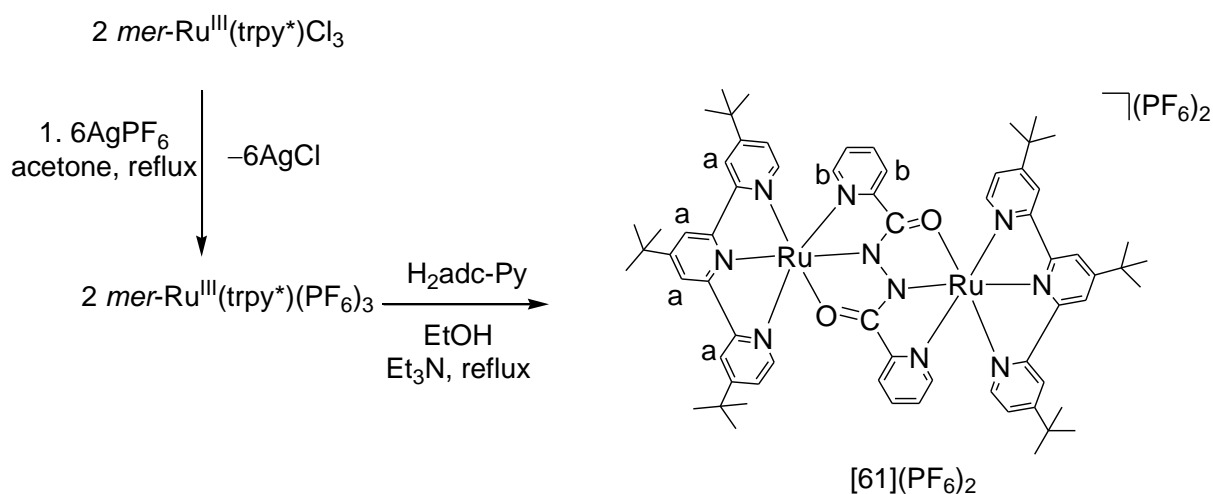
Scheme 6.2.1: Synthetic procedure for obtaining [61](PF$_6$)$_2$.

The bis-tridentate ligand, adc-Py(2-) did not form the target complex [61](PF$_6$)$_2$ after reacting the ligand with *mer*-Ru(trpy*)Cl$_3$ without using silver salt, instead a chloro complex [{(trpy*)Ru}$_2$(μ-adc-Py)Cl]PF$_6$ resulted as confirmed by mass spectroscopy (M-PF$_6$ peak at 1281.41). This is not unusual because the ligand adc-Py(2-) contains different kinds of donor atoms among which O from the carbonyl function is only very weakly coordinating. Therefore, the action of silver salts is necessary because then chloride ions are replaced by solvent molecules or weakly coordinating counter anions, easing coordination of the O atom from the bridging ligand.

Single crystals suitable for X-ray structural analysis were not obtained for [61](PF$_6$)$_2$. ^{1}H-NMR measurements in (CD$_3$)$_2$CO gave the calculated number of sharp proton signals, confirming the diamagnetic nature of the complex (Figure 6.2.1). The downfield shifted resonances in the region between 8.7 to 9.2 ppm can be correlated with singlet signals (8 protons) from trpy* and doublet signals (4 protons) from the adc-Py ligand for the marked protons (a and b, respectively) in Scheme 6.2.1. Signals from the *tert*-butyl (C(CH$_3$)$_3$) group arise in the characteristic alkyl region as shown in Figure 6.2.1. The NMR data suggest a non-symmetrical geometry according to the expected molecular symmetry (C$_{2h}$ point group) for the molecule and that is typical for multi-chelate systems.[50b]
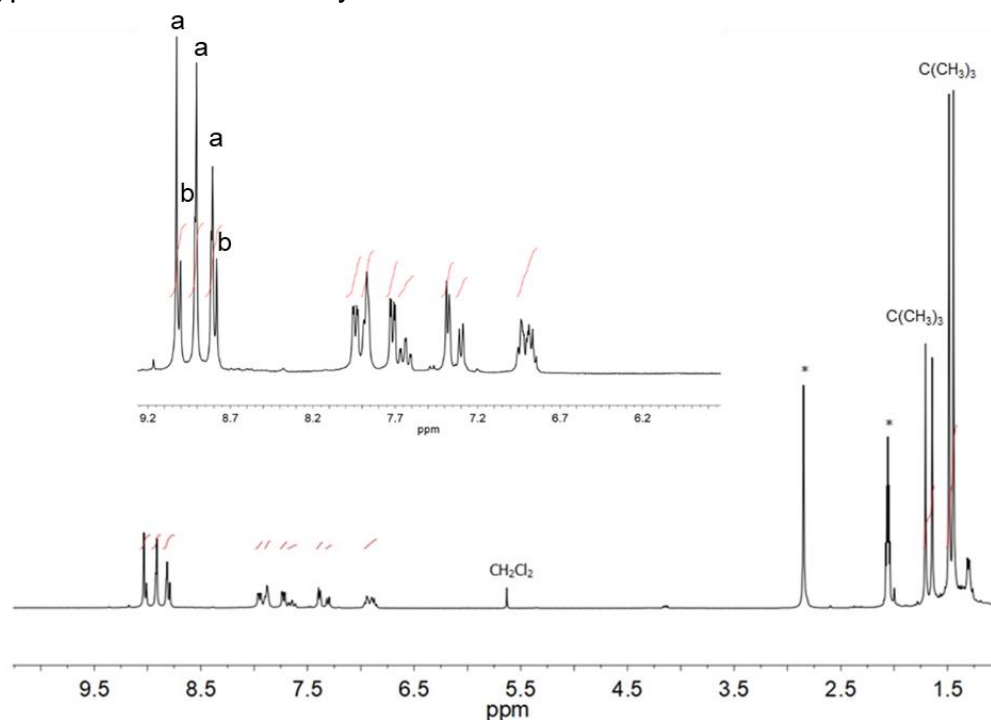
Figure 6.2.1: ^{1}H NMR spectrum of [61](PF$_6$)$_2$ in (CD$_3$)$_2$CO (*signals from solvent residual).

The reaction of *cis*-Ru(bpy)$_2$Cl$_2$ with H$_2$adc-Py in the presence of a base in refluxing ethanol produced a mixture of compounds, probably two diastereomers (A and B in Scheme 6.2.2) of the complex [{(bpy)$_2$Ru}$_2$(μ-adc-Py)](PF$_6$)$_2$ [62](PF$_6$)$_2$. By column chromatographic separation on neutral alumina, it was not possible to separate these two isomers (*meso* and *rac* form). Both isomers were collected together to obtain a brown solid for which further characterisation was performed. This brown product produced satisfactory micro-analytical data with respect to the chemical formula of [62](PF$_6$)$_2$ (*see* Chapter 7.3.3), it exhibits the molecular ion peak at a corresponding m/z value of 534.07 in mass spectroscopy (ESI).
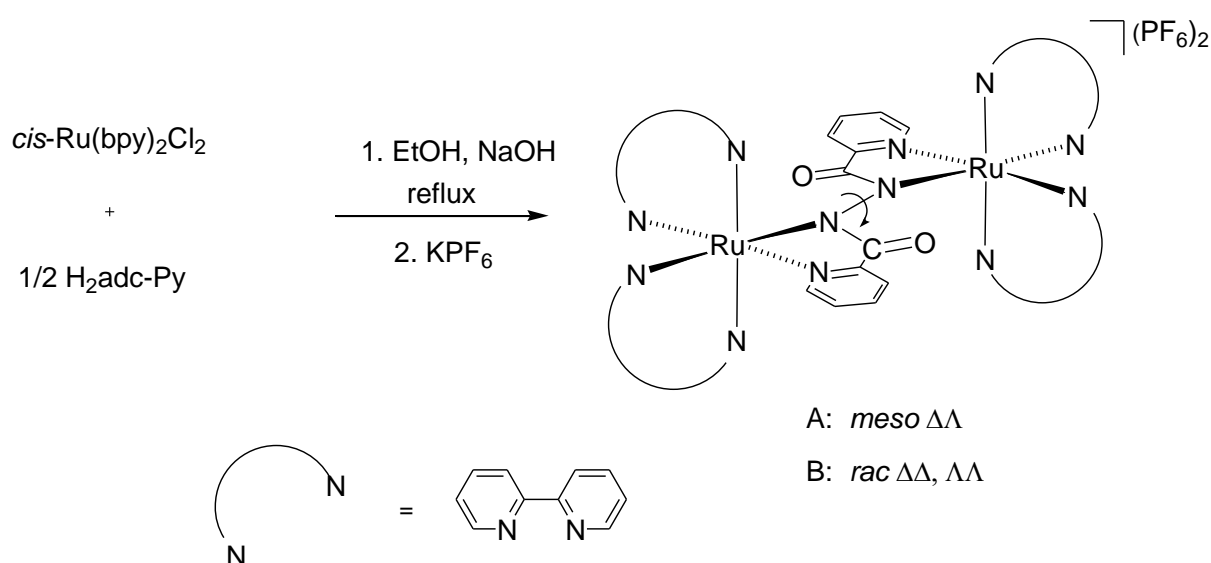
Scheme 6.2.2: Synthetic procedure for obtaining [62](PF$_6$)$_2$.

^{1}H-NMR spectra of [62](PF$_6$)$_2$ at variable temperatures (Figure 6.2.2) exhibit several overlapping signals in the "aromatic" region. The *meso* or the *rac* isomer could not be identified from these signals, but these spectra exhibit a dynamic behaviour of the complex in solution, probably originating from plausible rotation along N-N bond as depicted in Scheme 6.2.2. Noticeably, a new signal is arising around 10 ppm on going to the low temperature which can be associated with a proton connected to the carbon next to nitrogen in any of one pyridyl ring from bpy or the bridging ligand. However, due to this dynamic behaviour, it is not straightforward to predict the presence of the *meso, rac* or a mixture of both the isomers by ^{1}H NMR spectroscopy.

We have found crystals of the *meso* form from a dichloromethane solution of [62](PF_6)$_2$, but that does not exclude the probability of formation of both the isomers during synthesis. ^{13}C NMR spectroscopy needs to be performed because signals from the carbonyl group can be traced then to identify the isomers.
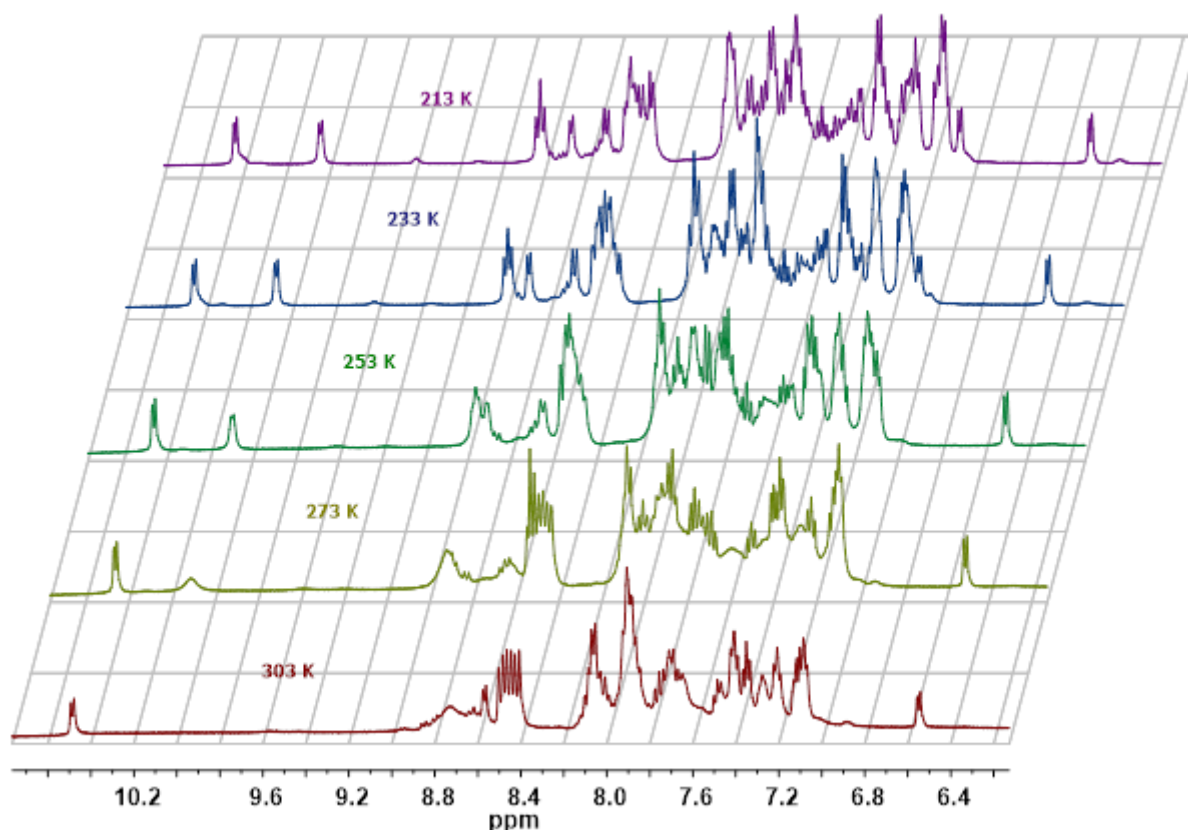
Figure 6.2.2: Variable-temperature ^{1}H NMR experiments (from 303 K to 213 K) of [62](PF_6)$_2$ in (CD$_3$)$_2$CO at 400 MHz.

6.3 Molecular structure analysis.

Single crystals of the *meso* form A (Scheme 6.2.2) were obtained by diffusing hexane into a dichloromethane solution of [62](PF_6)$_2$. The *meso* form crystallises in the space group P-1. Crystallographic data are given in Chapter 7 (Table 7.4.5). Two independent molecules have been found in the asymmetric unit (A1 and A2 in Figure 6.3.1) and they have very similar bond parameters. Selected bond lengths and angles are listed in Table 6.3.1.

The molecular structures (A1 and A2) confirm a bis(N,N') coordination of the bridging ligand. The structures show that the molecular halves are nearly orthogonal to each other due to free rotation along the N-N single bond. Because of such rotation, the symmetry of the complex is lower and thus stereochemistry becomes complicated. The torsion angles Ru-N-N-Ru (≈115°) and C-N-N-C (≈95°) are almost similar in both molecules A1 and A2. The Ru(bpy)$_2$ fragment is coordinated by the N$_{azo}$ (N atom involved in N-N bond) and N$_{py}$ atoms, forming a five-membered ring with a non-coordinating C=O group in each molecular half. The dihedral angles between the best planes of these five-membered chelate rings are around 69°. These results indicate a highly twisted M-L-M geometry because of which π conjugation will be disrupted.

The protonated form of the ligand adc-Py(2-) is also not planar.[115] The extent of the twist can be understood from the torsion angle C-N-N-C of -70(2)°, which is similar in the present system and has previously been reported for a bis(dichlorogold(III)) complex.[112] Bond lengths from the bridging ligand backbone are consistent with the hydrazido(2-) form. The N-N bond distances (1.444(13) and 1.427(14) Å) indicate a single bond character, while the non-coordinated C=O distances (≈1.25 Å) and short C-N distances (≈1.33 Å) suggest minor charge transfer on oxygen atoms due to charge resonance in the hydrazido(2−) form. Noticeably, the Ru-Ru distances of about 4.9 Å are in a similar range as reported diruthenium complexes where bridging adc-R(2−) ligands coordinate metal centres in an "S-frame" fashion.[48]
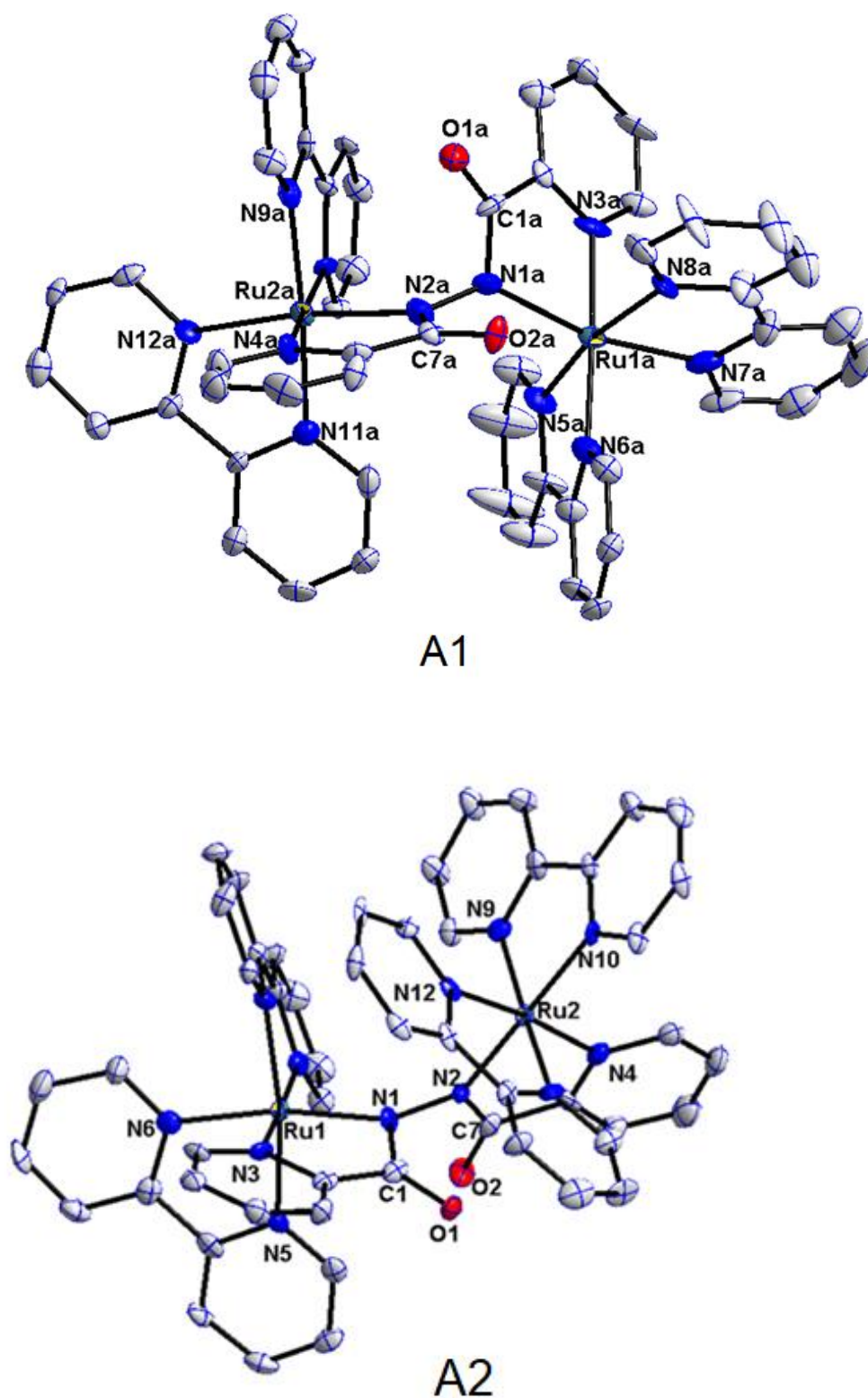
Figure 6.3.1: Molecular structure of the dications A1 and A2 in the crystal of [62](PF$_6$)$_2$. Thermal ellipsoids are given at the 50% probability level; H atoms are removed for clarity.

Table 6.3.1: Selected bond parameters of [62](PF$_6$)$_2$.

Distances / Å					
	A1	A2		A1	A2
Ru1-N1	2.124(11)	2.114(9)	N1-N2	1.427(14)	1.444(13)
Ru1-N3	2.059(10)	2.055(10)	C1-N1	1.315(16)	1.332(15)
Ru1-N6	2.074(11)	2.080(10)	C1-O1	1.256(15)	1.252(14)
Ru2-N2	2.095(11)	2.089(9)	C7-N2	1.333(16)	1.339(17)
Ru2 –N4	2.071(10)	2.066(10)	C7-O2	1.262(15)	1.252(16)
Ru2-N10	2.034(10)	2.043(10)	Ru1-Ru2	4.944	4.918
Angles / (°)					
N1-Ru1-N3	77.5(4)	77.8(4)	Ru2-N2-C7	116.8(8)	118.6(8)
Ru1-N1-C1	112.5(8)	113.1(8)	Ru1-N1-N2	134.2(8)	133.7(7)
N2-Ru2-N4	78.0(4)	77.5(4)	Ru2-N2-N1	124.9(8)	124.1(7)
Ru2-N2-N1-Ru1	-116.25	115.28	C7-N2-N1-C1	-94.67	95.52

6.4 Cyclic voltammetry.

Cyclic voltammetry measurements for [61](PF$_6$)$_2$ were carried out in dichloromethane / 0.1 M Bu$_4$NPF$_6$. The complex exhibits two reversible one-electron oxidation waves, which are separated by 0.58 V. Figure 6.4.1 represents the voltammogram. This electrochemical behaviour is very similar to that reported for an adc-Py(2–) bridged

diruthenium compound where unsubstituted terpyridine has been used as terminal ligand.[50b] Redox potentials of the reported and the present complex are compared in Table 6.4.1. Overall, the redox potentials for the present system are lower than the reported values; the electron-donating *tert*-butyl substituents are responsible for the observed cathodic shifts. Because of such substitution trpy* becomes a relatively strong donor ligand and thus facilitates the oxidation processes, which are mostly metal-centred. This kind of substitutional effect on electrochemical properties has also been observed for cyclometalated diruthenium systems.[116] The redox system $[61]^{2+/3+/4+}$ contains a stable intermediate ($K_c(3+) = 10^{9.8}$), which could be a mixed-valent or a radical-bridged species. The probable electronic situations of all redox species will be discussed in the following spectroelectrochemistry (UV-Vis-NIR, EPR) sections. The third oxidation wave, observed at around 1 V (Figure 6.4.1), was found to be irreversible.
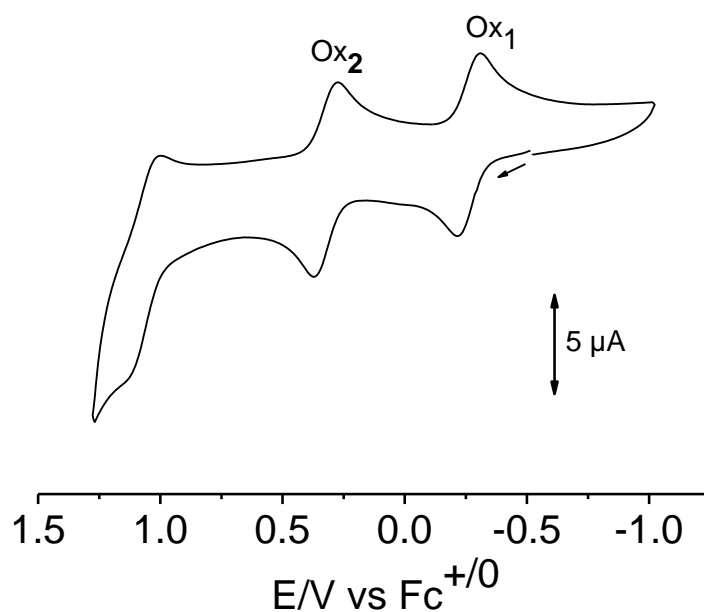
Figure 6.4.1: Cyclic voltammogram of [61](PF$_6$)$_2$ in CH$_2$Cl$_2$ / 0.1 M Bu$_4$NPF$_6$ at a scan rate of 100 mV / s.

Table 6.4.1: Half-wave redox potentials from cyclic voltammetry.

	Ox_1 (ΔE)	Ox_2 (ΔE)	K_c(3+)
[61](PF$_6$)$_2$[b]	-0.26 (90)	0.32 (90)	$10^{9.8}$
[61A](PF$_6$)$_2$[a,b]	-0.04	0.49	10^9
[62](PF$_6$)$_2$[c]	-0.19 (150)	0.30 (190)	$10^{8.3}$

[a] [61A](PF$_6$)$_2$[50b] = [{(trpy)Ru}$_2$(μ-adc-Py)](PF$_6$)$_2$, trpy = 2,2';6',2"-terpyridine, [b] Potentials in V vs. Fc$^{+/0}$ in CH$_2$Cl$_2$ / 0.1 M Bu$_4$NPF$_6$ at RT, [c] Potentials in V vs. Fc$^{+/0}$ in CH$_3$CN / 0.1 M Bu$_4$NPF$_6$ at RT, peak potential differences ΔE in mV.

Cyclic voltammetry measurements for [62](PF$_6$)$_2$ were carried out in acetonitrile. The complex exhibits two oxidation processes with a large potential gap (0.49 V) similar to [61](PF$_6$)$_2$. The voltammogram is shown in Figure 6.4.2 and the potentials are given in Table 6.4.1. It is quite surprising that the complex exhibits electrochemical features (K_c(3+) = $10^{8.3}$) like the reported, bis(bidentate) adc-R(2−) bridged, strongly interacting dinuclear systems.[51]
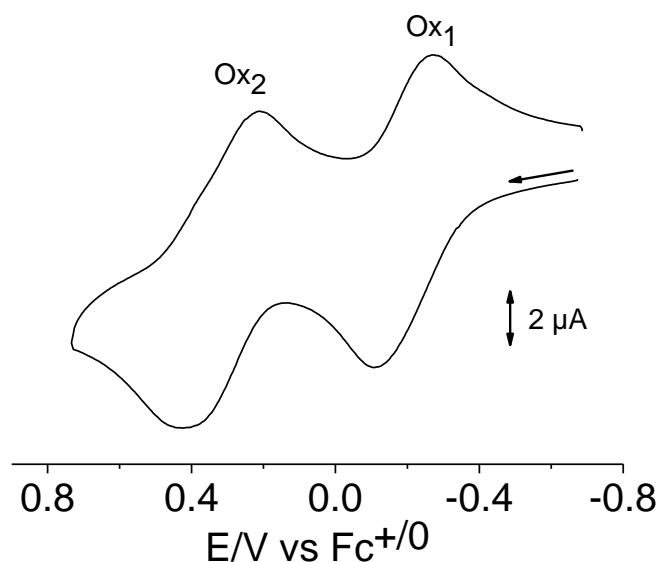
Figure 6.4.2: Cyclic voltammogram of [62](PF$_6$)$_2$ in CH$_3$CN / 0.1 M Bu$_4$NPF$_6$ at a scan rate of 100 mV / s.

Generally, in such a puckered system where π conjugation is restricted, the K_c value of the intermediate is expected to be much lower ($< 10^5$) like in Class I (non-interacting) or Class II (weakly interacting) mixed-valence systems.[32a] To carry forward the discussion, it should be noted that the *meso* and *rac* isomers of reported dinuclear ruthenium bipyridyl complexes have been found to exhibit very similar electrochemical and spectroscopic features.[97,117] Supported by this observation we can assume that spectroelectrochemical behaviour of [62](PF$_6$)$_2$ should not vary significantly if it consists *meso*, *rac* or mixture of both forms. Besides, it is noticeable that the oxidation potentials of the previously described assumedly planar complex [61](PF$_6$)$_2$ and that of the twisted [62](PF$_6$)$_2$ are very similar (Table 6.4.1). These results indicate that the twist is present only in the "native state" and planarisation occurs in the oxidised states.

6.5 UV-Vis-NIR spectroelectrochemistry.

UV-Vis-NIR spectroelectrochemical measurements for [61](PF$_6$)$_2$ were carried out in CH$_2$Cl$_2$ / 0.1 M Bu$_4$NPF$_6$ using an OTTLE[72] cell. Spectral changes during oxidation processes are depicted in Figure 6.5.1, which exhibit a behaviour similar to that of the reported complex ([61A](PF$_6$)$_2$) with unsubstituted terpyridine, mentioned in the cyclic voltammetry part (*see* 6.4). Absorption values of both complexes are compared in the Table 6.5.1 along with their probable assignment.

The native 2+ form of both complexes [61](PF$_6$)$_2$ and [61A](PF$_6$)$_2$ exhibit MLCT (dπ → π*(trpy)/(trpy*)) and LLCT (π(adc-Py) → π*(trpy)/(trpy*)) transitions in the visible region. On oxidation to the mixed-valent 3+ form, these MLCT bands are decreasing while a broad band at around 1000 nm arises for both complexes. The NIR absorption is appearing due to charge transfer inside the metal-ligand-metal fragment of the odd electron species and assigned as an intervalence charge transfer transition (IVCT). Noticeably, the NIR band for [61A]$^{3+}$ consists of two distinct absorption bands (λ_{max} = 840 and 1000 nm) which have been assumed to have an LMCT and an IVCT character, respectively. In contrast, a Gaussian-shaped broad band ($\Delta\nu_{1/2}$= 3900 cm^{-1}) has been observed in the present case of [61]$^{3+}$.

After the second oxidation, an LMCT transition, which is commonly seen in dinuclear systems with adc-R ligands, has been observed for $[61]^{4+}$ at around 875 nm, which is absent in case of $[61A]^{4+}$ according to the compared data in Table 6.5.1. A possibility of reversible Ru-O bond dissociation has been submitted as a reason for the absence. Nevertheless, both complexes exhibit reversibility for the spectral changes during the redox processes.

Table 6.5.1: Absorption values[a] for $[61]^n$ and $[61A]^n$ with tentative assignment.

n+	$[61]^n$		$[61A]^n$	
2+	367(13400)	MLCT	369(11900)	MLCT
	512(18400)	MLCT	500sh	
	670(sh)	LLCT	525(12400)	MLCT
			590sh	LLCT
3+	366(sh)		430(8200)	MLCT
	431(sh)		470sh	
	494(11500)	MLCT	530sh	
	$1163(2700)^b$	IVCT	615sh	
			$840(3600)^d$	LMCT
			$1000(3800)^e$	IVCT
4+	386(10500)		332sh	MLCT
	431(sh)	MLCT	405sh	MLCT
	660(2260)	MLCT	480sh	MLCT
	$875(9700)^c$	LMCT		

[a]Wavelengths λ_{max} in nm and molar extinction coefficient ε in M^{-1}cm^{-1} in parenthesis, $^{b,c,d,e}\Delta\nu_{1/2}$ / cm^{-1} = 3900[b], 1900[c], 1850[d], 2650[e]; $\Delta\nu_{1/2}$ = Bandwidth at half height.
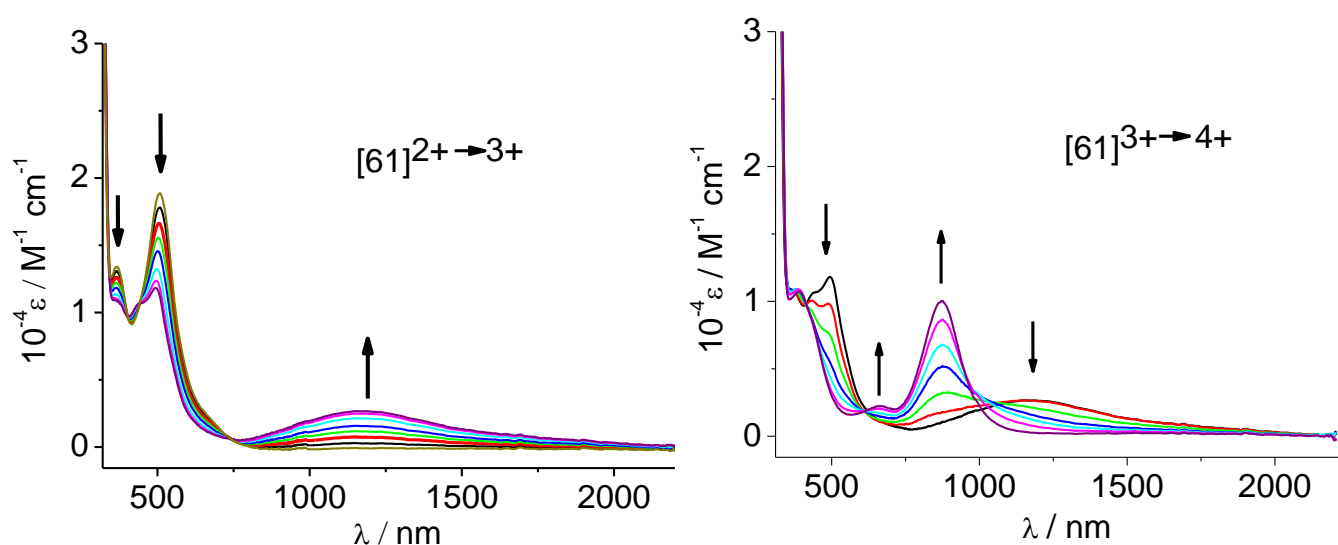
Figure 6.5.1: UV-Vis-NIR spectroelectrochemical response on stepwise oxidation of [61](PF$_6$)$_2$ in CH$_2$Cl$_2$/0.1 M Bu$_4$NPF$_6$.

Following the same procedure as applied for [61](PF$_6$)$_2$, the spectroelectrochemical changes were also measured for [62](PF$_6$)$_2$ in CH$_3$CN / 0.1 M Bu$_4$NPF$_6$. The native 2+ state exhibits the expected MLCT transitions (dπ → π*(bpy)) in the visible region and the one-electron oxidised species exhibits intense absorptions in the NIR region (Figure 6.5.2). The long-wavelength transition (λ_{max} > 2000 nm) in the 3+ form is expected to originate from a charge transfer between two molecular halves. The question is how such a process can occur in [62]$^{3+}$. An important observation is that the wavelength of this absorption is considerably longer at 2410 nm (Table 6.5.2) than that observed for [61]$^{3+}$ (1163 nm, Table 6.5.1) which indicates comparatively less metal/ligand/metal interaction in [62]$^{3+}$. In the 4+ form an intense NIR absorption appears at around 900 nm, which is identified as an LMCT transition like in the case of [61]$^{4+}$. Although the coordination geometry of [62](PF$_6$)$_2$ is puckered in the crystal, the complex exhibits an electrochemical and spectral behaviour like the typical planar dinuclear ruthenium systems.[50b,51]
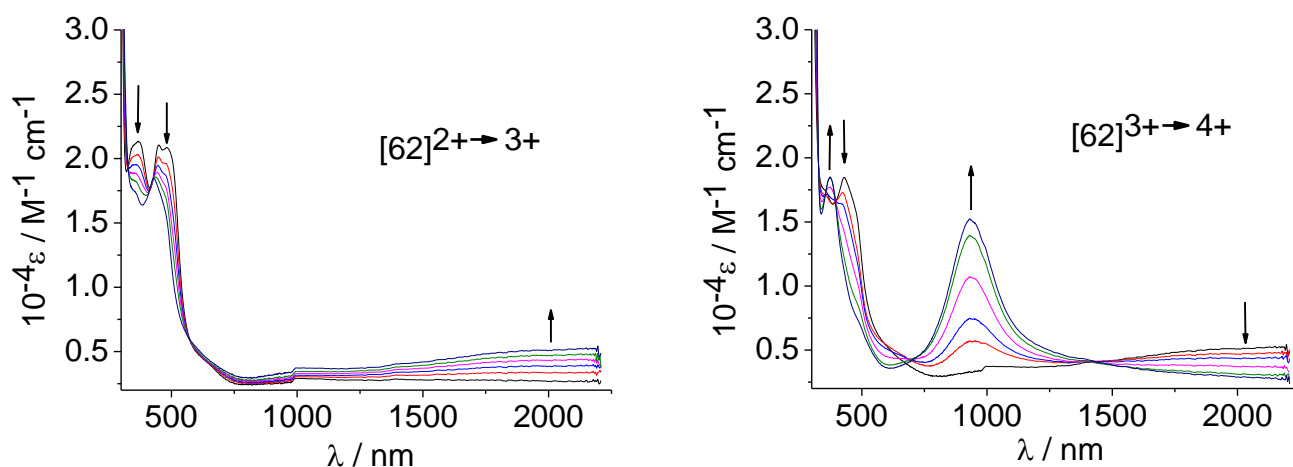
Figure 6.5.2: UV-Vis-NIR spectroelectrochemical response on stepwise oxidation of [62](PF$_6$)$_2$ in CH$_3$CN/0.1 M Bu$_4$NPF$_6$.

Table 6.5.2: UV-Vis-NIR spectroelectrochemical data for [62]$^{2+}$.

compound	λ_{max} / nm (10^{-4} ε / M^{-1}cm^{-1})
[62]$^{2+b}$	365(2.1), 450(2.1), 484(2.0), 646(sh)
[62]$^{3+}$	356(sh), 430(1.8), 613(sh), 2410^a
[62]$^{4+}$	370(1.8), 490(sh), 930(1.5)

^{a}Value taken from IR spectroelectrochemistry, corresponding to the absorption at 4150 cm^{-1}, ^{b}starting material [62](PF$_6$)$_2$.

6.6 IR spectroelectrochemistry.

IR spectroelectrochemical measurements were carried out mainly to monitor the free C=O stretching band present in the case of [62](PF$_6$)$_2$. Spectral changes are shown in Figure 6.6.1 and the vibrational data are listed in Table 6.6.1.

The 2+ form exhibits multiple bands within 1700 to 1500 cm^{-1}. Those are generally caused by bipyridine CN stretching and by C=O/C=N stretching from the bridging ligand. On oxidation from the 2+ to the 3+ form, bands around 1600 cm^{-1} (bipyridine vibration[63]) are arising while the 1582 and 1557 cm^{-1} bands from the bridging ligand have been shifted to higher wavenumbers (1642 cm^{-1}), indicating considerable involvement of the bridging ligand in the oxidation process. Besides, the low-energy

electronic absorption, as mentioned in the UV-Vis-NIR discussion, has been found at ν_{max} = 4150 cm^{-1} (= 2410 nm) for the 3+ form. This broad band extends to the mid-IR region, affecting the vibrational bands from the ligand backbone, which are sharp and relatively less intense.

The 4+ form, which is possibly a Ru^{III}-Ru^{III} species, exhibits one single band at 1604 cm^{-1} inside the above-mentioned region along with a weak band at around 1682 cm^{-1}.
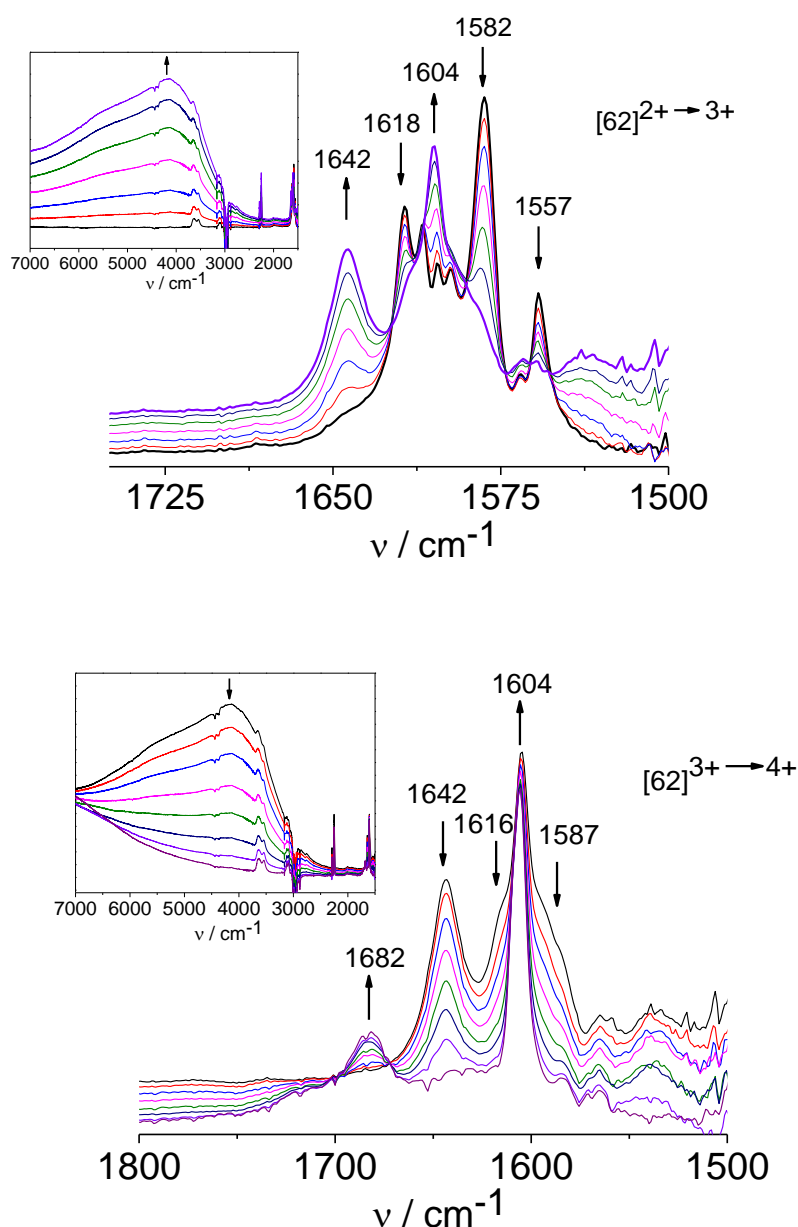
Figure 6.6.1: IR spectroelectrochemical response on stepwise oxidation (Ox$_1$ (top), Ox$_2$ (bottom)) of [62](PF$_6$)$_2$ in CH$_3$CN/0.1 M Bu$_4$NPF$_6$. Insets represent the electronic transition.

Table 6.6.1: Selected IR vibrational data of $[62]^n$.

n	ν / cm^{-1}
2+	1618, 1609, 1603, 1597, 1582, 1557
3+	1642, 1616(sh), 1604, 1587(sh)
4+	1682, 1604

In comparison to $[62](PF_6)_2$, $[61](PF_6)_2$ does not exhibit considerable shifts (Figure 6.6.2) of the vibrational bands which clearly suggests lesser involvement of ligand orbitals in the oxidation processes, in case of the latter. The stretching frequencies from the bridging ligand are shifted to the fingerprint region in case of $[61](PF_6)_2$, suggesting greater charge resonance in the bridging ligand.
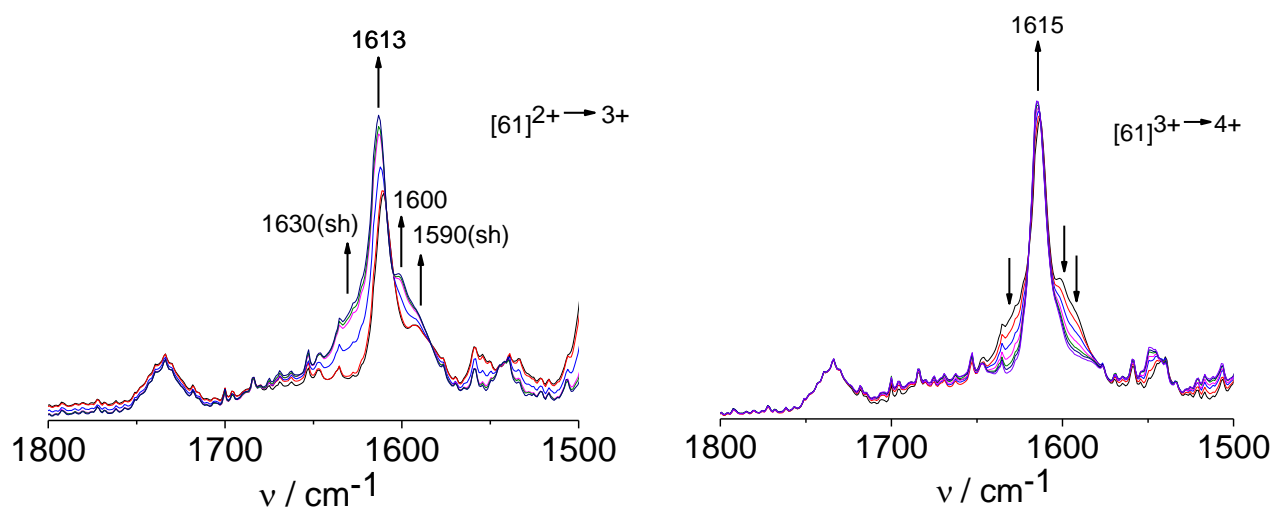
Figure 6.6.2: IR spectroelectrochemical response on stepwise oxidation (Ox_1 (left), Ox_2 (right)) of $[61](PF_6)_2$ in CH_2Cl_2/0.1 M Bu_4NPF_6.

6.7 EPR spectroelectrochemistry.

EPR measurements were carried out for the *in situ* electrochemically generated [61]$^{3+}$ ion in CH_2Cl_2/0.1 M Bu_4NPF_6. In the glassy frozen state (at 110 K) this charged species exhibits an axial signal with a g anisotropy (g_1-g_3) of 0.23. The EPR data of present system are comparable, with [61A]$^{3+}$ (g_1-g_3 = 0.20)[50b] suggesting that the change of the terminal ligand, i.e. unsubstituted to substituted terpyridine (trpy*), does not much affect the electronic situation of the paramagnetic species [(μ,η^3:η^3-adc-Py){RuL$_n$}]$^{3+}$. Such systems can be described as resonance hybrids Ru^{II}(adc-Py)$^{2-}$Ru^{III} $\leftrightarrow$ Ru^{II}(adc-Py)$^{\bullet-}$Ru^{II}.
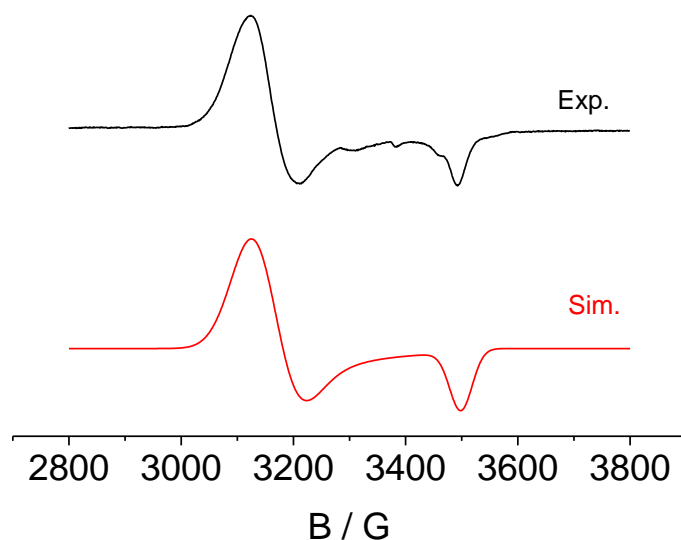
Figure 6.7.1: EPR spectrum of electrogenerated [61]$^{3+}$ in CH_2Cl_2/0.1 M Bu_4NPF_6 at 110 K with computer simulation (g_1 = 2.165, g_2 = 2.135, g_3 = 1.935; linewidths (l_x, l_y and l_z) = 80, 80 and 40 G; simulated assuming Gaussian lineshapes).

EPR spectroelectrochemical investigations of the *in situ* electrochemically generated bis(bidentate) system [62]$^{3+}$ in CH_3CN/0.1 M Bu_4NPF_6 produced a rhombic signal (Figure 6.7.2) with g_{av} = 2.06 and Δg = 0.22 in the glassy frozen state at 130 K.
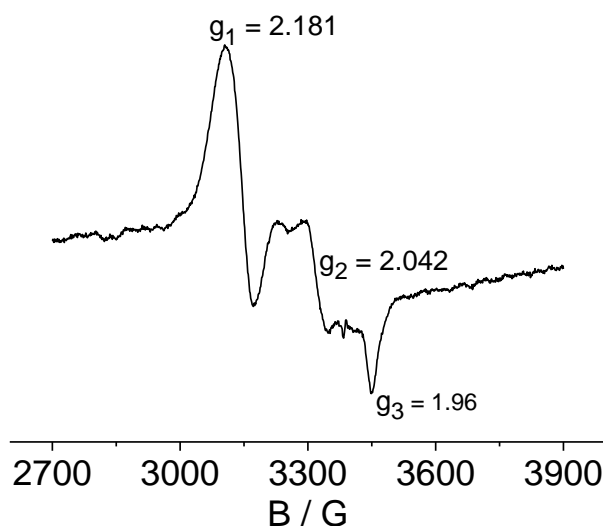
Figure 6.7.2: EPR spectrum of electrogenerated $[62]^{3+}$ in CH_3CN/0.1 M Bu_4NPF_6 at 130 K.

6.8 Conclusion.

The ligand adc-Py(2−) has variable binding modes such as bis(tridentate), bis(bidentate) and bidentate/tridentate (Scheme 6.1.1). The complex $[(\mu,\eta^3:\eta^3$-adc-Py)\{Ru(trpy*)\}_2](PF_6)_2$ ($[61](PF_6)_2$) with bis(N,N',O) ligand coordination exhibits two reversible oxidation processes which are predominantly metal-centred. The intermediate mixed-valent species (Ru^{II}-Ru^{III}) shows a moderately intense ($\varepsilon \approx 2700$ $M^{-1}cm^{-1}$), broad ($\Delta v_{1/2}$ = 3900 cm^{-1}) NIR absorption at around 1160 nm. The EPR investigation of this intermediate suggests considerable contribution from metal to the SOMO, according to the observed g anisotropy (g_1-g_3 = 0.23). The comparative analysis of the redox system $[61]^{2+/3+/4+}$ and of its previously reported analogue $[61A]^{2+/3+/4+}$ (unsubstituted terpyridine instead of trpy* as terminal ligands) does not produce any significant difference in electronic situations of the redox species.

On the other hand, the complex $[(\mu,\eta^2:\eta^2$-adc-Py)\{Ru(bpy)_2\}_2](PF_6)_2$ ($[62](PF_6)_2$) in the crystal with bis(N,N') coordination exhibits a twisted geometry with two orthogonal metal halves, as has been observed previously in dinuclear Au[112] and Fe[113] complexes. Electrochemical (K_c(3+) = $10^{8.3}$) and low-energy electronic absorption (v_{max} = 4150 cm^{-1}) data related to the intermediate 3+ form in $[62]^{2+/3+/4+}$ indicate weak

metal-metal interaction in that redox species. Above all, the observed high energy shifts of the vibrational bands from the bridging ligand during oxidation from the 2+ (1582, 1557 cm^{-1}) to the 3+ (1642 cm^{-1}) state suggests that the redox process is partially ligand centred.

To summarise, we have found different spectroelectrochemical responses for different coordination modes of diruthenium complexes of the bridging adc-Py($2-$). A remarkable finding is the very different interaction of the metal centres in the twisted bis(bidentate) vs. the non-twisted bis(tridentate) bridged diruthenium systems.

Chapter 7

Experimental section

7.1. Instrumentation.

Elemental analysis:

Ms. B. Förtsch performed C, H, N analyses on a Perkin Elmer Analyzer 240.

NMR spectroscopy:

Ms. M. Benzinger and Mr. B. Rau carried out ^{1}H and ^{13}C NMR spectroscopic measurements on a Bruker AC 250 spectrometer and a Bruker AM 400 spectrometer. ^{1}H NMR or ^{13}C NMR signals from respective solvents have been used as the internal standard for the NMR sectra.[129]

EPR spectroscopy:

X-band EPR spectra at 9.5 GHz were obtained from a Bruker EMX system ESP 300 equipped with a Hewlett-Packard Frequency counter 5350B, a Bruker ER035M gaussmeter for g values determination and a continuous flow cryostat ESR 900 of Oxford instruments for measurements at liquid helium temperature (4 K). For measurements between 110-300K, same instrumental configuration was used with liquid nitrogen cryostat. The oxidised species for X-band EPR were *in situ* generated either electrochemically by using a two-electrode capillary or by chemical oxidation using silver hexafluorophosphate and .ferrocenium hexaflurophosphate according to the required redox potentials.

Simulations of the spectra were done by using the Bruker WINEPR / Simfonia programs.

ESI-mass spectroscopy:

ESI mass spectra were recorded on Bruker Daltonics-micrOTOF-Q by Mr. J. Trinkner and Ms. K. Wohlbold.

IR spectroscopy:

IR spectra were obtained using a Nicolet 6700 FTIR instrument. The solution measurements were performed through CaF_2 windows.

UV-Vis-NIR spectroscopy:

Absorption spectra were recorded on J&M TIDAS spectrometer.

UV-Vis-NIR and IR spectroelectrochemistry measurements were mostly (all, except those complexes from Chapters 3 and 5) done by Mr. Jan Fiedler (J. Heyrovský Institute of Physical Chemistry, Academy of Sciences of the Czech Republic, Department of Molecular Electrochemistry, Prague). The measurements were performed using an Optically Transparent Thin Layer Electrochemical (OTTLE) cell, which has been developed by Mr. Krejcik.[72] The windows of the cell are made of CaF_2 plates. The working (platinum mesh), auxiliary (platinum mesh) and reference electrodes (silver wire as pseudo reference) are melt-sealed inside the cell.

Cyclic voltammetry:

Cyclic and Differential Pulse voltammetry were performed with a PAR 273 potentiostat. The measurements were carried out under argon atmosphere in 0.1 M tetrabutylammonium hexafluorophosphate solutions using a three electrode configuration (Pt working electrode, Pt counter electrode and Ag wire pseudoreference electrode). The ferrocenium/ferrocene couple ($Fc^{+/0}$) was used as the internal reference.

X-ray diffraction:

X-ray diffraction experiments were collected using a Bruker Kappa Apex2duo diffractometer by Dr. W. Frey. Monochromatic Mo-K radiation ($\lambda = 0.71073$ Å;

Monochromator: Graphite) or Cu-K radiation (λ = 1.5406 Å) at around 100 K (*see* 7.4) was used for the diffraction. Structures were solved and refined by full-matrix least-squares techniques on F^2 using the SHELX-97 program[130], which were performed by Drs. M. Bubrin, W. Frey and B. Schwederski.

DFT calculations:

DFT calculations were performed by Dr. S. Záliš (J. Heyrovsky Institute of Physical Chemistry, Academy of Sciences of the Czech Republic, Department of Electrochemistry, Prague) using the Gaussian 09[131] (G09) and ADF2014.06[132] program packages and by Dr. V. Filippou using the program package ORCA 3.0.3[133].

7.2 Solvents and working conditions.

All reactions involving ruthenium were carried out under argon atmosphere using a standard Schlenk-line technique to avoid uncontrolled oxidation to Ru^{III} by air. Most of the solvents were dried by refluxing under argon over calcium hydride (dichloromethane, acetonitrile, ethanol) and sodium (tetrahydrofuran, toluene, n-hexane). Others were dried over 3A molecular sieves overnight followed by distillation before use. They were degassed by freeze-pumped-thaw method.

7.3 Syntheses.

The 1,2-dicarbonyl hydrazine compounds [$(H_2adc\text{-}^tBu)$[134], $(H_2adc\text{-}CF_3)$[135], $(H_2adc\text{-}Ph)$[136], $(H_4adc\text{-}Sal)$[122a], $(H_3adc\text{-}Salph)$[100], $(H_2adc\text{-}Py)$[50b]] and the metal precursor complexes (*cis*-Ru(bpy)$_2$Cl$_2$[137], *mer*-Ru(trpy*)Cl$_3$[138], *cis*-Os(bpy)$_2$Cl$_2$[139]) were synthesised by following the literature procedures. All other chemicals and reagents were of reagent grade and used without further purification. HPLC grade solvents were used for electrochemical and spectroelectrochemical measurements. The complexes with perchlorate counter anion were synthesised and used for crystallisation purpose only.

Caution: Perchlorate salts can decompose explosively and should be handled with care.

7.3.1 Syntheses of mononuclear Ru complexes.
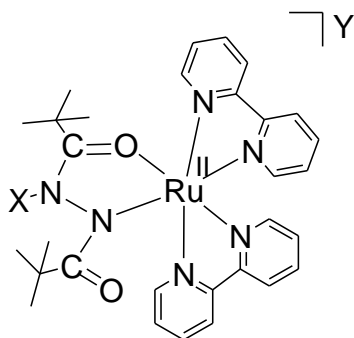
[Ru(bpy)₂(XL)]Y: X = H; Y = PF₆, ClO₄

[Ru(bpy)₂(XL)]Y: X = CH₃; Y = PF₆
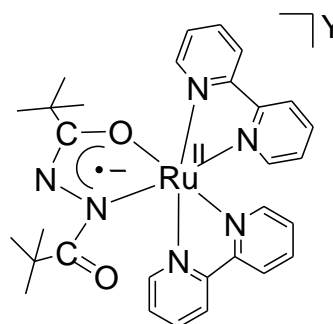
[Ru(bpy)₂(L)]Y: Y = PF₆, ClO₄

[Ru(bpy)₂(HL)]PF₆ (HL⁻ = Hadc-ᵗBu⁻)

A mixture of 100 mg (0.21 mmol) of *cis*-Ru(bpy)₂Cl₂.2H₂O, 41.4 mg (0.21 mmol) of H₂adc-ᵗBu and 8.4 mg (0.21 mmol) of NaOH in 30 ml of ethanol was refluxed under an argon atmosphere for 12 h. After that, the reaction mixture was cooled to room temperature, concentrated and charged with a saturated solution of KPF₆. A red-brown precipitate was formed which was filtered off and washed with cold water. The precipitate was then air-dried, dissolved in minimum volume of dichloromethane and subjected for column chromatographic purification on neutral alumina. With a 50:1 CH₂Cl₂/MeOH mixture a single red-brown band was eluted corresponding to [Ru(bpy)₂(HL)]PF₆. The solvent was removed under reduced pressure to obtain a red-brown solid residue.

Yield: 95 mg (60%); Anal. Calcd. (Found) for C₃₀H₃₅F₆N₆O₂PRu (757.67): C, 47.56 (47.32) H, 4.66 (4.80) N, 11.09 (10.90 %); m/z = 613.18 (M-PF₆); ¹H NMR (250 MHz, CD₂Cl₂): δ (ppm) = 11.79 (s, 1H), 8.91 (d, J = 4.9 Hz, 1H), 8.60 − 8.21 (m, 5H), 8.15 − 8.00 (m, 2H), 7.88 − 7.70 (m, 3H), 7.67 − 7.56 (m, 2H), 7.25 (d, J = 4.9 Hz, 1H), 7.11 (ddd, J = 13.2, 7.2, 1.2 Hz, 2H), 1.09 (s, 9H), 0.61 (s, 9H). ¹³C NMR (63 MHz, CD₂Cl₂)) δ (ppm) = 182.82 (s), 176.17 (s), 159.75 (d, J = 18.5 Hz), 158.65 (d, J = 2.3

Hz), 154.48 (s), 153.02 (s), 152.02 (s), 151.17 (s), 137.26 (s), 136.77 (d, J = 6.6 Hz), 135.53 (s), 127.16 − 126.59 (m), 126.38 (s), 123.75 (dd, J = 13.7, 1.6 Hz), 37.13 (s), 36.77 (s), 28.56 (s), 27.47 (s).

[Ru(bpy)$_2$(HL)]ClO$_4$ (HL$^-$ = Hadc-^{t}Bu$^-$)

[Ru(bpy)$_2$(HL)]ClO$_4$ was synthesised and purified by repeating the procedure for [Ru(bpy)$_2$(HL)]PF$_6$. Saturated solution of NaClO$_4$ was used for the precipitation of [Ru(bpy)$_2$(HL)]ClO$_4$.

Yield: 87 mg (58%); Anal. Calcd. (Found) for C$_{30}$H$_{35}$ClN$_6$O$_6$Ru (712.16): C, 50.60 (50.35) H, 4.95 (5.08) N, 11.80 (11.40 %); m/z = 613.18 (M-ClO$_4$).

[Ru(bpy)$_2$(CH$_3$L)]PF$_6$ (CH$_3$L$^-$ = CH$_3$adc-^{t}Bu$^-$)

The mononuclear protonated complex [Ru(bpy)$_2$(HL)]PF$_6$ (50 mg, 0.07 mmol) and 5 mg (0.13 mmol) of NaOH were dissolved in 30 ml degassed Acetonitrile/H$_2$O (2:1) in a brown Schlenk flask and the mixture stirred under argon for 30 min. After that, an excess amount of iodomethane (0.06 ml, ≈10eq.) was slowly added to the reaction mixture and the stirring was continued for another 2 h. Then the reaction mixture was concentrated and re-charged with a saturated KPF$_6$ solution to produce a precipitate corresponding to [Ru(bpy)$_2$(CH$_3$L)]PF$_6$. The precipitate was filtered of, washed with chilled water, air-dried and purified by neutral alumina column chromatography. Using 50:1 CH$_2$Cl$_2$/MeOH mixture a rose-red band was eluted. The solvent was evaporated under reduced pressure to obtain an air-stable solid.

Yield: 42 mg (78%); Anal. Calcd. (Found) for C$_{31}$H$_{37}$F$_6$N$_6$O$_2$PRu (771.7): C, 48.25 (47.90) H, 4.83 (5.09) N, 10.89 (10.56 %) ; m/z = 627.20 (M-PF$_6$); ^{1}H NMR (250 MHz, CD$_2$Cl$_2$) δ (ppm) = 8.69 (dd, J = 5.6, 0.7 Hz, 1H), 8.61 − 8.53 (m, 1H), 8.37 − 8.28 (m, 2H), 8.21 (dd, J = 8.0, 3.4 Hz, 2H), 8.07 − 7.94 (m, 2H), 7.84 − 7.67 (m, 3H), 7.63 − 7.49 (m, 2H), 7.46 − 7.40 (m, 1H), 7.08 (dddd, J = 11.0, 7.4, 5.7, 1.3 Hz, 2H), 2.73 (s, 3H), 1.23 (s, 9H), 1.02 (s, 9H). ^{13}C NMR (63 MHz, CD$_2$Cl$_2$) δ (ppm) = 185.06 (s), 178.45 (s), 159.90 (s), 159.22 − 157.83 (m), 153.11 (s), 151.85 (s), 150.91 (s), 136.86 − 135.82 (m), 134.74 (s), 127.56 − 127.04 (m), 126.93 (s), 126.37 (d, J = 30.2

Hz), 123.90 – 123.72 (m), 123.34 (dd, J = 16.1, 14.6 Hz), 61.50 (s), 40.57 (s), 36.56 (s), 29.17 (s), 28.01 (s).

[Ru(bpy)$_2$(L)]PF$_6$ (L$^{\cdot-}$ = adc-^{t}Bu$^{\cdot-}$)

The mononuclear protonated complex [Ru(bpy)$_2$(HL)]PF$_6$ (50 mg, 0.07 mmol) and 18 mg (0.07 mmol) of AgPF$_6$ were dissolved in 30 ml CH$_2$Cl$_2$ and the mixture was stirred under argon for 30 min. The elemental silver thus formed was filtered off and to the filtrate a few drops of Et$_3$N was added which caused an instant colour change from red-brown to green. The reaction mixture was then concentrated *in vacuo* and 20 ml of n-hexane was added. The green coloured precipitate thus obtained was collected, washed with diethyl ether and dried under vacuum to obtain [Ru(bpy)$_2$(L)]PF$_6$.

Yield: 46 mg (87%); Anal. Calcd. (Found) for C$_{30}$H$_{34}$F$_6$N$_6$O$_2$PRu (756.66): C, 47.62 (47.76) H, 4.53 (4.80) N, 11.11 (10.98 %); m/z = 612.18 (M-PF$_6$).

[Ru(bpy)$_2$(L)]ClO$_4$ (L$^{\cdot-}$ = adc-^{t}Bu$^{\cdot-}$)

The procedure for [Ru(bpy)$_2$(L)]PF$_6$ was repeated to obtain green coloured [Ru(bpy)$_2$(L)]ClO$_4$ from the protonated perchlorate complex using AgClO$_4$ instead of AgPF$_6$.

Yield: 42 mg (85%); Anal. Calcd. (Found) for C$_{30}$H$_{34}$ClN$_6$O$_6$Ru (711.15): C, 50.67 (50.33) H, 4.82 (4.91) N, 11.82 (11.70 %); m/z = 612.18 (M-ClO$_4$).

7.3.2 Synthesis of mononuclear Os complex.
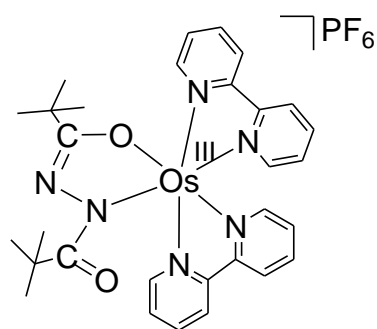
[Os(bpy)$_2$(L)]PF$_6$

[Os(bpy)$_2$(L)]PF$_6$ (L^{2-} = adc-^{t}Bu^{2-})

The precursor complex *cis*-Os(bpy)$_2$Cl$_2$ (100 mg, 0.17 mmol), 35 mg (0.17 mmol) of H$_2$adc-^{t}Bu and 16 mg (0.4 mmol) of NaOH were dissolved in 30 ml of ethanol/water (5:1) mixture and the reaction mixture was heated to reflux in aerobic condition for 24 h. After cooling to the room temperature, the reaction mixture was concentrated and a saturated KPF$_6$ solution was added into it to produce a bluish-green precipitate, which was collected, washed with chilled water to remove excess KPF$_6$ and air-dried. This residue was purified using column chromatography (neutral alumina). With a solvent mixture CH$_2$Cl$_2$/MeOH (50:1), a green coloured band was eluted first which was collected and the solvent was then evaporated to obtain [Os(bpy)$_2$(L)]PF$_6$.

Yield: 43 mg (30%); Anal. Calcd. (Found) for C$_{30}$H$_{34}$F$_6$N$_6$O$_2$OsP (845.82): C, 42.60 (42.73) H, 4.05 (4.34) N, 9.94 (9.73 %); m/z = 702.24 (M-PF$_6$).

7.3.3 Syntheses of dinuclear Ru complexes.

[{Ru(trpy*)Cl}$_2$(μ-adc-Ph)]PF$_6$

[{Ru(trpy*)Cl}$_2$(μ-adc-Ph)]PF$_6$
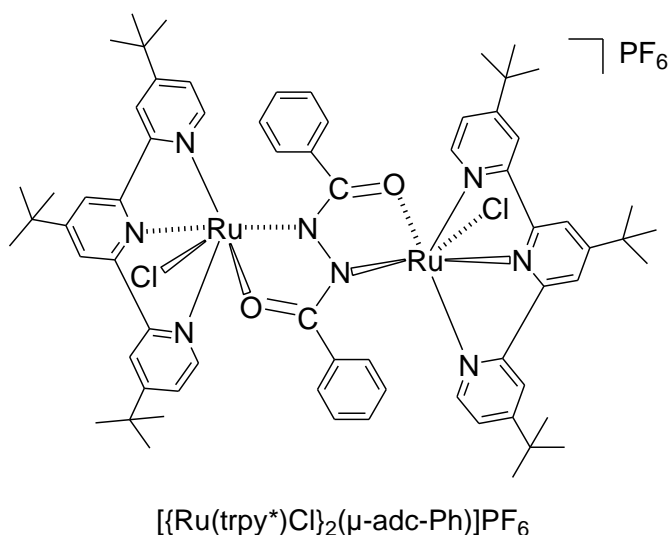
To a mixture of 100 mg (0.16 mmol) of *mer*-Ru(trpy*)Cl$_3$ and an amount of 20 mg (0.08 mmol) H$_2$adc-Ph, dissolved in 20 ml of EtOH, a few drops of Et$_3$N were added and the mixture was heated to reflux for 15 h. The initial greenish yellow solution

gradually changed to deep purple. After cooling to room temperature 0.5 g of KPF$_6$ dissolved in 25 ml water were added and the precipitate thus obtained was filtered off and washed with cold water and purified with a neutral Al$_2$O$_3$ column. With DCM/Acetone (10:1) solvent mixture a purple solution corresponding to [{Ru(trpy*)Cl}$_2$(μ-adc-Ph)]PF$_6$ was eluted. The solvent was removed under reduced pressure to obtain a deep purple coloured product.

Yield: 55 mg (46%); Anal. Calcd. (Found) for C$_{68}$H$_{80}$Cl$_2$F$_6$N$_8$O$_2$PRu$_2$ (1459.42): C, 55.96 (55.67) H, 5.53 (5.88) N, 7.68 (7.70 %) ; m/z = 1314.3 (M-PF$_6$); ^{1}H NMR (250 MHz, (CD$_3$)$_2$CO): δ (ppm) = 20.74 (s, 4H), 13.52 (s, 4H), 9.26 (b, 4H) 8.80 (b, 6H), 6.28 (s, 4H), 5.33 (s, 4H), 1.85 (s, 36H), 1.49 (s, 18H).

[{Ru(trpy*)Cl}$_2$(μ-adc-CF$_3$)]

{Synthesised by Lorenz Julian Fahrner (Bachelor Thesis)}
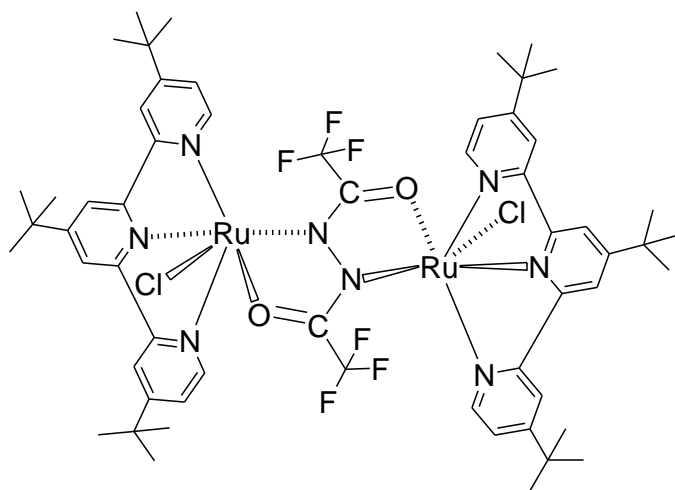
[{Ru(trpy*)Cl}$_2$(μ-adc-CF$_3$)]

Initially, 100 mg (0.16 mmol) of the precursor complex *mer*-Ru(trpy*)Cl$_3$, 18.4 mg (0.08 mmol) of the ligand H$_2$adc-CF$_3$ and 13 mg (0.328 mmol) of sodium hydroxide were dissolved in 30 ml of methanol. Subsequently, the solution was refluxed for 20 h. The color of the reaction solution changed from orange to violet after five minutes. At the end of the 20 h reflux, the solvent was removed, the residue was dissolved in DCM and transferred onto neutral alumina column for purification. A violet major fraction was eluted with dichloromethane which was collected, the solvent was

evaporated under reduced pressure, the residue was dried under vacuum to obtain the solid product corresponding to [{Ru(trpy*)Cl}$_2$(μ-adc-CF$_3$)].

Yield: 35%; Anal. Calcd. (Found) for C$_{58}$H$_{70}$Cl$_2$F$_6$N$_8$O$_2$Ru$_2$ (1298.27): C, 53.66 (53.78) H, 5.43 (5.42) N, 8.63 (8.54 %) ; m/z = 1263.3 (M-Cl); ^{1}H NMR (250 MHz, (CD$_3$)$_2$CO): δ (ppm) = 8.17 (s, 8H), 7.71 (d, J = 5.9 Hz, 4H), 7.23 (dd, J = 5.9, 2.0 Hz, 4H) 1.62 (s, 18H), 1.49 (s, 36H).

[{Ru(trpy*)}$_2$(μ-adc-Sal)]X/Y (X = PF$_6$ or ClO$_4$, Y = (PF$_6$)$_2$)

[{(trpy*)Ru}$_2$(μ-adc-Sal)]X/Y

X = PF$_6$ or ClO$_4$

Y = (PF$_6$)$_2$
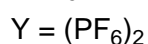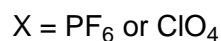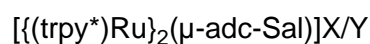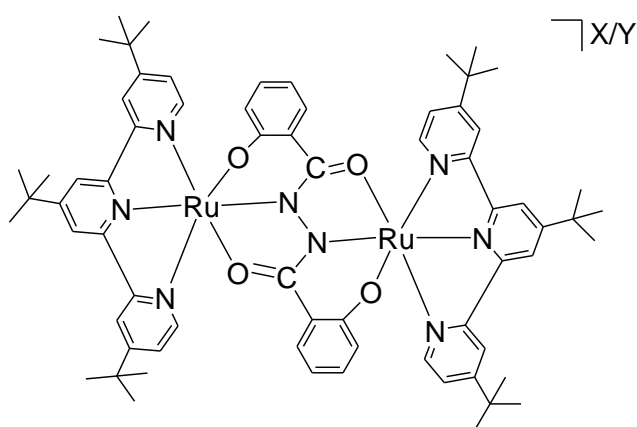
[{Ru(trpy*)}$_2$(μ-adc-Sal)]PF$_6$

To a mixture of 50 mg (0.08 mmol) of *mer*-Ru(trpy*)Cl$_3$ and an amount of 11.18 mg (0.04 mmol) H$_4$adc-Sal, dissolved in 20 ml of EtOH, a few drops of Et$_3$N were added and the mixture was heated to reflux for 15 h. The initial greenish yellow solution gradually changed to deep purple. After cooling to room temperature a saturated solution of Potassium hexaflurophosphate (KPF$_6$) were added, the precipitate thus obtained was filtered off, washed with cold water.and purified with a neutral Al$_2$O$_3$ column. With CH$_2$Cl$_2$/CH$_3$OH (100:1) a purple solution corresponding to [{Ru(trpy*)}$_2$(μ-adc-Sal)]PF$_6$ was eluted. The solvent was removed under reduced pressure to obtain a deep purple residue.

Yield: 50%; Anal. Calcd. (Found) for [{Ru(trpy*)}$_2$(μ-adc-Sal)]PF$_6$ x 0.25CH$_3$OH x 0.25CH$_2$Cl$_2$, C$_{68.5}$H$_{79.5}$Cl$_{0.5}$F$_6$N$_8$O$_{4.25}$PRu$_2$ (1418.5): C, 56.83 (56.82) H, 5.53 (5.52) N, 7.74 (7.73%); m/z = 1274.43 (M-PF$_6$); ^{1}H NMR (250 MHz, (CD$_3$)$_2$CO): δ (ppm) = 19.77 (s, 4H), 8.26 (s, 4H), 7.30 (s, 4H), 7.02 (s, 2H), 4.85 (d, J = 7.9 Hz, 2H), 2.59 (s, 2H), 1.57 (s, 36H), 1.39 (s, 18H), 0.54 – 0.27 (m, 6H).

[{Ru(trpy*)}$_2$(μ-adc-Sal)]ClO$_4$

[{Ru(trpy*)}$_2$(μ-adc-Sal)]ClO$_4$ was synthesised following the same procedure as of [{Ru(trpy*)}$_2$(μ-adc-Sal)]PF$_6$. Instead of Potassium hexaflurophosphate (KPF$_6$), a saturated solution of sodium perchlorate (NaClO$_4$) was used in this case.

Yield: 38%; Anal. Calcd. (Found) for C$_{68}$H$_{78}$ClN$_8$O$_8$Ru$_2$ (1373.3): C, 59.49 (59.25) H, 5.73 (5.63) N, 8.16 (7.90%); m/z = 1274.42 (M-ClO$_4$); ^{1}H NMR (250 MHz, (CD$_3$)$_2$CO): δ (ppm) = 19.34 (s, 4H), 8.33 (s, 4H), 7.33 (s, 4H), 7.01 (s, 2H), 4.88 (d, J = 7.9 Hz, 2H), 2.59 (s, 2H), 1.56 (s, 36H), 1.41 (s, 18H), 0.61 – 0.48 (m, 6H).

[{Ru(trpy*)}$_2$(μ-adc-Sal)](PF$_6$)$_2$

The doubly charged complex [{Ru(trpy*)}$_2$(μ-adc-Sal)](PF$_6$)$_2$ was synthesised by chemical oxidation of [{Ru(trpy*)}$_2$(μ-adc-Sal)]PF$_6$ with slightly excess ferrocenium hexaflurophosphate (1.1 eq) in CH$_2$Cl$_2$. The oxidised green coloured product was isolated by precipitation into hexane with a reasonable yield of 90%.

Anal. Calcd. (Found) for C$_{68}$H$_{78}$F$_{12}$N$_8$O$_4$P$_2$Ru$_2$ (1564.3): C, 52.24 (51.90) H, 5.03 (5.10) N, 7.17 (7.37%); m/z = 637.21 (M-2PF$_6$)/2; ^{1}H NMR (250 MHz, (CD$_3$)$_2$CO): δ (ppm) = 28.72 (s, 2H), 20.20 (s, 2H), 18.02 (s, 4H), 5.22 (s, 5H), 4.62 (s, 5H), 1.44 (s, 36H), 1.18 (s, 18H), - 9.36 (s, 4H), - 31.74 (s, 2H).

[{Ru(trpy*)}₂(μ-adc-Salph)Cl]PF₆
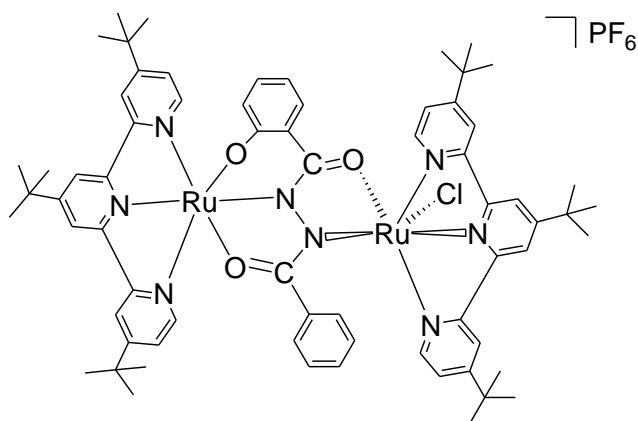
[{(trpy*)Ru}₂(μ-adc-Salph)Cl]PF₆

The purple coloured complex [{Ru(trpy*)}₂(μ-adc-Salph)Cl]PF₆ was synthesised and purified by following the procedure, described for [{Ru(trpy*)}₂(μ-adc-Ph)]PF₆.

Yield: 40 mg (34%); Anal. Calcd. (Found) for $C_{68}H_{79}ClF_6N_8O_3PRu_2$ (1438.96): C, 56.76 (55.62) H, 5.53 (5.50) N, 7.79 (7.65 %); m/z = 1294.4 (M-PF₆); ^{1}H NMR (250 MHz, (CD₃)₂CO) δ (ppm) = 14.73 (s, 3H), 11.63 (d, J = 5.5 Hz, 5H), 9.89 (s, 3H), 8.37 (s, 2H), 6.40 (s, 3H), 6.19 (s, 5H), 5.75 (s, 4H), 1.84 (s, 18H), 1.43 (s, 9H), 1.41 (s, 18H), 1.16 (s, 9H).

[{Ru(trpy*)}₂(μ-adc-Py)](PF₆)₂
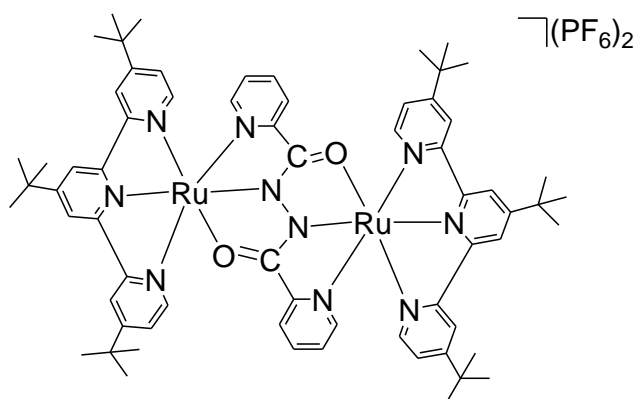
[{(trpy*)Ru}₂(μ-adc-Py)](PF₆)₂

100 mg (0.16 mmol) of *mer*-Ru(trpy*)Cl₃ and 126 mg (0.5 mmol) AgPF₆ were dissolved in 20 ml of acetone and heated for 12 h in dark. After cooling, precipitated

AgCl was filtered off over a celite bed and the filtrate was evaporated to dryness. The residue was dissolved in 20 ml of absolute ethanol, 19 mg (0.08 mmol) of H$_2$adc-Py and a few drops of Et$_3$N were added, then the mixture was refluxed for another 12 h. After that, the solvent was removed under reduced pressure and the residue was purified by neutral alumina column chromatography. With DCM/MeOH (25:1) solvent mixture a brown coloured major band was eluted, which was collected and the solvent was removed by rotary evaporation to obtain [{Ru(trpy*)}$_2$(μ-adc-Py)](PF$_6$)$_2$. Yield: 45 mg (37%); Anal. Calcd. (Found) for C$_{66}$H$_{78}$F$_{12}$N$_{10}$O$_2$P$_2$Ru$_2$ (1535.46): C, 51.63 (51.55) H, 5.12 (5.20) N, 9.12 (8.92 %); m/z = 623.2 (M-2PF$_6$)/2; ^{1}H NMR (250 MHz, (CD$_3$)$_2$CO) δ (ppm) = 8.71 (d, J = 5.9 Hz, 4H), 8.61 (d, J = 2.6 Hz, 4H), 8.50 (t, J = 4.1 Hz, 4H), 7.64 (dd, J = 5.9, 1.9 Hz, 2H), 7.58 (d, J = 4.3 Hz, 2H), 7.41 (dd, J = 5.9, 2.0 Hz, 2H), 7.33 (td, J = 7.7, 1.7 Hz, 1H), 7.08 (d, J = 4.0 Hz, 2H), 7.04 − 6.94 (m, 1H), 6.69 − 6.52 (m, 2H), 1.40 (s, 9H), 1.33 (s, 9H), 1.17 (s, 18H), 1.13 (s, 18H).

[{Ru(bpy)$_2$}$_2$(μ-adc-Py)](PF$_6$)$_2$

[{(bpy)$_2$Ru}$_2$(μ-adc-Py)](PF$_6$)$_2$
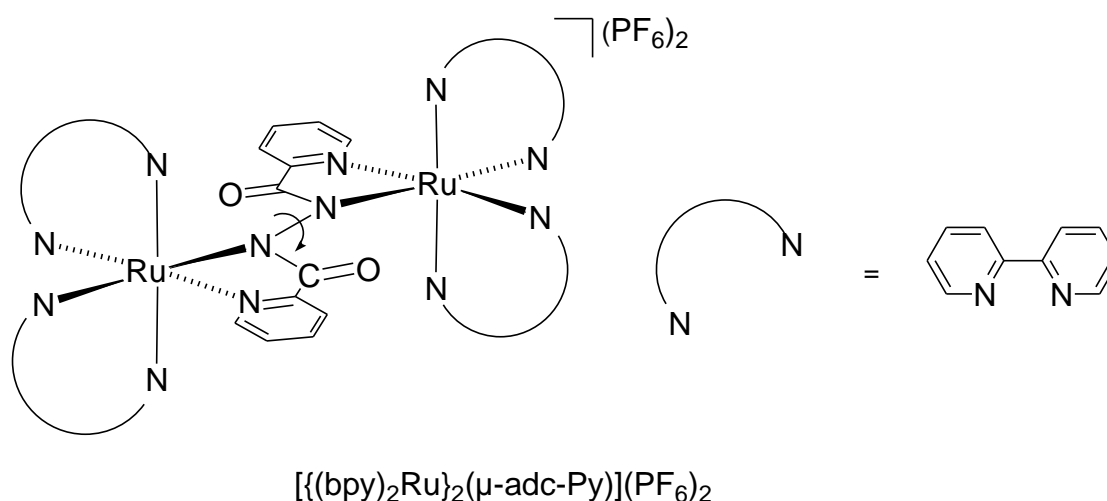
A mixture of 100 mg (0.21 mmol) of *cis*-Ru(bpy)$_2$Cl$_2$.2H$_2$O, 26 mg (0.11 mmol) of H$_2$adc-Py and 16 mg (0.4 mmol) of NaOH, dissolved in 25 ml of ethanol was refluxed for 24 h. After that, the reaction mixture was cooled to room temperature and charged with a saturated solution of KPF$_6$. A red-brown precipitate thus obtained was filtered off and washed with cold water. The precipitate was air-dried, then dissolved in minimum volume of dichloromethane and transferred to neutral alumina column. With 25:1 CH$_2$Cl$_2$/MeOH solvent mixture an yellowish-brown major band was eluted which was collected and evaporated to dryness to obtain [{Ru(bpy)$_2$}$_2$(μ-adc-Py)](PF$_6$)$_2$.

Yield: 65 mg (43%); Anal. Calcd. (Found) for $C_{52}H_{40}F_{12}N_{12}O_2P_2Ru_2$ (1357.02): C, 46.02 (45.90) H, 2.97 (2.82) N, 12.39 (12.45 %); m/z = 534.07 (M-2PF$_6$)/2.

7.4 Selected crystallographic data.

Table 7.4.1: Selected crystallographic parameters of [M(bpy)$_2$(adc-^{t}Bu)]X (M/X = Ru/ClO$_4$, Os/PF$_6$)

	[Ru(bpy)$_2$(adc-^{t}Bu)]ClO$_4$	[Os(bpy)$_2$(adc-^{t}Bu)] PF$_6$
Empirical formula	$C_{60}H_{68}Cl_2N_{12}O_{12}Ru_2$	$C_{30}H_{34}F_6N_6O_2OsP$
Formula weight	1422.30	845.80
Temperature/K	99.99	129.98
Crystal system	triclinic	triclinic
Space group	P-1	P-1
a/Å	10.8859(8)	14.0044(8)
b/Å	13.1440(8)	16.0912(9)
c/Å	13.9177(10)	17.8091(10)
α/°	111.032(4)	67.374(3)
β/°	98.060(4)	73.253(3)
γ/°	93.315(4)	76.812(3)
Volume/Å^3	1827.7(2)	3515.9(4)
Z	1	4
ρ_{calc}g/cm^3	1.292	1.598
μ/mm^{-1}	0.547	3.739
F(000)	730.0	1668.0
Radiation	MoKα (λ = 0.71073)	MoKα (λ = 0.71073)
2Θ range/°	3.342 to 53.864	3.064 to 52.99
Data/restraints/parameters	7471/0/403	14043/0/841
Goodness-of-fit on F^2	0.938	1.009
R$_1$, wR$_2$ [I>=2σ (I)]	0.0452, 0.0781	0.0499, 0.1068

R$_1$, wR$_2$ [all data]	0.0789, 0.0848	0.1201, 0.1394
Largest diff. peak/hole/e Å^{-3}	0.55/-0.54	5.15/-2.51

Table 7.4.2: Selected crystallographic parameters of [{Ru(trpy*)Cl}$_2$(μ-adc-R)]X (R/X = CF$_3$/-, Ph/PF$_6$)

	[{Ru(trpy*)Cl}$_2$(μ-adc-CF$_3$)]	[{Ru(trpy*)Cl}$_2$(μ-adc-Ph)]PF$_6$
Empirical formula	C$_{58}$H$_{70}$N$_8$O$_2$F$_6$Cl$_2$Ru$_2$	C$_{68}$H$_{80}$Cl$_2$F$_6$N$_8$O$_2$PRu$_2$
Formula weight	1298.26	1459.41
Temperature/K	100.0	100.0
Crystal system	monoclinic	monoclinic
Space group	$P2_1$/c	$P2_1$/c
a/Å	12.5156(6)	16.3645(7)
b/Å	23.7590(11)	24.1847(10)
c/Å	11.3626(5)	20.6390(9)
α/°	90	90
β/°	96.138(3)	105.491(2)
γ/°	90	90
Volume/Å^3	3359.4(3)	7871.6(6)
Z	2	4
ρ$_{calc}$g/cm^3	1.283	1.231
μ/mm^{-1}	0.588	4.396
F(000)	1332.0	3004.0
Radiation	MoKα (λ = 0.71073)	CuKα (λ = 1.54178)
2Θ range/°	3.272 to 56.668	5.604 to 132.992
Data/restraints/parameters	8344/0/388	13428/0/883
Goodness-of-fit on F^2	1.126	1.019
R$_1$, wR$_2$ [I>=2σ (I)]	0.0398, 0.0641	0.0432, 0.1067

R$_1$, wR$_2$ [all data]	0.0584, 0.0689	0.0572, 0.1174
Largest diff. peak/hole/e Å^{-3}	0.51/-0.79	1.47/-0.6

Table 7.4.3: Selected crystallographic parameters of [{(trpy*)Ru}$_2$(μ-adc-Sal)]X (X = PF$_6$, ClO$_4$)

	[{(trpy*)Ru}$_2$(μ-adc-Sal)]PF$_6$	[{(trpy*)Ru}$_2$(μ-adc-Sal)]ClO$_4$
Empirical formula	C$_{70}$H$_{82}$Cl$_4$F$_6$N$_8$O$_4$PRu$_2$	C$_{68}$H$_{78}$ClN$_8$O$_8$Ru$_2$
Formula weight	1588.35	1372.97
Temperature/K	100(2)	100(2)
Crystal system	triclinic	monoclinic
Space group	P-1	$P2_1$/c
a/Å	13.4892(8)	14.6359(17)
b/Å	14.9827(9)	21.0039(19)
c/Å	20.1161(12)	21.924(2)
α/°	109.584(3)	90
β/°	96.688(3)	104.626(8)
γ/°	99.814(3)	90
Volume/Å^3	3707.7(4)	6521.3(12)
Z	2	4
ρ$_{calc}$g/cm^3	1.423	1.398
μ/mm^{-1}	0.639	4.614
F(000)	1630	2844
Radiation	MoKα (λ = 0.71073)	CuKα (λ = 1.54178)
2Θ range/°	1.56 to 25.50	3.12 to 64.99
Data/restraints/parameters	13515 / 117 / 935	10569 / 170 / 861
Goodness-of-fit on F^2	1.033	1.051
R$_1$, wR$_2$ [I>=2σ (I)]	0.0620, 0.1564	0.1149, 0.2437

R₁, wR₂ [all data]	0.0825, 0.1670	0.1599, 0.2624
Largest diff. peak/hole/e Å⁻³	1.846 / -1.523	2.019 / -1.073

Table 7.4.4: Selected crystallographic parameters of [{(trpy*)Ru)}₂(μ-adc-Salph)Cl]PF₆.

Empirical formula	$C_{70}H_{83}Cl_3F_6N_8O_3PRu_2$
Formula weight	1537.90
Temperature/K	129.98
Crystal system	orthorhombic
Space group	Pbca
a/Å	26.4444(14)
b/Å	20.2037(11)
c/Å	31.2528(17)
α/°	90
β/°	90
γ/°	90
Volume/Å³	16697.6(16)
Z	8
ρ_{calc}g/cm³	1.224
μ/mm⁻¹	0.534
F(000)	6328.0
Radiation	MoKα (λ = 0.71073)
2Θ range/°	3.028 to 61.238
Data/restraints/parameters	25524/0/856
Goodness-of-fit on F²	1.094
R₁, wR₂ [I>=2σ (I)]	0.0889, 0.2455
R₁, wR₂ [all data]	0.1107, 0.2652

| Largest diff. peak/hole/e $Å^{-3}$ | 2.88 / -1.84 |

Table 7.4.5: Selected crystallographic parameters of [{(bpy)$_2$Ru)}$_2$(μ-adc-Py)](PF$_6$)$_2$.

Empirical formula	$C_{52}H_{40}F_{12}N_{12}O_2P_2Ru_2$
Formula weight	1357.03
Temperature/K	100.0
Crystal system	triclinic
Space group	*P*-1
a/Å	14.7248(9)
b/Å	17.7006(11)
c/Å	23.6929(15)
α/°	100.482(2)
β/°	104.274(2)
γ/°	107.852(2)
Volume/Å^3	5470.0(6)
Z	4
ρ_{calc}g/cm^3	1.6477
μ/mm^{-1}	0.705
F(000)	2704.4
Radiation	Mo Kα (λ = 0.71073)
2Θ range/°	3.02 to 50.1
Data/restraints/parameters	19266/0/1477
Goodness-of-fit on F^2	1.081
R_1, wR_2 [I>=2σ (I)]	0.1089, 0.2941
R_1, wR_2 [all data]	0.1494, 0.3314
Largest diff. peak/hole/e Å^{-3}	9.63/-1.89

Chapter 8

Summary.

Intramolecular electron transfer in mixed-valent diruthenium complexes with low-spin d^5/d^6 configuration and an organic bridge has been the point of interest since the Creutz-Taube ion $[(NH_3)_5Ru(pyz)Ru(NH_3)_5]^{5+}$ was first described by in 1967.[11,12] Investigations of various related manifestations with redox-active ("non-innocent") bridges have revealed electronically interesting situations as well as remarkable redox properties. In this doctoral work, the non-innocence and thus electron transferring ability of azodicarbonyl/hydrazido ligands (adc-$R^{0/\cdot-/2-}$) in metal/ligand or metal/ligand/metal formats is explored by integrating useful structural information (e.g. distances d_{N-N}), spectroelectrochemical (UV-Vis-NIR, IR, EPR) properties and computational results. Drs. V. Filippou and S. Záliš carried out theoretical calculations. Hydrazine molecules listed in the following table were employed in their deprotonated forms to prepare various mononuclear and dinuclear complexes.

Table 8.1: Utilised Hydrazine molecules.

R₁ \ R₂	CF_3	$C(CH_3)_3$	C_6H_5	C_6H_4OH	C_6H_5N
CF_3	$H_2adc\text{-}CF_3$				
$C(CH_3)_3$		$H_2adc\text{-}^tBu$			
C_6H_5			$H_2adc\text{-}Ph$	$H_3adc\text{-}Salph$	
C_6H_4OH				$H_4adc\text{-}Sal$	
C_6H_5N					$H_2adc\text{-}Py$

In **Chapter 2**, mononuclear complexes with adc-^{t}Bu (adc-R, R = C(CH$_3$)$_3$) ligands have been studied. Two monocationic complexes were isolated and characterised as intermediate species in a two-step redox system [M(bpy)$_2$(adc-

^{t}Bu)]$^{0/+/2+}$ (M = Ru, Os). Structural characterisation of both monocations (M = Ru with ClO$_4^-$ and M = Os with PF$_6^-$ as counter anions; Figure 8.1) does not show any significant difference because of metal/ligand orbital mixing. The N1-N2 distances (1.39 ± 0.01 Å) indicate an intermediacy between the fully oxidised (0) and the reduced (2−) ligand redox states.
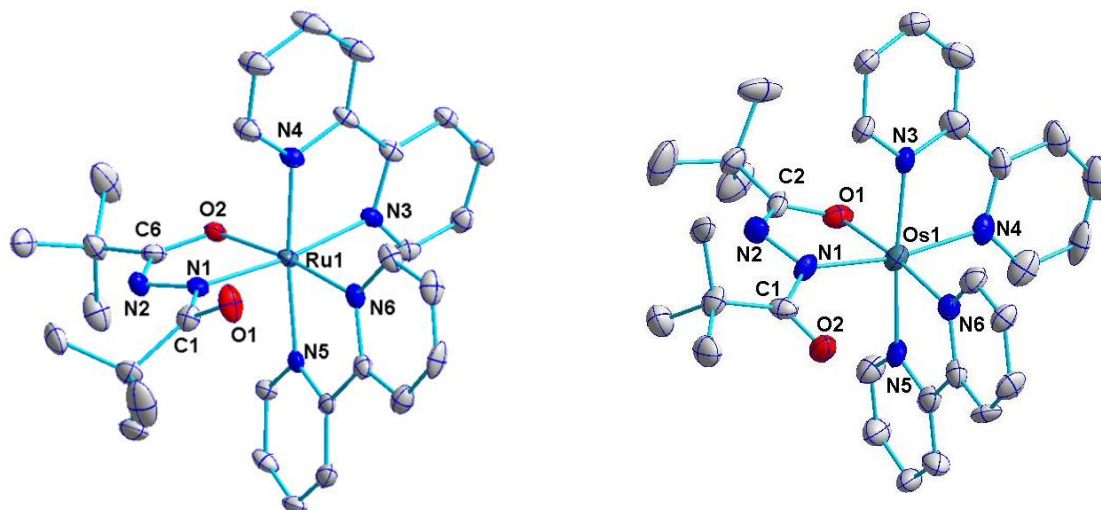
Figure 8.1: Molecular structures of the cations in the crystals of [Ru(bpy)$_2$(adc-^{t}Bu)]ClO$_4$ (left) and [Os(bpy)$_2$(adc-^{t}Bu)]PF$_6$ (right).

These systems are best described by a resonance hybrid of two contributing electronic structures, M^{II}(bpy)$_2$(adc-^{t}Bu)$^{\cdot-}$ ↔ M^{III}(bpy)$_2$(adc-^{t}Bu)$^{2-}$. In most instances, EPR-responses give useful information to find out the dominating contributor; in the present case, an isotropic signal (g = 2.027, at 298 K) for M = Ru points to the former while a rhombic signal (Δg = 1.104, at 5 K) for M = Os points to the latter. DFT calculations also support these results by predicting an increased spin density on the osmium centre (46 vs. 29 % for M = Ru). Absorption behaviour of these species in the visible and the NIR regions is also affected by such strong orbital mixing, the cations exhibit absorption features related to both contributing electronic structures. Redox processes [M(bpy)$_2$(adc-^{t}Bu)]$^{0/+/2+}$ (M = Ru, Os) were found reversible, involving both metal and ligand orbitals. This involvement is reflected by the stretching frequency of the uncoordinated C=O bond. Starting from the reduced (0) form, the frequency experiences a high-energy shift of around 90 and 120 cm^{-1}, respectively, in each successive redox processes. Most importantly, the K$_c$ value of

the intermediate (+) species is lower in case of Os ($10^{12.9}$ vs. $10^{14.6}$ for Ru), suggesting relatively smaller metal/ligand orbital mixing.

Chapter 2 describes two more ruthenium monocationic complexes with the adc-^{t}Bu(2−) ligand in its singly protonated Hadc-^{t}Bu(1−) and methylated CH₃adc-^{t}Bu(1−) forms, respectively. The complexes [M(bpy)₂(Radc-^{t}Bu)]PF₆ (R= H, CH₃) were characterised by ^{1}H-NMR spectroscopy with characteristic N-H and N-CH₃ signals in the respective cases. The protonated complex shows an irreversible redox behaviour in CH₃CN, exhibiting two oxidative responses in differential pulse voltammetry. Spectroelectrochemical (UV-Vis and IR) measurements suggest the formation of the deprotonated dication ([M(bpy)₂(adc-^{t}Bu)]$^{2+}$) after the second oxidation. On the other hand, the methylated species exhibits a metal-centred reversible one-electron oxidation process which is confirmed by a small shift (1533 to 1562 cm^{-1}) of the non-coordinated C=O stretching frequency and by DFT-calculated 51 % spin density at the metal centre. In effect, a parallel redox path (Scheme 8.1) relating to the Ru/Os redox series has been set off.

<u>charge</u>   <u>charge</u>

2+ $M^{III}(L^{\bullet-})$ ⟷ $M^{II}(L^0)$

                            − e⁻ ‖ + e⁻

+ $M^{II}(L^{\bullet-})$ ⟷ $M^{III}(L^{2-})$ $M^{III}(RL^-)$ ⟷ $M^{II}(RL^{\bullet})$ 2+
           M = Ru   M = Os

                                                        + e⁻
                                                        + R⁺   − e⁻ ‖ + e⁻
                            − e⁻ ‖ + e⁻   − e⁻
0          $M^{II}(L^{2-})$ − R⁺ $M^{II}(RL^-)$ +

                                                                    M = Ru
                                                                    R = H, CH₃
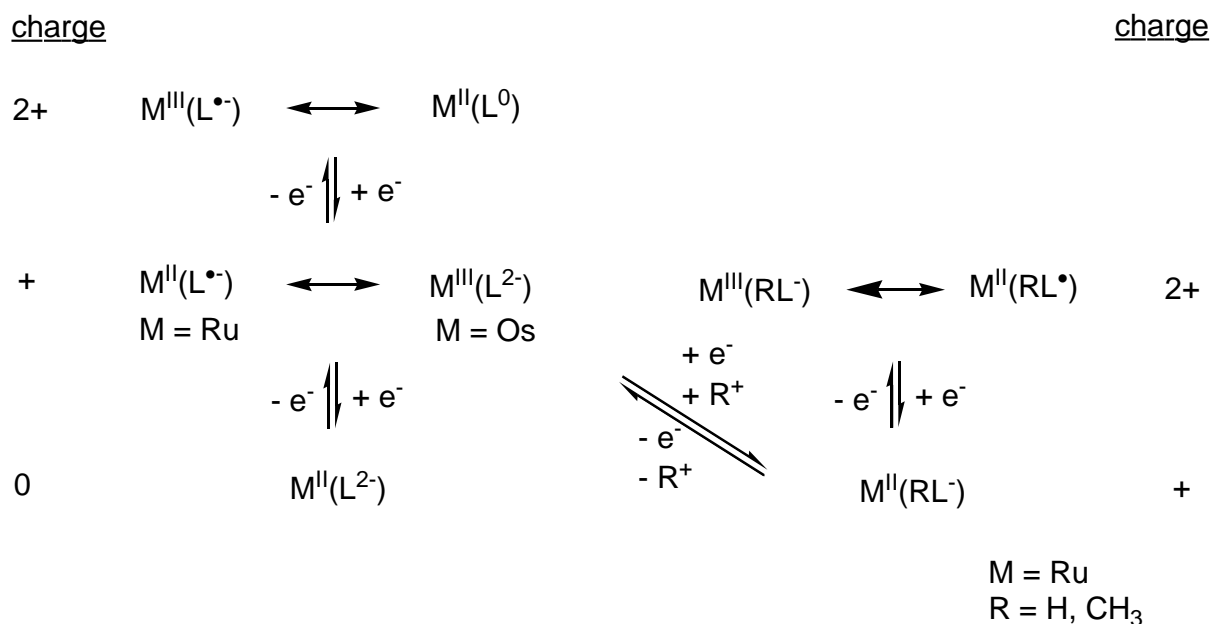
Scheme 8.1: Redox scheme for various monocationic complexes ([M(bpy)₂(RL)]$^+$, L = adc-^{t}Bu) showing assumed metal/ligand electron distributions.

Chapter 3 describes dinuclear complexes where two [Ru(trpy*)Cl]$^{n+}$ (trpy* = 4,4′,4″-tri-*tert*-butyl-2,2′:6′,2″-terpyridine) centres are interacting with bis-bidendate bridging ligands, adc-Ph(2−) (Ph = C₆H₅) and adc-CF₃(2−). The complexes belong to

a two-step redox system ([{(trpy*)ClRu}$_2$(μ-adc-R)]$^{0/+/2+}$, R = Ph, CF$_3$) with a stable mixed-valent (Ru^{II}/Ru^{III}) intermediate (K$_c$ ≈ 10$^{8.5}$). Both mixed-valent monocations produce characteristic inter-valence-charge-transfer (IVCT) bands in the NIR region (λ$_{max}$ between 1500 to 1600 nm), which are absent in the one-electron reduced (0) or the fully oxidised (2+) forms. The high intensity (ε ≈ 10000 M^{-1}cm^{-1}) and narrow bandwidth (< 2000 cm^{-1}) of these absorptions as well as the high K$_c$ value of the mixed-valent intermediates suggest a valence delocalised (Ru$^{2.5}$/Ru$^{2.5}$) situation. Structural characterisation (Figure 8.2, R = Ph) also supports the delocalised formulation with similar Ru-N distances (Ru2-N2 = 2.057(3) Å, Ru1-N1 = 2.051(3) Å) across the bridge.

The structures of the mixed-valent monocation (R = Ph) and of the neutral species (R = CF$_3$) exhibit a distorted and a planar M-L-M geometry, respectively, while both of them show similar connectivity around the metal centre, i.e. *trans* confirmation. The bond parameters exhibit the expected differences, which arise because of the different charges of these species. Most importantly, the N-N bond distances (>1.40 Å) indicate the presence of the hydrazido(2−) as compared to the radical(·−) form of the bridging ligand in both cases.
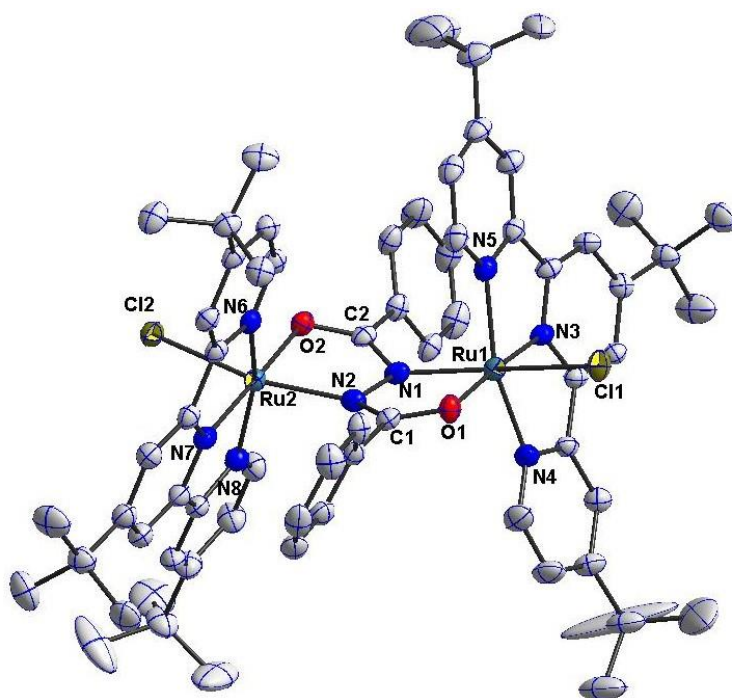
Figure 8.2: Molecular structure of the cation in the crystal of [{(trpy*)ClRu}$_2$(μ-adc-Ph)] PF$_6$, showing a distorted metal-ligand metal geometry. Torsion angles: C1-N2-N1-C2 = −160.1(3)°, Ru1-N1-N2-Ru2 = 163.15(14)°.

Chapter 4 descibes a diruthenium complex where two [Ru(trpy*)]$^{n+}$ centres are interacting with a bis-tridentate bridging ligand, adc-Sal(4-) (Table 8.1). The complex   [(trpy*)Ru(μ-adc-Sal)Ru(trpy*)]PF$_6$ was   characterised   structurally, electrochemically and spectroscopically as an intermediate (Ru^{II}(μ-adc-Sal)$^{4-}$Ru^{III}) of the three-step redox system [(trpy*)Ru(μ-adc-Sal)Ru(trpy*)]$^{0/+1/+2/+3}$. The structural characterisation (Figure 8.3) gives an intermediate value for the N1-N2 distance (1.392 Å), as was seen for the mononuclear complex [Ru(bpy)$_2$(adc-^{t}Bu)]ClO$_4$. It also gives similar Ru-N distances (1.990(4) Å) inside the M-L-M bridge. The complex exhibits a broad asymmetric absorption band in the NIR region which was deconvoluted by assuming Lorentzian line shape into three bands at λ$_{max}$ = 2140, 1645, and 1485 nm with 10^{-4}ε = 0.1, 0.7 and 0.5 M^{-1}cm^{-1}, respectively. The N1-N2 bond length, the intense multiple absorption bands, EPR data (Δg = 0.45) and DFT calculated spin density (0.31 on each Ru and 0.35 on bridging ligand) indicate a strong orbital interaction of the bridging ligand with both metal centres up to the point that the spin is distributed equally over bridging ligand and metal centres. Moreover, these results clearly indicate the non-innocent nature of the bridging ligand and the propensity to mediate electronic interaction between the two metal centres. The complex can thus be described as a resonance hybrid, [Ru$^{2.5}$(adc-Sal)$^{4-}$Ru$^{2.5}$]$^+$ ↔ [Ru^{II}(adc-Sal)$^{3\bullet-}$Ru^{II}]$^+$.
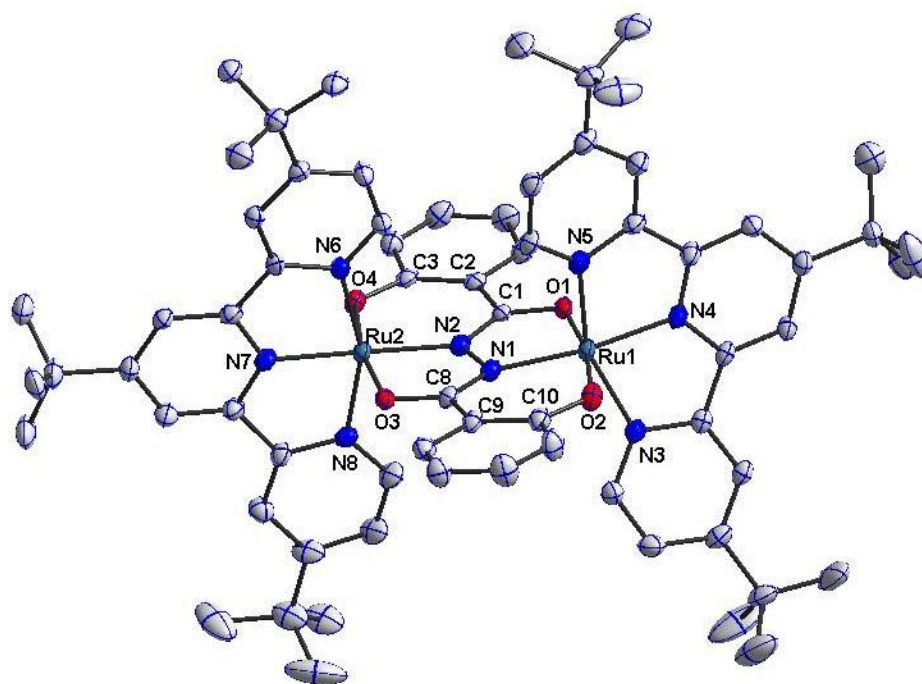
Figure 8.3: Molecular structure of the cation in the crystal of [{(trpy*)Ru}$_2$(μ-adc-Sal)] PF$_6$.

Chapter 5 extends the discussion regarding symmetric mixed-valent complexes in Chapters 3 and 4 to the asymmetric complex, [{(trpy*)Ru(μ-adc-Salph)Ru(trpy*)Cl]PF$_6$. As a strategy, the small bis-bidentate organic bridging unit (O=C-N-N-C=O) of the adc-R(2–) ligand is assembled with one potentially coordinating arm (C$_6$H$_4$O$^-$) to develop the non-symmetrical ligand adc-Salph(3–) (Table 8.1). This strategy helps to connect two different ruthenium fragments (Figure 8.4) in order to lift the degeneracy of electron exchange between two metal centres.
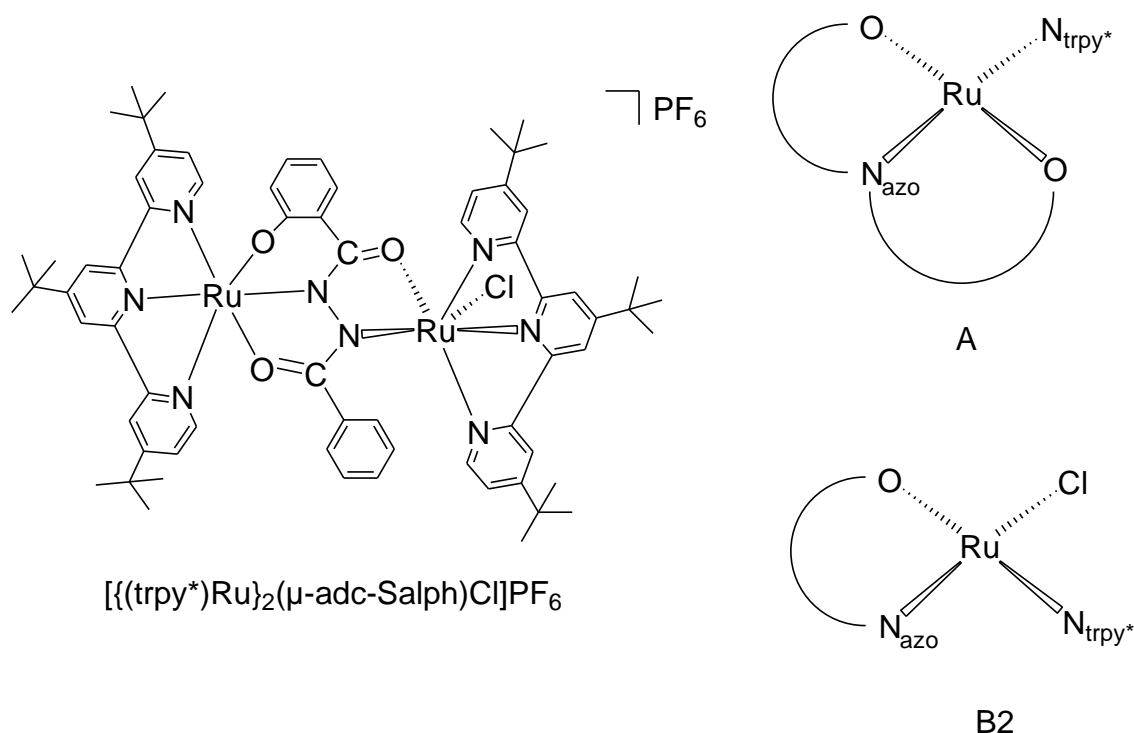
Figure 8.4: Chemical structure of [{(trpy*)Ru(μ-adc-Salph)Ru(trpy*)Cl]PF$_6$ and representation of coordination environments around the metal centres (only equatorial positions) in different molecular halves A and B2.

Interestingly, the complex exhibits similar absorption features in the NIR region (λ_{max} = 1464 nm with $10^{-4}\varepsilon$ = 0.7 M^{-1}cm^{-1}) like symmetric mixed-valence complexes, which have been presented in previous chapters. Such intense NIR activity suggests the presence of strongly coupled metal centres. Relatively higher K$_c$ value ($10^{9.8}$) also reflect the same along with the potential difference between two different metal fragments. The system can be explained by an equilibrium (i) between two mixed-valence isomers I and II.

$$[\{(trpy^*)Ru^{III}(\mu\text{-adc-Salph})Ru^{II}(trpy^*)Cl]^+ \rightleftharpoons [\{(trpy^*)Ru^{II}(\mu\text{-adc-Salph})Ru^{III}(trpy^*)Cl]^+ \quad (i)$$

I   II
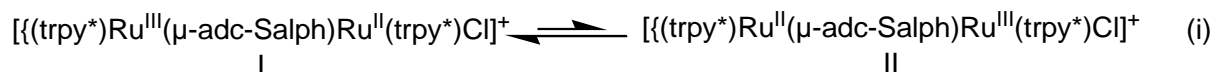
The isolated and structurally characterised complex can be assigned to the energetically more stable conformer (Isomer I) where the Ru^{III} centre is coordinated in a bis(meridional) fashion and the Ru^{II} is coordinated to a chloride ion. In present case, the valence-delocalised description is questionable because even after complete charge transfer there should be a residual charge difference as the coordination environment in two metal fragments is different. By manipulating the coordination environment (e.g. replacing chloride with a stronger π-donating ligand), it should be possible to decrease the energy gap between two isomers to such an extent that both of them can be isolable. Additionally, the N-N bond distance (1.427(6) Å) displays a single bond character, indicating that the ligand is in the fully reduced(3−) form. Accordingly, a highly anisotropic rhombic EPR-signal (Δg = 0.35 at 4.5 K) has been found for the mixed-valent monocation. Noticeably, the Δg value is comparable to that of the previously described symmetric complexes (in Chapters 3 and 4) which indicates similar percentages of metal and ligand contributions to the SOMO.

Chapter 6 describes different binding modes of the bridging ligand adc-Py(2-) (Table 8.1). Interaction of this ligand with $[Ru(trpy^*)]^{2+}$ has produced a symmetric dinuclear complex $[\{(trpy^*)Ru\}_2(\mu,\eta^3:\eta^3\text{-adc-Py})](PF_6)_2$. The one-electron oxidised mixed-valent intermediate exhibits spectroscopic (UV-Vis-NIR, EPR) features similar to the reported diruthenium system with adc-Py(2-) where unsubstituted terpyridine has been used as a terminal ligand.

Another dicationic complex $[\{(bpy)_2Ru\}_2(\mu,\eta^2:\eta^2\text{-adc-Py})](PF_6)_2$ (Figure 8.5) was prepared for which possible *meso* and *rac* isomers could not be separated. From the mixture, a crystalline compound precipitated which was characterised structurally as the *meso* isomer and a bis(N,N') coordination of the bridging ligand has been found. The coordinated bridge is twisted around the N-N bond to produce two orthogonal metal/ligand halves for which the metal-metal communication is assumed to be restricted. The one-electron oxidised form has a high K_c value ($10^{8.3}$) and exhibits moderately intense electronic absorption in the IR region (ν_{max} = 4150 cm^{-1} with ε ≈

5000 M^{-1}cm^{-1}, Figure 8.5). Experimental work is still under progress, targeting the isolation of the oxidised trication, while theoretical calculations are needed to better understand the electronic situations and absorption properties of the redox species involved in [{(bpy)$_2$Ru}$_2$(μ,η^2:η^2-adc-Py)]$^{2+/3+/4+}$.
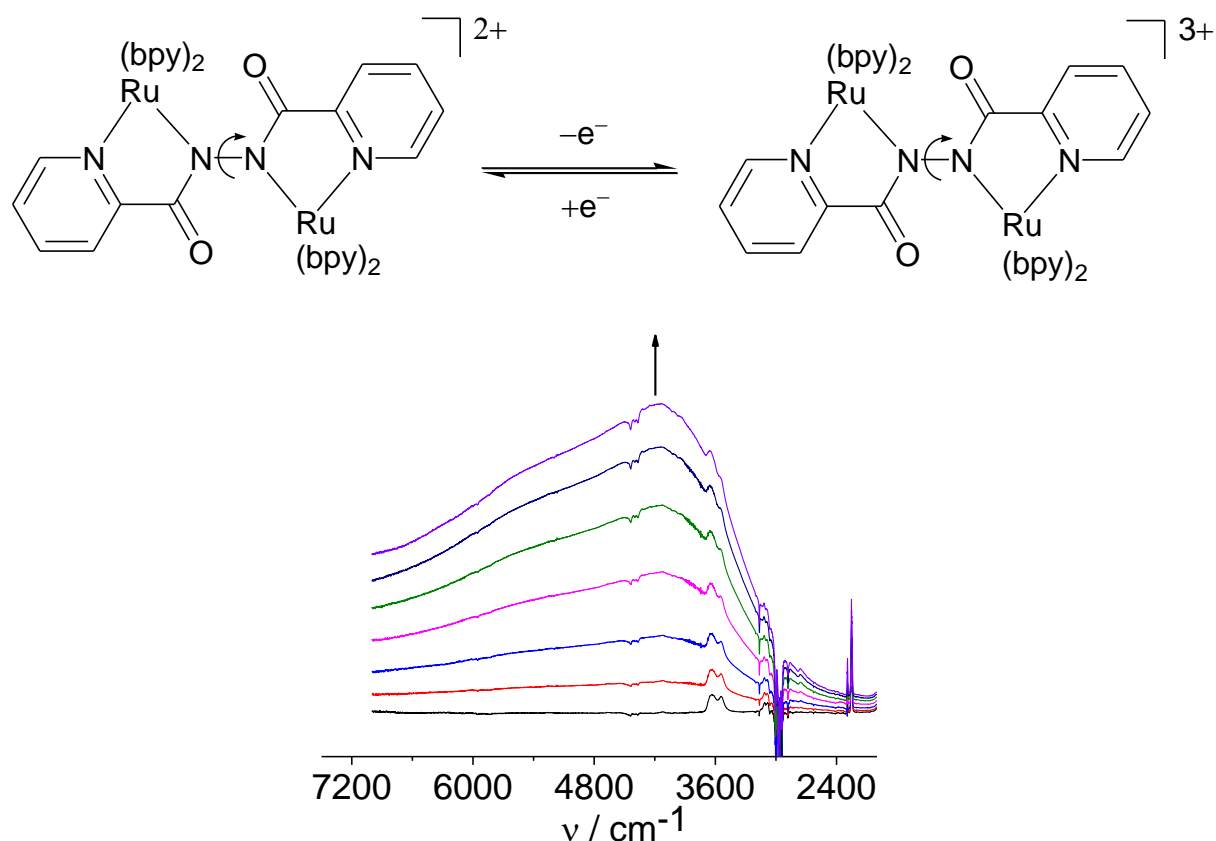
Figure 8.5: IR spectroelectrochemical responses on oxidation of [{(bpy)$_2$Ru}$_2$(μ,η^2:η^2-adc-Py)]$^{2+}$ in CH$_3$CN / 0.1 M Bu$_4$NPF$_6$ at 298 K.

The discussion in Chapter 6 confirms different metal/ligand interaction in the mixed-valent states with bis(tridentate) and bis(bidentate) ligand coordination of adc-Py(2−).

Perspective.

The doctoral work is an extension and thus incudes modification of previously developed[51,69] dinuclear Ru/Os systems with π-donor adc-R(2−) ligands. The work contains structurally characterised mixed-valence systems (Ru^{II}/Ru^{III}) with unusual

meridional coordination mode of the bridging ligand (e.g. $\mu,\eta^3{:}\eta^3$, $\mu,\eta^2{:}\eta^3$). Especially, the $\mu,\eta^3{:}\eta^3$ configuration of π-donating bridges is very rare in the research connecting to the symmetrical mixed valence systems. Most of such bridges have offered cyclometallation as developed[15b-d] by Sauvage and co-workers and further extended[50c-e,94] by Abruña, Zhong and co-workers, whereas we have investigated non-cyclometallated examples. Considering the non-innocent ligand behaviour, unusual structural frame work and distinct multiple NIR absorptions, the investigation with the bis(tridentate) ligand adc-Sal(4-) (Chapter 4) demands further study incorporating congeners of ruthenium such as osmium and iron. In fact, all isolated mixed-valent complexes described in the thesis have produced strong NIR activity, which make them potential candidates in communication technology.[128] In addition to the description of dinuclear systems of adc-R ligands, this thesis reveals variable metal/ligand interactions in mononuclear analogues as well. Especially, the result of the electrochemical investigations for the alkylated or protonated metal/ligand framework (Chapter 2) as well as for the twisted dinuclear complex (Chapter 6) stimulate a broader perspective on research with regard to investigation of chemical and/or structural transformations induced by electron transfer.

Chapter 9

Zusammenfassung.

Seit der Entdeckung des Creutz-Taube-Ions $[(NH_3)_5Ru(pyz)Ru(NH_3)_5]^{5+}$ im Jahr 1967 ist intramolekularer Elektronentransfer in gemischtvalenten Dirutheniumkomplexen mit low-spin d^5/d^6-Konfiguration und einem organischen Brückenliganden von Interesse.[11,12] Untersuchungen an verschiedenen verwandten Komplexen mit redoxaktiven ("nicht-unschuldigen") Brückenliganden zeigten elektronisch interessantes Verhalten und beeindruckende Redoxeigenschaften. In dieser Arbeit werden die nicht-unschuldigen und damit elektronenübertragenden Eigenschaften von Azodicarbonyl/hydrazido-Liganden (adc-R$^{0/\cdot-/2-}$) in Metall/Ligand- oder Metall/Ligand/Metall-Einheiten unter Verwendung struktureller Informationen (z.B. Bindungslängen d_{N-N}), spektroelektrochemischer (UV-Vis-NIR, IR, EPR) Eigenschaften sowie Ergebnissen aus DFT-Berechnungen untersucht. Drs. V. Filippou und S. Záliš führten die theoretischen Berechnungen durch. Für die Untersuchungen wurden die in Tabelle 8.1 aufgeführten Hydrazine in ihrer deprotonierten Form zur Darstellung der verschiedenen ein- und zweikernigen Komplexe verwendet.

Tabelle 8.1: Zur Darstellung benutzte Hydrazine.

R_1 \ R_2	CF_3	$C(CH_3)_3$	C_6H_5	C_6H_4OH	C_6H_5N
CF_3	H_2adc-CF_3				
$C(CH_3)_3$		H_2adc-^{t}Bu			
C_6H_5			H_2adc-Ph	H_3adc-Salph	
C_6H_4OH				H_4adc-Sal	
C_6H_5N					H_2adc-Py

In **Kapitel 2** wurden einkernige Komplexe mit adc-^{t}Bu (adc-R, R = C(CH$_3$)$_3$) Liganden untersucht. Zwei einfach positiv geladene Komplexe wurden als Zwischenprodukte in den Zweistufen-Redoxsystemen [M(bpy)$_2$(adc-^{t}Bu)]$^{0/+/2+}$ (M = Ru, Os) isoliert und charakterisiert. Die strukturelle Charakterisierung beider Monokationen (M = Ru mit ClO$_4^-$ und M = Os mit PF$_6^-$ als Gegenanionen; Abb. 8.1) zeigt aufgrund der Mischung von Metall- und Ligandorbitalen keine signifikanten Unterschiede. Die N1-N2-Bindungslängen (1.39 ± 0.01 Å) weisen auf einen Zustand zwischen den vollständig oxidierten (0) und den reduzierten (2−) des Redoxzuständen des Liganden hin.
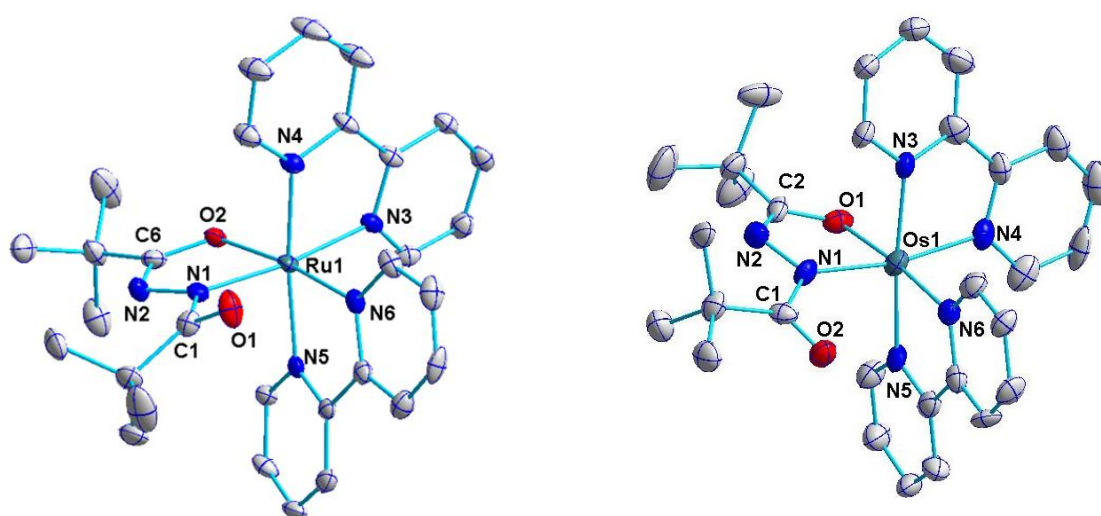
Abbildung 8.1: Molekülstrukturen der Kationen in den Kristallen von [Ru(bpy)$_2$(adc-^{t}Bu)]ClO$_4$ (links) und [Os(bpy)$_2$(adc-^{t}Bu)]PF$_6$ (rechts).

Diese Systeme können am besten durch Resonanzhybride zweier elektronischer Strukturen M^{II}(bpy)$_2$(adc-^{t}Bu)$^{\bullet-}$ ↔ M^{III}(bpy)$_2$(adc-^{t}Bu)$^{2-}$ beschrieben werden. In den meisten Fällen kann die ESR-Spektroskopie wichtige Informationen zur Bestimmung der vorherrschenden elektronischen Konfiguration liefern; im vorliegenden Fall deutet ein isotropes Signal (g = 2.027, at 298 K) für M = Ru auf die erste Formulierung mit zweiwertigem Ru hin, während ein rhombisches Signal (Δg = 1.104, at 5 K) für M = Os eher auf dreiwertiges Os schließen lässt. DFT-Berechnungen unterstützen diese Ergebnisse, indem sie eine zunehmende Spindichte auf dem Osmiumzentrum (46 vs. 29 % für M = Ru) vorhersagen. Die Absorptionsspektren dieser Spezies im Sichtbaren sowie im NIR-Bereich sind ebenfalls durch diese starke Orbitalmischung beeinflusst, die Kationen zeigen Absorptionsbanden entsprechend beider

elektronischen Strukturen. Die beobachteten Redoxprozesse $[M(bpy)_2(adc\text{-}{}^tBu)]^{0/+/2+}$ (M = Ru, Os) waren reversibel, auch sie involvierten sowohl Metall- als auch Ligandorbitale; im IR-Spektrum kann dies anhand der Frequenz der Streckschwingung der unkoordinierten C=O-Bindung gezeigt werden. Ausgehend von der reduzierten (0) Form verschiebt sich die Frequenz mit jedem Redoxprozess etwa 90 bzw. 120 cm^{-1} zu höherer Energie. Noch bedeutender ist jedoch, dass der K_c-Wert der (+)-Zwischenstufe im Fall des Osmiums kleiner ist ($10^{12.9}$ vs. $10^{14.6}$ für Ru), was auf eine vergleichsweise geringere Mischung der Metall/Ligandorbitale hindeutet.

Kapitel 2 beschreibt zwei weitere einfach positive geladene Rutheniumkomplexe mit dem adc-${}^tBu(2-)$-Liganden in seiner einfach protonierten Hadc-${}^tBu(1-)$ sowie der methylierten $CH_3adc\text{-}{}^tBu(1-)$-Form. Die Komplexe $[M(bpy)_2(Radc\text{-}{}^tBu)]PF_6$ (R= H, CH_3) wurden durch ^{1}H-NMR-Spektroskopie charakterisiert mit jeweils eindeutigen N-H- und $N\text{-}CH_3$-Signalen. Der protonierte Komplex zeigt irreversibles Redoxverhalten in CH_3CN mit zwei oxidativen Prozessen in der Differential-Puls-Voltammetrie. Spektroelektrochemische (UV-Vis und IR) Messungen legen die Bildung eines deprotonierten Dikations ($[M(bpy)_2(adc\text{-}{}^tBu)]^{2+}$) nach der zweiten Oxidation nahe. Die methylierte Verbindung hingegen zeigt eine metallzentrierte reversible Einelektronen-Oxidation, was durch eine geringe Verschiebung (1533 to 1562 cm^{-1}) der Frequenz der Streckschwingung des unkoordinierten C=O und durch eine per DFT-Rechnung ermittelte Spindichte von 51 % am Metallzentrum bestätigt wird. Das parallele Redoxschema (Schema 8.1) für die Ru/Os-Redoxreihe konnte dementsprechend aufgestellt werden.

<u>charge</u>   <u>charge</u>

2+ $M^{III}(L^{\bullet-})$ ⟷ $M^{II}(L^0)$

                        $-e^-$ ⇅ $+e^-$

+ $M^{II}(L^{\bullet-})$ ⟷ $M^{III}(L^{2-})$ $M^{III}(RL^-)$ ⟷ $M^{II}(RL^{\bullet})$ 2+
           M = Ru   M = Os

                        $-e^-$ ⇅ $+e^-$ $+e^-$ $-e^-$ ⇅ $+e^-$
                                                 $+R^+$
                                                 $-e^-$
0          $M^{II}(L^{2-})$ $-R^+$ $M^{II}(RL^-)$ +

                                                          M = Ru
                                                          R = H, CH$_3$
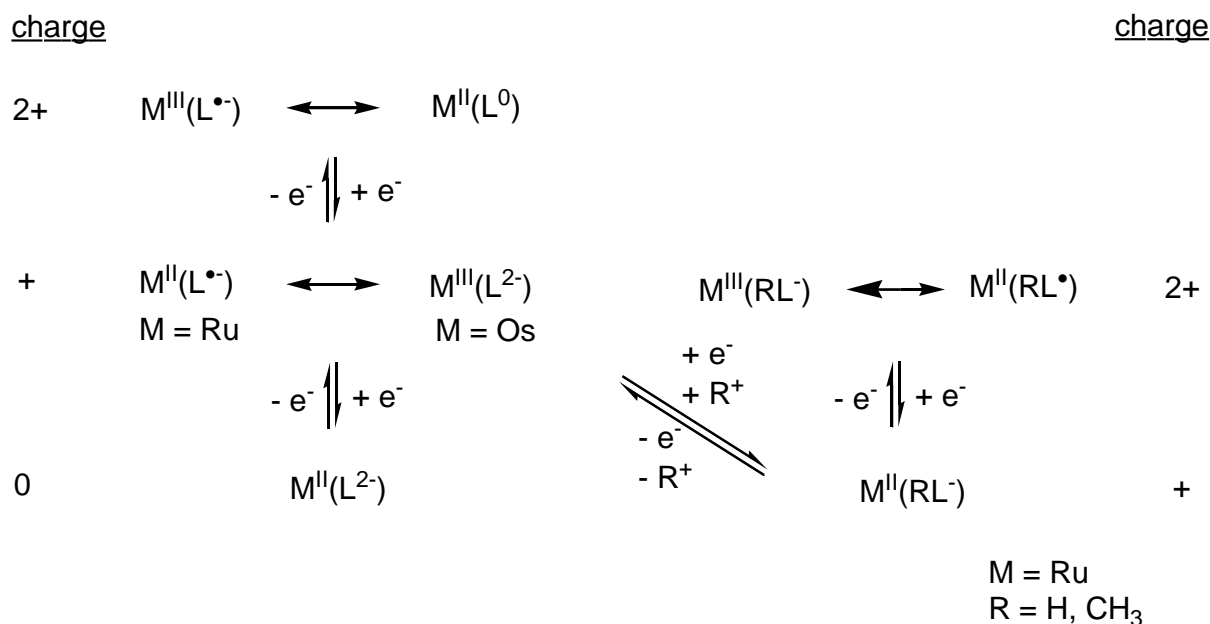
Schema 8.1: Redoxschema für verschiedene einfach positive geladene Komplexe ([M(bpy)$_2$(RL)]$^+$, L = adc-^{t}Bu) mit den postulierten Metall/Ligand-Elektronenverteilungen.

Kapitel 3 beschreibt zweikernige Komplexes in denen zwei [Ru(trpy*)Cl]$^{n+}$ (trpy* = 4,4′,4″-tri-*tert*-butyl-2,2′:6′,2″-Terpyridin) Zentren mit bis-bidentaten verbrückenden Liganden, adc-Ph(2−) (Ph = C$_6$H$_5$) und adc-CF$_3$(2−) wechselwirken. Die Komplexe gehören zu einem Zweistufen-Redoxsystem ([{(trpy*)ClRu}$_2$(μ-adc-R)]$^{0/+/2+}$, R = Ph, CF$_3$) mit einer stabilen gemischtvalenten (Ru^{II}/Ru^{III}) Zwischenstufe (K$_c$ ≈ 10$^{8.5}$). Beide gemischtvalenten Monokationen weisen charakteristische Inter-valenz-Charge-Transfer- (IVCT) Banden im NIR-Bereich (λ$_{max}$ zwischen 1500 und 1600 nm) auf, welche in der Einelektronenreduzierten (0) oder der vollständig oxidierten (2+) Form nicht auftreten. Die hohe Intensität (ε ≈ 10000 M^{-1}cm^{-1}) und die geringe Bandbreite (< 2000 cm^{-1}) dieser Absorptionen sowie der hohe K$_c$-Wert der gemischtvalenten Zwischenstufe legen eine Valenz-delokalisierte Formulierung (Ru$^{2.5}$/Ru$^{2.5}$) nahe. Die strukturelle Charakterisierung (Abb 8.2, R = Ph) bestätigt diese delokalisierte Formulierung ebenfalls mit ähnlichen Ru-N-Abständen (Ru2-N2 = 2.057(3) Å, Ru1-N1 = 2.051(3) Å) entlang der Brücke.

Die Strukturen des gemischtvalenten Monokations (R = Ph) sowie der neutralen Spezies (R = CF₃) zeigen eine verzerrte bzw. eine planare M-L-M-Geometrie, während die Koordination um das Metallzentrum bei beiden eine *trans*-Konfirmation aufweist. Die Bindungsparameter zeigen die erwarteten Unterschiede, die in den unterschiedlichen Ladungen der Spezies begründet sind. Wichtig ist weiterhin, dass in beiden Fällen die N-N-Bindungslängen (>1.40 Å) auf die Hydrazido(2−)− und nicht die radikalische (•−) Form des verbrückenden Liganden hindeuten.
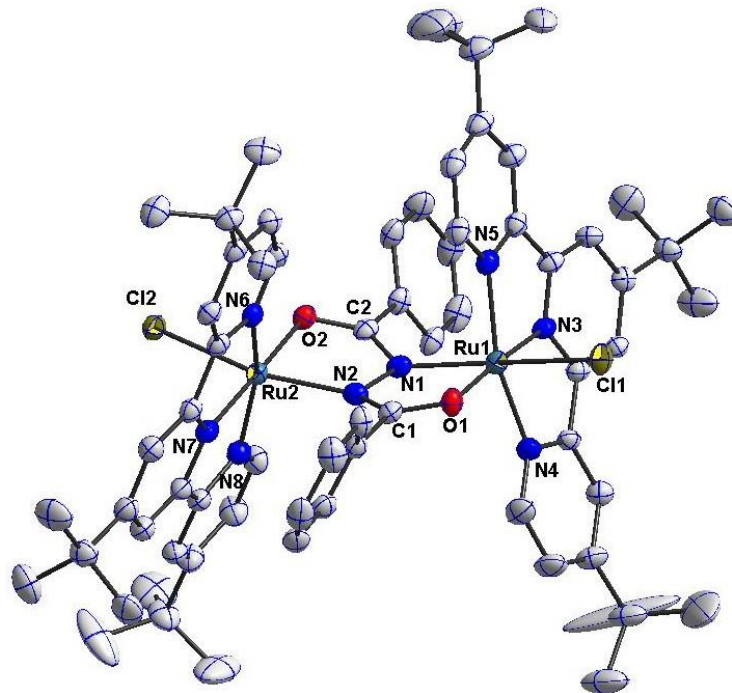
Abbildung 8.2: Molekülstruktur des Kations im Kristall von [{(trpy*)ClRu}₂(μ-adc-Ph)] PF₆ mit einer verzerrten Metall-Ligand-Metall-Geometrie. Torsionswinkel: C1-N2-N1-C2 = −160.1(3)°, Ru1-N1-N2-Ru2 = 163.15(14)°.

Kapitel 4 beschreibt einen Dirutheniumkomplex, in dem zwei [Ru(trpy*)]ⁿ⁺-Zentren mit einem bis-tridentaten Brückenliganden, adc-Sal(4-), wechselwirken (Tabelle 8.1). Der Komplex [(trpy*)Ru(μ-adc-Sal)Ru(trpy*)]PF₆ wurde strukturell, elektrochemisch und spektroskopisch als eine Zwischenstufe (Ruᴵᴵ(μ-adc-Sal)⁴⁻Ruᴵᴵᴵ) des dreistufigen Redoxsystems [(trpy*)Ru(μ-adc-Sal)Ru(trpy*)]⁰/⁺¹/⁺²/⁺³ identifiziert. Die strukturelle Charakterisierung (Abbildung 8.3) gibt einen mittleren Wert für die N1-N2-Bindungslänge (1.392 Å), so wie es auch für den einkernigen Komplex [Ru(bpy)₂(adc-ᵗBu)]ClO₄ gefunden wurde. Weiterhin wurden ähnliche Ru-N-Abstände (1.990(4) Å) innerhalb der M-L-M-Brücke gefunden. Der Komplex zeigt eine breite

asymmetrische Absorptionsbande in der NIR-Region, die unter der Annahme einer Lorentz-Linienform in drei Banden bei λ_{max} = 2140, 1645 und 1485 nm mit $10^{-4}\varepsilon$ = 0.1, 0.7 bzw. 0.5 $M^{-1}cm^{-1}$ zerlegt werden konnte. Die N1-N2-Bindungslänge, die intensiven multiplen Absorptionsbanden, ESR-Daten (Δg = 0.45) und DFT-berechnete Spindichten (0.31 auf jedem Ru und 0.35 auf dem Brückenliganden) weisen auf starke Orbital-Wechselwirkungen auf dem Brückenliganden mit beiden Metallzentren hin. Dies kann so weit gehen, dass der Spin gleichmäßig auf Brückenligand und den Metallzentren verteilt ist.. Weiterhin belegen diese Ergebnisse eindeutig die nicht-unschuldige Natur des Brückenliganden und seine Fähigkeit, elektronische Wechselwirkungen zwischen den zwei Metallzentren zu vermitteln. Der Komplex kann daher als ein Resonanzhybrid, $[Ru^{2.5}(adc\text{-}Sal)^{4-}Ru^{2.5}]^+$ $\leftrightarrow [Ru^{II}(adc\text{-}Sal)^{3\bullet-}Ru^{II}]^+$ dargestellt werden.
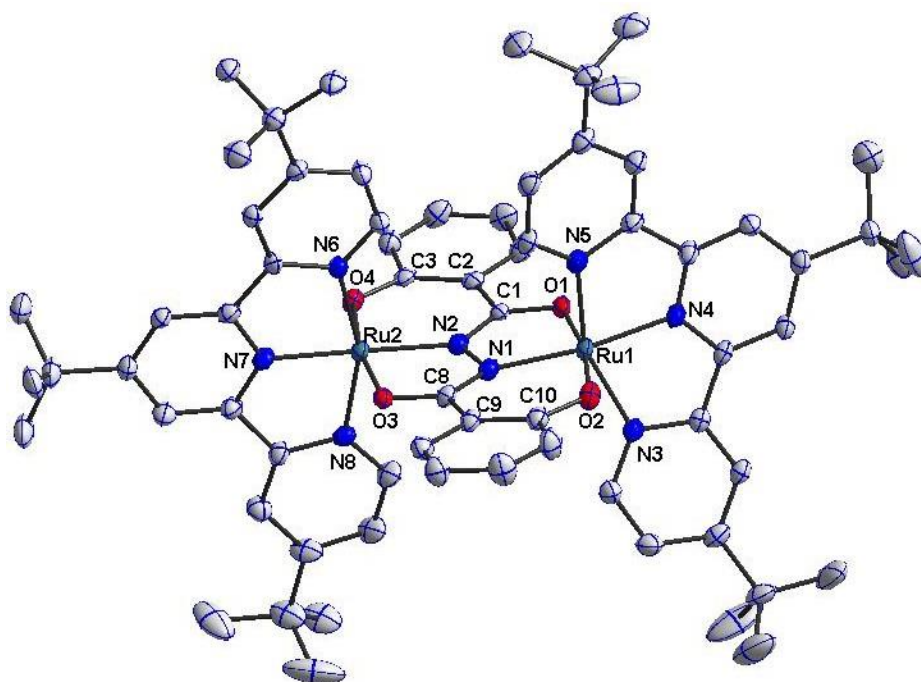
Abbildung 8.3: Molekülstruktur des Kations im KrIstall von [{(trpy*)Ru}$_2$(µ-adc-Sal)] PF$_6$.

Kapitel 5 erweitert die Diskussion über symmetrische gemischtvalente Komplexe in den Kapiteln 3 und 4 um den asymmetrischen Komplex, [{(trpy*)Ru(µ-adc-Salph)Ru(trpy*)Cl]PF$_6$. Hierbei wird die kleine bis-bidentate organische Brücke (O=C-N-N-C=O) des adc-R(2−)-Liganden mit einem potentiell koordinierenden Arm (C$_6$H$_4$O$^-$) zu dem unsymmetrischen Liganden adc-Salph(3−) verbunden (Tabelle 8.1).

Durch diese Strategie können zwei unterschiedliche Rutheniumfragmente (Abbildung 8.4) verknüpft und so die Entartung des Elektronenaustauschs zwischen den Metallzentren aufgehoben werden.
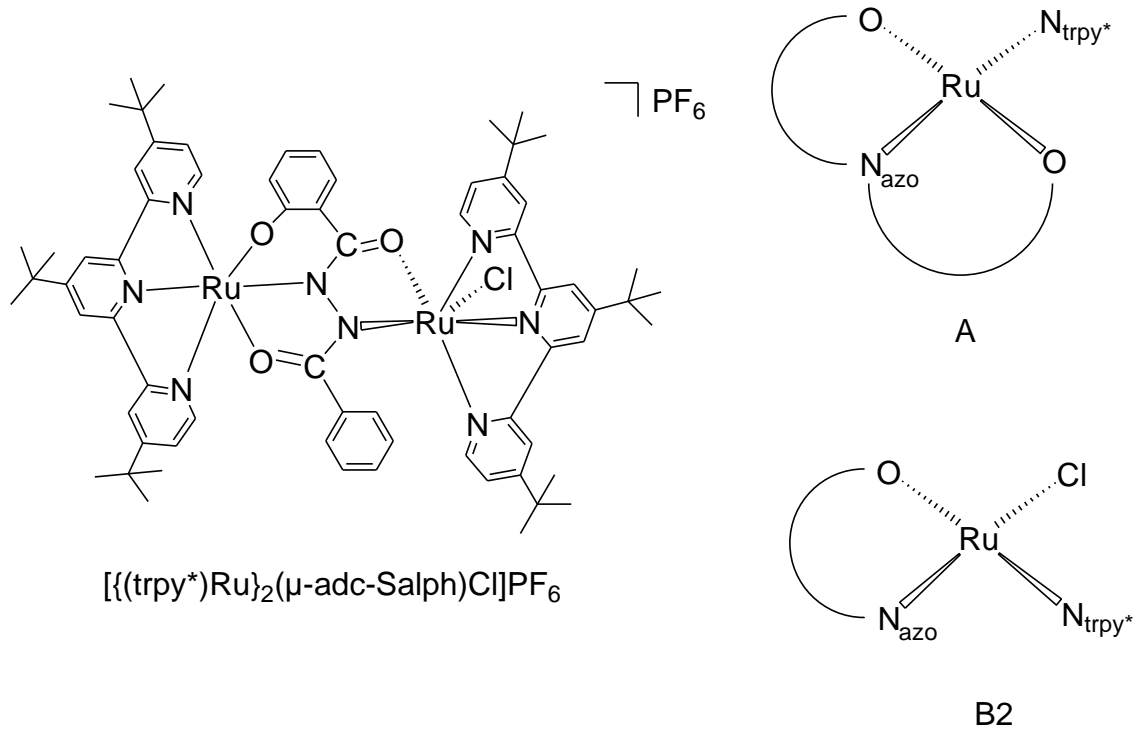
Abbildung 8.4: Chemische Struktur von [{(trpy*)Ru(μ-adc-Salph)Ru(trpy*)Cl]PF$_6$ und Darstellung der Koordinationumgebung der Metallzentren (nur equatoriale Positionen) in den unterschiedlichen Molekülhälften A und B2.

Interessanterweise zeigt dieser Komplex ähnliche Absorptionsbanden in der NIR-Region (λ_{max} = 1464 nm mit $10^{-4}\varepsilon$ = 0.7 M^{-1}cm^{-1}) wie die symmetrischen gemischtvalenten Komplexe, die in den vorangegangenen Kapiteln vorgestellt wurden. Solche intensive NIR-Aktivität legt die Anwesenheit stark gekoppelter Metallzentren nahe. Relativ hohe K$_c$-Werte ($10^{9.8}$) sowie the Potentialdifferenz zwischen zwei unterschiedlichen Metallfragmenten weisen ebenfalls darauf hin. Das System kann durch ein Gleichgewicht (i) zwischen zwei gemischtvalenten Isomeren I und II beschrieben werden.

$$[\{(trpy^*)Ru^{III}(\mu\text{-adc-Salph})Ru^{II}(trpy^*)Cl]^+ \rightleftharpoons [\{(trpy^*)Ru^{II}(\mu\text{-adc-Salph})Ru^{III}(trpy^*)Cl]^+ \quad (i)$$

I   II
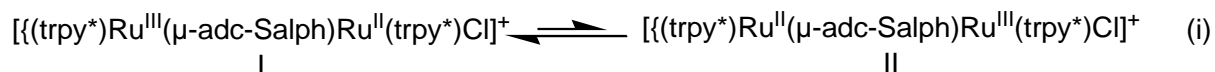
Der isolierte und strukturell charakterisierte Komplex kann dem energetisch stabileren Konformer (Isomer I) zugeordnet werden, in dem das Ru^{III}-Zentrum bis-meridional und das Ru^{II} an ein Chloridion gebunden ist. Im vorliegenden Fall ist die valenzdelokalisierte Beschreibung fragwürdig, weil sogar nach vollständigem Ladungstransfer eine Restdifferenz an Ladungsdichte vorhanden sein sollte, da die Koordinationumgebung in den Metallfragmenten unterschiedlich ist. Durch Manipulation der Koordinationsumgebung (z.B. Ersatz von Chlorid durch einen stärkeren π-Donor-Liganden) sollte es möglich sein, die Energiedifferenz zwischen den beiden Isomeren so zu verändern, dass beide isoliert werden können. Die N-N-Bindungslänge (1.427(6) Å) zeigt Einzelbindungscharakter, d.h., der Ligand liegt in der vollständig reduzierten(3−) Form vor. In Übereinstimmung damit wurde ein stark anisotropes rhombisches ESR-Signal ($\Delta g = 0.35$ bei 4.5 K) für das gemischtvalente Monokation gefunden. Der Δg-Wert ist vergleichbar mit dem des vorher beschriebenen symmetrischen Komplexes (in Kapitel 3 und 4), was auf ein ähnliches Verhältnis der Metall- und Ligand-Beiträge zum SOMO schließen lässt.

Kapitel 6 beschreibt unterschiedliche Bindungstypen des Brückenliganden adc-Py(2-) (Tabelle 8.1). Wechselwirkung dieses Liganden mit [Ru(trpy*)]$^{2+}$ führte zu einem symmetrischen zweikernigen Komplex [{(trpy*)Ru}$_2$($\mu,\eta^3{:}\eta^3$-adc-Py)](PF$_6$)$_2$. Die Einelektronen-oxidiierte gemischtvalente Zwischenstufe zeigt spektroskopisches Verhalten (UV-Vis-NIR, ESR) ähnlich dem der beschriebenen Dirutheniumsysteme mit adc-Py(2-), in denen unsubstituiertes Terpyridin asl terminaler Ligand benutzt wurde.

Ein weiterer dikationischer Komplex [{(bpy)$_2$Ru}$_2$($\mu,\eta^2{:}\eta^2$-adc-Py)](PF$_6$)$_2$ (Abbildung 8.5) wurde dargestellt, jedoch konnten hier *meso*- und *rac*-Isomere nicht getrennt werden. Aus einer Mischung wurden Kristalle erhalten, die als das *meso*-Isomer strukturell charakterisiert werden konnten, wobei eine bis(N,N')-Koordination des Brückenliganden gefunden wurde. Die koordinierte Brücke ist entlang der N-N-Bindung verdreht und führt so zu zwei orthogonalen Metall/Ligand- Hälften, für die eine Metall-Metall-Kommunikation vermutlich beschränkt ist. Die Einelektronen-

oxidierte Form hat einen hohen K_c-Wert ($10^{8.3}$) und zeigt moderat intensive Absorptionen in der IR-Region (ν_{max} = 4150 cm^{-1} mit $\varepsilon \approx$ 5000 M^{-1}cm^{-1}, Abbildung 8.5). Weitere Experimente zur Isolierung des oxidierten Trikations stehen noch aus, und es werden theoretische Berechnungen benötigt, um die elektronische Situation und die Absorptionseigenschaften der beteiligten Redoxspezies [{(bpy)$_2$Ru}$_2$(μ,η^2:η^2-adc-Py)]$^{2+/3+/4+}$zu erklären.
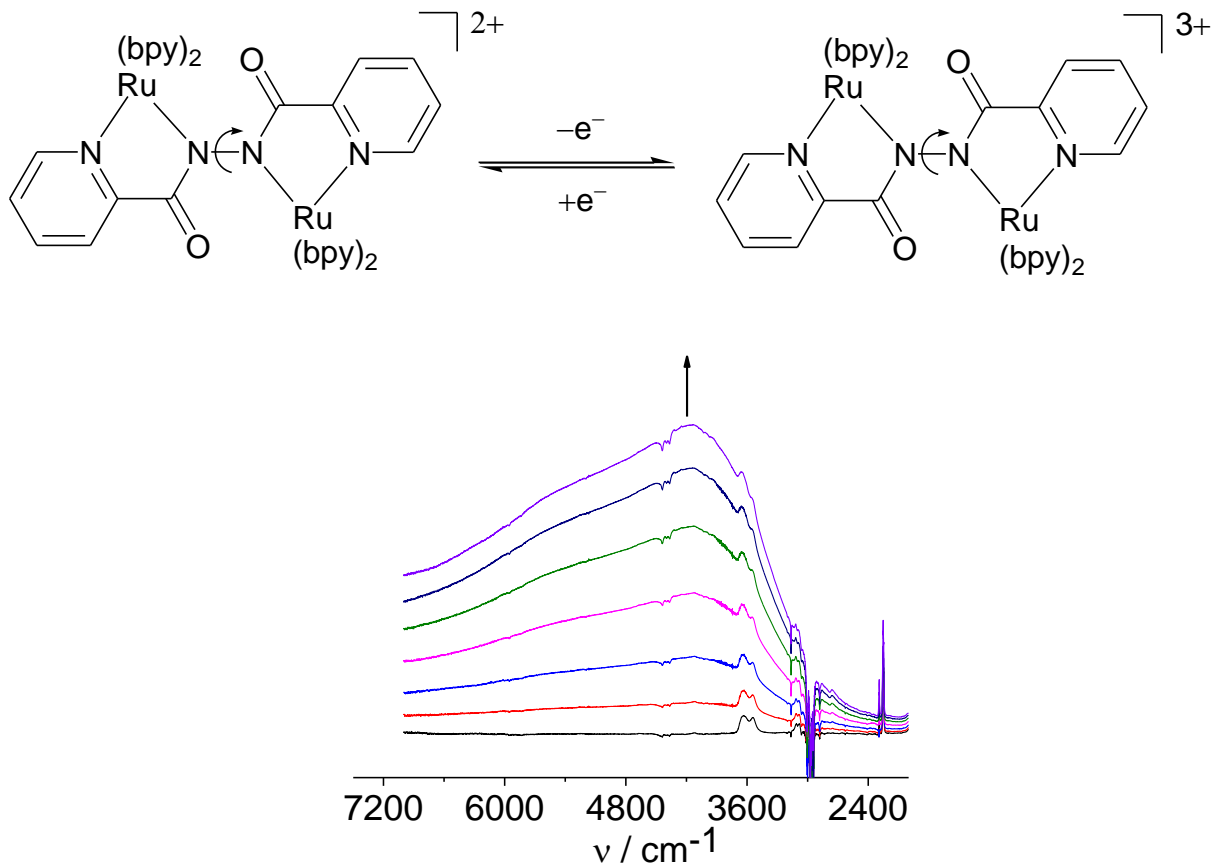
Abbildung 8.5: IR-spektroelektrochemisches Verhalten nach Oxidation von [{(bpy)$_2$Ru}$_2$(μ,η^2:η^2-adc-Py)]$^{2+}$ in CH$_3$CN / 0.1 M Bu$_4$NPF$_6$ bei 298 K.

Die Diskussion in Kapitel 6 bestätigt unterschiedliche Metall/Ligand-Wechselwirkungen in den gemischtvalenten Zuständen mit bis-tridentater oder bis-bidentater Ligandenkoordination von adc-Py(2−).

Ausblick.

Diese Doktorarbeit ist eine Erweiterung und Modifikation der Arbeiten über bereits entwickelte[51,69] zweikernige Ru/Os-Systeme mit π-Donor adc-R(2−)-Liganden. Die Arbeit beschreibt strukturell charakterisierte gemischtvalente Systeme (Ru^{II}/Ru^{III}) mit einem ungewöhnlichen meridionalen Koordinationsmodus des Brückenliganden (z.B. $\mu,\eta^3:\eta^3$, $\mu,\eta^2:\eta^3$). Insbesondere die $\mu,\eta^3:\eta^3$−Konfiguration von π-Donor-Brücken ist innerhalb des Forschungsgebiets über symmetrische gemischtvalente Systeme sehr selten. Die meisten dieser Brücken zeigen Zyklometallalierung, wie von Sauvage und Mitarbeitern entdeckt[15b-d] und von Abruña, Zhong und Mitarbeitern erweitert[50c-e,94]; in dieser Arbeit werden jedoch nicht-zyklometallierte Beispiele beschrieben. Betrachtet man das nicht-unschuldige Ligandverhalten, den ungewöhnlichen strukturellen Rahmen und die unterscheidbaren multiplen NIR-Absorptionen, so muss man zu dem Schluss kommen, dass weitere Untersuchungen u.a. mit den bis-tridentaten Liganden adc-Sal(4-) (Kapitel 4) mit den Homologen des Rutheniums, also Osmium und Eisen, von großem Interesse sind. Tatsächlich zeigen alle gemischtvalenten Komplexe, die in dieser Arbeit beschrieben wurden, starke NIR-Aktivität, was sie zu interessanten Kandidaten in der Kommunikationstechnologie macht.[128] Zusätzlich zur Beschreibung zweikerniger Komplexe mit adc-Liganden zeigt diese Arbeit auch variable Ligand/Metall-Wechselwirkungen in ihren einkernigen Analogen. Insbesondere die Ergebnisse der elektrochemischen Untersuchungen des alkylierten bzw. protonierten Metall/Ligand-Gerüsts (Kapitel 2) sowie des verdrehten zweikernigen Komplexes (Kapitel 6) liefern eine weite Perspektive bezüglich der Untersuchung chemischer und/oder struktureller Umwandlungen, die durch Elektronentransfer induziert werden.

10 Appendix

10.1 DFT and TD-DFT calcuted results

10.1.1 DFT calculated shapes of frontier MOs involved in the excitations, listed in Table 2.7.1 and 2.7.2:

αLUMO   αLUMO+1

SOMO   αHOMO-1   αHOMO-2
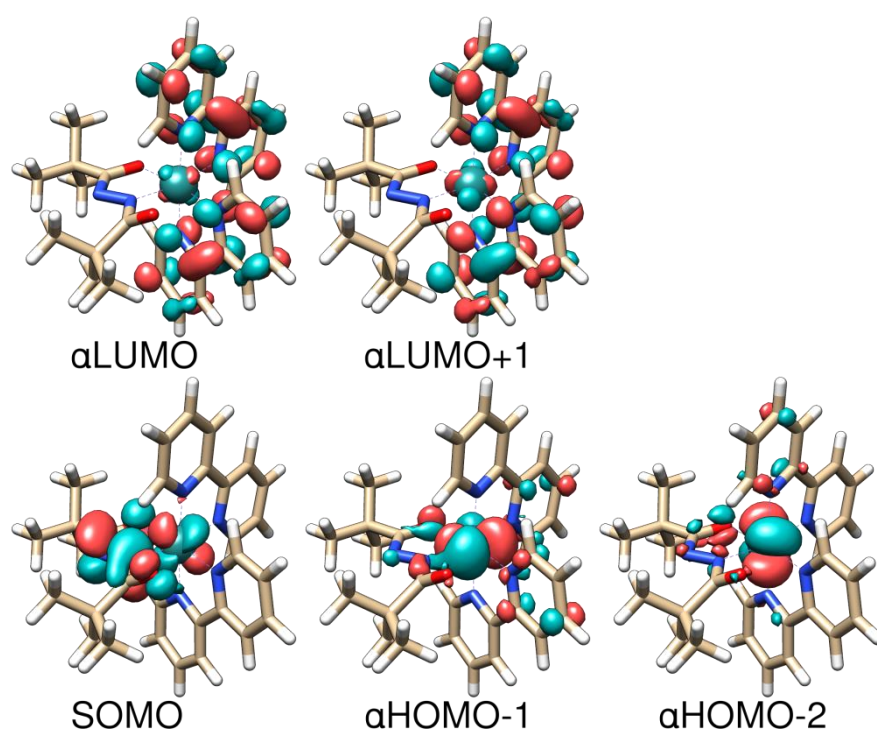
Figure 10.A1: The representation of frontier α-spin orbitals of [Ru(bpy)$_2$(adc-^{t}Bu)]]$^+$.

βLUMO   βLUMO+1   βLUMO+2
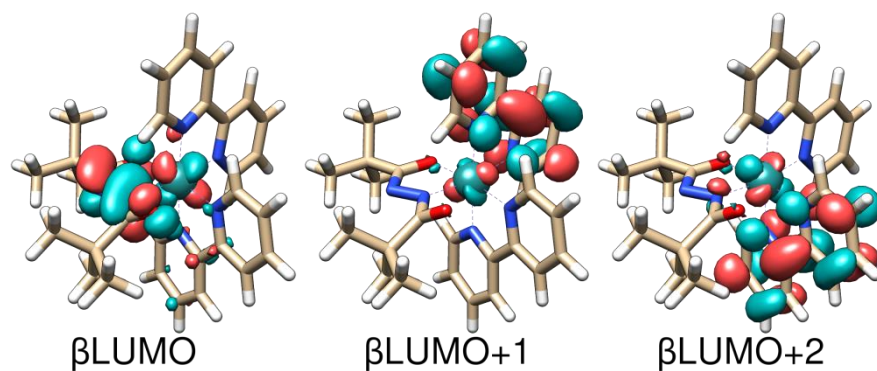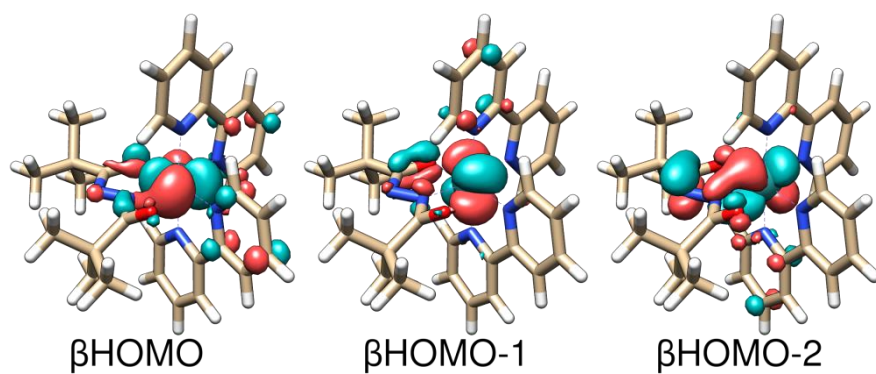
Figure 10.A2: The representation of frontier β-spin orbitals of [Ru(bpy)₂(adc-ᵗBu)]]⁺.
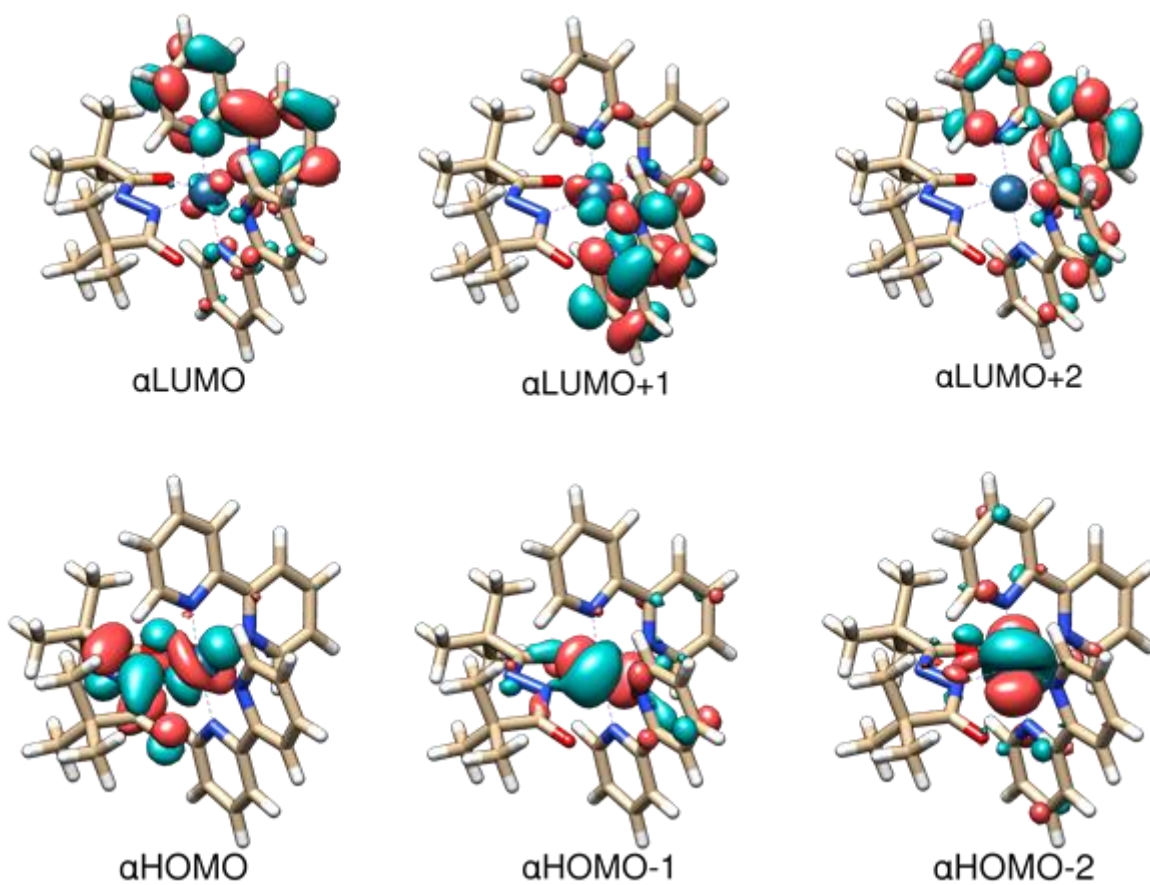
Figure 10.A3: The representation of frontier α-spin orbitals of [Os(bpy)₂(adc-ᵗBu)]]⁺.
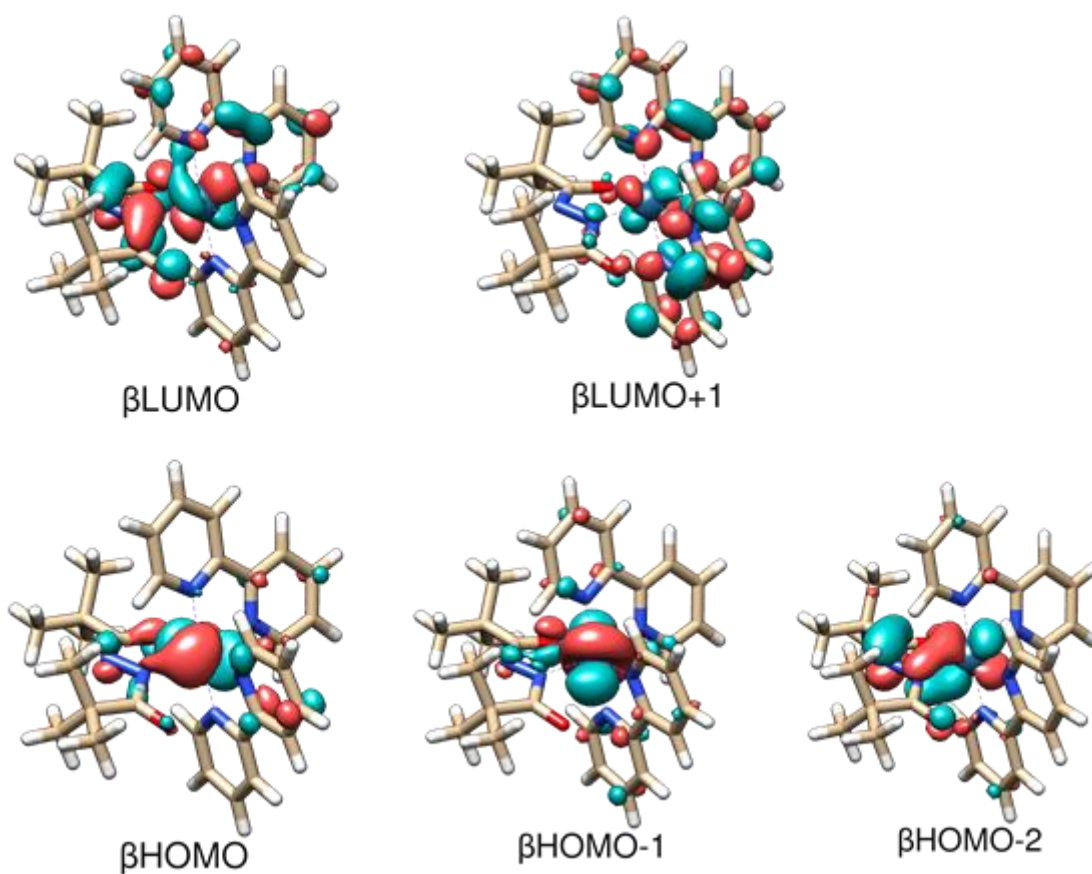
Figure 10.A4: The representation of frontier β-spin orbitals of [Os(bpy)₂(adc-ᵗBu)]]⁺.

10.1.2 DFT and TD-DFT calculated results corresponding to the data listed in Table 4.6.2:

Table 10.A1: TD-DFT (PBE0/PCM-CH$_2$Cl$_2$) calculated lowest singlet excitation energies (eV) for [(trpy')Ru(μ-adc-Sal)Ru(trpy')]$^{n+}$ with oscillator strengths larger than 0.005. Selected MOs involved in excitations are depicted in Figures 10.A6 and 10.A7.

n	state	main contributing excitations [%]	transition energy[a] [eV (nm)]	oscill. strength	expt. absorption (nm)	molar absorption coefficient [10^4 M^{-1}cm^{-1}]
	b^{1}A	47 (HOMO-1 $\rightarrow$ LUMO)	1.65 (750)	0.033	798	sh
		47 (HOMO-2 $\rightarrow$ LUMO+3)				
	c^{1}A	42 (HOMO-3 $\rightarrow$ LUMO+1)	2.17 (571)	0.112		
		23 (HOMO-3 $\rightarrow$ LUMO)				
					605	2.1
0	d^{1}A	mixed	2.28 (543)	0.219		
	e^{1}A	63 (HOMO $\rightarrow$ LUMO+3)	2.37 (524)	0.074		
		14 (HOMO $\rightarrow$ LUMO+2)				
	f^{1}A	63 (HOMO-1 $\rightarrow$ LUMO+5)	2.99 (414)	0.130	439	2.4
	g^{1}A	63 (HOMO-1 $\rightarrow$ LUMO+6)	3.00 (413)	0.138		
	b^{2}A	44 (βHOMO-1 $\rightarrow$ βLUMO)	0.57 (2156)	0.027	2140	0.1
		46 (βHOMO-2 $\rightarrow$ βLUMO)				
		8 (βHOMO-5 $\rightarrow$ βLUMO)				
	c^{2}A	51 (βHOMO-1 $\rightarrow$ βLUMO)	0.78 (1580)	0.181	1645	0.7
		45 (βHOMO-2 $\rightarrow$ βLUMO)				
	d^{2}A	97 (βHOMO-4 $\rightarrow$ βLUMO)	0.90 (1373)	0.003	1485	0.5
	e^{2}A	88 (βHOMO-5 $\rightarrow$ βLUMO)	1.73 (715)	0.013		

1	f^{2}A	65 (αHOMO $\rightarrow$ αLUMO)	1.94 (638)	0.015		
	g^{2}A	76 (αHOMO-1 $\rightarrow$ αLUMO)	2.19 (567)	0.012		
	h^{2}A	mixed	2.56 (484)	0.178	541	1.6
	b^{3}A	73(βHOMO $\rightarrow$ βLUMO)	1.28 (961)	0.007	926	sh
	c^{3}A	57(βHOMO-1 $\rightarrow$ βLUMO+1)	1.57 (791	0.120		
	d^{3}A	54(βHOMO-3 $\rightarrow$ βLUMO)	1.41 (741)	0.073	717	0.6
2	e^{3}A	mixed	1.77 (702)	0.067		
	f^{3}A	53(βHOMO-6 $\rightarrow$ βLUMO)	2.66 (467)	0.036	449	sh
	g^{3}A	46(βHOMO-6 $\rightarrow$ βLUMO+1)	2.68 (463)	0.014		
	h^{3}A	43 (αHOMO $\rightarrow$ αLUMO+4)	2.92 (423)	0.034		
	i^{3}A	54(βHOMO-2 $\rightarrow$ βLUMO+5)	2.93 (423)	0.012		
	j^{3}A	mixed	2.98 (415)	0.035	406	1.4
	k^{3}A	mixed	3.03 (409)	0.026		
	l^{3}A	45 (αHOMO-1 $\rightarrow$ αLUMO+2)	3.05 (406)	0.070		
	b^{2}A	mixed	0.85 (1453)	0.018		
	c^{2}A	63(βHOMO $\rightarrow$ βLUMO)	1.02 (1216)	0.030		
	d^{2}A	40(βHOMO-2 $\rightarrow$ βLUMO)	1.16 (1067)	0.092	983	sh
		38(βHOMO-1 $\rightarrow$ βLUMO)				
	e^{2}A	mixed	1.62 (765)	0.182	777	1.1
3	f^{2}A	61(βHOMO $\rightarrow$ βLUMO+1)	1.68 (738)	0.044		
	g^{2}A	53 (αHOMO-2 $\rightarrow$ αLUMO)	2.03 (612)	0.050		
	h^{2}A	46(βHOMO-5 $\rightarrow$ βLUMO)	2.09 (592)	0.036		
	i^{2}A	mixed	2.37 (523)	0.021		
	j^{2}A	mixed	2.40 (516)	0.021		
	k^{2}A	64(βHOMO-9 $\rightarrow$ βLUMO)	2.51 (493)	0.030		
	l^{2}A	mixed	2.55 (486)	0.016	437	1.3
	m^{2}A	70(βHOMO-8 $\rightarrow$ βLUMO+1)	2.81 (440)	0.030		

n[2]A mixed   2.93 (423)   0.010

^a Wavelength in parenthesis.
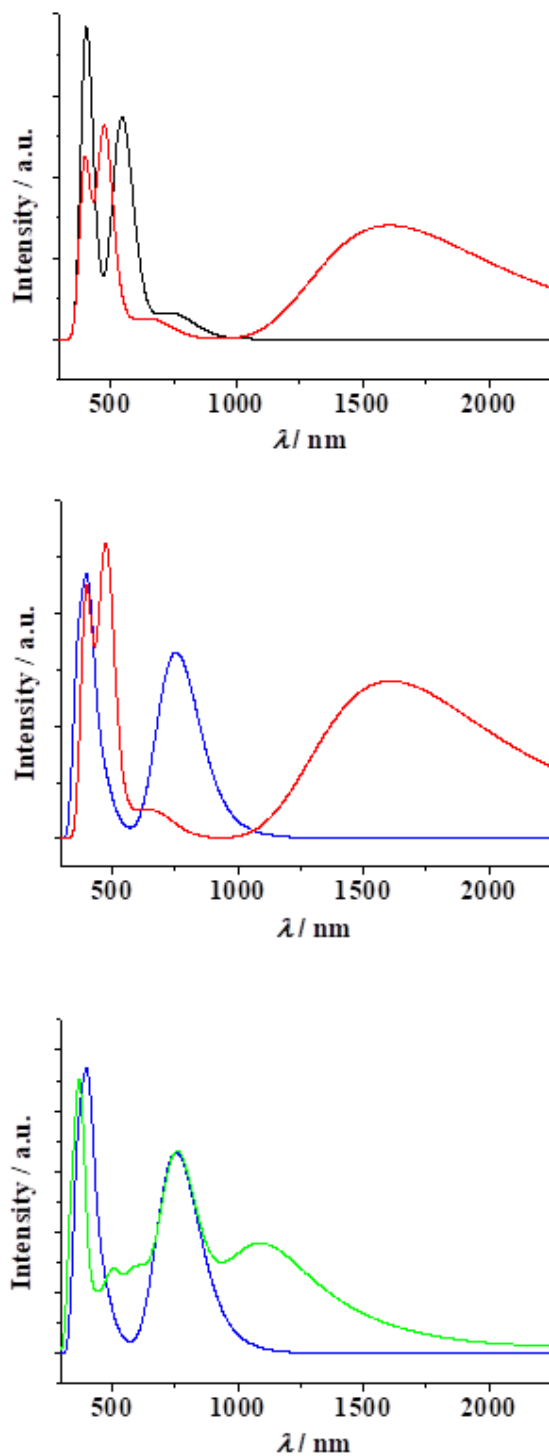
Figure 10.A5. TD-DFT simulated UV-Vis-NIR spectra of [(trpy')Ru(μ-adc-Sal)Ru(trpy')]ⁿ⁺ ; n = 0 (black line), n = 1 (red line), n = 2 (blue line) and n = 3 (green line).

n=0
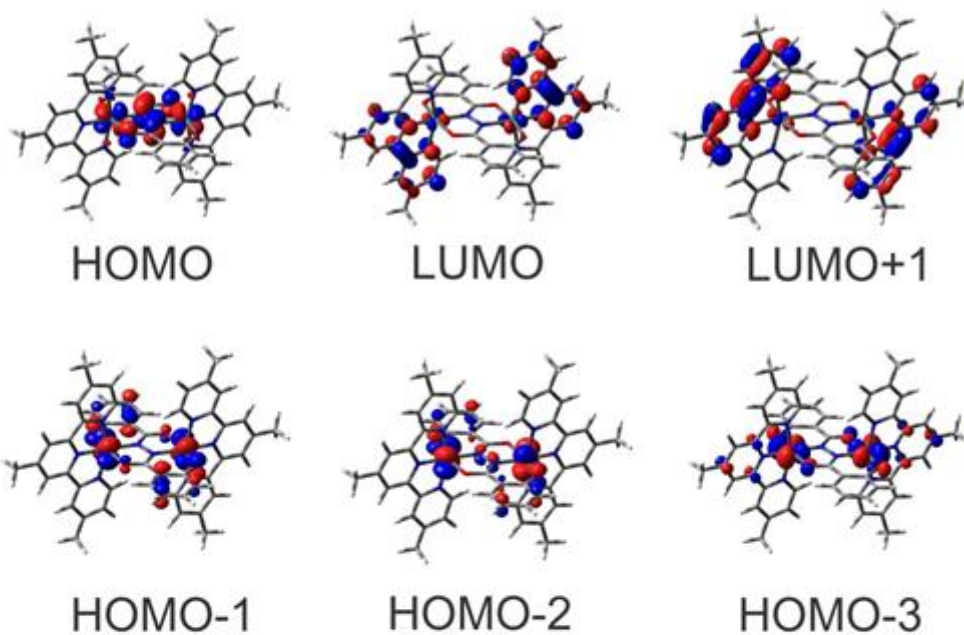
n=1
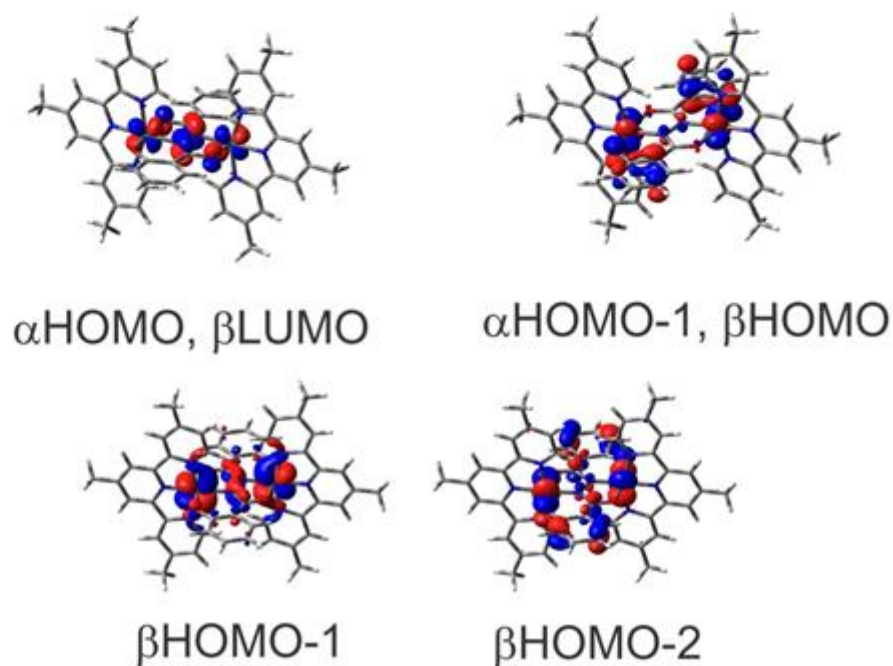
Figure 10.A6. DFT calculated shapes of frontier MOs involved in the lowest lying excitations of [(trpy')Ru(μ-adc-Sal)Ru(trpy')]$^{n+}$, n = 0 and 1.

n=2

βLUMO βLUMO+1

βHOMO βHOMO-1 βHOMO-3

n=3

βLUMO βLUMO+1

βHOMO-1 βHOMO-1 βHOMO-2
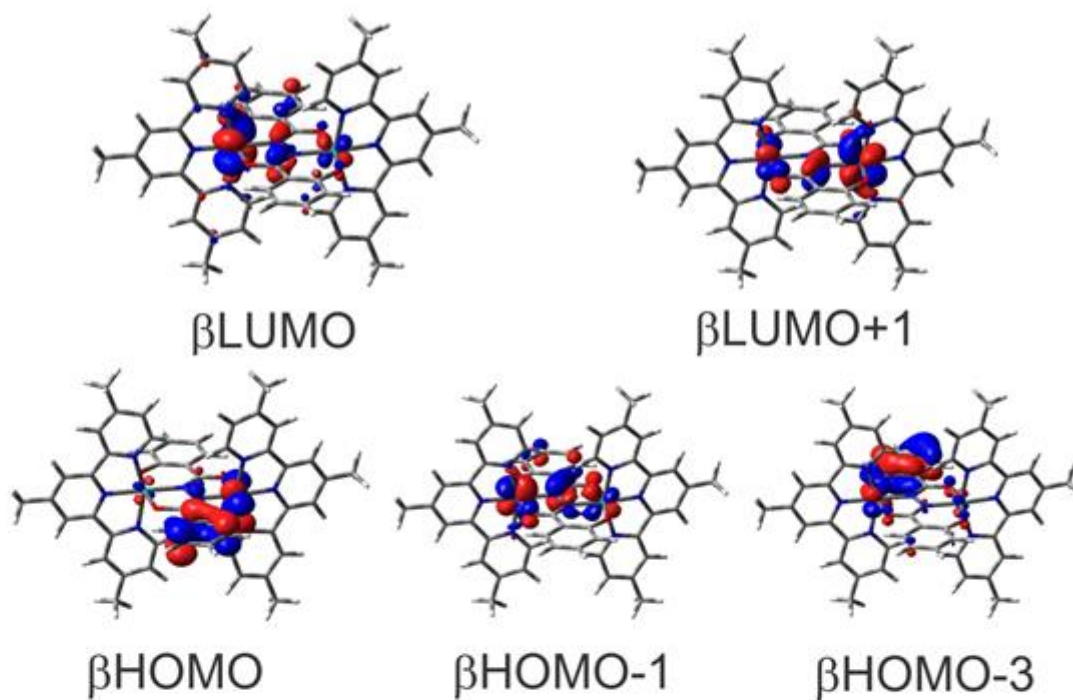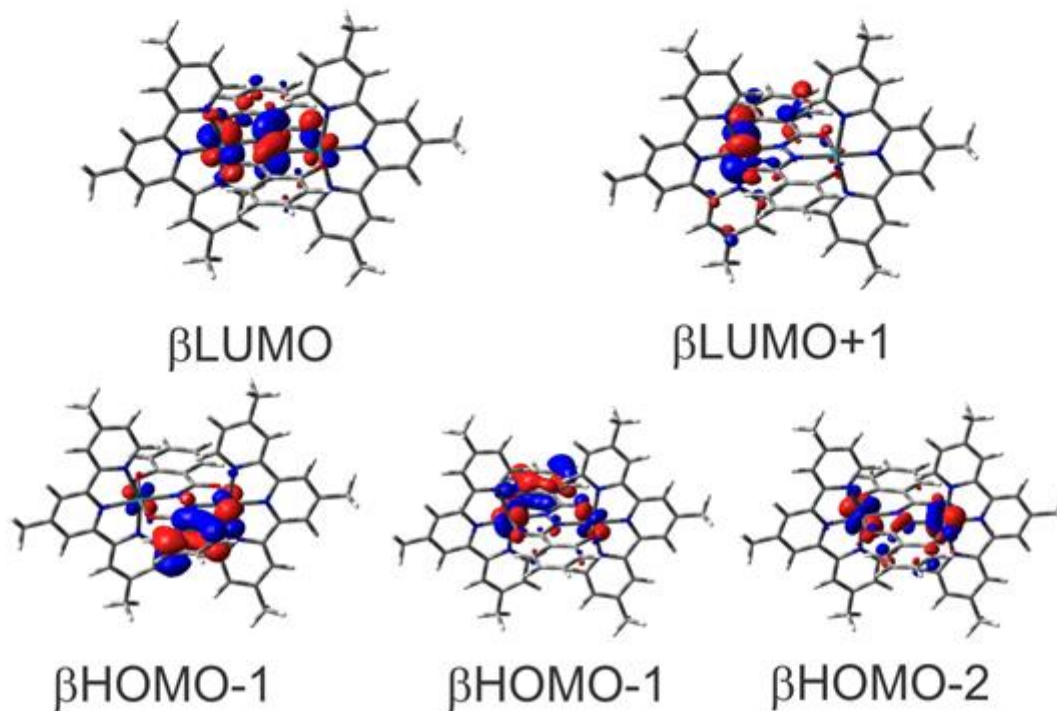
Figure 10.A7. DFT calculated shapes of frontier MOs involved in the lowest lying excitations of [(trpy')Ru(μ-adc-Sal)Ru(trpy')]$^{n+}$, n = 2 and 3.

10.2 Abbreviation

acac	acetylacetonate
adc-R	azodicarbonyl-ligand
adc-R(2-)	1,2-dicarbonylhydrazido(2-)
b	broad (NMR signal)
B	magnetic field
BL	bridging ligand
bpy	2,2´-bipyridine
Bu_4NPF_6	tetrabutylammonium hexafluorophosphate
C	chemical reaction
calc.	calculated
cm	centimeter
d	doublet
dd	doublet of a doublet
deconv.	deconvoluted
δ	chemical shift
Δg	g anisotropy
$\Delta\nu_{1/2}$	band width at half height
E	potential / electron transfer reaction
ε	molar extinction coefficient
EPR	Electron Paramagnetic Resonance
ET	electron transfer
Et_3N	triethylamine
EtOH	ethanol
exp.	experimental
$Fc^{+/0}$	ferrocenium/ ferrocene
g	gram
g_e	free electron g value
G	gauss
H_{ab}	electronic coupling parameter
H_2adc-^tBu	1,2-bis(pivaloyl)hydrazine
H_2adc-CF_3	1,2-bis(trifluoroacetyl)hydrazine
H_2adc-Ph	1,2-bis(benzoyl)hydrazine

H$_2$adc-Py	1,2-bis(picolinoyl)hydrazine
H$_4$adc-Sal	1,2-bis(salicyloyl)hydrazine
H$_3$adc-Salph	1-benzoyl-2-salicyloylhydrazine
HOMO	Highest Occupied Molecular Orbital
Hz	hertz
I	nuclear spin
ILCT	Intra Ligand Charge Transfer
IR	infrared
IVCT	Inter Valence Charge Transfer
K_c	comproportionation constant
L	ligand
λ	wavelength
LLCT	ligand to ligand charge transfer
LMCT	ligand to metal charge transfer
LUMO	Lowest Unoccupied Molecular Orbital
m	mole / multiplet
M	molar / metal
MeOH	methanol
MeCN	acetonitrile
mer	meridional
mg	miligram
MHz	megahertz
mL	mililitre
MLCT	Metal to Ligand Charge Transfer
MLLCT	Metal-Ligand to Ligand Charge Transfer
MMCT	metal to metal charge transfer
mmol	milimole
MO	molecular orbital
mol	mole
mV	millivolt
MV	mixed-valent/mixed-valence
ν	wavenumbers
nat.	natural
NHE	normal hydrogen electrode

NIR	near infrared
nm	nanometer
NMR	Nuclear Magnetic Resonance
n.o.	not observed
°	degree
°C	degree centigrade
OTTLE cell	Optically Transparent Thin Layer Electrochemical cell
ox	oxidaton
Ph	phenyl
ppm	parts per million
pz	pyrazine
R	gas constant
red	reduction
S	electron spin
SCE	standard calomel electrode
sh	shoulder (UV or IR band)
sim.	simulated
SOMO	Singly Occupied Molecular Orbital
SSCE	saturated sodium chloride calomel electrode
t	triplet
T	temperature
trpy	2,2´:6´,2´´-terpyridine
trpy*	4,4′,4″-tri-*tert*-butyl-2,2′:6′,2″-terpyridine
trpy’	4,4′,4″-trimethyl-2,2′:6′,2″-terpyridine
UV	ultra violet
V	volt
vs.	versus
vis	visible

References.

(1)   Jørgensen, C. K. *Coord. Chem. Rev.* **1966**, *1*, 164.

(2)   Ward, M. D.; McCleverty, J. A. *J. Chem. Soc., Dalton Trans.* **2002**, 275.

(3)   a) Kaim, W. *Proc. Natl. Acad. Sci., India, Sect. A Phys. Sci.* **2016**, *86*, 445. b) Kaim, W. *Eur. J. Inorg. Chem.* **2012**, 343. c) Kaim, W. *Inorg. Chem.* **2011**, *50*, 9752. d) Kaim, W.; Beyer, K.; Filippou, V.; Záliš, S. *Coord. Chem. Rev.* **2018**, *355*, 173. e) Kaim, W.; Schwederski, B. *Coord. Chem. Rev.* **2010**, *254*, 1580.

(4)   Sproules, S.; Wieghardt, K. *Coord. Chem. Rev.* **2011**, *255*, 837.

(5)   a) Luca, O. R.; Crabtree, R. H. *Chem. Soc. Rev.* **2013**, *42*, 1440. b) Lyaskovskyy, V.; de Bruin, B. *ACS Catal.* **2012**, *2*, 270. c) Chirik, P. J.; Wieghardt, K. *Science* **2010**, *327*, 794.

(6)   Demir, S.; Jeon, I.; Long, J. R.; Harris, T. D. *Coord. Chem. Rev.* **2015**, *289–290*, 149.

(7)   Kaim, W. *Coord. Chem. Rev.* **2001**, *219-221*, 463.

(8)   Frantz, S.; Reinhardt, R.; Greulich, S.; Wanner, M.; Fiedler, J.; Duboc-Toia, C.; Kaim, W. *Dalton Trans.* **2003**, 3370.

(9)   Ehret, F.; Bubrin, M.; Hübner, R.; Schweinfurth, D.; Hartenbach, I.; Záliš, S.; Kaim, W. *Inorg. Chem.* **2012**, *51*, 6237.

(10)   Roy, S.; Sieger, M.; Sarkar, B.; Schwederski, B.; Lissner, F.; Schleid, T.; Fiedler, J.; Kaim, W. *Angew. Chem. Int. Ed.* **2008**, *47*, 6192.

(11)   Creutz, C.; Taube, H. *J. Am. Chem. Soc.* **1969**, *91*, 3988.

(12)   Creutz, C.; Taube, H. *J. Am. Chem. Soc.* **1973**, *95*, 1086.

(13)   Heckmann, A.; Lambert, C. *Angew. Chem. Int. Ed.* **2012**, *51*, 326.

(14)   Kaim, W.; Sarkar, B. *Coord. Chem. Rev.* **2007**, *251*, 584.

(15)   a) Collin, J.-P.; Lainé, P.; Launay, J.-P.; Sauvage, J.-P.; Sour, A. *J. Chem.*

Soc., Chem. Commun. **1993**, 434. b) Beley, M.; Collin, J.-P.; Louis, R.; Metz, B.; Sauvage, J.-P. *J. Am. Chem. Soc.* **1991**, *113*, 8521. c) Sutter, J.-P.; Grove, D. M.; Beley, M.; Collin, J.-P.; Veldman, N.; Spek, A. L.; Sauvage, J.-P.; van Koten, G. *Angew. Chem. Int. Ed.* **1994**, *33*, 1282. d) Beley, M.; Chodorowski-Kimmes, S.; Collin, J.-P.; Lainé, P.; Launay, J.-P.; Sauvage, J.-P. *Angew. Chem. Int. Ed.* **1994**, *33*, 1775.

(16) Mallick, S.; Cheng, T.; Chen, L.; Meng, M.; Zhang, Y. Y.; Liu, C. Y. *Dalton Trans.* **2017**, *46,* 5711.

(17) Rocha, R. C.; Rein, F. N.; Jude, H.; Shreve, A. P.; Concepcion, J. J.; Meyer, T. J. *Angew. Chem. Int. Ed.* **2008**, *47*, 503.

(18) Gluyas, J. B. G.; Gückel, S.; Kaupp, M.; Low, P. J. *Chem. Eur. J.* **2016**, *22*, 16138.

(19) Mandal, A.; Agarwala, H.; Ray, R.; Plebst, S.; Mobin, S. M.; Priego, J. L.; Jiménez-Aparicio, R.; Kaim, W.; Lahiri, G. K. *Inorg. Chem.* **2014**, *53*, 6082.

(20) Nagashima, T.; Nakabayashi, T.; Suzuki, T.; Kanaizuka, K.; Ozawa, H.; Zhong, Y. W.; Masaoka, S.; Sakai, K.; Haga, M. A. *Organometallics* **2014**, *33*, 4893.

(21) Sarkar, B.; Patra, S.; Fiedler, J.; Sunoj, R. B.; Janardanan, D.; Lahiri, G. K.; Kaim, W. *J. Am. Chem. Soc.* **2008**, *130*, 3532.

(22) Solomon, E. I.; Xie, X.; Dey, A. *Chem. Soc. Rev.* **2008**, *37*, 623.

(23) Siegbahn, P. E. M. *Acc. Chem. Res.* **2009**, *42*, 1871.

(24) Dau, H.; Limberg, C.; Reier, T.; Risch, M.; Roggan, S. *ChemCatChem* **2010**, *2*, 724.

(25) Schinzel, S.; Schraut, J.; Arbuznikov, A. V; Siegbahn, P. E. M.; Kaupp, M. *Chem. Eur. J.* **2010**, *16*, 10424.

(26) Low, P. J. *Dalton Trans.* **2005**, 2821.

(27) Lu, Y.; Quardokus, R.; Lent, C. S.; Justaud, F.; Lapinte, C.; Kandel, S. A. *J. Am. Chem. Soc.* **2010**, *132*, 13519.

(28) Brunschwig, B. S.; Creutz, C.; Sutin, N. *Chem. Soc. Rev.* **2002**, *31*, 168.

(29) Launay, J.-P. *Coord. Chem. Rev.* **2013**, *257*, 1544.

(30) Chisholm, M. H. *Coord. Chem. Rev.* **2013**, *257*, 1576.

(31) Low, P. J. *Coord. Chem. Rev.* **2013**, *257*, 1507.

(32) a) Kaim, W.; Klein, A.; Glöckle, M. *Acc. Chem. Res.* **2000**, *33*, 755. b) Kaim, W.; Lahiri, G. K. *Angew. Chem.* **2007**, *119*, 1808; *Angew.Chem. Int. Ed.* **2007**, *46*, 1778.

(33) Demadis, K. D.; Hartshorn, C. M.; Meyer, T. J. *Chem. Rev.* **2001**, *101*, 2655.

(34) D'Alessandro, D. M.; Keene, F. R. *Chem. Soc. Rev.* **2006**, *35*, 424.

(35) a) Marcus, R. A.; Sutin, N. *Biochim. Biophys. Acta* **1985**, *811*, 265. b) Marcus, R. A. *Angew. Chem.* **1993**, *105*, 1161.

(36) a) Hush, N. S. *Coord. Chem. Rev.* **1985**, *64,* 135. b) Hush, N. S. *Prog. Inorg. Chem.* **1967**, *8*, 391.

(37) Dong, T. Y.; Hwang, M.-Y.; Hsu, T.-L.; Schei, C.-C.; Yeh, S.-K. *Inorg. Chem.* **1990**, *29*, 80.

(38) Pieslinger, G. E.; Alborés, P.; Slep, L. D.; Baraldo, L. M. *Angew. Chem. Int. Ed.* **2014**, *53*, 1293.

(39) Zoerb, M. C.; Henderson, J. S.; Glover, S. D.; Lomont, J. P.; Nguyen, S. C.; Hill, A. D.; Kubiak, C. P.; Harris, C. B. *J. Phys. Chem. B* **2015**, *119*, 10738.

(40) Dong, T.-Y.; Lai, X.-Q.; Lin, Z.-W.; Lin, K.-J. *Angew. Chem. Int. Ed.* **1997**, *36*, 2002.

(41) Oh, D. H.; Sano, M.; Boxer, S. G. *J. Am. Chem. Soc.* **1991**, *113*, 6880.

(42) Winter, R. F. *Organometallics* **2014**, *33*, 4517.

(43) Chen, Y. J.; Kao, C.-H.; Lin, S. J.; Tai, C.-C.; Kwan, K. S. *Inorg. Chem.* **2000**, *39*, 189.

(44) Wu, S.-H.; Burkhardt, S. E.; Yao, J.; Zhong, Y.-W.; Abruña, H. D. *Inorg. Chem.* **2011**, *50*, 3959.

(45) Salsman, J. C.; Kubiak, C. P.; Ito, T. *J. Am. Chem. Soc.* **2005**, *127*, 2382.

(46) Kaim, W.; Kasack, V.; Binder, H.; Roth, E.; Jordanov, J. *Angew. Chem. Int. Ed.* **1988**, *27*, 1174.

(47) Kaim, W.; Kohlmann, S. *Inorg. Chem.* **1987**, *26*, 68.

(48) Jana, R.; Sarkar, B.; Bubrin, D.; Fiedler, J.; Kaim, W. *Inorg. Chem. Commun.* **2010**, *13*, 1160.

(49) a) Zhao, H.; Neamati, N.; Sunder, S.; Hong, H.; Wang, S.; Milne, G. W. A.; Pommier, Y.; Burke, T. R. Jr. *J. Med. Chem.* **1997**, *40*, 937. b) Neamati, N.; Lin, Z.; Karki, R. G.; Orr, A.; Cowansage, K.; Strumberg, D.; Pais, G. C. G.; Voigt, J. H.; Nicklaus, M. C.; Winslow, H. E.; Zhao, H.; Turpin, J. A.; Yi, J.; Skalka, A. M.; Burke, T. R. Jr.; Pommier, Y. *J. Med. Chem.* **2002**, *45*, 5661.

(50) a) Yao, C.; Zhong, Y.; Yao, J. *J. Am. Chem. Soc.* **2011**, *133*, 15697. b) Knödler, A.; Fiedler, J.; Kaim, W. *Polyhedron* **2004**, *23*, 701. c) Zhong, Y. W.; Wu, S. H.; Burkhardt, S. E.; Yao, C. J.; Abruña, H. D. *Inorg. Chem.* **2011**, *50*, 517. d) Wang, L.; Yang, W. W.; Zheng, R. H.; Shi, Q.; Zhong, Y. W.; Yao, J. *Inorg. Chem.* **2011**, *50*, 7074. e) Wu, S. H.; Burkhardt, S. E.; Zhong, Y. W.; Abruña, H. D. *Inorg. Chem.* **2012**, *51*, 13312.

(51) Kasack, V.; Kaim, W.; Binder, H.; Jordanov, J.; Roth, E. *Inorg. Chem.* **1995**, *34*, 1924.

(52) a) Marelius, D. C.; Bhagan, S.; Charboneau, D. J.; Schroeder, K. M.; Kamdar, J. M.; McGettigan, A. R.; Freeman, B. J.; Moore, C. E.; Rheingold, A. L.; Cooksy, A. L.; Smith, D. K.; Paul, J. J.; Papish, E. T.; Grotjahn, D. B.; *Eur. J. Inorg. Chem.* **2014**, 676. b) Benavides, P. A.; Matias, T. A.; Araki, K.; *Dalton Trans.* **2017**, *46*, 15567.

(53) a) Maloth, S.; Pal, S. *Inorg. Chim. Acta* **2011,** *372*, 407. b) Hoover, J. M.; DiPasquale, A.; Mayer, J. M.; Michael, F. E. *J. Am. Chem. Soc.* **2010,** *132*, 5043. c) Congrave, D. G.; Hsu, Y.; Batsanov, A. S.; Beeby, A.; Bryce, M. R. *Organometallics* **2017,** *36*, 981.

(54) a) Marabella, C. P.; Enemark, J. H.; Newton, W. E.; McDonald, J. W. *Inorg. Chem.* **1982,** *21,* 623. b) Ittel, S. D.; Ibers, J. A. *Inorg. Chem.* **1973,** *12,* 2290.

(55) Kaim, W.; Paretzki, A. *Coord. Chem. Rev.* **2017**, *344,* 345.

(56) Mandal, A.; Schwederski, B.; Fiedler, J.; Kaim, W.; Lahiri, G. K. *Inorg. Chem.* **2015,** *54,* 8126.

(57) a) Bhattacharya, S.; Boone, S. R.; Fox, G. A.; Pierpont, C. G. *J. Am. Chem. Soc.* **1990,** *112,* 1088. b) Haga, M.; Isobe, K.; Boone, S. R.; Pierpont, C. G. *Inorg. Chem.* **1990,** *29,* 3795.

(58) a) Feese, M. D.; Ingason, B. P.; Goranson-Siekierke, J.; Holmes, R. K.; Hol, W. G. J. *J. Biol. Chem.* **2001,** *276,* 5959. b) Roach, P. L.; Clifton, I. J.; Hensgens, C. M. H.; Shibata, N.; Schofield, C. J.; Hajdu, J.; Baldwin, J. E. *Nature* **1997,** *387,* 827. c) White, A.; Ding, X.; vanderSpek, J. C.; Murphy, J. R.; Ringe, D. *Nature*, **1998,** *394,* 502.

(59) Stone, A. J. *Mol. Phys.* **1964**, *7*, 311.

(60) Ye, S.; Sarkar, B.; Duboc, C.; Fiedler, J.; Kaim. W. *Inorg. Chem.* **2005,** *44,* 2843.

(61) Diggle, J. W.; Parker, A. J. *Electrochim. Acta* **1973,** *18,* 975. b) Sahami, S.; Weaver, M. J. *J. Solution Chem.* **1981,** *10,* 199.

(62) Ebadi, M.; Lever, A. B. P. *Inorg. Chem.* **1999,** *38,* 467.

(63) Mukuta, T.; Fukazawa, N.; Murata, K.; Inagaki, A.; Akita, M.; Tanaka, S.; Koshihara, S.; Onda, K. *Inorg. Chem.* **2014,** *53,* 2481.

(64) Lahiri, G. K.; Bhattacharya, S.; Ghosh, B. K.; Chakravorty, A. *Inorg. Chem.* **1987,** *26*, 4324.

(65) Haga, M.; Dodsworth, E. S.; Lever, A. B. P. *Inorg. Chem.* **1986,** *25*, 447

(66) .Salassa, L.; Garino, C.; Salassa, G.; Nervi, C.; Gobetto, R.; Lamberti, C.; Gianolio, D.; Bizzarri, R.; Sadler, P. J. *Inorg. Chem.* **2009,** *48*, 1469.

(67) Hesek, D.; Inoue, Y.; Everitt, S. R. L.; Ishida, H.; Kunieda, M.; Drew, M. G. B. *J. Chem. Soc., Dalton Trans.* **1999**, 3701.

(68) Kaim, W.; Sarkar, B. *Coord. Chem. Rev.* **2013**, *257*, 1650.

(69) Kaim, W.; Kasack, V. *Inorg. Chem.* **1990**, *29*, 4696.

(70) Roy, S.; Sarkar, B.; Imrich, H.-G.; Fiedler, J.; Záliš, S.; Jimenez-Aparicio, R.; Urbanos, F. A.; Mobin, S. M.; Lahiri, G. K.; Kaim, W. *Inorg. Chem.* **2012**, *51* 9273.

(71) Roy, S.; Sieger, M.; Singh, P.; Niemeyer, M.; Fiedler, J.; Duboc, C.; Kaim, W. *Inorg. Chim. Acta* **2008**, *361*, 1699.

(72) Krejčík, M.; Daněk, M.; Hartl, F. *J. Electroanal. Chem.* **1991**, *317*, 179.

(73) Waser, J.; Carreira, E. M. *Angew. Chem. Int. Ed.* **2004**, *43*, 4099.

(74) Waser, J.; Gaspar, B.; Nambu, H.; Carreira, E. M. *J. Am. Chem. Soc.* **2006**, *128*, 11693.

(75) Köthe, C.; Metzinger, R.; Limberg, C. *Eur. J. Inorg. Chem.* **2013**, 3937.

(76) Muñiz, K.; Nieger, M. *Angew. Chem. Int. Ed.* **2006**, *45*, 2305.

(77) Uhl, W.; Voß, M.; Hepp, A. *Z. Anorg. Allg. Chem.* **2011**, *637*, 1845.

(78) Einstein, F. W. B.; Nussbaum, S.; Sutton, D.; Willis, A. C. *Organometallics* **1983**, *2*, 1259.

(79) Nikolić, S.; Ćirić, I.; Roller, A.; Lukeš, V.; Arion, V. B.; Grgurić-Šipka, S. *New J. Chem.* **2017**, *41*, 6857.

(80) Zheng, Y.; Batsanov, A. S.; Fox, M. A.; Al-Attar, H. A.; Abdullah, K.; Jankus, V.; Bryce, M. R.; Monkman, A. P. *Angew. Chem. Int. Ed.* **2014**, *53*, 11616.

(81) Johnson, B. A.; Agarwala, H.; White, T. A.; Mijangos, E.; Maji, S.; Ott, S. *Chem. Eur. J.* **2016**, *22*, 14870.

(82) Concepcion, J. J.; Jurss, J. W.; Brennaman, M. K.; Hoertz, P. G.; Patrocinio, A. O. T.; Iha, N. Y. M.; Templeton, J. L.; Meyer, T. J. *Acc. Chem. Res.* **2009**, *42*, 1954.

(83) Chen, Z.; Kang, P.; Zhang, M.-T.; Meyer, T. J. *Chem. Commun.* **2014**, *50*, 335.

(84) Chrzanowska, M.; Katafias, A.; Impert, O.; Kozakiewicz, A.; Surdykowski, A.; Brzozowska, P.; Franke, A.; Zahl, A.; Puchta, R.; van Eldik, R. *Dalton Trans.* **2017**, *46*, 10264.

(85) Nakamura, G.; Kondo, M.; Crisalli, M.; Lee, S. K.; Shibata, A.; Ford, P. C.; Masaoka, S. *Dalton Trans.* **2015**, *44*, 17189.

(86) Lahiri, G. K.; Kaim, W. *Dalton Trans.* **2010**, *39*, 4471.

(87) Sui, L. Z.; Yang, W. W.; Yao, C. J.; Xie, H. Y.; Zhong, Y. W. *Inorg. Chem.* **2012**, *51*, 1590.

(88) Pal, A. K.; Hanan, G. S. *Chem. Soc. Rev.* **2014**, *43*, 6184.

(89) Hage, R.; Haasnoot, J. G.; Nieuwenhuis, H. A.; Reedijk, J.; De Ridder, D. J. A.; Vos, J. G. *J. Am. Chem. Soc.* **1990**, *112*, 9245.

(90) Goldsby, K. A.; Meyer, T. J. *Inorg. Chem.* **1984**, *23*, 3002.

(91) Otsuki, J.; Imai, A.; Sato, K.; Li, D.-M.; Hosoda, M.; Owa, M.; Akasaka, T.; Yoshikawa, I.; Araki, K.; Suenobu, T.; Fukuzumi, S. *Chem. Eur. J.* **2008**, *14*, 2709.

(92) Matheis, W.; Kaim, W. *Inorg. Chim. Acta* **1991**, *181*, 15.

(93) Laidlaw, W. M.; Thompson, A. L.; Denning, R. G. *Dalton Trans.* **2013**, *42*, 4695.

(94) Zhong, Y. W.; Gong, Z. L.; Shao, J. Y.; Yao, J. *Coord. Chem. Rev.* **2016**, *312*, 22.

(95) Mandal, A.; Hoque, M. A.; Grupp, A.; Paretzki, A.; Kaim, W.; Lahiri, G. K. *Inorg. Chem.* **2016**, *55*, 2146.

(96) Rocha, R. C.; Toma, H. E. *Inorg. Chim. Acta* **2000**, *310*, 65.

(97) Yang, W.-W.; Yao, J.; Zhong, Y.-W. *Organometallics* **2012**, *31*, 8577.

(98) Pieslinger, G. E.; Aramburu-Trošelj, B. M.; Cadranel, A.; Baraldo, L. M. *Inorg. Chem.* **2014**, *53*, 8221.

(99) Kaim, W. *Coord. Chem. Rev.* **2011**, *255*, 2503.

(100) Liu, S.-X.; Lin, S.; Lin, B. Z.; Lin, C.-C.; Huang, J.-Q. *Angew. Chem. Int. Ed.* **2001**, *40*, 1084.

(101) Majumder, A.; Goswami, S.; Batten, S. R.; Salah El Fallah, M.; Ribas, J.; Mitra, S. *Inorg. Chim. Acta* **2006**, *359*, 2375.

(102) Sutradhar, M.; Kirillova, M. V.; Guedes da Silva, M. F. C.; Martins, L. M. D. R. S.; Pombeiro, A. J. L. *Inorg. Chem.* **2012**, *51*, 11229.

(103) Luo, W.; Wang, X.-T.; Meng, X.-G.; Cheng, G.-Z.; Ji, Z.-P. *Polyhedron* **2009**, *28*, 300.

(104) Luo, W.; Meng, X.-G.; Xiang, J.-F.; Duan, Y.; Cheng, G.-Z.; Ji, Z.-P. *Inorg. Chim. Acta* **2008**, *361*, 2667.

(105) Luo, W.; Wang, X.-T.; Meng, X.-G.; Cheng, G.-Z.; Ji, Z.-P. *Inorg. Chem. Commun.* **2008**, *11*, 1044.

(106) Kamatchi, T. S.; Mondal, S.; Scherer, T.; Bubrin, M.; Natarajan, K.; Kaim, W. *Chem. Eur. J.* **2017**, *23*, 17810.

(107) Sedney, D.; Ludi, A. *Inorg. Chim. Acta* **1981**, *47*, 153.

(108) Gooden, V. M.; Dasgupta, T. P.; Gordon, N. R.; Sadler, G. G. *Inorg. Chim. Acta* **1998**, *268*, 31.

(109) Ito, T.; Imai, N.; Yamaguchi, T.; Hamaguchi, T.; Londergan, C. H.; Kubiak, C. P. *Angew. Chem. Int. Ed.* **2004**, *43*, 1376.

(110) Yu, W. Y.; Meng, M.; Lei, H.; He, X. D.; Liu, C. Y. *J. Phys. Chem. C* **2016**, *120*, 12411.

(111) Kaim, W.; Schwederski, B.; Klein, A. *Bioinorganic Chemistry*, 2nd Edition; Wiley: Chichester, U.K., 2013.

(112) Dogan, A.; Schwederski, B.; Schleid, T.; Lissner, F.; Fiedler, J.; Kaim, W. *Inorg. Chem. Commun.* **2004**, *7*, 220.

(113) Bernhardt, P. V; Chin, P.; Richardson, D. R. *Dalton Trans.* **2004**, 3342.

(114) Bu, X.-H.; Liu, H.; Du, M.; Zhang, L.; Guo, Y.-M. *Inorg. Chem.* **2002**, *41*, 1855.

(115) Shao, S.; Zhu, D.; Song, Y.; You, X. Z.; Raj, S. S. S.; Fun, H.-K. *Acta Crystallogr., Sect. C* **1999**, *55*, 1841.

(116) Yao, C.-J.; Nie, H.-J.; Yang, W.-W.; Yao, J.; Zhong, Y.-W. *Inorg. Chem.* **2015**, *54*, 4688.

(117) D'Alessandro, D. M.; Keene, F. R. *Chem. Phys.* **2006**, *324*, 8.

(118) a) D'Alessandro, D. M. *Chem. Commun.* **2016**, *52*, 8957. b) Faust, T. B.; D'Alessandro, D. M. *RSC Adv.* **2014**, *4*, 17498.

(119) a) Day, P., ed., *Molecules Into Materials*; World Scientific Publishing: Singapore, 2007. b) Borrás-Almenar, J. J.; Clemente-Juan, J. M.; Coronado, E.; Palii, A.; Tsukerblat, B. S. in *Magnetic Properties of Mixed-Valence Clusters: Theoretical Approaches and Applications, in Magnetism: Molecules to Materials I: Models and Experiments*; Miller, J. S.; Drillon, M., eds.; Wiley-VCH: Weinheim (Germany), 2001. (c) Kaim, W.; Bruns, W.; Poppe, J.; Kasack, V. *J. Mol. Struct.* **1993**, *292*, 221. (d) Prassides, K. *Mixed Valency Systems: Applications in Chemistry, Physics and Biology*; Kluwer Academic Publishers: Dordrecht (The Netherlands), 1991. (e) Launay, J.-P.; Verdaguer, M. *Electrons in Molecules*; Oxford University Press: Oxford, 2014.

(120) a) Creutz, C. *Progr. Inorg. Chem.* **1983**, *30*, 1. b) Poppe, J.; Moscherosch, M.; Kaim, W. *Inorg. Chem.* **1993**, *32*, 2640. c) Baumann, F.; Kaim, W.; Garcia Posse, M.; Katz, N. E. *Inorg. Chem.* **1998**, *37*, 658.

(121) a) Ruminki, R.; Kiplinger, J.; Cockroft, T.; Chase, C. *Inorg. Chem.* **1989**, *28*, 370. b) Chanda, N.; Laye, R. H.; Chakraborty, S.; Paul, R. L.; Jeffery, J. C.; Ward, M. D.; Lahiri, G. K. *J. Chem. Soc., Dalton Trans.* **2002**, 3496. c) Chanda, N.; Sarkar, B.; Fiedler, J.; Kaim, W.; Lahiri, G. K. *Dalton Trans.* **2003**, 3550. d) Chanda, N.; Sarkar, B.; Fiedler, J.; Kaim, W.; Lahiri, G. K. *Inorg. Chem.* **2004**, *43*, 5128. (e) Ghumaan, S.; Sarkar, B.; Chanda, N.; Sieger, M.; Fiedler, J.; Kaim, W.; Lahiri, G. K. *Inorg. Chem.* **2006**, *45*, 7955. f) Koley, M.; Sarkar, B.; Ghumaan, S.; Bulak, E.; Fiedler, J.; Kaim, W.; Lahiri, G. K. *Inorg. Chem.* **2007**, *46*, 3736.

(122) a) Cheaib, K.; Martel, D.; Clément, N.; Eckes, F.; Kouaho S.; Rogez, G.; Dagorne, S.; Kurmoo, M.; Choua, S.; Welter, R. *Dalton Trans.* **2013**, *42*, 1406. (b) Bernhardt, P. V.; Chin, P.; Sharpe, P. C.; Wang, J.-Y. C.; Richardson, D. R. *J. Biol Inorg. Chem.* **2005**, *10*, 761.

(123) Mondal, P.; Chatterjee, M.; Paretzki, A.; Beyer, K.; Kaim, W.; Lahiri, G. K. *Inorg. Chem.* **2016**, *55*, 3105.

(124) Rieger, P. H. *Electron Spin Resonance*; The Royal Society of Chemistry: Cambridge, U.K., 2007.

(125) a) Kumbhakar, D.; Sarkar, B.; Maji, S.; Mobin, S. M.; Fiedler, J.; Urbanos, F. A.; Jimnez-Aparicio, R.; Kaim. W.; Lahiri, G. K. *J. Am. Chem. Soc.* **2008**, *130*, 17575. b) Chaudhuri, P.; Verani, C. N.; Bill, E.; Bothe. E.; Weyhermuller, T.; Wieghardt, K. *J. Am. Chem. Soc.* **2001**, *123*, 2213.

(126) Ye, S.; Sarkar, B.; Lissner, F.; Schleid, T.; van-Slageren, J.; Fiedler, J.; Kaim, W. *Angew. Chem. Int. Ed.* **2005**, *44*, 2103.

(127) Stebler, A.; Ammeter, J. H.; Fürholz, U.; Ludi, A. *Inorg. Chem.* **1984**, *23*, 2764.

(128) a) LeClair, G.; Wang, Z. Y. *J. Solid State Electrochem.* **2009**, *13*, 365 b) Wang, Z. Y.; Zhang, J.; Wu, X.; Birau, M.; Yu, G.; Yu, H.; Qi, Y.; Desjardin, P.; Meng, X.; Gao, J. P.; Todd, E.; Song, N.; Bai, Y.; Beaudin, A. M. R.; LeClair, G. *Pure Appl. Chem.* **2004**, *76*, 1435. c) Qi, Y.; Desjardins, P.; Wang, Z. Y. *J. Opt. A: Pure Appl. Opt.* **2002**, *4*, S273. d) Qi, Y.; Wang, Z. Y. *Macromolecules* **2003**, *36*, 3146. e) Wang, S.; Li, X.; Xun, S.; Wan, X.; Wang, Z. Y. *Macromolecules* **2006**, *39*, 7502. f) Xun, S.; LeClair, G.; Zhang, J.; Chen. X.; Gao, J. P.; Wang,

Z. Y. *Org. Lett.* **2006**, *8*, 1697. g) Xun, S.; Zhang, J.; Li, X.; Ma, D.; Wang, Z. Y. *Synth. Met.* **2008**, *158*, 484.

(129) Fulmer, G. R.; Miller, A. J. M.; Sherden, N. H.; Gottlieb, H. E.; Nudelman, A.; Stoltz, B. M.; Bercaw, J. E.; Goldberg, K. I. *Organometallics* **2010**, *29*, 2176.

(130) Sheldrick, G. M. *SHELXL-97: Program for Crystal Structure Determination*; University of Gottingen: Göttingen, Germany, 1997.

(131) Gaussian 09, Revision D.01, Frisch, M. J.; Trucks, G. W.; Schlegel, H. B.; Scuseria, G. E.; Robb, M. A.; Cheeseman, J. R.; Scalmani, G.; Barone, V.; Mennucci, B.; Petersson, G. A.; Nakatsuji, H.; Caricato, M.; Li, X.; Hratchian, H. P.; Izmaylov, A. F.; Bloino, J.; Zheng, G.; Sonnenberg, J. L.; Hada, M.; Ehara, M.; Toyota, K.; Fukuda, R.; Hasegawa, J.; Ishida, M.; Nakajima, T.; Honda, Y.; Kitao, O.; Nakai, H.; Vreven, T.; Montgomery, J. A., Jr.; Peralta, J. E.; Ogliaro, F.; Bearpark, M.; Heyd, J. J.; Brothers, E.; Kudin, K. N.; Staroverov, V. N. Kobayashi, R.; Normand, J.; Raghavachari, K.; Rendell, A.; Burant, J. C.; Iyengar, S. S.; Tomasi, J.; Cossi, M.; Rega, N.; Millam, J. M.; Klene, M.; Knox, J. E.; Cross, J. B.; Bakken, V.; Adamo, C.; Jaramillo, J.; Gomperts, R.; Stratmann, R. E.; Yazyev, O.; Austin, A. J.; Cammi, R.; Pomelli, C.; Ochterski, J. W.; Martin, R. L.; Morokuma, K.; Zakrzewski, V. G.; Voth, G. A.; Salvador, P.; Dannenberg, J. J.; Dapprich, S.; Daniels, A. D.; Farkas, O.; Foresman, J. B.; Ortiz, J. V.; Cioslowski, J.; Fox, D. J. Gaussian, Inc., Wallingford CT, 2009.

(132) a) te Velde, G.; Bickelhaupt, F. M.; van Gisbergen, S. J. A.; Fonseca Guerra, C.; Baerends, E. J.; Snijders, J. G.; Ziegler, T. *J. Comput. Chem.* **2001**, *22*, 931. b) ADF2014.06, SCM, Theoretical Chemistry, Vrije Universiteit, Amsterdam, The Netherlands, http://www.scm.com.

(133) Neese, F. *WIREs Comput Mol Sci* **2012**, *2*, 73.

(134) Groszkowski, S.; Wesolowska, B. *Arch. Pharm.* **1981**, *314*, 880.

(135) Reitz, D. B.; Finkes, M. J. *J. Heterocyclic Chem.* **1989**, *26*, 225.

(136) Butler, R. N.; Hanniffy, H. N.; Stephens, J. C.; Burke, L. A. *J. Org. Chem.* **2008**, *73*, 1354.

(137) Sullivan, B. P.; Salmon, D. J.; Meyer, T. J. *Inorg. Chem.* **1978**, *17*, 3334.

(138) Hadda, T. B.; Bozec, H. L. *Inorg. Chim. Acta* **1993**, *204*, 103.

(139) Lay, P. A.; Sargeson, A. M.; Taube, H. *Inorg. Synth.* **1986**, *24*, 291.

(140) Spek, A. L. *Acta Crystallogr., Sect. D* **2009**, *65*, 148.